

Scientific Report No. 22-2008

# Global Atmospheric Climatologies from Radio Occultation Data and Derivation of Diagnostic Parameters for Climate Monitoring

Michael Borsche

June 2008

Financially supported by

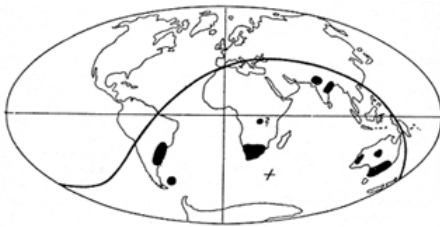


Wegener Center  
[www.wegcenter.at](http://www.wegcenter.at)



The **Wegener Center for Climate and Global Change** combines as an interdisciplinary, internationally oriented research center the competences of the University of Graz in the research area „Climate, Environmental and Global Change“. It brings together, in a dedicated building close to the University central campus, research teams and scientists from fields such as geo- and climate physics, meteorology, economics, geography, and regional sciences. At the same time close links exist and are further developed with many cooperation partners, both nationally and internationally. The research interests extend from monitoring, analysis, modeling and prediction of climate and environmental change via climate impact research to the analysis of the human dimensions of these changes, i.e, the role of humans in causing and being effected by climate and environmental change as well as in adaptation and mitigation. The director of the center, hosting about 35 researchers, is the geophysicist Gottfried Kirchengast, the lead partner and deputy director is the economist Karl Steininger. (more information at [www.wegcenter.at](http://www.wegcenter.at))

The present report is the result of a PhD thesis work completed in February 2008. The work was funded by the Austrian Research Promotion Agency–Aeronautics and Space Agency (FFG-ALR Project CHAMPCLIM) and the Austrian Science Fund (FWF Project CLIMROCC).



**Alfred Wegener** (1880-1930), after whom the Wegener Center is named, was founding holder of the University of Graz Geophysics Chair (1924-1930) and was in his work in the fields of geophysics, meteorology, and climatology a brilliant, interdisciplinary thinking and acting scientist and scholar, far ahead of his time with this style. The way of his ground-breaking research on continental drift is a shining role model — his sketch on the relationship of the continents based on traces of an ice age about 300 million years ago (left) as basis for the Wegener Center Logo is thus a continuous encouragement to explore equally innovative scientific ways: *ways emerge in that we go them* (Motto of the Wegener Center).

## Wegener Center Verlag • Graz, Austria

© 2008 All Rights Reserved.

Selected use of individual figures, tables or parts of text is permitted for non-commercial purposes, provided this report is correctly and clearly cited as the source. Publisher contact for any interests beyond such use: [wegcenter@uni-graz.at](mailto:wegcenter@uni-graz.at).

ISBN 978-3-9502308-9-5

June 2008

Contact: Dr. Michael Borsche  
[michael.borsche@uni-graz.at](mailto:michael.borsche@uni-graz.at)

Wegener Center for Climate and Global Change  
University of Graz  
Leechgasse 25  
A-8010 Graz, Austria  
[www.wegcenter.at](http://www.wegcenter.at)

# Global Atmospheric Climatologies from Radio Occultation Data and Derivation of Diagnostic Parameters for Climate Monitoring

Dissertation

zur Erlangung des akademischen Grades

**Doktor der Naturwissenschaften**

vorgelegt von

**MAG. MICHAEL BORSCHÉ**

an der Naturwissenschaftlichen Fakultät  
der Karl-Franzens-Universität Graz

Betreuer:

Univ.-Prof. Mag. Dr. Gottfried Kirchengast

Mitbetreuer:

Mag. Dr. Ulrich Foelsche



Wegener Center  
[www.wegcenter.at](http://www.wegcenter.at)



Wegener Zentrum für Klima und Globalen Wandel  
und  
Institutsbereich Geophysik, Astrophysik und Meteorologie  
Institut für Physik  
Karl-Franzens-Universität Graz

GRAZ, FEBRUAR 2008



# Acknowledgments

I would like to very much thank the supervisor of my PhD thesis Prof. G. Kirchengast for his excellent, inspiring and time-consuming scientific and personal support during the course of research for this study. I very much appreciate it that I not only was funded during my studies through the CHAMPCLIM and CLIMROCC projects but also was allowed to witness and be part of the formation of the Wegener Center of which G. Kirchengast is the founder and head. Furthermore, I would like to thank Dr. Ulrich Foelsche for inviting me to his research team in the CLIMROCC project. I very much value his continuous support and countless number of fruitful scientific discussions. Without my team colleague Barbara Pirscher the CLIMROCC team would not be complete. I like to thank her for her every day joyful teamwork, excellent discussions and her tireless support throughout my thesis.

I would like to thank all my colleagues of the Wegener Center, especially my three room mates and our broader research team of the Atmospheric Remote Sensing and Climate System (ARSCLISys) Research Group, for a terrific scientific environment to work in and to be proudly part of. I thank anyone who has helped me throughout my studies with quick, expert and unbureaucratic support. I got the most out of this group as diverse as it is and hope I could return to the group as well.

My studies continue the work done by Dr. Andreas Gobiet and his colleagues and relies heavily on the development of the End-to-end Generic Occultation Performance Simulator (EGOPS) software tool. In addition, my study used CHAMP RO phase delay and orbital data provided by the GeoForschungsZentrum (GFZ) Potsdam for which I would like to thank them very much, in particular Dr. Jens Wickert and Dr. Torsten Schmidt, including the one month of GRACE data which filled the gap of CHAMP data in July/August 2006. Furthermore, operational analyses were continuously downloaded from the European Centre for Medium-Range Weather Forecast (ECMWF) for our retrieval process.

My deepest gratitude goes to my wife who has entered my life so unexpectedly and prominently yet most welcome. I am also deeply grateful for the endless encouragement and support of my parents and family.



# Contents

|   |            |
|---|------------|
| <b>Acknowledgments</b>  | <b>iii</b> |
| <b>Introduction</b>   | <b>1</b>   |
| <b>1 Monitoring of Climate Change and Variability</b>                     | <b>3</b>   |
| 1.1 Climate Records in the Free Atmosphere . . . . .                      | 4          |
| 1.1.1 The (A)MSU Climate Record . . . . .                                 | 4          |
| 1.1.2 The Radiosonde Climate Record . . . . .                             | 7          |
| 1.1.3 Climate Records in the Middle Atmosphere . . . . .                  | 9          |
| 1.2 Natural Variability and Temperature Trends in the Free Atmosphere . . | 12         |
| 1.2.1 The Troposphere and Lower Stratosphere . . . . .                    | 12         |
| 1.2.2 Temperature Trends in the Stratosphere and Mesosphere . . . . .     | 15         |
| 1.3 The Tropopause . . . . .  | 18         |
| 1.3.1 Definitions of the Tropopause . . . . .                             | 19         |
| 1.3.2 Double Tropopauses . . . . .  | 21         |
| 1.3.3 Global Distribution of the Tropopause . . . . .                     | 23         |
| 1.3.4 Stratosphere-Troposphere Exchange . . . . .                         | 26         |
| 1.3.5 Trends in Tropopause Parameters . . . . .                           | 32         |
| <b>2 The Radio Occultation Technique</b>                                  | <b>35</b>  |
| 2.1 Radio Occultation (RO) Data Obtained by Satellites . . . . .          | 35         |
| 2.1.1 Proof-of-Concept Missions . . . . .                                 | 36         |
| 2.1.2 Present Day RO Satellite Missions . . . . .                         | 37         |
| 2.1.3 Future RO Missions . . . . .  | 38         |
| 2.2 Concise Introduction to the RO Method . . . . .                       | 40         |
| 2.3 Climate Benchmark Requirements for RO Measurements . . . . .          | 45         |
| 2.3.1 S.I. Traceability . . . . .   | 46         |
| <b>3 Climate Processing System and Set-Up</b>                             | <b>49</b>  |
| 3.1 Status of the Pre-Operational Processing System . . . . .             | 49         |
| 3.1.1 Enhancement of the Profile Retrieval: Tropopause Parameters . .     | 51         |
| 3.1.2 Enhancement of the Profile Retrieval: Geoid Altitudes . . . . .     | 52         |
| 3.2 Set-Up of Climatologies . . . . .                                     | 54         |
| 3.2.1 Vertical Resolution of the Climatologies . . . . .                  | 55         |
| 3.2.2 Binning Strategy for the Climatologies . . . . .                    | 57         |
| <b>4 Atmospheric Climatologies from CHAMP</b>                             | <b>61</b>  |

---

|          |  |            |
|----------|--|------------|
| 4.1      | Multi-Year Climatologies . . . . .               | 62         |
| 4.1.1    | Climatology of Dry Temperature . . . . .         | 64         |
| 4.1.2    | Climatology of Refractivity . . . . .            | 67         |
| 4.1.3    | Climatology of Dry Pressure . . . . .            | 69         |
| 4.1.4    | Climatology of Dry Geopotential Height . . . . . | 72         |
| 4.2      | Error Analysis of Climatologies . . . . .        | 75         |
| 4.2.1    | Systematic Difference . . . . .                  | 78         |
| 4.2.2    | Sampling Error . . . . .                         | 87         |
| <b>5</b> | <b>Use of Climatologies in Climate Studies</b>   | <b>99</b>  |
| 5.1      | Tropical Tropopause Study . . . . .              | 99         |
| 5.2      | Sampling Error Model for Climatologies . . . . . | 106        |
|          | <b>Summary and Outlook</b>                       | <b>115</b> |
|          | <b>Bibliography</b>                              | <b>117</b> |
|          | <b>List of Abbreviations</b>                     | <b>135</b> |
|          | <b>List of Figures</b>                           | <b>139</b> |
| <b>A</b> | <b>Appendix</b>                                  | <b>141</b> |

# Introduction

The present thesis may be classified in to the broad field of climate research and specializes on climate monitoring of the free atmosphere. The motivation for climate research studies most often lies in better understanding of the variability and trends of the climate system and the role of human activities contributing to it. Since the early 1990's four assessment reports on the newest findings of climate research have been published by the Intergovernmental Panel on Climate Change (IPCC), emphasizing the rapid pace of understanding gained of the changing climate system. The new Summary for Policimakers (*Soloman et al., 2007*) states that "Warming of the climate system is unequivocal, as is now evident from observations . . .". Furthermore, it states that "Most of the observed increase in global average temperatures since the mid-20th century is *very likely* [confidence greater than 90%] due to the observed increase in anthropogenic greenhouse gas concentrations." This is a further advance in confidence to even the previous assessment report in which this confidence was stated to be only greater than 66%.

Whereas the IPCC assessment reports concentrate on the findings of climate processes and climate change of that part of the environment which directly influences us human beings, the surface and near-surface environment, climate change also occurs and may be detected in the free atmosphere above the atmospheric boundary layer. Changes of temperature over time are of the order of less than 1 K per decade and are challenging to detect even on the ground, where instruments may be routinely maintained. Temperature changes in the free atmosphere have to either be detected "in-situ" by, for instance, radiosonde soundings or "remotely" by satellite measurements. Both methods have in common that the measurement instruments cannot be directly maintained while measuring and error characteristics are even more unknown than with ground measurements.

Nowadays, climate records of the free atmosphere up to an altitude of about 35 km exist, spanning a time period of about thirty years for satellite Microwave Sounding Unit (MSU) instruments and of about fifty years for radiosonde soundings. They encompass the upper troposphere and lower stratosphere (UTLS) region, which turned out to be a region especially sensitive to temperature changes. However, the data of these climate records were obtained with instruments originally designed to serve needs of weather forecasting, which generally imposes far less stringent demands on the systematic error characteristics of the measurement than would be necessary for climate monitoring measurements. Learning from that, the urgency arises to create climate benchmark records which have to satisfy very strict accuracy and stability requirements and for which in addition auxiliary data need to be archived in order to be able to fully reproduce the results in the future.

Within the last decade a new technique for probing the state of the atmosphere was developed: the radio occultation (RO) method. Today, RO measurements have already

advanced to be operationally assimilated into numerical weather prediction models. The method utilizes radio signals of the global navigation satellite system (GNSS) which are recorded on a satellite in low Earth orbit (LEO). Measurements are recorded only during the time when the signal from a GNSS satellite on its way to the LEO satellite passes through the atmosphere and is bent by the atmospheric refractive index field, thus the actual measurement is constituted by the Doppler shift of the radio signal. From these Doppler shifts, or phase delay changes, atmospheric parameters like refractivity, geopotential height, pressure, and temperature can be obtained. One of the major attractions of this method, especially from the perspective of climate monitoring, is that the measurement is traceable to the second (unit of time), which is a fundamental S.I. (Système International d'Unités) unit maintained as a metrological standard to an extremely high accuracy. Due to this characteristic, RO measurements have the potential to be formed into a climate benchmark record.

In the present thesis, more than five years of RO measurements of the CHALLENGING Minisatellite Payload (CHAMP) satellite were formed into seasonal climatologies of the parameters refractivity, geopotential height, pressure, and temperature. Global climatologies were carefully created and analyzed for possible discontinuities by comparing them against operational analyses of the European Centre for Medium-Range Weather Forecasts (ECMWF). It turned out that the RO climatologies are of excellent accuracy by which they were even able to point out discontinuities within the operational ECMWF analyses. Within this work a special case study for the tropical tropopause region was performed.

The thesis is structured into five chapters. Chapter 1 gives an overview of global temperature climate records in the free atmosphere constructed from data of the radiosonde network and the (A)MSU satellite instruments in the troposphere and lower stratosphere. Temperature records for the middle stratosphere all the way through to the mesopause are obtained from rocketsonde and lidar measurements, however, they do not cover the whole globe but only parts of the equatorial and northern hemispheric regions. Furthermore, the tropopause is introduced as well as the latest studies of temperature properties in the UTLS region are summarized.

In Chapter 2 the radio occultation (RO) method is concisely summarized. Background information on RO measurements is given such as a short historical overview of the evolution of the RO method itself and past, present, and planned future RO satellite missions are introduced. At the end of this chapter a discussion about climate benchmark records is appended and the notion of S.I. traceability is formulated.

Chapter 3 presents the climate processing system of the WEGCENTER/UNI GRAZ and explains how climatologies based on CHAMP RO data were set-up. In Chapter 4 the seasonal RO climatologies of the atmospheric parameters temperature, refractivity, pressure, and geopotential height, and temperature are presented in global latitude-longitude versus height depictions as well as in a way to demonstrate the temporal evolution of each parameter.

Chapter 5 finalizes with a case study within the tropical tropopause region in which RO climatologies in that altitude and region are compared against operational ECMWF analyses. In addition a model was constructed which estimates the climatological sampling error inherent to the CHAMP seasonal temperature climatologies.

# 1 Monitoring of Climate Change and Variability

During the last decade climate change issues have become a global concern and climate change science has emerged to become a publicly recognized and appreciated discipline. In early 2007 the fourth report (Fourth Assessment Report, AR4) in a series of the Intergovernmental Panel on Climate Change (IPCC) has been published (*Soloman et al.*, 2007) by Working Group I concerning the physical science basis. It summarizes the newest findings in oceanic, atmospheric, and environmental related climate studies and gives projections on climate variability and change until the end of this century on parameters influencing the immediate sphere of human beings, called the biosphere, such as surface temperature.

In this study, a climatological temperature record derived from radio occultation (RO) measurements from five years of CHAMP (CHALLENGING Minisatellite Payload) satellite data is presented for the free atmosphere. Global climatological data sets for the free atmosphere already exist since around 1958 obtained by radiosonde measurements and since 1978/79 with the beginning of the satellite era obtained by measurements of the Microwave Sounding Unit (MSU). The evaluation and interpretation of these data records has been of great concern and were lately summarized in a comprehensive study by *Trenberth et al.* (2007) within the IPCC AR4 and a related report by *Karl et al.* (2006). However, only these two independent data sets are available with a reference or transfer standard (e. g., *Thorne et al.*, 2005a) missing entirely against which the data sets could be absolutely validated. The absence of a transfer standard intrinsically is prone to exhibit the potential of large structural uncertainty. Therefore, on the one hand it is most desirable to produce new and independent climate records for inter-comparison purposes and on the other hand to introduce a reference standard for temperature measurements with climate accuracy in the free atmosphere. In the RO community, we think both points are addressed and can be met by measurements utilizing the radio occultation technique (cf. [Chapter 2](#)).

In the following section, the climate records of the MSU, which in 1998 was upgraded to the Advanced Microwave Sounding Unit (AMSU), as well as the radiosonde network are introduced and discussed. In addition, climate records obtained from Rayleigh lidar and rocketsonde measurements will be discussed. The next section gives an overview of the results obtained from both records with emphasis on climate variability and change within the free atmosphere. The last section gives a thorough description on recent and ongoing science aimed at better understanding the upper troposphere lower stratosphere (UTLS) region with emphasis on the two parameters of tropopause temperature and altitude.

## 1.1 Climate Records in the Free Atmosphere

Building climate records is a very challenging task especially when there is no reference standard to check the results. The main challenge is to produce a record with the desired accuracy and representativeness to firstly distinguish a possible climate trend from natural climate variability and secondly be able to reliably identify possible human contribution to the climate trend. There are many potential error sources with satellite and *in-situ* measurements in general and with the MSU and radiosonde records in particular of which the most important will be discussed below.

The main error source in building climate records from these two measurement records is related to the actual process of producing them. When correcting for external error sources and spurious non-climatic signals in the raw data and in the light of sparse or completely missing metadata, expert judgment is necessary. The choices being made differ between each group even though all process the same data. The systematic differences which are thus introduced have been termed “structural uncertainty” (*Thorne et al., 2005a; Christy et al., 2006*). Structural uncertainty is most relevant when creating the (A)MSU climate record because satellite instruments cannot be regularly maintained and checked for possible inconsistencies or a slow degradation of the instrument. A radiosonde sensor is used for one ascent only on which it also cannot be controlled, thus when creating a climate record from radiosonde data structural uncertainty will also be inevitable. The main differences between various climate records and remaining systematic errors can largely be attributed to structural uncertainty.

### 1.1.1 The (A)MSU Climate Record

The MSU is a backscatter radiometer which passively measures microwave radiation emitted back from Earth’s atmosphere at around 60 GHz. At that spectral wavelength the emission of molecular oxygen is measured whose abundance in the atmosphere is very stable in space and time and thus acts as an excellent tracer for atmospheric temperature monitoring (*Spencer et al., 1990*). Under the assumption that the atmosphere is emitting all radiation that it absorbs, i. e., behaves as a “black body”, a brightness temperature which is equal to a thermometric temperature can be inverted from the radiation measurements. The detailed retrieval method is explained in *Spencer et al. (1990)* and is enhanced in later works (for references see below).

The MSU instrument was first flown on the Television Infrared Observation Satellite (TIROS-N) spacecraft launched in late 1978, following on satellites from the National Oceanographic and Atmospheric Administration (NOAA), NOAA-6 through NOAA-12 and NOAA-14, up to 1998. In 1998 the four channel MSU instrument was “advanced” to the 16-channel AMSU with better calibration, more stable station-keeping, and higher spatial and temporal sampling resolution (e. g., *Goodrum et al., 2000; CIRA, 2007*). The AMSU instrument is flown on the NOAA-15 through NOAA-18 satellites as well as on the Aqua (latin: water) satellite (*NASA, 2007*) by NASA (National Aeronautics and Space Administration).

The (A)MUS instruments measure the emissivity of the atmosphere in nadir mode,

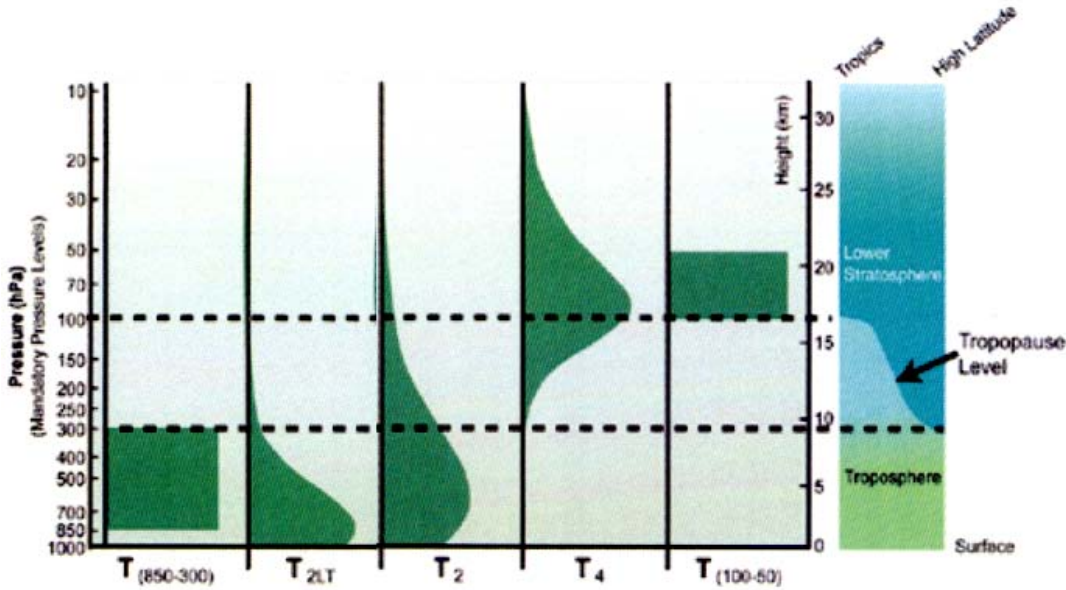


**Figure 1.1:** Weighting functions of the MSU instruments in the lower troposphere ( $T_{2LT}$ ), mid-troposphere ( $T_2$ ), and lower stratosphere ( $T_4$ ); height-weighted averages of radiosonde-based layer temperatures to mimic MSU bulk temperatures are given between 850 hPa and 300 hPa ( $T_{850-300}$ ) and 100 hPa to 50 hPa ( $T_{100-50}$ ). Note that  $T_2$  has contributions from the stratosphere and  $T_4$  from the troposphere as indicated on the right side which shows the global tropopause altitude variation with latitude (adopted from *Karl et al. (2006)*).

i. e., perpendicular downwards from the flying spacecraft and receive the emission at a certain wavelength not only from a specific height but from a bulk layer of the atmosphere. Thus the brightness temperature inverted from MSU measurements represents a bulk temperature as a single value representative for the relatively thick atmospheric layer. **Figure 1.1** shows the weighting functions for three MSU channels, denoted  $T_4$  for temperature representative for the lower stratosphere,  $T_2$  for the mid-troposphere, and  $T_{2LT}$  for the lower troposphere.  $T_2$  and  $T_{2LT}$  have emission contributions from the surface amounting to about 10% for the latter. Channel 2 temperature has contributions of the stratosphere and channel 4 from the troposphere, both up to about 15% depending on latitude. Channel 3 temperatures are not taken into account for long term climate studies because the MSU instruments on NOAA-6 and NOAA-9 satellites exhibited significant drifts. Furthermore, it covers the height range of the UTLS region which complicates temperature trend detection because it receives contributions from the stratosphere and troposphere alike.

The bulk atmospheric temperature is far less informative than a temperature from a discrete height level as obtained, for instance, from radiosonde measurements. However, the spatial and also temporal coverage of satellite measurements is far superior to radiosonde soundings. When comparing both temperatures the difference between the bulk and discrete-level temperature has to be accounted for by intending to mimic the

MSU bulk temperature with an height-weighted average of radiosonde-based temperatures as depicted in [Figure 1.1](#). These height-weighted average temperatures are given by  $T_{850-300}$  for the troposphere and by  $T_{100-50}$  for the stratosphere. In principle there are two approaches as described in detail by *Christy et al.* (2006). On the one hand, one can use a static weighting function which is to be applied to the radiosonde temperature profile taking into account differences over the ocean and continents. On the other hand, one can use a radiative transfer model which is fed with the complete temperature and humidity profiles of the radiosonde measurement and takes into account the variation of different atmospheric parameters. Whereas the latter method is more accurate it also takes much more computer power to perform and for climate applications the results of both methods differ only slightly.

There are mainly three groups who are working actively on producing and updating their climate records from (A)MSU satellite data. All three groups have made their data publicly available at well maintained internet sites. These are *Christy et al.* (2003) and *Spencer et al.* (2006) at the University of Alabama Huntsville (UAH) hereafter referred to as the UAH record and found at <http://vortex.nsstc.uah.edu/data/msu/>; *Mears et al.* (2003) and *Mears and Wentz* (2005) from the Remote Sensing Systems, hereafter referred to as RSS and found at [http://www.remss.com/msu/msu\\_data\\_description.html](http://www.remss.com/msu/msu_data_description.html); and *Grody et al.* (2004) and *Vinnikov et al.* (2006) at the University of Maryland, hereafter referred to as UMD, who published their data created for the *Karl et al.* (2006) report at <http://www.atmos.umd.edu/~kostya/CCSP/>.

The first two groups produce climate records for the three MSU channels labeled  $T_{2LT}$ ,  $T_2$ , and  $T_4$ , whereas the UMD group produces a climate record for  $T_2$  only. There are two other smaller groups who have created temperature trends utilizing MSU measurements. *Prabhakara et al.* (2000) have developed yet another different approach how to deal with non-climatic error sources of the data. Unfortunately, they have not continued their work and updated their climatic record. *Zhou et al.* (2006) have only recently started to construct temperature trends from MSU data. They used simultaneous nadir overpasses from different satellites to inter-calibrate the MSU instruments and thus reduce the data for spurious non-climatic errors.

The method of handling all sorts of external and inherent error sources differs for each group considerably, as described in detail in the given references, influencing their final product, the climate temperature record. Temporal overlap times between each (A)MSU carrying satellite differs over a wide range and mostly involves two satellites only. Temporal overlap of satellites provide an essential measure for inter-calibration of satellite instruments to avoid spurious temperature trends. Further error sources affecting the determination of an accurate climate temperature trend from satellite measurements in general include orbital decay, calibration shifts and changes, and diurnal sampling. The orbit of satellites decreases with time because the thin atmosphere still drags on the spacecraft which changes the viewing geometry of the instrument. For MSU measurements, this issue mainly affects  $T_{2LT}$  temperatures and introduces a spurious temperature trend of about 0.1 K per decade (*Christy et al.*, 2000, 2006).

Calibration shifts and changes within the MSU series poses a major problem which is approached differently throughout all groups. Calibration not only changes from pre-

launch conditions to in-orbit conditions for one instrument, but also changes over time for the same instrument and is different for each and single one instrument (*Christy et al.*, 2000; *Mears et al.*, 2003). The calibration target temperature can change by tens of K over the course of the life of a satellite due to orbit- and season-dependent solar heating. Adjustments for calibration errors vary and also amount to about 0.1 K per decade. For instance, over 40% of the difference in temperature trends retrieved by different groups may be due to the different calibration treatment of only one satellite (*Christy et al.*, 2006). Another source of error originates from drift of polar orbiting satellites in local time and therefore in sampling the diurnal cycle, introducing spurious trends related to the natural diurnal cycle of daily temperature on the order of a few hundredths of Kelvin per decade on the temperature trend (*Mears and Wentz*, 2005; *Christy et al.*, 2006).

The importance of continuously enhancing the climate record is very instructively illustrated by *Christy et al.* (2006) on the oldest data set available which was produced by UAH. They had already started in the late 1980's (*Spencer et al.*, 1990) to create a climate record from MSU measurements and have improved it since. Additional adjustments and corrections were introduced over time such as for linear diurnal drift, orbital decay, and hot target calibrations. Even a different group when using this record applying different techniques pointed out still another correction not applied yet (*Mears and Wentz*, 2005). With each enhancement, the long term temperature trend was altered on the order of plus or minus a few hundredths of Kelvin per decade.

### 1.1.2 The Radiosonde Climate Record

Radiosonde measurements are performed via an expendable electrical measurement package which is dragged most often by a balloon from the surface through the troposphere into the lower to mid-stratosphere up to a height at which the balloon bursts. The package typically measures temperature, humidity, and pressure. Radiosondes which include the measurement of wind speed and direction are called rawinsondes. Temperature is directly inferred from electrical resistance, capacitance, or voltage of a material, as opposed to the indirect measurement of passive satellite emission measurements (*AMS*, 2000). Radiosonde sounding are performed all over the world at 00 and/or 12 Coordinated Universal Time (UTC). In total there are over 1000 stations globally, most of which have started with measurements as early as the late 1950's or early 1960's.

The locations of the radiosonde stations are unevenly distributed with highest density over Europe and North America and lowest in the southern hemisphere (SH), namely over South America, Africa, and Antarctica introducing a sampling bias towards the northern hemisphere (NH). Furthermore, over the oceans only on very few scattered island radiosonde stations are in operation limiting most of the measurements to the land masses. Of those roughly 1000 stations only about 700 have stayed at the same location during the last four decades or so while others have been moved or completely shut down (*Christy et al.*, 2006). For the radiosonde record this poses a unique problem of having to decide which radiosonde record to include into the climate analysis and which to leave out. On the contrary, for the MSU data usually all measurements are used.

In addition to the limited temporal (only once or twice a day) and spatial (unevenly over land, very few over ocean) sampling, radiosonde measurements exhibit many more error sources which complicate an accurate determination of a climatic temperature trend. If the measurement package before launch is not allowed to fully adapt to atmospheric conditions, measurements in the lowest part of the atmosphere are not representative. Changes in instrumentation most often introduce spurious temperature changes or shifts. Solar heating poses a big concern because it heats up the thermometer while rising. In the stratosphere due to the low air density the thermometer cannot keep up with sudden temperature changes (e. g., *Mears et al.*, 2006). Additionally, it was found that the introduction of new and more stable balloons introduced a spurious cooling trend in stratospheric temperature because those balloons could suddenly rise higher than the balloons before (*Parker and Cox*, 1995).

Radiosonde soundings were not primarily intended for climate record purposes but instead serve the immediate needs of the numerical weather prediction (NWP) centers for real time assimilation. For climate needs it is very important that a long time homogeneous data set is ensured with all changes concerning the complete measurement system be recorded by means of so-called metadata. Unfortunately, for most radiosonde stations metadata is missing or at best available only very sparsely. Furthermore, most of the time raw data of the soundings are not archived but only the processed data which complicates tracing changes on the one hand within the raw data and on the other hand in the processing system algorithms.

Radiosonde measurements are reported at least on fifteen “mandatory vertical pressure levels” at 1000 hPa, 850 hPa, 700 hPa, 500 hPa, 400 hPa, 300 hPa, 250 hPa, 200 hPa, 150 hPa, 100 hPa, 70 hPa, 50 hPa, 30 hPa, 20 hPa, 10 hPa. With these levels the vertical resolution of the radiosonde temperature measurements is far superior compared to the bulk temperature of the MSU instrument. When comparing radiosonde soundings to MSU satellite measurements the layer thickness of the satellites’ bulk temperature has to be mimicked with radiosonde data, as described above.

There are mainly two radiosonde data sets which have been carefully created for use of climate temperature studies. *Lanzante et al.* (2003a,b) have selected 87 radiosonde stations following strict quality criteria and applied homogeneity adjustments. However, this record terminates in 1997 and has not been updated since. But it serves as the basis for the Radiosonde Air Temperature Products for Assessing Climate (RATPAC) which is freely available in the Internet at <http://www.ncdc.noaa.gov/oa/climate/ratpac>. It is updated regularly (*Free et al.*, 2005) and uses data from the Integrated Global Radiosonde Archive (IGRA, *Durre et al.* (2006)). The second data set widely used was created by the Hadley Centre by the UK Meteorological Office called the Hadley Centre Atmospheric temperature Data Set Version 2 (HadAT2; *Thorne et al.* (2005b)) and is also freely available at <http://www.hadobs.org/>. They incorporate almost 700 stations using all available digital radiosonde data. The temperature climate record is provided on 9 of the aforementioned mandatory pressure levels between 850 hPa and 30 hPa. Their approach to account for non-climatic inconsistencies and biases within the radiosonde data is based on neighbor comparison to assure spatial as well as temporal consistency.

Despite these efforts of constructing homogenized global radiosonde data records sig-

nificant and uncorrected biases remain, as summarized and analyzed in detail by *Mears et al.* (2006) and *Trenberth et al.* (2007). The most prominent biases, which will be outlined as an example for radiosonde biases in general, are related to changes in instrumentation over time and solar heating of the sensors while rising through the atmosphere. *Sherwood et al.* (2005) have investigated the daytime heating of the sensors and compared it to the nighttime soundings at the same stations. They found a decrease in the heating of the sensors over time possibly related to enhancements in instrument design which introduces a spurious cooling trend at stratospheric heights in the retrieved radiosonde temperature trend. This effect was found most prominent at tropical and pacific island stations which is in accordance what *Randel and Wu* (2006) found in their study when investigating a sub sample of tropical stations. They found jumps and discontinuities in individual station records which are related to solar heating and changes in the radiation correction applied. These again introduce a spurious cooling trend, but this time not only in the stratosphere but at all heights. In total, however, it is not yet clear if a preferred sign of a spuriously introduced trend exists when accounting for all biases involved with radiosonde measurements (*Mears et al.*, 2006), as indicated by the two aforementioned studies.

### 1.1.3 Climate Records in the Middle Atmosphere

This section will give an overview of three climate temperature records of the middle atmosphere. The first two data sets to be discussed consist of a long term record at only one station. The third climate record had consisted of several sites but many of them were shut down in recent years due to funding issues and only a few remain today.

#### Radio Wave Reflection Heights

Radio wave reflection height measurements, as described by *Taubenheim et al.* (1997), are performed by measuring the phase difference of radio waves between those reflected in the ionospheric D region and the ground waves which propagate on the surface from the transmitter to the receiver. The transmitter is located at the French station of Allouis and transmits radio waves with a frequency of 164 kHz. These are received in the northern part of Germany at Kühlungsborn located 1030 km away. In mid-way of the reflection path, the reflection height is located. A temperature record for that mid-latitude measurement has thus been produced for the time period 1963 through 1995.

*Taubenheim et al.* (1997) have found that the reflection height is connected to a fixed value of the electron density following the diurnal height variation of the D region electron density which in turn is forced by the solar zenith angle. When applying the appropriate calculations a characteristic value of the solar zenith angle as a function of the (reflection) height can be determined. In that study, the reflection height was chosen to equal 81.8 km. Since the main absorber of solar radiation at this height is molecular oxygen, which is proportional to the neutral air pressure profile, any variation of the solar zenith angle at the reflection height immediately indicates a variation of

air pressure at that height. By applying the hydrostatic equation between the pressure level of 1 hPa (the height of the stratopause) and the reflection height of 81.8 km, in addition a mesospheric column-mean temperature was obtained. These measurements can be considered fully homogeneous because the geographic configuration and radio wave frequency used remained the same from the beginning. Furthermore, instrumental degradation is excluded in principle by the method applied.

### Rayleigh Lidar

Rayleigh lidar measurements were performed at two French stations: since January 1979 at the Observatory of Haute-Provence and since March 1986 at Biscarrosse. With the two installed lidar systems, temperature profiles can be gained between around 30 km and 100 km. The principle limitation of this method are weather conditions, thus, not more than 19 profiles per month were recorded at any time throughout the 15 years.

The method applied was first described by *Chanin and Hauchcorne (1981)*. From the measurement of a Rayleigh back-scattered monochromatic light pulse (usually a laser beam) by air molecules, air density and then temperature can be determined. The two lidars installed at these sites utilize a laser which emits a light pulse of around 10 ns at the wavelength of 532.2 nm (*Keckhut et al., 1993*). When collecting and counting the back-scattered pulses a device with a very large dynamic range is needed because the intensity of the light varies by a factor of  $10^5$  (*Hauchcorne et al., 1991*). The vertical resolution can mainly be adjusted by the integration time of collecting back-scattered light. The integration period in which one profile is gained influences the averaging of atmospheric influences. The two lidars operate with a 3 km vertical resolution and an integration period of 3 hrs to 4 hrs.

*Keckhut et al. (1993)* have performed a thorough error analysis for these two instruments and the Rayleigh lidar method. The measurement method provides an absolute temperature measurement and the instruments do not need adjustment or external calibration rendering it an ideal candidate for long-term climate monitoring (*Keckhut et al., 1995*). The observed error sources can be divided into two height regimes. At the top of the profile the extraction of background noise, photon noise, and the initialization of the pressure profile introduce errors and can be the source of spurious trend signals. However, these influences decrease exponentially with decreasing height and at a height of about 70 km they are reduced to about 1 K.

At the lower part of the profile, error sources are related to the presence of aerosols, the error characteristics of the photomultiplier used for detecting the back-scattered photons, and the geometric alignment of the transmitting and receiving axes of the photons. These errors are difficult to be quantified precisely, however remain at about 1 K above 30 km to 35 km. After the major volcanic eruption of El Chichón (1982) it had been necessary to raise the lower end of the temperature profile to 40 km and then 35 km. The aerosol clouds of Mt. Pinatubo (1991) had not been localized above 32 km. In summary, *Keckhut et al. (1993)* found that the mean accuracies obtained by the instruments amount to about 1 K between 30 km and 70 km, 3 K at 80 km, and 10 K at 90 km.

## Rocketsonde Soundings

At last, a data set of rocketsonde soundings will be discussed. Rockets had been launched from quite a few stations operationally but mainly because of cost restraints have been reduced considerably in recent time. The rocketsonde network essentially consists of Russian, Japanese, North American, and globally distributed tropical stations. Temperature profiles from rocketsonde soundings can be gained at a height range between 28 km to 80 km with a vertical resolution of about 1 km. Stations at which rocketsonde launches were performed regularly over a time period longer than a decade are very sparse and the data sets very unique. Globally roughly a dozen such stations exist, therefore their coverage of the mid-atmosphere is much superior than that of the two measurements formerly introduced and extends from the tropics to northern mid-latitudes. *Dunkerton et al.* (1998) investigated six tropical stations with records covering the time period from 1962 to 1991; *Keckhut et al.* (1999) analyzed six U.S. rocketsonde records with only one differing compared to those analyzed by the former group in the time period from 1969 to 1993; *Kubicki et al.* (2006) investigated the climate record of one Russian rocketsonde record from Volgograd at northern mid-latitudes covering the time period from 1969 to 1995.

Rockets are equipped with a meteorological measurement package which carries a thermistor for measuring temperature. This package is transported and ejected by the rockets at apogee (highest point of their path) and descends decelerated by a parachute, called “Starute”. The descending package is tracked by a radar to determine its position relative to time (*Keckhut et al.*, 1999).

Despite large differences in technology and schedule times between countries, all systems were confronted with the similar measurement uncertainties. By measuring temperature directly “in-situ” with a thermistor leads to the same uncertainties as with radiosondes. Most notably are uncertainties related to radiative and aerodynamic heating as well as sensor reaction and adjustment time, which drastically increase at heights above  $\sim 50$  km. Instrumentation and launch vehicle changes add to the uncertainties and if not corrected for can introduce spurious trend signals as well as sudden temperature changes. *Dunkerton et al.* (1998) also found spurious trend signals due primarily to a change from uncorrected to corrected temperature measurements. As described in *Keckhut et al.* (1999) and *Kubicki et al.* (2006), these changes have occurred with both the U.S. American and Russian rocket soundings, respectively, and much effort was needed to quantify and reduce these uncertainties. *Schmidlin* (1981) has found that rocket soundings are repeatable to within 1 K up to 53 km, increasing to about 3.8 K at 65 km and to 7.5 K at 70 km.

**Table 1.1:** Linear temperature trend in K per decade with the 95% confidence interval in parenthesis for the periods 1958 through 2004 for radiosonde and 1979 through 2004 for MSU data (adopted from *Karl et al. (2006)*).

| Source  | Period    | T <sub>2LT</sub> | T <sub>850-300</sub> | T <sub>2</sub>     | T <sub>4</sub> | T <sub>100-50</sub> |
|---|-----------|------------------|----------------------|--------------------|----------------|---------------------|
| <b>Radiosonde Retrieved Temperature Trends [K per decade]</b> |           |                  |                      |                    |                |                     |
| RATPAC  | 1958–2004 | 0.13 (0.03)      | 0.13 (0.03)          | 0.07 (0.03)        | −0.36 (0.08)   | −0.41 (0.09)        |
|   | 1979–2004 | 0.13 (0.06)      | 0.10 (0.07)          | <i>0.02</i> (0.07) | −0.65 (0.21)   | −0.70 (0.24)        |
| HadAT2  | 1958–2004 | 0.16 (0.04)      | 0.14 (0.04)          | 0.08 (0.04)        | −0.38 (0.08)   | −0.39 (0.08)        |
|   | 1979–2004 | 0.14 (0.07)      | 0.12 (0.08)          | <i>0.03</i> (0.08) | −0.64 (0.21)   | −0.63 (0.24)        |
| <b>MSU Retrieved Temperature Trends [K per decade]</b>        |           |                  |                      |                    |                |                     |
| UAH   | 1979–2004 | 0.12 (0.08)      |                      | <i>0.04</i> (0.08) | −0.45 (0.42)   |                     |
| RSS   | 1979–2004 | 0.19 (0.08)      |                      | 0.13 (0.08)        | −0.33 (0.38)   |                     |
| UMd   | 1979–2004 |                  |                      | 0.20 (0.07)        |                |                     |

## 1.2 Natural Variability and Temperature Trends in the Free Atmosphere

### 1.2.1 The Troposphere and Lower Stratosphere

In this section results obtained from the radiosonde and (A)MSU records will be presented. Climate temperature anomalies and trends of the products created by the groups introduced above will be discussed. Emphasis will be given to natural variability of temperature anomalies in the free atmosphere as well as its influence on temperature trend detection. As before, most of the results are taken from *Trenberth et al. (2007)* and the report by *Karl et al. (2006)*, mainly from the part by *Lanzante et al. (2006)*.

In [Table 1.1](#) linear temperature trends in K per decade obtained from radiosonde and MSU data for the periods 1958 through 2004 and 1979 through 2004, respectively, are listed. The numbers in parenthesis represent the approximate 95% confidence interval of the linear trend. To emphasize the significance of the retrieved temperature trends, those trends which are not statistically different from zero are displayed in italics. Temperature trends for the radiosonde data are given for the RATPAC and HadAT2 data records for layer average temperatures of five atmospheric layers corresponding to T<sub>2LT</sub>, T<sub>2</sub>, and T<sub>4</sub> of the MSU instrument, and to two layers which solely reside either in the troposphere (T<sub>850-300</sub>) or in the stratosphere (T<sub>100-50</sub>). Temperature trends retrieved from the MSU data record are given for the three groups as introduced above. The group of the university of Maryland only calculates temperature trends for the T<sub>2</sub> channel.

Two major features which are represented throughout the products of all five groups and both time periods can be inferred from [Table 1.1](#): since 1958 the troposphere has

warmed while the stratosphere has cooled. The average amount of warming in the troposphere as measured by radiosonde and MSU data, i. e., as in  $T_{2LT}$  and  $T_{850-300}$ , and for both periods equals to about 0.13 K per decade, although the measure of RSS for the period 1979 through 2004 at  $T_{2LT}$  with 0.19 K per decade lies about 50% higher than that. The linear temperature trend seems not to vary much in the troposphere for both time periods.

In the stratosphere, the linear temperature trend of both layer averages  $T_4$  and  $T_{100-50}$  are strongly negative with values reaching as low as  $-0.63$  K to  $-0.70$  K per decade for the radiosonde data during the satellite era of 1979 through 2004. Within the radiosonde era 1958 through 2004 the negative trend was measured to be almost half of this reaching about  $-0.38$  K per decade. The MSU retrieved trends for the satellite era are much lower than obtained from radiosonde data and vary considerably more.

Channel 2 results are most ambiguous and hard to interpret. They show a slight warming trend for radiosonde data within the radiosonde era and a trend not statistically different from zero within the satellite era. However, temperature trends retrieved from satellite data range between not being statistically different from zero (UAH) to an even stronger warming than recorded in the lower troposphere (RSS with 0.20 K per decade). Most of this ambiguity is related to the fact that channel 2 data receives contributions mainly from the troposphere but to about 10%–15% also from the lower stratosphere, as was first detected by *Spencer and Christy* (1992) (cf. [Figure 1.1](#)). There were efforts to subtract the stratospheric contributions from  $T_2$  by *Fu et al.* (2004) and use a newly created temperature,  $T_G^*$ , globally for the troposphere (*Johanson and Fu*, 2006) which results in almost the same temperature as  $T_2$  (not shown here).

In [Table 1.1](#) temperature trends are given as linear trends over a period as long as almost 60 years for the most non-linear process like the climate. Many authors caution to use linear trends to describe climate variability of the past. *Thorne et al.* (2005b) have found that tropospheric temperature evolution at least in the HadAT2 data set was too nonlinear to justify the indiscriminate use of a linear trend. *Seidel and Lanzante* (2004) have investigated three alternative simple statistical models involving breakpoints and suggest consideration of such alternatives in climate change detection and attribution studies even though it is hard to prove that they provide a better fit to the data.

[Figure 1.2](#) shows temperature anomalies in the three atmospheric layers of the lower stratosphere ( $T_4$ ), mid-troposphere to lower stratosphere ( $T_2$ ), and lower troposphere ( $T_{2LT}$ ) from top to bottom, respectively. The time series spans almost 60 years from 1958 through 2004 depicting results from the radiosonde and MSU data record, where applicable. The series depicts anomalies based on the Jan. 1979 to Dec. 1997 average and is smoothed with a 7-month running average (*Karl et al.*, 2006). Superimposed are the three major volcanic eruptions of Mt. Agung (1963), El Chichón (1982), and Mt. Pinatubo (1991).

In the stratosphere, the overall cooling trend is interrupted by these three explosive volcanic eruptions by an abrupt rise in temperature of about 1 K. It is caused by the injection of volcanic aerosols into the stratosphere which absorb solar radiance and last for about 2 to 3 years until they are removed from the atmosphere by natural processes. However, a certain ambiguity remains, especially for the last two major

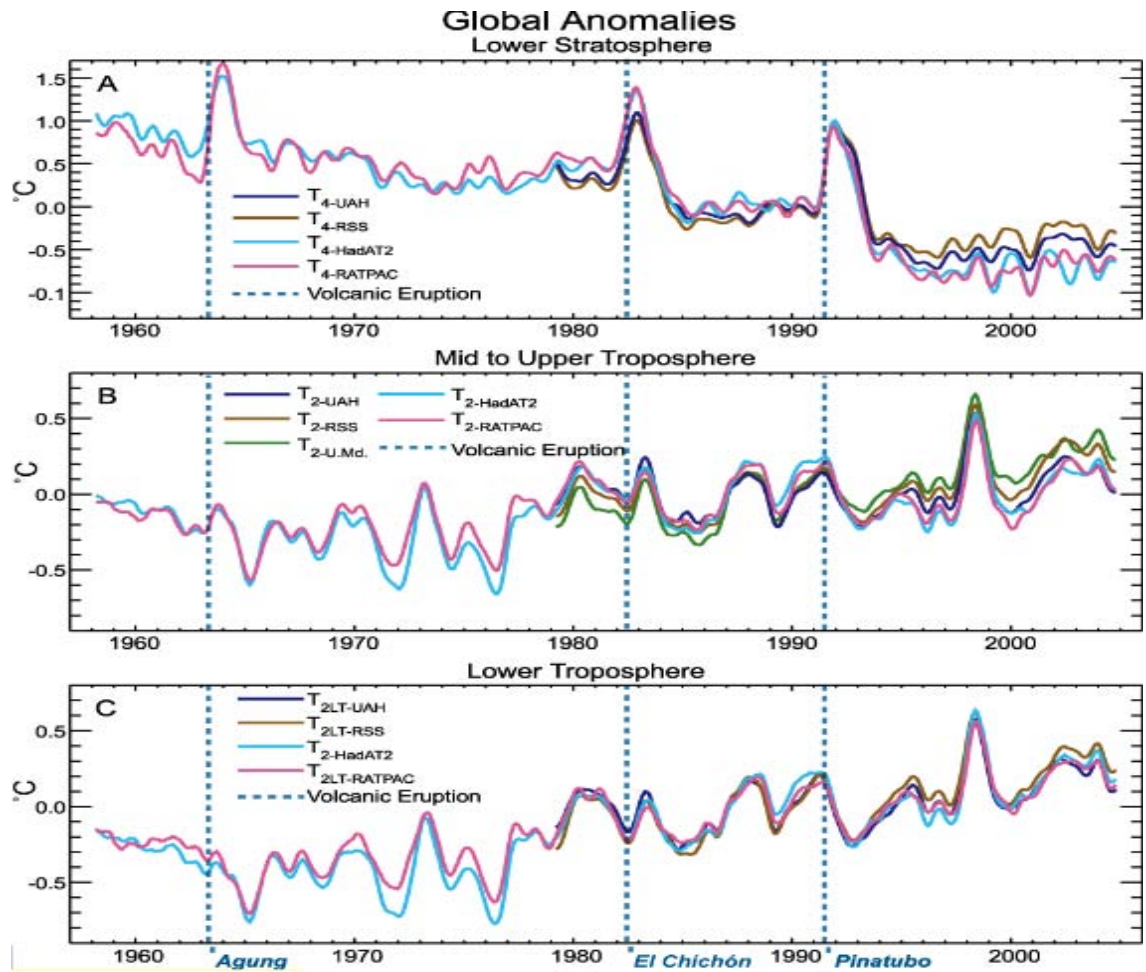


**Figure 1.2:** Temperature anomalies for the time period 1958 through 2004 as obtained from radiosonde and (A)MSU data for the lower stratosphere (A), mid-troposphere to lower stratosphere (B), and lower troposphere (C). All time series are smoothed with a 7-month running average and expressed as departures from the Jan. 1979 to Dec. 1997 average (adopted from (Trenberth *et al.*, 2007)).

eruptions, as to whether the temperature in the lower stratosphere returns to its earlier value or experiences a step-like decline after each eruption (Seidel and Lanzante, 2004). Furthermore, throughout the time series small variations of about 2 to 3 years can be seen which result from the QBO (Seidel *et al.*, 2004).

In the troposphere, three features are of major interest. At first, the volcanic eruptions have a cooling effect on the troposphere (e.g., Karl *et al.*, 2006) as can be nicely seen for the Mt. Agung and Mt. Pinatubo events. The cooling response from El Chichón is masked by an El Niño/Southern Oscillation (ENSO) warming event. ENSO events result in a relatively large warm anomaly (e.g., Karl *et al.*, 2006) amounting to about 0.5K. Especially the strong ENSO event in 1998 can clearly be followed for all four data records. A third feature inherent to the tropospheric temperature trend is a well

studied and documented climate shift occurring in 1976 (*Trenberth, 1990; Trenberth and Hurrell, 1994; Deser et al., 2004*). This climate shift occurs in the (tropical) troposphere and is characterized by a sudden rise in average temperature around 1976. The average temperature about a decade before 1976 was around 0.3 K colder than the average temperature of about a decade after 1976. Both time periods before and after 1976 additionally feature highly varying tropospheric temperature due to ENSO events, and the sudden temperature rise in 1976 was accompanied by an ENSO event of nearly 0.5 K (see [Figure 1.2](#)). Because the climate shift occurs just before the satellite era it can only be documented with the radiosonde data. Since the mean temperature before and after the shift does not change much this event acts as a very strong argument to use step-like trend models instead of the linear trend (*Seidel and Lanzante, 2004*).

With all the difficulties involved in building climate records it is very impressive how well these five (with UMD only producing  $T_2$  temperatures) almost completely independent data products agree with each other. However, at closer examination and as can be inferred from [Table 1.1](#) at times large differences prevail. In the lower stratosphere, both radiosonde data sets differ largely at the peak of volcanic warming associated with the Mt. Agung in 1963 and El Chichón in 1982. More climatically important biases between the radiosonde products are subtle differences in temperature which result in RATPAC having a larger stratospheric trend than HadAT2 (*Lanzante et al., 2006*).

In the troposphere both radiosonde products agree very well even though the HadAT2 product uses almost ten times as many stations as the RATPAC data set. There have been studies which have examined the different spatial sampling of the two products (*Free and Seidel, 2005; Thorne et al., 2005a*) and concluded that on a global scale the amount of stations used in the RATPAC data set are sufficient for a representative temperature trend detection. At the end of the climate record, the data starts to overlap with continuous RO measurements. This is especially noteworthy since the MSU satellite and radiosonde products seem to disagree by a relative large amount since around the mid 90's. Very recently, a climate trend study including RO measurements has been performed by *Steiner et al. (2007)*.

The effects of the volcanic eruptions on the temperature trend are represented with differing precision throughout data products. The stratospheric warming resulting from the El Chichón eruption is represented around 0.3 K colder in the satellite record compared to the radiosonde record, whereas the warming effect of the Mt. Pinatubo eruption is represented equally throughout all four data sets. For the satellite data the overall stratospheric temperature trend is much lower than for the radiosonde data. Up to 1991 satellite stratospheric temperature seems to be colder than radiosonde temperature whereas after the volcanic eruption it is warmer. This systematic difference mainly accounts for the large difference in temperature trend difference between satellite and radiosonde products (see [Table 1.1](#)) and is largely attributed to difficulties in accurately determining radiosonde temperature in the stratosphere (see discussion in [Chapter 1.1](#)).

### 1.2.2 Temperature Trends in the Stratosphere and Mesosphere

*Taubenheim et al. (1997)* present a 32 year record of a column-mean temperature of the

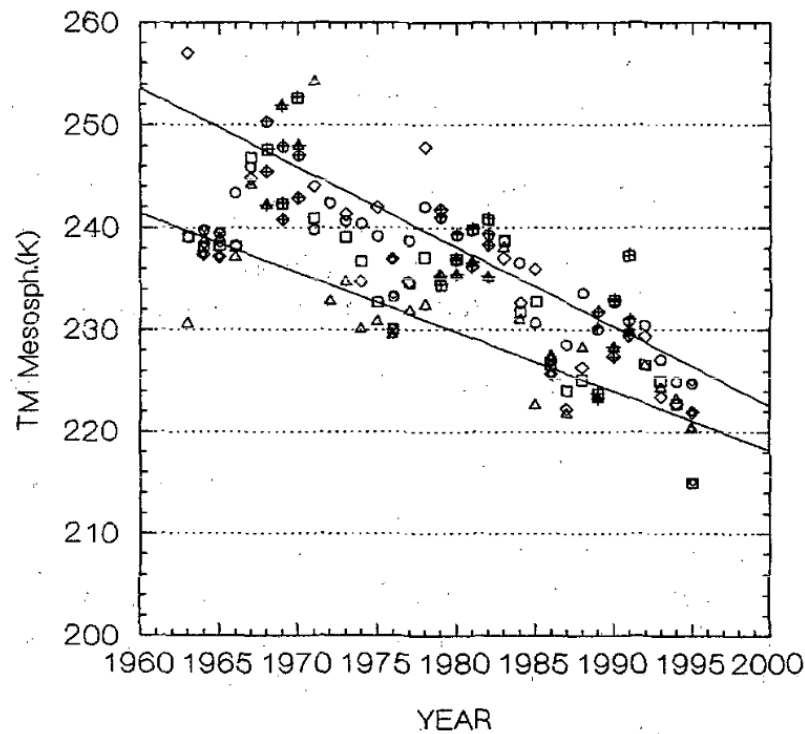


**Figure 1.3:** Column-mean temperature between stratopause and 81.8 km height for the time period 1963 to 1995 inferred from radio wave reflection heights (taken from *Taubenheim et al. (1997)*).

mesosphere between the stratopause at 1 hPa (corresponds to a height of about 50 km) and 81.8 km inferred from radio wave reflection heights. Because of large dynamical variation in the middle atmosphere in wintertime which is expressed by an anomaly in radio waves, they limited their data analysis to the months May through August. They find a long-term temperature trend independent of solar activity of  $-5.8 \pm 0.9 \text{ K/decade}$ . This trend is indicated by the lower line in [Figure 1.3](#) as a linear fit of the temperatures occurring during the times of solar minimum activity. *Taubenheim et al. (1997)* suggest that the main contribution of that decrease in temperature results from the height range 60 km to 75 km where rocketsonde soundings indicate large cooling (as discussed below). They conclude that such a large decrease cannot be attributed to greenhouse gas forcing alone but instead must be regarded as the signal of an intrinsic long-term variation in the middle atmosphere.

*Hauchcorne et al. (1991)* and *Keckhut et al. (1995)* have produced long-term temperature records by means of Rayleigh lidars and have focused on determining natural long-term variability which could mask long-term temperature trends. They have investigated seasonal variability, which is greater in wintertime, as well as contributions of the Quasi-Biennial Oscillation (QBO) and from solar activity in form of the solar cycle. Due to smaller variability, linear trends were calculated for the summertime (April

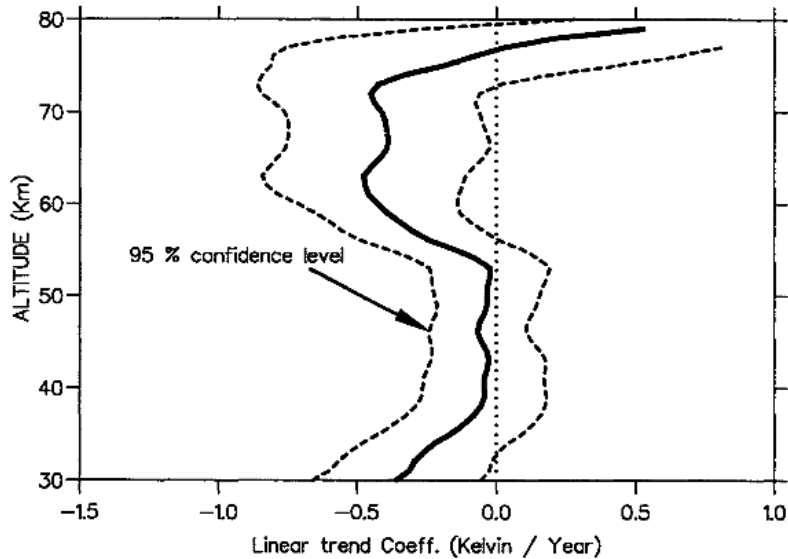


**Figure 1.4:** Linear mean temperature trend profile as a function of height as observed by Rayleigh lidars during the time period 1979 to 1994 (taken from *Keckhut et al. (1995)*).

through September) only as displayed in [Figure 1.4](#). They observed a significant cooling trend in the mesosphere between 60 km and 75 km of 4 K per decade and a smaller and non-significant trend in the upper stratosphere of 1 K per decade peaking at around 45 km. At the height range between 30 km and 40 km they find a cooling trend of 1 K per decade to 3 K per decade peaking at 30 km, however, *Keckhut et al. (1995)* have not much confidence in that trend because of instrumental limitations. The same is true for the positive trend of 10 K per decade at 80 km where many possible error sources give poor confidence in that value.

Results from rocketsonde soundings reveal a similar situation in the middle atmosphere. *Dunkerton et al. (1998)* and *Keckhut et al. (1999)*, who have analyzed almost the same six tropical rocketsonde records differ in their approach of determining temperature trends. *Dunkerton et al. (1998)* have included all data of the 29 year time period from 1962 through 1991 whereas *Keckhut et al. (1999)* have taken data starting only in 1969 up to 1991. Furthermore, they excluded data contaminated by volcanic eruptions such as the time periods after 1975, 1982, and 1991 corresponding to the Fuego, El Chichón, and Mt. Pinatubo eruptions, respectively. *Keckhut et al. (1999)* state that the total amount of profiles they included into their analysis before the exclusion due to volcanic eruptions amount between 1,800 and 2,800 (1,100 for one station). They found a temperature trend estimation as a distinct function of height with  $-1.1 \pm 0.6$  K per decade at 25 km,  $-1.7 \pm 0.6$  K per decade in the height range of 35 km through 50 km, and  $-3.3 \pm 0.9$  K per decade near 60 km as depicted in [Figure 1.5](#) by the profile with the open circles. *Dunkerton et al. (1998)* only state to have found a cooling trend in the height range between  $\sim 30$  km to 60 km of  $-1.7$  K per decade with an approximate cooling of  $-2$  K per decade in the upper stratosphere and more than  $-4$  K per decade in the lower mesosphere.

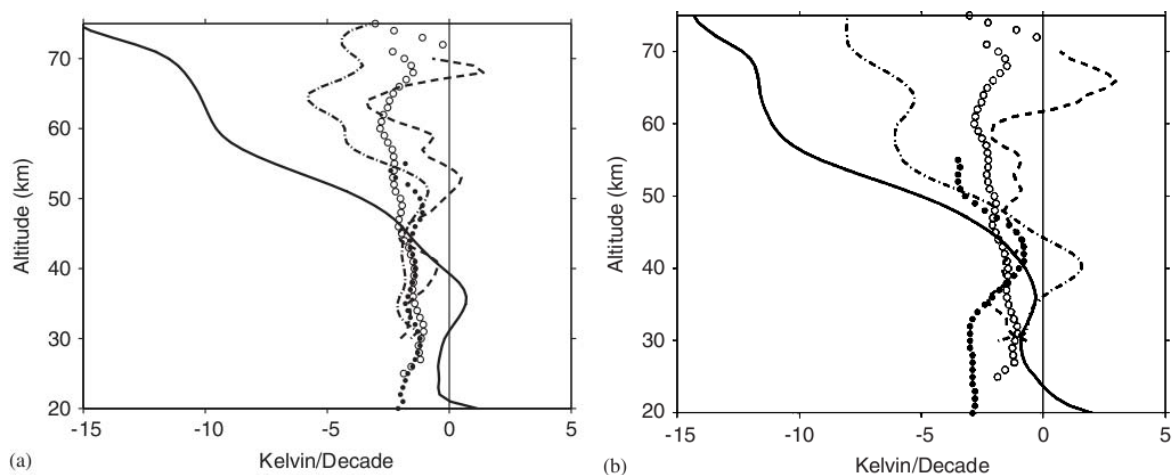


**Figure 1.5:** Temperature trend profile for the summer (a) and winter (b) seasons as obtained by rocketsonde soundings in Volgograd (solid line), Wallops Island (dashed line), Ryori (solid dots), mean tropical soundings by *Keckhut et al.* (1999) (open circles), and by the French lidar as published in *Ramaswamy et al.* (2001) (dash-dotted line) (taken from *Kubicki et al.* (2006)).

Temperature trend estimations of the Russian rocketsonde record as reported by *Kubicki et al.* (2006) amount to an insignificant cooling of less than  $-1$  K per decade below the height of 40 km. Above that height a sharp increase of the cooling trend with height was observed as shown for both winter and summer months in [Figure 1.5](#) with a relatively constant value of 11 K per decade between 55 km and 65 km. These trend estimates are much larger than reported by any other group.

### 1.3 The Tropopause

The tropopause is a well defined region in the atmosphere which marks the boundary between the troposphere and the stratosphere. It can be found throughout the globe at high-, mid-, and low-latitudes, however at different heights and of different thickness; there are occurrences of double tropopauses mainly linked to the subtropical jet streams. Many different definitions of the tropopause exist, which range from a very simple hydrostatic definition (100 hPa isobar), over adiabatic (lapse rate of the temperature profile), mixing ratios of ozone, humidity and others, and dynamical relations (potential vorticity), as well as definitions based on radiation properties.

The tropopause acts as a barrier between the troposphere and stratosphere impeding exchange between these two air masses. The nature of the exchange between the two atmospheric parts has since long been of scientific interest and recent research is still ongoing. The tropopause region has been established as a transition layer in which the stratosphere-troposphere exchange takes place under specific atmospheric constraints. The tropical tropopause layer (TTL) has already been identified long ago as the main source for tropospheric air in the stratosphere. Recently, also the extratropical tropopause layer was identified in different ways to contribute considerably to stratosphere-troposphere exchange, as will be explained further below.

### 1.3.1 Definitions of the Tropopause

The simplest, and therefore most incorrect, definition of the tropopause defines it at a constant pressure level. The 225 hPa pressure level was suggested by *Scherhag* (1948) as were many other levels, mainly 200 hPa and 250 hPa, as a reasonably good approximation of the tropopause. However, radiosonde as well as other data show that the tropopause can vary between 400 hPa in polar regions and 100 hPa in the tropics, leaving the 225 hPa isobar in the troposphere in the tropics and in the stratosphere mostly at all other latitudes (*Hoinka*, 1998). Even as a proxy the 100 hPa isobar performs poorly as has been shown by *Seidel et al.* (2001) who have studied the tropical tropopause with radiosonde data spanning a thirty year time period. Concerning the 100 hPa isobar they conclude that it shows significantly less temporal and spatial variability than tropopause heights determined differently. Similar results were found by *Schmidt et al.* (2004) who performed a study on tropical tropopause parameters with CHAMP RO data.

The operationally used definition of the tropopause is associated with the difference of temperature lapse rate of tropospheric and stratospheric air. This definition was agreed upon already in 1957 by the World Meteorological Organization (WMO) (*WMO*, 1957) (see also *WMO*, 1986, 1992) and states that:

- (a) The first tropopause is defined as the lowest level at which the lapse rate decreases to  $2^{\circ}\text{C}/\text{km}$  or less, provided also the average lapse rate between this level and all higher levels within 2 km does not exceed  $2^{\circ}\text{C}/\text{km}$ .
- (b) If above the first tropopause the average lapse rate between any level and all higher levels within 1 km exceeds  $3^{\circ}\text{C}/\text{km}$ , then a second tropopause is defined by the same criterion as under (a). This tropopause may be either within or above the 1 km layer.

This so called lapse rate tropopause (LRT) is widely used with data, i.e., radiosonde or RO temperature profiles, and model output because of its simple implementation. However, *Highwood and Hoskins* (1998) argue that the LRT is an arbitrary definition for operational use that has limited physical relevance especially in the tropics. They continue in arguing that there is little direct connection between convective processes, which influence especially the tropical stratosphere-troposphere exchange (see below).

Above the LRT, a cold point tropopause (CPT) is defined by the local minimum of the temperature profile (*Highwood and Hoskins*, 1998) (not to confuse with the absolute minimum of the temperature profile which usually resides at the mesopause). In rare occasions in polar and high mid-latitude regions the stratosphere can be very cold (predominately in the winter polar vortices) which can lead to unreasonably high CPT altitudes. For that reason, the CPT is technically defined to be lower than 20 km and higher than the LRT. The physical relevance of the CPT is given by its better correlation to convective processes in the stratosphere-troposphere exchange (*Schmidt et al.*, 2004; *Highwood and Hoskins*, 1998).

Another definition often used is that of a dynamical tropopause which was suggested by *Reed* (1955) and defined by *WMO* (1986). The definition is based on potential

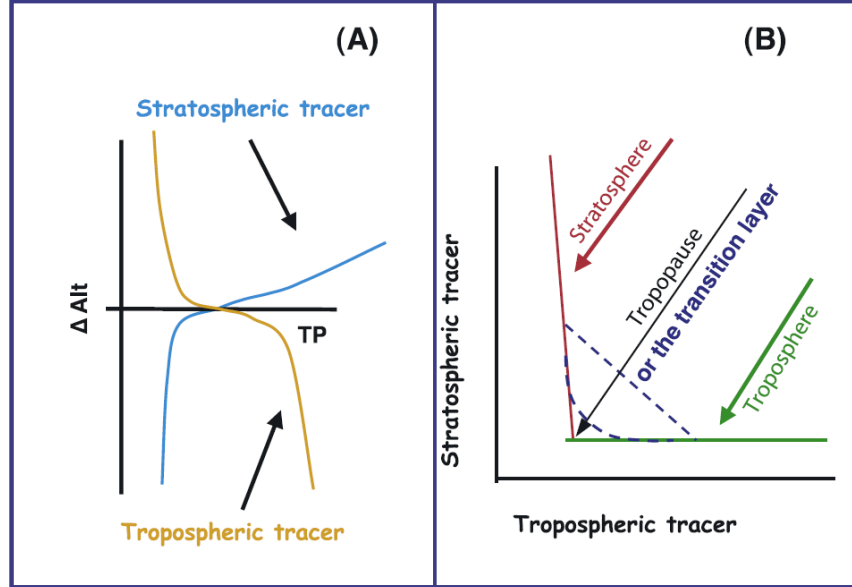


**Figure 1.6:** A concept by *Pan et al.* (2004) to identify the tropopause transition layer by trace gas relations. In (A) a stratospheric and tropospheric tracer are illustrated in altitude space relative to the tropopause; in (B) the same is schematically shown in tracer-tracer space.

vorticity which in isentropic coordinates is given by:

$$P_{\Theta} = -g(\zeta_{\Theta} + f) \left( \frac{\partial p}{\partial \Theta} \right)^{-1}, \quad (1.1)$$

where  $\zeta_{\Theta}$  is the relative vorticity along the isentropic surface (surface of equal potential temperature  $\Theta$ ),  $f$  is the Coriolis parameter,  $p$  the pressure, and  $g$  the gravitational constant.  $P_{\Theta}$  defines the dynamical tropopause in units of potential vorticity (PVU [ $1.0 \times 10^{-6} \text{ km}^2 \text{ kg}^{-1} \text{ s}^{-1}$ ]), which is understood to be a near-zero-order discontinuity which separates low values in the troposphere and high values in the stratosphere (*Hoinka*, 1998). In *WMO* (1986) the dynamical tropopause is defined at 1.6 PVU. However, there have been many studies suggesting different values ranging from 1 PVU to as high as 5 PVU (see *Hoinka*, 1998, and references therein). However, most commonly a value of 2 PVU is used (e.g., *Stohl et al.*, 2003). This definition of the tropopause is used when studying dynamic processes such as tropopause breaks or folds which appear as multiple stable layers in the vertical temperature profile although they represent the same discontinuity surface. Because potential vorticity is conserved under adiabatic and frictionless flow, *Ertel* (1942) and *Hoskins* (1991) emphasized the material-surface nature of the tropopause, which can be used to identify these discontinuity surfaces.

The last tropopause definition discussed here is that of the chemical tropopause. The concept behind that definition is to locate the quasi material-surface that identifies the

chemical transition layer between the stratosphere and the troposphere (*Holton et al.*, 1995; *Pan et al.*, 2004). At first, the profile of ozone was used to identify the tropopause (e.g., *Hoinka*, 1997; *Pan et al.*, 2004), because the concentration of ozone increases rapidly in the vicinity of the tropopause towards the stratosphere. In a simulation study, *Joeckel et al.* (2002) have defined the monthly average chemical tropopause by ozone mixing ratio of  $150 \text{ nmol mol}^{-1}$ . In many observational studies, the trace gas relationship of  $\text{O}_3$ -CO was investigated in the mid-latitude tropopause. In particular, *Fischer et al.* (2000); *Hoor et al.* (2002) have observed a chemical mixing layer in the lowermost stratosphere which they concluded was due to stratosphere-troposphere exchange. This layer was then referred to as a transition layer between the troposphere and stratosphere which was characterized by *Pan et al.* (2004). From aircraft measurements in mid-latitudes they have investigated the relationship of the stratospheric tracer ozone ( $\text{O}_3$ ) and the tropospheric tracer carbon monoxide (CO). Based on their measurements, they have developed a schematic shown in [Figure 1.6](#) which illustrates the connection of trace gases of tropospheric (e.g., CO,  $\text{H}_2\text{O}$ ) and stratospheric (e.g.,  $\text{O}_3$ ) origin, of which idealized profiles are shown in the left panel of [Figure 1.6](#). In tracer-tracer space (right panel of [Figure 1.6](#)) the profiles of both trace gas species form an “L”- shape, in which the stratospheric trace gas forms the upper part of the “L” while the lower part is formed by the tropospheric trace gases. In the vicinity of the tropopause, each trace gas abundance decreases away from its origin.

Following these observations, *Pan et al.* (2004) suggest that “the transition point between the two branches should be considered as the chemical tropopause”. Furthermore, the characteristics between the two branches of the “L”-shape provides information of the sharpness of the tropopause. Applying their measurements to this schematic of the chemical tropopause, *Pan et al.* (2004) showed that this approach is a powerful tool to characterize the extra-tropical tropopause region. In particular, they showed that a trace gas relationship is more accurate to identify the tropopause than the ozone profile alone. As a result, they conclude to view the extra-tropical tropopause as a chemically mixed transition layer, rather than as a surface, with a thickness of  $\sim 2 \text{ km}$  to  $3 \text{ km}$  away from the subtropical jet and about twice as thick in its vicinity.

### 1.3.2 Double Tropopauses

Usually, the tropopause occurs only once in a vertical profile at a given location, and the dynamical tropopause makes sure of that *per definitionem*. However, when defined thermally, double (*WMO*, 1957) and even multiple (*WMO*, 1992) tropopauses can occur, caused by overlapping of tropical and mid-latitude air masses. Early studies had already mentioned that a thermal definition allows for double or multiple tropopauses at a given location (e.g., *Bjerknes and Palmén*, 1937; *Defant and Taba*, 1957, 1958).

[Figure 1.7](#) shows an occurrence of a double tropopause as measured by *Pan et al.* (2004) in the vicinity of the northern subtropical jet. The thermal tropopause, indicated as black crosses, was retrieved in situ with a Microwave Temperature Profiler aboard an aircraft. Shown are also potential vorticity (solid lines) and zonal winds (dashed lines) taken from United Kingdom Meteorological Office (UKMO) analyses (*Swinbank and*

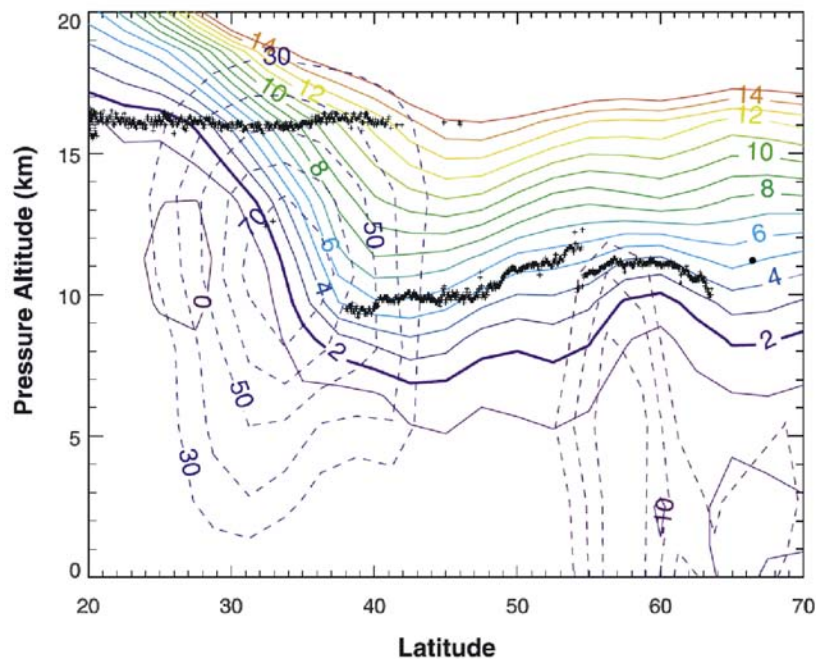


**Figure 1.7:** Double tropopause measured as described in *Pan et al.* (2004). Black crosses refer to thermal tropopause measurements with a Microwave Temperature Profiler on board an aircraft from 11 December 1995. Potential Vorticity (solid contours) and zonal wind fields (dashed contours, where blue present westerlies and purple easterlies) were taken from UKMO analyses. A double tropopause exists between about 38°N and 41°N.

*O'Neill*, 1994). In this example, the double tropopause occurs between 38°N and 41°N in the vicinity of the subtropical jet stream marking the so-called tropopause break (*Sprenger and Wernli*, 2003). The difference in height between the first and second tropopause amounts to about 6 km to 7 km. In comparison, the dynamical tropopause, if defined at 2PVU, sometimes differs from the thermal tropopause by more than 2 km as can be seen in [Figure 1.7](#). The most significant difference occurs in the vicinity of the subtropical jet stream where the second tropopause level reaches as far out as to about 12 PVU.

*Schmidt et al.* (2006) have performed a climatological study of the global occurrence and distribution of multiple tropopauses using Global Positioning System (GPS) RO data from CHAMP and SAC-C (Satellite de Aplicaciones Cientificas-C). The time period studied covers four years of data from May 2001 to April 2005. The thermal tropopause definition of *WMO* (1957) was used to identify single and multiple tropopauses. They found an occurrence distribution which follows closely the climatological location of the subtropical jet. Highest relative occurrence of double tropopauses with 80% were found during winter months on the NH, values on the SH were found to be generally lower. Furthermore, at high-latitudes an additional annual cycle of the occurrence of multiple

tropopauses was observed starting in late autumn and lasting until late winter caused by intensifying of the polar jet (*Schmidt et al.*, 2006). The maximum thickness of multiple tropopauses was determined to be greater than 5 km, which agrees well with *Pan et al.* (2004) and *Bischoff et al.* (2007) (see below).

*Bischoff et al.* (2007) have performed a thorough study on the climatological distribution and occurrence of the subtropical to southern mid-latitudinal tropopause using three Argentine operational rawinsonde records spanning the time period 1968 to 1997. The stations are located in Argentina at 27°S, 35°S, and 45°S, respectively, and all near the 60°W meridian. They have established a climatology of single and double tropopause occurrences. The annual cycle of the northernmost station is most pronounced with a double tropopause occurrence of 10% in summer (February) and 45% in winter (June, July, August). The southernmost station exhibits a reduced annual cycle with a double tropopause occurrence of 45% in January and 30% in June. Thus, the annual cycle of double tropopause occurrence is reversed from the subtropics to mid-latitudes (*Bischoff et al.*, 2007). In addition to *Pan et al.* (2004), *Bischoff et al.* (2007) have linked the formation of double tropopauses also to frontal jets. As they clearly demonstrate, jets close to the tropopause – whether they occur as the well established subtropical jet or jets associated with frontal activity – can lead to tropopause breaks and in succession to double or even multiple tropopauses.

### 1.3.3 Global Distribution of the Tropopause

Now that different definitions of the tropopause have been discussed, the structure of globally distributed temperature profiles and the global distribution of the tropopause itself will be analyzed. In the study presented here, LRT and CPT were used, thus this discussion will concentrate on the tropopause parameters obtained with these two definitions applied to CHAMP profiles. There were many studies which have investigated the global distribution of the tropopause with diverse observation techniques. At first, reanalyses were used to examine the tropopause region globally (*Hoerling et al.*, 1991; *Hoinka*, 1998; *Hoinka*, 1999). This technique was continuously refined, and recently the newest reanalyses products were compared to climate models concerning the detection of climate change in tropopause parameters (*Santer et al.*, 2004). Radiosonde measurements were first used to describe tropical tropopause characteristics (e. g., *Seidel et al.*, 2001) and then these were also tested against reanalyses data (*Randel et al.*, 2000; *Zhou et al.*, 2001). Even recently, radiosonde studies were performed investigating how much of the climate change effect can be diagnosed by radiosondes (*Seidel and Randel*, 2006). As a new technique, RO has also been used to investigate tropopause characteristics in the tropics (*Schmidt et al.*, 2004; *Borsche et al.*, 2007) and on a global scale (*Schmidt et al.*, 2006).

In [Figure 1.8](#) temperature profiles obtained from RO data of the CHAMP satellite (cf. [Chapter 4](#)) for high-, mid-, and low-latitudes (90°N/S to 60°N/S, 60°N/S to 30°N/S, and 30°S to 30°N, respectively) are shown. Depicted are profiles of June 1st, 2003 as a representative example of northern hemispheric summer profiles. The high-latitude profiles are colored differently for northern (blue) and southern (purple) hemispheric

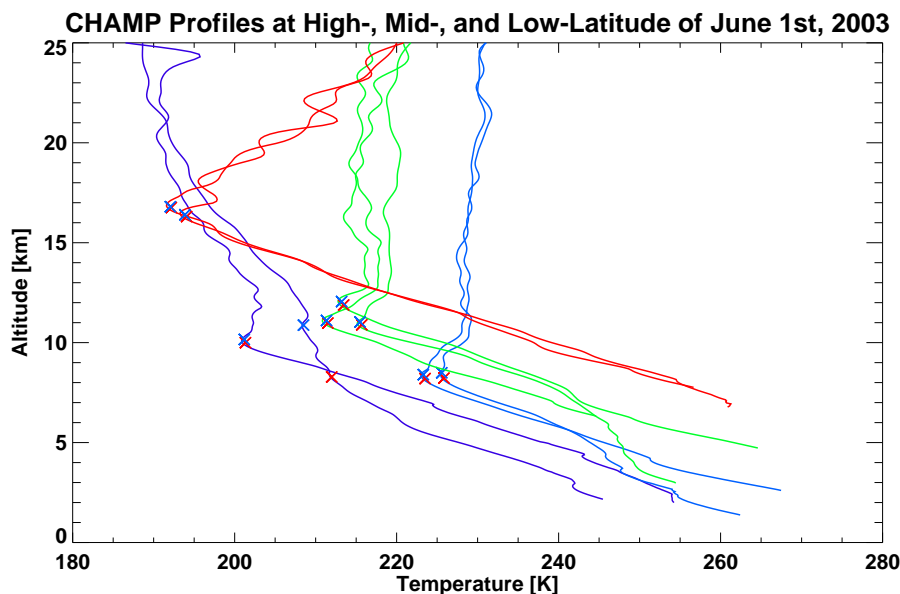


**Figure 1.8:** CHAMP profiles taken from June 1st, 2003 at high-latitudes (blue northern and purple southern hemisphere), mid-latitudes (green), and low-latitudes (red). The crosses indicate the LRT (red) and CPT (blue).

profiles. Each profile is marked with two crosses indicating the LRT (red cross) and CPT (blue cross). The low-latitude profiles (red) are distinctly different to the others because the tropopause is by far highest and coldest (see also [Figure 1.9](#)), and the tropopause marks a pronounced minimum in the temperature profile. Above the minimum, the temperature increases with a greater lapse rate and more consistent than with the profiles from other latitude ranges. Because of that, at low-latitudes the tropopause is easiest to determine also for climatological studies because even in an ensemble of profiles that distinct temperature structure exhibits the least variation (cf. [Chapter 5.1](#)). Due to intense convection processes, the low-latitude troposphere is adiabatically well mixed, thus leading to a more constant decrease in temperature below the tropopause as compared to other latitude ranges.

The mid-latitude profiles (green) are shown for the NH and SH. LRT and CPT are much lower than at low-latitudes by roughly 5 km. Above the tropopause, at mid-latitudes the temperature does not increase as much as at low-latitudes but stays almost constant in the lower stratosphere. Finally, high-latitude profiles are shown in blue and purple, separating northern and southern hemispheric profiles, respectively. The high-latitude tropopause is lowest, and especially the winter polar tropopause can be very tricky to determine. As can be seen in [Figure 1.8](#), the temperature minimum of both southern hemispheric (winter) polar profiles is not reached below 20 km, thus the CPT represents only a local temperature minimum of the profile. Additionally, the lapse rate criterion of one of those profiles is already reached about 3 km below the CPT. In polar winter regions the atmosphere cools substantially throughout the stratosphere because

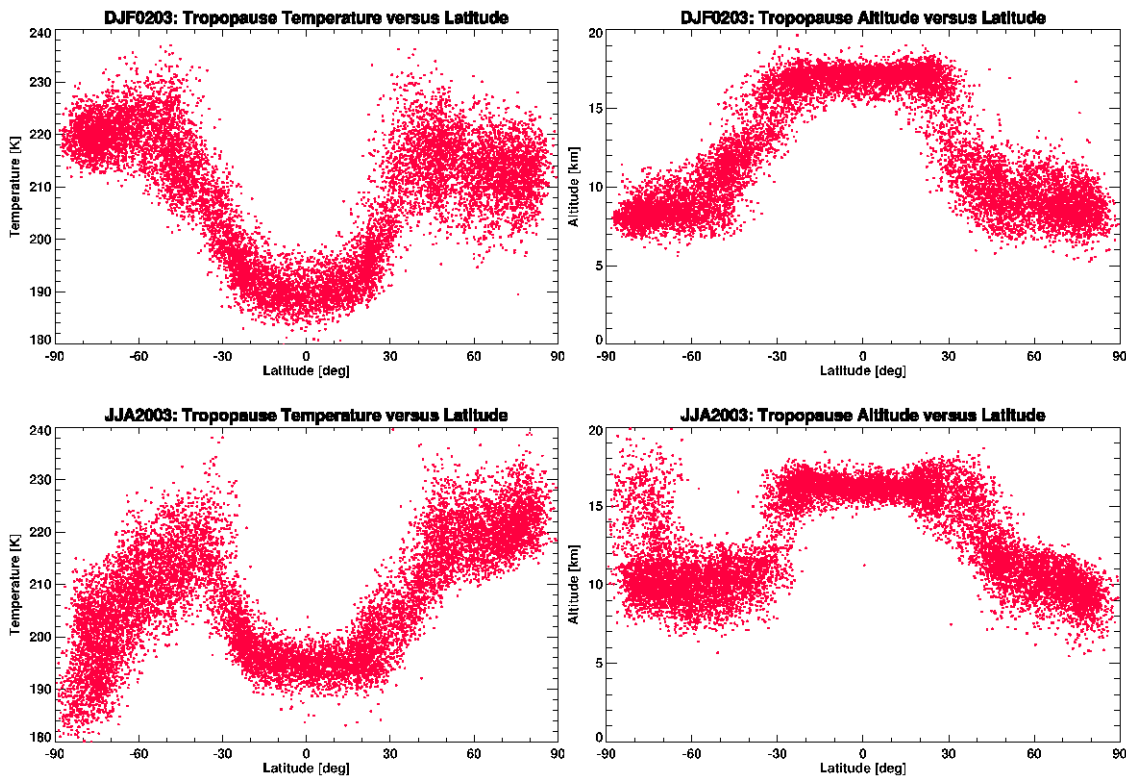


**Figure 1.9:** Seasonal illustration of LRT temperature (left) and altitude (right) versus latitude for the seasons DJF0203 (upper panels) and JJA2003 (lower panels). Shown are all profiles of the CHAMP satellite of which a lapse rate tropopause could be calculated within each season. The annual cycle between summertime and winter is pictured as a representative example of the global thermal tropopause.

the radiative heating of the sun and chemical heating of the ozone production cycle are both missing. The northern hemispheric profiles (blue) are characterized by an almost constant or even slightly increasing temperature in the lower stratosphere, as are the mid-latitude profiles.

Figure 1.9 shows the global distribution of the LRT for northern hemispheric winter DJF 0203 (December, January, February 2002/03) in the upper two panels, and for northern hemispheric summer JJA 2003 (June, July, August 2003) in the lower two panels. The left panels depict the temperature distribution with latitude, and the right panels the LRT altitude distribution with latitude. The LRT was calculated on all available CHAMP profiles for these two seasons (cf. Section 5.1) and is used here as a representative example to picture the global distribution of LRT temperature and altitude.

Globally, the coldest tropopause temperatures can be found at low-latitudes and in the southern hemispheric winter polar vortex. Northern hemispheric winter tropopause temperatures on average reach as low as 190 K (ca.  $-85^{\circ}\text{C}$ ) at low-latitudes, whereas in

summer the average temperature is about 5 K warmer at 195 K. For the southern polar vortex region in northern hemispheric summertime, it is not reasonable to calculate an average temperature because it continuously decreases from around 225 K at 30°S to around 185 K close to the South Pole. At mid-latitudes and especially in high-latitude winter regions the lapse rate of temperature profiles is as an ensemble less uniform due to the special winter atmospheric layering. This leads to difficulties when applying the LRT criterion of *WMO (1957)*.

The LRT altitude also varies throughout the year but not as strongly as temperature. Generally, the low-latitude tropopause is highest reaching 17 km to 18 km in winter and 16 km to 17 km in summer. Throughout the Hadley cell, the altitude decreases to about 8 km to 10 km, more rapidly on the winter hemisphere. In the winter hemispheric polar regions the tropopause altitude varies more than on the summer hemisphere. In the cold southern winter polar vortex air, the troposphere can cool so much, that the LRT altitude can reach as high as almost 20 km. Concluding from these two seasons of CHAMP data, which are taken to illustrate the global distribution of LRT temperature and altitude, the two coldest tropopause regions are the southern winter polar vortex and the tropics during (northern hemispheric) summertime; the low-latitudes also mark the highest tropopause region around the globe.

### 1.3.4 Stratosphere-Troposphere Exchange

As was discussed in the sections above, the tropopause marks a distinct transition layer between the troposphere and stratosphere, allowing for transport of air masses on the large scale from the troposphere to the stratosphere and vice versa only under certain conditions. Stratosphere-troposphere exchange (STE) does take place especially in the tropics through the TTL. However, much scientific attention has recently been paid to the extra-tropical tropopause exchange and its quantification. In connection with double tropopauses, a first glance on extra tropical STE was given by the works of *Pan et al. (2004)* and *Bischoff et al. (2007)*. In the following section, a short overview of recent findings concerning extra-tropical STE will be given.

As is emphasized by *Stohl et al. (2003)* there may be confusion of notion concerning STE. *Stohl (2001)* and *Wernli and Bourqui (2002)* use STE only in the meaning of the one-way transport from the stratosphere to the troposphere, and TSE for the other direction from the troposphere to the stratosphere. This nomenclature can also be found in many tropospheric chemical studies. However, it is proposed by *Stohl et al. (2003)*, and adopted here, to use STE for stratosphere-troposphere exchange in general for both directions, and if specifically accentuating one or the other direction of transport then either TST for troposphere-stratosphere transport or STT for stratosphere-troposphere transport will be used.

**Figure 1.10**, taken from *Holton et al. (1995)*, shows a latitude-altitude cross section from pole to pole and from about the ground to 30 hPa height (roughly 25 km) for January 1993; data were taken from UKMO analyses (*Swinbank and O'Neill, 1994*). Depicted are zonally averaged potential temperature (solid lines) and physical temperature (dashed lines). The heavy solid contour starting in the tropics and moving

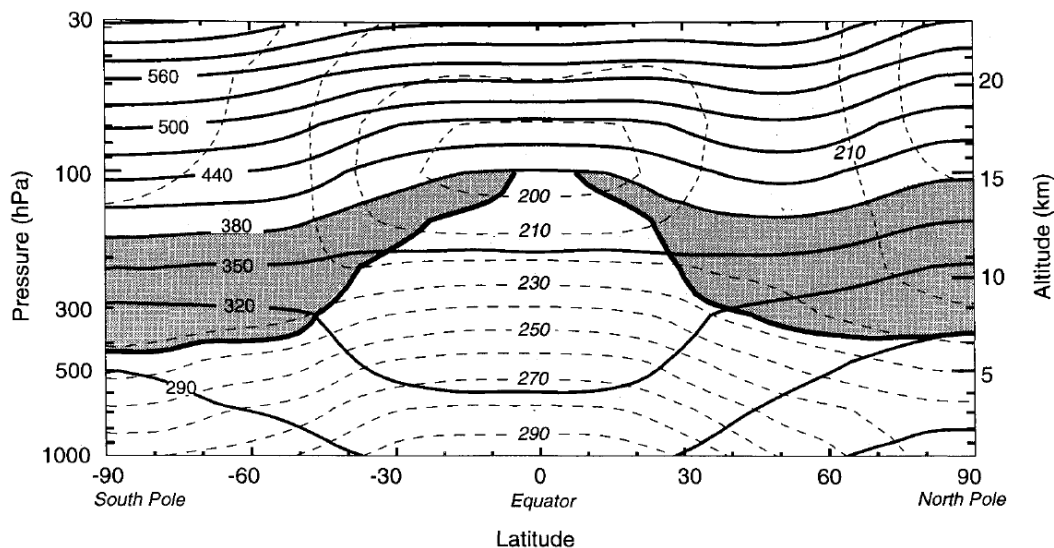


**Figure 1.10:** Zonally averaged global distribution of potential temperature (solid contours) and physical temperature (dashed contours) are pictured. The shaded area, which denotes the lowermost stratosphere, is spanned by the 2 PVU potential vorticity contour below (heavy solid line) and the 380  $\Theta$  isentrope above. Data are taken from UKMO for January 1993, illustration from *Holton et al. (1995)*.

polewards marks the 2 PVU potential vorticity contour, which in this monthly averaged case approximates the climatological tropopause quite well. The shaded area between the 2 PVU contour and the 380- $\Theta$  isentrope denotes the “lowermost stratosphere”.

The lowermost stratosphere is characterized by isentropic surfaces which lie partly within this region, at polar- and mid-latitudes, and partly outside in the tropics. *Hoskins (1991)* has referred to this part of the atmosphere as the “middleworld”. Here, STE is enabled along isentropic surfaces which is relatively fast (*Stohl et al., 2003*) and can indeed occur in both directions (*Chen, 1995; Holton et al., 1995*) because the tropopause intersects the isentropes. The middleworld is embedded above by the “overworld” and beneath by the “underworld”. The overworld lies completely in the stratosphere above the 380  $\Theta$  isentrope, whereas the underworld lies completely in the troposphere. STT to the underworld as well as TST to the overworld is slow because in either case the air is required to cross isentropic surfaces which requires adiabatic cooling or heating, respectively.

In [Figure 1.11](#) the above mentioned principle of STE is shown schematically for one hemisphere illustrating the global aspects of STE. Viewed globally, the Brewer-Dobson circulation (*Brewer, 1949*) determines the air flow from the tropical troposphere into the stratosphere by large scale ascent in the so called “tropical pipe” (*Plumb, 1996*). Air is then transported to the extra-tropical stratosphere caused by Rossby wave breaking in conjunction with westerlies at mid-latitudes at, and below, the tropopause (*Waugh,*

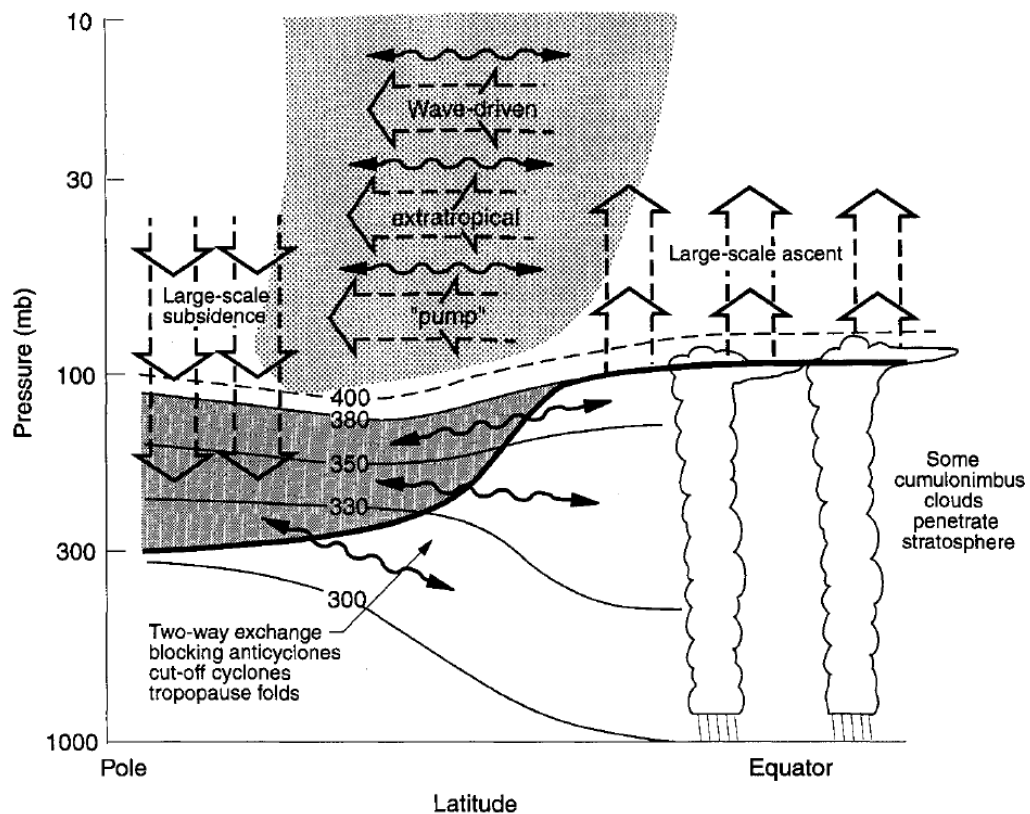


**Figure 1.11:** Large scale dynamical aspects of STE understood and summarized by *Holton et al. (1995)*. The thick line denotes the tropopause which is encompassed by the 380  $\Theta$  isentropes on top; lower isentropes intersect the tropopause and reach from the lowermost stratosphere (shaded area) into the tropical troposphere where STE of various sources can take place. Note that according to today's knowledge cumulonimbus clouds do not reach into the stratosphere. Large scale dynamical circulation, the Brewer-Dobson circulation, is the main drive for STE with rising above the tropics and subsidence in mid- to high-latitudes.

1996). This movement of air from the tropical lower stratosphere to extra-tropical stratosphere is also referred to a "suction pump" (*Holton et al., 1995; Stohl et al., 2003*) or just the "extra-tropical pump" which is the driving mechanism of the Brewer-Dobson circulation. Finally, air flow is then directed downwards from the stratosphere into the troposphere at mid- and high-latitudes (*Holton et al., 1995*).

To determine the net STE mass flux, *Holton et al. (1995)* have argued that using the tropopause as control surface is not essential and may even be misleading. They suggest to use the 380- $\Theta$  isentropes contour as control surface instead, because it separates the overworld from the middleworld rather than the middleworld from the underworld as does the tropopause at high- and mid-latitudes. In addition, it is more convenient to use the 380- $\Theta$  isentropes contour because the transport across this surface can be described on global scales. This avoids knowledge of smaller scale synoptic processes and processes in the vicinity of the tropopause.

Applying this approach, *Appenzeller et al.* (1996) have calculated with a simple model the annual cycle of the net mass transport across the extra-tropical tropopause. They found a distinct net mass cycle in the NH whereas in the SH the variations are found to be weak. The annual net mass cycle they found for the NH has a maximum in late spring and a minimum in autumn. *Appenzeller et al.* (1996) found this net mass flux to be a combined effect of the seasonal variation of the global-scale meridional circulation (Brewer-Dobson circulation) and the seasonal variation of the mass of the lowermost stratosphere which are closely linked to the annual zonal mean changes of the tropopause height. Many more calculations of the STE have been performed, and especially *Wei* (1987) has developed a method to diagnose STE directly from the output of general circulation models (GCMs). Of course, numerical problems arise and are manifold (see discussion in *Stohl et al.* (2003)).

Estimates of global net cross-tropopause mass flux, as performed by *Appenzeller et al.* (1996), characterize extra-tropical STE insufficiently (*Stohl et al.*, 2003) because of three important limitations: They are spatially and temporally averaged and only account for the net mass flux. Especially when incorporating trace gas species into STE estimates, spatial and temporal variations play an important role. Furthermore, the net mass approach renders estimates for trace gas species, which have sources and sinks in the lowermost stratosphere, inadequate.

The STACCATO project (the final report (*STACCATO Team*, 2002) is available from <http://www.forst.tu-muenchen.de/EXT/LST/METEO/staccato>) has extended the approaches by *Wei* (1987) and *Appenzeller et al.* (1996) arguing that, to characterize the effects of STE more completely, tropospheric and lower stratospheric transport preceding or following the crossing of the tropopause plays an important role as well. That is, to distinguish between “deep” and “shallow” exchange events, e.g., between events that connect points outside the tropopause region and such that only connect points within the tropopause region. In that manner, **Figure 1.12** shall be understood which is an adaptation of **Figure 1.11** by *Holton et al.* (1995) but with the new findings of *STACCATO Team* (2002) superimposed.

The main findings of *STACCATO Team* (2002) were, in order to calculate the net mass flux through the tropopause more accurately, to consider the depths and residence times of STT and TST. In **Figure 1.12** these characteristics are shown schematically by the green arrows labeled with the principles of interest which can be divided into “shallow” exchange (shallow and transient exchange, exchange within tropopause region) and “deep” exchange (deep stratospheric intrusion and warm (cold) conveyor belt). The scientific importance in dividing deep and shallow exchange lies in the chemical reaction speed of the induced air. Short exchange events have probably little impact because of the limited probability for mixing and chemical reaction within the new environment (*Wernli and Bourqui*, 2002).

To distinguish between deep and shallow exchange events it is necessary to implement a Lagrangian method as was proposed and first applied to a 1-month data set by *Wernli and Davis* (1997) and then by *Wernli and Bourqui* (2002) to a longer time period. The Lagrangian method is trajectory based and studies the behavior of many trajectories of air parcels started at different locations at the same time in a model. Thus, distinct

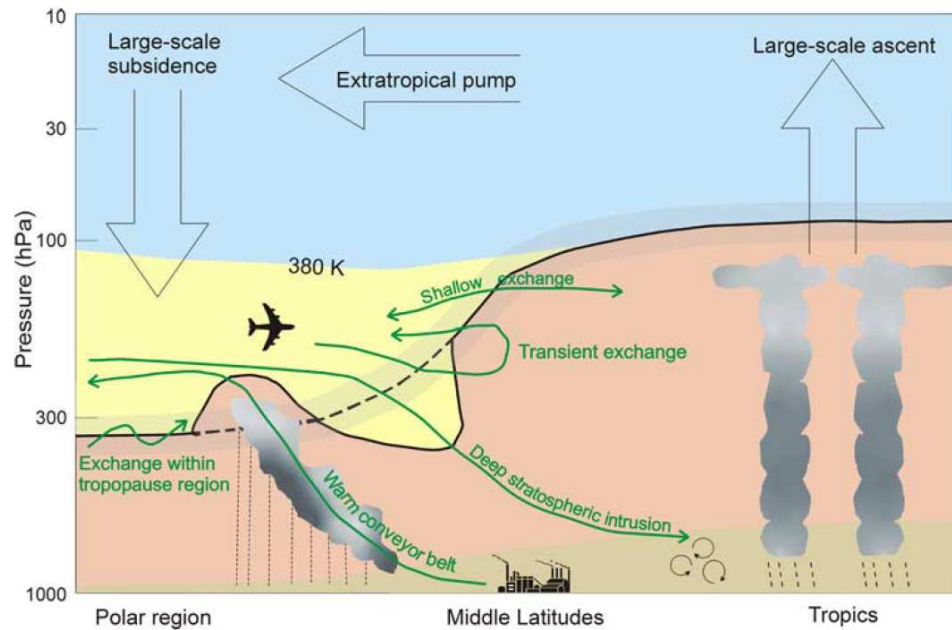


**Figure 1.12:** In this version of *Stohl et al. (2003)* the blue area denotes the stratosphere, the yellow area the lowermost stratosphere which occasionally penetrates into the free troposphere (pink shade) displacing the troposphere from its climatological mean (heavy black line). The brown shade denotes the atmospheric boundary layer in and from which air can be removed from and into the stratosphere, respectively. Note that the pressure is not to scale.

criteria can be defined and applied to each air parcel. *Wernli and Davis (1997)*, *Wernli (1997)*, and *Wernli and Bourqui (2002)* have classified airstreams selecting trajectories to certain criteria. For instance, *Stohl (2001)* has defined deep stratospheric intrusions by a descent of an air parcel of more than 5000 m from any level at or above 5500 m, STT to originate above 2 PVU and arrive at its destination at below 1 PVU, and vice versa for TST. With that approach, *Stohl (2001)* effectively eliminated shallow exchange, e. g., transfer of an air parcel across the 2 PVU control surface from 1.9 PVU to 2.1 PVU, and vice versa, within the tropopause region. This kind of exchange does not play an important role in atmospheric chemistry and is likely to be reversible within a short period of time.

A different method to exclude shallow exchange from the STE calculations was pursued by *Wernli and Bourqui (2002)* and *Sprenger et al. (2003)* who used a residence time criterion: Air parcels which crossed the dynamical tropopause to the troposphere (stratosphere) (2 PVU) and remained there less (more) than 4 days and returned to its origin were considered shallow (significant) exchange events. Exchange events are labeled deep of which the original stratospheric air parcel (STT) penetrates to levels below 700 hPa, and the original tropospheric air parcel (TST) from below the 700 hPa level is injected into the stratosphere within 4 days. However, this concept of residence

time is not yet finalized, because a representative timescale for irreversible mixing is unknown (*Sprenger et al.*, 2003) and therefore the chosen threshold of 4 days is quite arbitrary.

The results obtained from the above stated studies will be presented in the following which present an important link between detailed single case analyses and coarser-scale global estimates of cross-tropopause transport (*Sprenger et al.*, 2003). The residence time criterion applied to exchange events has shown that the major part of air parcels return in less than 4 days to their origin and that thus the quantitative estimate of STT and TST mass fluxes is highly sensitive to the time criterion value used. *James et al.* (2003a,b) have found that more than 90% of cross-tropopause mass fluxes are transient in nature and return within less than 6 hours to their origin. Only about 1%–2% of STT and TST mass fluxes are found to be deep exchange events. Furthermore, it is of great importance to consider not only the net cross-tropopause mass flux but also STT and TST individually, especially “canceling” (of a mass perspective) two-way exchange, termed “symmetrical two-way exchange”.

The annual cycle of the hemispherically integrated net exchange mass flux in the extra-tropics compares well with the results obtained by *Appenzeller et al.* (1996). However, the zonally integrated meridional distributions differ substantially from previous Eulerian studies based upon the Wei approach (*Wernli and Bourqui*, 2002). These meridional integrated distributions describe a fairly simple pattern with maximum STE in the southern mid-latitudes and maxima of TSE in the subtropics and northern mid-latitudes. South of 30°N and north of 70°N the resulting net exchange is upward and in between downward. As is indicated in [Figure 1.12](#), STT events were found to differ significantly from the location of the climatological tropopause and occur some 150 hPa below the tropopause, whereas TST events occur generally at or slightly above the tropopause. This indicates that cross-tropopause exchange preferably takes place in the vicinity of strongly disturbed tropopause as for instance around the Pacific and Atlantic storm tracks. Deep exchange events were found to exhibit a distinct annual cycle with a maximum of occurrence in winter and a minimum with almost no occurrence in summertime. The mass flux varies by more than a factor of 10 between winter and summer.

TSE was found to correspond to the storm track entrance regions near the Asian and North American east coasts at mid-latitudes. Because they originate in the high-emission areas of Japan and North America, these events, especially warm-conveyor belts, represent the main source of anthropogenic emissions in the upper troposphere and lowermost stratosphere. Similarly, STT events can transport stratospheric air into the atmospheric boundary layer and impact the surface O<sub>3</sub> budget. In the NH there are three regions where this can happen, along the North American west coast, the beginning of the Atlantic storm track, and – weaker – in the Mediterranean region.

None of the three climatological studies discussed here (*James et al.*, 2003a,b; *Sprenger et al.*, 2003) have identified a trend in STE for the past. All three have investigated the fifteen year long European Centre for Medium-Range Weather Forecasts (ECMWF) Reanalyses (ERA-15) (*Gibson et al.*, 1997) time span from 1979 to 1993. However, *Sprenger et al.* (2003) state that the inter-annual variability of STE can be substantial which is related to the North Atlantic Oscillation (NAO) and ENSO. During positive

phases of the NAO, the locations of tropopause crossings in the North Atlantic shifts toward higher latitudes and altitudes. During ENSO phases, STE in the eastern tropical Pacific shifts toward higher altitudes and intensifies (Stohl *et al.*, 2003).

### 1.3.5 Trends in Tropopause Parameters

In [Chapter 1.2](#) natural variability and temperature trends due to climate change in the upper troposphere and lower stratosphere (UTLS) region were discussed. In this Section, a short review of science done on trends of tropopause parameters in particular, such as tropopause temperature and height, will be given. Long term observations were performed with the radiosonde network as well as the MSU/AMSU instruments aboard satellites (e.g., Karl *et al.*, 2006) which both present a valuable and thoroughly studied climate record. Here, results obtained from the radiosonde network will be discussed because they measure temperature and pressure at discrete altitude levels whereas the MSU/AMSU measure only an average bulk temperature (cf. [Section 1.1](#)). RO data from various satellites does not yet exist long enough to be able to determine a trend in measured parameters, because to do so in a substantial scientific way a time series of at least seven to thirteen years of data has to be available (Leroy *et al.*, 2006a). However, reanalyses of established weather centers around the world serve as an excellent data set to investigate past climate trends.

Radiosonde data are characterized by high vertical resolution which predestines them for determining tropopause parameters. However, this data set is limited by the continent bound distribution and by instrumentation changes over the years. These changes in instruments and methods have been shown to affect long-term temperature trend analyses (Seidel *et al.*, 2001; Gaffen *et al.*, 2000b). For instance, Seidel *et al.* (2001) have shown that a change in instruments from one brand to another can affect the tropopause temperature by up to 3–4K. One way of coping with that kind of observational problem and also natural oscillating variation, Zhou *et al.* (2001) have adjusted the radiosonde data by fitting correction equations to it in order to determine a trend free of any forcings. However, these corrections themselves again may be erroneous and can profoundly alter trend estimates (Gaffen *et al.*, 2000a).

For a data set of 83 radiosondes, Seidel *et al.* (2001) have investigated changes in the tropical tropopause for the time period 1961 to 1990. They found a multi-decadal linear increase in  $Z_{\text{LRT}}$  of +20 m per decade, a decrease in  $p_{\text{LRT}}$  of about +0.5 hPa per decade, and an accompanying decrease in  $T_{\text{LRT}}$  of  $-0.5$  K per decade. For a subset of this data set, Randel *et al.* (2000) found a comparable linear temperature trend for the time period 1979–1997 of  $(-0.57 \pm 0.18)$  K per decade. In both analyses, the trend was intermitted by short and strong decreases of tropopause height and increases of tropopause temperature due to the volcanic eruption of El Chichón in 1982 and Mount Pinatubo in 1991. Omitting data of the years 1982–1983, Randel *et al.* (2000) found a reduction of the linear temperature trend to  $(-0.28 \pm 0.17)$  K, highlighting the sensitivity of trends to anomalies especially at the beginning (and end) of short data records. Zhou *et al.* (2001) report a temperature trend of the tropical cold point tropopause temperature of  $-0.57$  K per decade obtained by operational radiosonde data from 1973–1998, however,

they accounted for instrumental changes and natural oscillations such as sea surface temperature and the QBO. Very recently, *Seidel and Randel (2006)* have performed a global study using 1980–2004 radiosonde data. They have found an estimated global trend in  $Z_{\text{LRT}}$  of  $+64 \pm 21$  m per decade, a corresponding decrease in  $p_{\text{LRT}}$  of  $(-1.7 \pm 0.6)$  hPa per decade, and a  $T_{\text{LRT}}$  decrease of  $(-0.41 \pm 0.09)$  K per decade. Around the globe they found an increase in tropopause height and an accompanying decrease in tropopause pressure. The largest height and temperature trends they found in the southern hemisphere subtropics, and the smallest in the northern hemispheric polar regions. Everywhere but the most northerly polar regions they found tropopause temperature trends to be negative with the strongest cooling of 0.78 K per decade in the southern hemisphere subtropics.

Many studies have investigated trends in tropopause parameters which occur in reanalysis data. *Randel et al. (2000)* have done so with the National Centers for Environmental Prediction (NCEP)/National Center for Atmospheric Research (NCAR) reanalysis data set (referred to hereafter as the NCEP data). These data span the time period from 1957 to present (*Kalnay and et al., 1996*), and use 28 vertical levels with a vertical resolution of 2 km in the UTLS region. In late 1978, a large discontinuity in tropopause parameters of the NCEP reanalyses was found (*Randel et al., 2000*) which is manifested by a sudden increase in tropopause temperature by around 3 K and in tropopause pressure by about 2 hPa to 3 hPa. With the introduction of satellite data, data sparse regions such as the upper troposphere and lower stratosphere as well as the polar regions suddenly became much better sampled. Because of this discontinuity in reanalyses, trend studies utilizing reanalysis data in general are only significant from 1979 onwards. Even though NCEP data exhibit relatively poor vertical resolution in the tropopause region, *Randel et al. (2000)* found high correlation of inter-annual and seasonal anomalies between radiosonde and NCEP data. However, for the time period 1978–1997 there are substantial biases in the NCEP data with the analyses being 3 K to 5 K warmer than the radiosonde data. Furthermore, *Randel et al. (2000)* have found no trend in tropical tropopause temperature in NCEP reanalyses.

*Hoinka (1999)* has performed a global study in which tropopause parameters such as height and temperature, amongst others, were investigated and compared with radiosonde data. In this and a previous study (*Hoinka, 1998*), no global trend in tropopause height and temperature were found. However, the author states that trends are much greater for smaller regions or even locally. *Hoinka (1998)* has determined  $p_{\text{LRT}}$  trends for the northern and southern hemispheres separately with  $+0.5$  hPa and  $-0.6$  hPa per decade, respectively. *Hoinka (1999)* has found even greater trends for the Arctic and Antarctic with a decrease of  $-1.4$  hPa and  $-1.7$  hPa per decade, respectively, in tropopause pressure which corresponds to an increase in tropopause height which again corresponds to an increase in tropospheric temperature (see also [Section 1.2](#)). On the other hand, *Santer et al. (2003)* found a decreasing global-mean trend of  $p_{\text{LRT}}$  with  $-2.16$  hPa per decade in NCEP data for the time period 1979 to 2000, and  $-1.13$  hPa per decade in data of the ECMWF for 1979 to 1993 which is consistent with those estimated from radiosondes by *Seidel et al. (2001)*. Even in the tropics the trend found was significant in  $p_{\text{LRT}}$  with  $-1.05$  hPa per decade. These differences of the two research groups might be explained by the use of different algorithms of *Hoinka (1998)*

and *Hoinka* (1999) compared to *Santer et al.* (2003). In a recent study *Santer et al.* (2004) have performed a global climate change study in which they used the new ERA-40 reanalysis data (*Simmons and Gibson, 2000*). They found a global trend for  $p_{\text{LRT}}$  of  $(-2.36 \pm 0.47)$  hPa per decade for the satellite time period 1979 to 2001.

## 2 The Radio Occultation Technique

In this chapter a concise overview of the radio occultation (RO) method will be given. It will not be exhaustive because there have been many studies discussing in excessive detail any aspect of the method. Furthermore, the presented study did not aim at improving the method itself but instead apply it to the use of climate studies utilizing RO measurements.

The early days of the RO method are summarized in *Yunck et al. (2000)* giving an overview of the history of GPS sounding. The RO method was developed in the field of space science when in the early days of interplanetary flight the idea emerged to deduce atmospheric properties from flybys. The first results were obtained from the Martian atmosphere (*Fjeldbo and Von Eshleman, 1968*), but soon almost every planet and moon with an atmosphere was probed by radio occultation – except for the Earth itself.

Only with the installation of the American GPS satellite constellation it became feasible to apply the method to Earth's atmosphere. Only then the problem of a reliable and continuous transmitter was solved so that atmospheric profiles obtained via RO yielded competitive, or even better, results compared to already established remote sensing methods. Finally, in 1995 the first proof-of-concept mission GPS/MET was launched and turned out to be an unqualified success (see below). As of today, about ten satellites are carrying a GPS receiver to perform RO measurements with the COSMIC constellation consisting of six satellites alone. The future of probing Earth's atmosphere with RO measurements looks quite promising and might see anything from dozens to hundreds of nano-satellites swarming in low Earth orbit (LEO) to provide hundred of thousands of measurements daily to very sophisticated satellite constellations which measure not only the classic properties of the atmosphere but in addition trace gases and wind speed and direction.

In the following section a historical overview as well as a short outlook of possible future satellite missions of RO measurements from satellites will be given in the following section. In the next section the RO method will be introduced and in the last section its relevance in climate monitoring will be outlined.

### 2.1 Radio Occultation (RO) Data Obtained by Satellites

In order for RO measurements to work, not only permanent and reliable transmitters have to be available but also an extensive ground network to supply reference data and to collect data from satellites. Today, the International GPS Service, operated by civilian organizations of both scientific and commercial origin, have installed a globally

distributed network of over 250 tracking stations providing orbit determination (reference data) with cm accuracy and some even with mm accuracy (*Anthes et al.*, 2000; *Yunck et al.*, 2000). The GPS satellite constellation, fully operational since the early 1990's, today consists of 29 active GPS satellites which are flying in six planes with five to six satellites each (<http://www.navcen.uscg.gov/>). The GPS satellites were originally deployed for navigation and positioning purposes by the U.S. Department of Defense and served primarily military use. Civilian usage was granted but possible only in a degraded mode limiting the positioning to about 100 m. This degradation by encryption of the signals was turned off in April 2000.

### 2.1.1 Proof-of-Concept Missions

NASA's MicroLab I spacecraft was the first research LEO satellite to carry a GPS receiver to perform RO measurements, called the GPS/MET (GPS/Meteorology) receiver. It was launched on April 3, 1995 and was planned as a proof-of-concept experiment. It had turned out to be an exceptional success even though it was designed very simply. The geometry of a LEO satellite with one receiver and the 24 GPS satellites active at that time allowed for about 250 occultations per day. Earlier RO missions were equipped with one receiver which looks behind the satellite thus recording occultations of setting GPS satellites, called setting occultations. Nowadays, RO missions are usually equipped with two receivers, one looking in front and one backwards recording setting and rising occultations effectively doubling the amount of possible measurements for each LEO satellite. The GPS/MET receiver under optimum conditions, however, was able to collect only about 150 setting occultations per day (*Rocken et al.*, 1997). Furthermore, the GPS signal at that time was usually degraded by anti-spoofing encryption and only during so-called "prime times" the encryption was turned off. For these prime times the recorded RO profiles were of excellent quality from which atmospheric profiles of density, pressure, temperature, and moisture were computed (*Ware et al.*, 1996). *Rocken et al.* (1997) compared more than 1,200 atmospheric profiles retrieved from GPS/MET to NCEP and ECMWF analyses, radiosondes, and satellite data including GOES-8 (Geodetic Earth Orbiting Satellite), TOVS (TIROS Operational Vertical Sounder), HALOE (Halogen Occultation Experiment), and MLS (Microwave Limb Sounder) instruments (*Rocken et al.*, 1997).

After the successful GPS/MET experiment, two further very small spacecrafts were launched: The Danish Ørsted, which was mainly aimed at measuring the Earth's magnetic field but carried a GPS receiver alike to that of the GPS/MET experiment; and the South African Sunsat, which was a satellite designed by students and carried a high resolution imager. Both satellites were launched in late February 1999. Unfortunately, the Ørsted satellite suffered many problems like low signal-to-noise ratio, encryption of the GPS signals turned on during the complete lifetime of Ørsted, interference with the attitude control system causing data gaps, and at times a rotating satellite platform (*Larsen et al.*, 2005). The Sunsat mission suffered from antenna constraints and also from continuous GPS signal encryption. *Larsen et al.* (2005) report on a 20-day continuous measurement campaign of the Ørsted satellite in February 2000 in which more than

1,200 profiles were obtained. Even though they were limited to one of the GPS frequencies ( $L_1$ ) due to the encryption, they retrieved refractivity and dry temperature profiles. When comparing against ECMWF analyses they found a difference in temperature of 0.5K in the height range between 500 hPa and 30 hPa (around 5 km to 20 km).

### 2.1.2 Present Day RO Satellite Missions

Following these proof-of-concept and experimental satellite missions, the first two research satellites were launched with an enhanced GPS receiver developed by the Jet Propulsion Laboratory (JPL), California, U.S.A., called BlackJack. On July 15, 2000 the German geoscience satellite CHAMP (*Wickert et al., 2001b; Wickert et al., 2004*) was launched followed by the Argentine SAC-C satellite in late November 2000 (*Hajj et al., 2004; Schmidt et al., 2005*). Both satellites carry many more instruments on board and are mainly aimed at exploring the Earth's magnetic field. The CHAMP satellite has provided a continuous data flow of RO measurements since September 2001 with a varying amount of occultations per day, but since March 2002 a full and (almost) continuous data flow was established (cf. [Figure 3.1](#)). The CHAMP satellite has been extremely successful and as of today has outlasted its projected lifetime by far which is now expected to last until 2009 (*Wickert et al., 2007b*). The data of this satellite provides the first opportunity to build RO based climatologies and serves as data basis for this presented study.

The SAC-C satellite, on the contrary, was rather used as an experimental platform for testing, e. g., for software uploads, open loop tracking, and much more (*Hajj et al., 2004*). Thus, the coverage of RO measurements of the SAC-C satellite has varied considerably and only a period of about a year is provided by JPL as a continuous data record (C. Ao, JPL, personal communication 2006). Nevertheless, the available RO data obtained from the SAC-C satellite has also turned out to be of great value and a first inter-comparison of different RO measurements was possible (*Hajj et al., 2004*) which proved three central claims in favor of the RO method: (1) GPS soundings are effectively free of instrumental bias and drift; (2) individual temperature profiles are accurate to  $< 0.5$  K between  $\sim 5$  km and 20 km; and (3) averaged profiles for climate studies can be accurate to  $< 0.1$  K.

On March 17, 2002 the twin Gravity Recovery And Climate Experiment (GRACE) satellites (A and B) were launched carrying GPS receivers alike of CHAMP. The GRACE satellites, separated by around 200 km, were equipped each with one GPS receiver with the first satellite to carry out rising occultations and the second satellite setting occultations. In this way, the amount of occultations compared to those of the CHAMP satellite is doubled. The first activation of the RO experiment on board the GRACE-B satellite (setting occultations) occurred on July 28 and 29, 2004 (*Wickert et al., 2005*). Comparison with CHAMP measurements showed excellent agreement to within 1% to 2% in refractivity between 5 km and 30 km. Unfortunately, even though GRACE-A occultations are operating continuously since May 22, 2006 and were already successfully assimilated into NWP models (*Healy, 2007*), dissemination of GRACE RO phase delay measurements to the scientific community as of today is still restricted (*Wickert, personal communication 2007*).

On April 14, 2006 the first constellation of six RO satellites was launched called the Constellation Observing System for Meteorology, Ionosphere & Climate (COSMIC) (*Anthes et al.*, 2000; *Rocken et al.*, 2000). All six satellites carry a further enhanced GPS receiver which allows to track about 90% to 95% of the profiles to within 1 km close to the surface – a huge improvement compared to the previous missions. Additionally, all six satellites are able to perform setting and rising occultations which gives a theoretical amount of around 3,000 profiles daily. With the COSMIC measurements, enhancements were possible especially in the lower troposphere because of the open loop tracking functionality of the receiver. This allows for tracking the occultations further down also in humid regions which in turn allows for better water vapor retrieval.

The European Meteorological Operational (MetOp) satellite carrying a Global navigation satellite system (GNSS) Receiver for Atmospheric Sounding (GRAS) finally was launched on October 19, 2006. Three identical satellites have been built and are planned to be put into orbit one after the other assuring 14 years of continuous operational measurements. These are the first satellites whose RO measurements are aimed for operational meteorological and climate monitoring which are planned to be assimilated into NWP models. Unfortunately, EUMETSAT (European Organization for the Exploitation of Meteorological Satellites) still has problems with an operational dissemination of RO measurements even to NWP centers (*von Engeln et al.*, 2007). However, first results of a test suite of MetOp RO measurements look very promising with profiles reaching as far down (as can be judged of now) as with the COSMIC satellites. Also bending angle profiles appear to produce robust bias statistics up to a height of 40 km with the noise of most profiles less than  $1 \mu\text{rad}$  at 70 km (for comparison CHAMP profiles produce  $\sim 3 \mu\text{rad}$  of noise at the same height). Very recently, at the WEGCENTER/UNI GRAZ *Pirscher et al.* (2007b) performed an initial validation of one day of GRAS RO data and confirmed the accuracy and precision of the data for retrieved atmospheric parameters like refractivity and dry temperature.

The most recent satellite launched with a RO receiver on board was the German TerraSAR-X satellite, launched June 15, 2007. It is mainly aimed at providing radar images with unprecedented quality and resolution. Orbit determination of this satellite is provided with good quality and RO measurements, not being the primary mission goal, are in commissioning phase (*Wickert et al.*, 2007a).

With all of these satellite programs featuring RO measurements under way, the RO method seems to have established itself within the scope of only one decade. What the successful CHAMP mission has set out to provide – the first RO based data set suited for climate monitoring – will very probably be continued and enriched because of the inherent self calibrating feature of the RO method thus allowing for the assembly of different RO data sets into one abundant and continuous climate record.

### 2.1.3 Future RO Missions

The future of RO measurements from space seems as bright as ever before. Not only are many very promising satellite missions planned but in addition the GNSS satellite constellation is on the merge of being considerably upgraded. Russia operates its

own GLObal Navigation Satellite System (GLONASS) of which the first satellite was launched in 1982. However, today there are only eight satellites functioning which does not suffice for a global navigation coverage. But there are plans to make GLONASS fully functional in the near future (<http://www.glonass-ianc.rsa.ru/>). The European Union is planning to install its own GNSS satellite system, called Galileo (<http://www.esa.int/esaNA/galileo.html>). It is planned to be fully operational in 2013 with 27 operating satellites which transmit radio signals compatible to those of the American navigation system. Furthermore, China is planning to install its own satellite navigation system as well, which is called Compass Navigation Satellite System (CNSS) with five satellites in geostationary orbit and 30 satellites in medium Earth orbit. China has already installed the Compass Navigation Satellite Experimental System (CNSES) including three satellites launched in 2000 and 2001 which already provide functioning positioning and navigation services (<http://www.sinodefence.com/strategic/spacecraft/beidou2.asp>). With the installation of all these GNSS, the amount of possible RO measurements will linearly increase as long as it will be assured that research satellites can receive the transmitted radio frequencies.

Of course scientists do not rely on these improvements alone but enhance their research spacecrafts as well. Korea is planning their KOMPSAT-5 (Korea Multi-Purpose SATellite) research satellite which carries a GPS receiver for RO measurements. It is scheduled to be launched in 2010 (*Cho and Chung, 2007*). Italy plans the ROSA (Radio Occultation Sounder for Atmosphere studies) mission to be installed on the Indian OCEANSAT-2 satellite which is scheduled for launch as soon as Spring 2008 (*Perona et al., 2007*). Both missions will provide RO measurements on a single platform basis with potentially setting and rising occultations summing up to around 500 profiles daily for each satellite.

In addition to newly planned RO missions, some of which will be introduced below, occultation instruments will stay irresistible as add-on missions to already planned ones as well as to future Earth observing missions. The additional payload is very small adding a valuable new science dimension to the spacecraft (*Yunck et al., 2000*). These features have helped RO measurements to their popularity today and in the future will potentially make them a part of almost any LEO satellite launched.

*Yunck et al. (2000)* propose a far more revolutionary idea which actually only carries on the fast developments of RO measurement technology in the last decade. They propose to develop dozens or even hundreds of small and very cheap “nano-sats”, which will weigh only a few kilograms, consuming less than 10 W of power, and costing a few hundred thousand dollars each to produce in volume. With such an array of RO satellites deployed in space, tens of thousands of RO measurements would be possible daily, having great impact on weather prediction, storm and hurricane track and intensity prediction, and on the prediction of many more severe meteorological events. In *Yunck et al. (2007)* the idea has evolved and been named the Community Initiative for Continuing Earth Radio Occultation (CICERO): the funding for the project is to come from private sponsors, by 2011 it is planned to already have 24 nano-satellites in orbit and by 2016 possibly as many as 100.

A different approach is pursued by two groups which are led by Kirchengast, who pro-

poses the ACCURATE (Atmospheric Climate and Chemistry in the UTLS Region And climate Trends Explorer) project (*Kirchengast and Schweitzer, 2007; Kirchengast et al., 2007*), and by Kursinski, who proposes the ATOMMS (Active Temperature, Ozone, and Moisture Microwave Spectrometer) project (*Kursinski et al., 2004, 2007*). Both projects have the same principle idea in common which does not solely rely on GPS – LEO occultations but which introduces the concept of LEO – LEO cross links. Whereas Kursinski proposes to rely on the approved concept of utilizing radio waves, the group of Kirchengast proposes a new innovation by additionally using infrared wavelengths for the LEO – LEO cross links. With this new concept and the usage of infrared wavelengths, a complete new suite of observables can be detected like trace gases and their isotopes, aerosols, and wind fields.

## 2.2 Concise Introduction to the RO Method

is a passive, limb sounding method to probe the atmosphere with satellite measurements. The geometry of that method is summarized in [Figure 2.1](#). One GPS satellite, orbiting at  $\sim 20,000$  km altitude (above ground) transmits two radio signals at  $f_1 = 1,575.42$  MHz and  $f_2 = 1,227.60$  MHz. These are received by a LEO satellite at about 500 km to 800 km (above ground) altitude just during that time in which the radio signals pass through the atmospheric layers. Due to the refractive field of the atmosphere the signals are bent, slightly differently in the dispersive ionosphere, and a phase delay on the signals is imposed which can be determined by the receivers. In order to retrieve atmospheric quantities from these phase delays, several steps of calculations have to be followed which include a very precise determination of the orbit characteristics of the GPS and LEO satellites, solution of the raypath geometry of the occultation, the inversion to retrieve refractive index, and the retrieval of atmospheric parameters. Advantages of this method are manifold and include a low cost satellite payload and all weather capability, very high precision and accuracy as well as long-term stability making it ideal for climate monitoring purposes. Due to the utilization of radio waves, RO measurements are hardly affected by humid conditions and not at all by aerosols giving it an advantage over most other commonly used remote sensing methods.

The dry air RO processing chain starting with the occultation measurement itself and ending up with highly accurate and precise atmospheric parameters is described in many publications and over time has been very much refined. For the concise introduction below, information was mainly taken from *Kursinski et al. (1997)*, *Kursinski et al. (2000)*, and *Hajj et al. (2002)* who give a thorough review of the method and perform an overall error analysis of possible error sources inherent to the retrieval chain. The retrieval used in this study was developed by *Gobiet (2005)* and error analyses of it were performed by *Gobiet and Kirchengast (2004)* and *Steiner and Kirchengast (2005)*. There are many early theoretical studies which paved the way for our understanding of the RO method and the practical use of it today which are not mentioned here. Furthermore, ongoing research of specific fields, such as advanced retrieval schemes of the bending angle in the lower humid troposphere via wave optics, will not be commented on below.

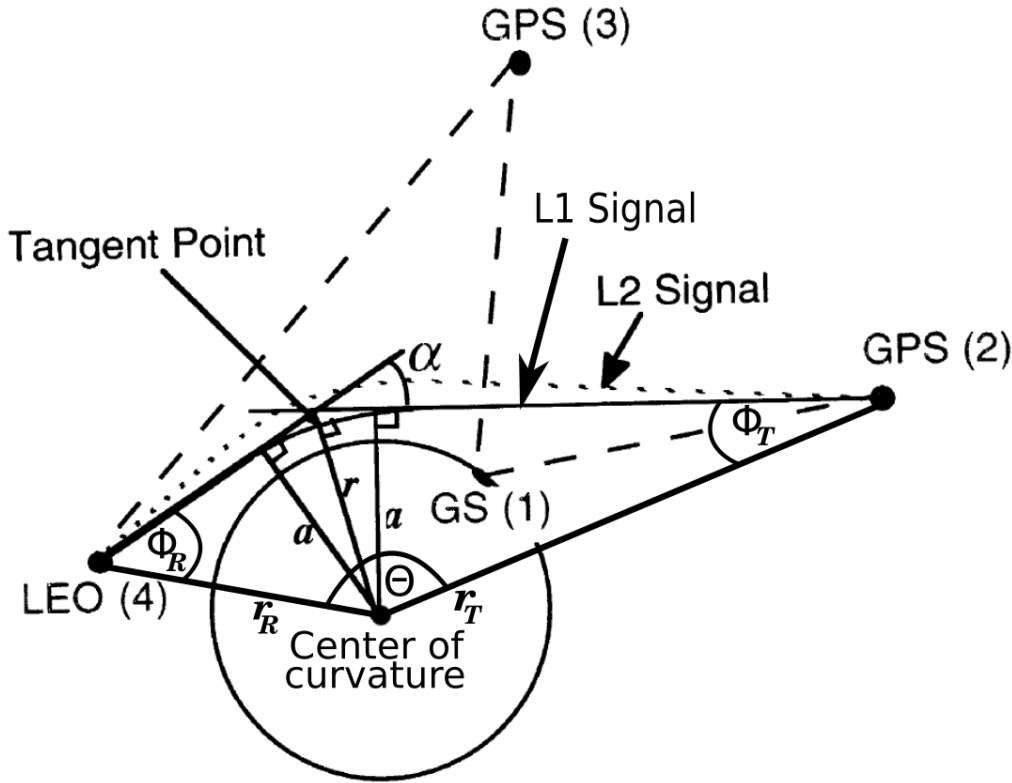


**Figure 2.1:** GPS RO method geometry showing the transmitting GPS (2) satellite and receiving LEO (4) satellite as well as a reference GPS (3) satellite and the ground station (1). Defined are the bending angle  $\alpha$ , impact parameter  $a$ , and Earth radius  $r$  as well as the two slightly different paths of the L1 and L2 radio signals transmitted by the GPS satellites (adopted from *Hajj et al. (2002)* and modified).

As a user of RO measurements one is provided with phase delays by the data centers such as the GeoForschungsZentrum (GFZ), Potsdam, Germany. However, great effort of these centers has been taken to precisely calibrate RO measurements in order to gain high quality phase delay data (e.g., *Wickert et al., 2001a; Wickert et al., 2004*). In order to precisely allocate the RO measurement to the according time of the phase delays, that is the altitude of the impact parameter, clock uncertainties of each satellite have to be accounted for. This can be achieved by a highly stable and precise atomic clock situated at the ground station and the inclusion of a reference GPS satellite (see [Figure 2.1](#)). Furthermore, extreme accurate orbit determination of the GPS and LEO satellites (better than 0.05 mm/sec in velocity) has to be achieved for the RO method to result in accurate atmospheric profiles.

When considering a double difference of a linear combination of the transmitter (GPS) and receiver (LEO) as well as the ground station phases, clock instabilities of the satellites and the encryption modulation of the GPS satellite are effectively eliminated. *Hajj et al. (2002)* have described an even more accurate method used at JPL but state that

for non-encrypted phases (since April 2000) the double-differencing method produces results of satisfying accuracy. In addition to clock error, errors due to atmospheric scintillations, which are caused by sharp vertical moisture and temperature gradients, have to be accounted for. These atmospheric structures lead to multipath propagation of the GPS signal connecting the same transmitter and receiver positions which seriously complicates the tracking of the GPS signals so that in the worst case the tracking receiver loses the GPS lock completely.

After the calibration process, which resulted in the phase delays for both the L1 and L2 GPS signal frequencies, the phase delays are smoothed from their original 50 Hz sampling rate down to 10 Hz, regularized and filtered. The regularization process implemented in the retrieval used for this study is described in detail by *Syndergaard* (1999) applying a third order difference operator. Following the regularization, the atmospheric Doppler shift as the first time derivative of the phase delays has to be determined. After the filtering and regularization process a simple differentiation scheme can be applied to calculate the Doppler shift (*Gobiet*, 2005).

After the calibration process, which resulted in the phase delays for both the L1 and L2 GPS signal frequencies, the atmospheric Doppler shift as the first time derivative of the phase delays has to be determined. The process of deriving the Doppler shift within the retrieval used for this study is described in *Syndergaard* (1999). Usually, the phase delays are smoothed from their original 50 Hz sampling rate down to 10 Hz, regularized and filtered, which then allows for a simple differentiation scheme to be applied (*Gobiet*, 2005).

The atmospheric Doppler shift can then be combined with satellite position and velocity vector measurements to determine the atmospheric bending angle  $\alpha$  as a function of the impact parameter  $a$  (as indicated in [Figure 2.1](#)). The bending angle  $\alpha(a)$  in the transmitter frequency  $f_T$  is given by

$$f_D = \frac{f_T}{c} (\mathbf{v}_T \mathbf{e}_R + \mathbf{v}_R \mathbf{e}_R) \quad (2.1)$$

$$= -\frac{f_T}{c} (v_T^r \cos \Phi_T + v_T^\ominus \sin \Phi_T + v_R^r \cos \Phi_R - v_R^\ominus \sin \Phi_R) \quad (2.2)$$

where  $\mathbf{v}_T$  and  $\mathbf{v}_R$  are the transmitter and receiver velocities,  $v^r$  and  $v^\ominus$  the radial and tangential components of the velocity vectors,  $\mathbf{e}_R$  and  $\mathbf{e}_R$  the unit vectors of the velocity vectors, and  $\Phi_T$  and  $\Phi_R$  (cf. [Figure 2.1](#)) the angles between the ray path and the spacecraft position vectors at the transmitter and the receiver.

The assumption of spherical symmetry of the Earth's atmosphere is essential for further determining the bending angle and impact parameter. With this assumption the oblateness of the Earth is neglected which can lead to a temperature error of up to 6 K (*Syndergaard*, 1998). To avoid that error, *Syndergaard* (1998) suggest to approximate the ellipticity of the Earth by moving the center of curvature to the middle of the circle which best fits the ellipsoid at the tangent point of the occultation. For the calculation of the complete occultation this new, local center of curvature (cf. [Figure 2.1](#)) is assumed and can be as far as 40 km off from the real center of the Earth. With the help of

that method, errors in temperature reduce to less than 0.1K at the surface and vanish entirely above  $\sim 8$  km (*Syndergaard, 1998*). With the assumption of spherical symmetry, the next two equations needed to determine the bending angle and impact parameter are simplified to

$$\alpha = \Phi_T + \Phi_R + \Theta - \pi \quad (2.3)$$

$$a = r_T \sin \Phi_T = r_R \sin \Phi_R \quad (2.4)$$

where  $\Theta$  is the angle between the transmitter and receiver position vectors, and  $r_T$  and  $r_R$  the distances of the transmitter and receiver to the center of curvature, respectively (cf. [Figure 2.1](#)). The Doppler shift  $f_D$  can then be iteratively calculated from [Equation 2.2](#) through [Equation 2.4](#).

The retrieved bending angle and impact parameter account for the complete neutral atmosphere. However, the upper half is made up of the dispersive ionosphere in which the two radio frequencies travel at slightly different paths (cf. [Figure 2.1](#)). The separation of the two frequencies near the tangent point can vary as much as about 5 km depending on tangent height, solar activity, and local time and location. If the ionospheric effect is not corrected for, temperature errors of several Kelvin may be propagated downwards into the UTLS region. Within the RO method, nowadays the most widely used method to account for the ionospheric dispersion was developed by *Vorob'ev and Krasil'nikova (1994)*. It is a linear correction scheme which accounts for both the L1 and L2 ray paths:

$$\alpha_{na} = \frac{f_1^2 \alpha_1(a_1) - f_2^2 \alpha_2(a_2)}{f_1^2 - f_2^2}, \quad (2.5)$$

with  $\alpha_{na}$  the corrected bending angle of the neutral atmosphere,  $f_1$  and  $f_2$  the L1 and L2 carrier frequencies, respectively, and  $\alpha_1(a_1)$  and  $\alpha_2(a_2)$  the bending angles of L1 and L2 frequencies, respectively. Because there are two GPS frequencies and the refractivity is proportional to  $1/f^2$  the ionospheric effect can be eliminated with the above linear combination. It removes first-order dispersive ionospheric bending contributions, however, higher order terms remain and may influence the retrieved atmospheric profile. *Mannucci et al. (2006)* state that with the refined retrieval algorithms nowadays the ionospheric correction poses one of the major error sources in the RO processing chain in terms of producing a long-term stable climate record (see below). The only way to further reduce ionospheric errors is to incorporate knowledge of the state of the ionosphere at the time and location of the occultation.

With the assumption of spherical symmetry of the atmosphere, the bending angle as a function of impact parameter can be related to the index of refraction  $n$  via

$$\alpha(a) = -2\alpha \int_a^\infty \frac{1}{\sqrt{(a'^2 - a^2)}} \frac{d \ln(n)}{da'} da'. \quad (2.6)$$

This integral can be inverted by using an Abelian transformation to express  $n(a)$  in

terms of  $\alpha$  and  $a$  (Fjeldbo *et al.*, 1971):

$$n(a) = \exp \left( \frac{1}{\pi} \int_a^\infty \frac{\alpha}{\sqrt{(a'^2 - a^2)}} da' \right). \quad (2.7)$$

The Abelian inversion is a crucial step within the RO processing chain and has to be treated very carefully. High altitude bending angle, and any errors within like an incorrect ionospheric correction, is propagated downwards. Furthermore, in practice the integral is not solved for the entire positive halfroom but is initialized at a high altitude. The procedure of how this is done for the retrieval used in this study is described in detail in Gobiet (2005). In general a high altitude climatological initialization by means of a statistical optimization scheme with background data is performed.

The refractive index as a function of altitude at radio wavelengths can be related to refractivity which in turn depends on four main sources. In order of importance these are the number density of dry atmosphere molecules of the neutral atmosphere, water vapor molecules, free electrons in the ionosphere, and particulates such as liquid water and are related for every altitude step via (Kursinski *et al.*, 1997):

$$N = (n - 1) \cdot 10^6 = k_1 \frac{p}{T} + k_2 \frac{p_w}{T^2} + k_3 \frac{n_e}{f^2} + k_4 W, \quad (2.8)$$

where  $p$  is pressure in hPa,  $p_w$  partial pressure of water vapor,  $T$  temperature in K,  $n_e$  electron density in  $m^{-3}$ ,  $f$  radio frequency in  $s^{-1}$ , and  $W$  liquid water or ice content in  $g/m^3$ . The constants have the values  $k_1 = 77.6 \text{ K hPa}^{-1}$ ,  $k_2 = 3.73 \cdot 10^5 \text{ K}^2 \text{ hPa}^{-1}$ ,  $k_3 = 4.03 \cdot 10^7 \text{ s}^2 \text{ m}^{-3}$ , and  $k_4 = 0.6 \text{ m}^3 \text{ g}^{-1}$  for ice content and  $k_4 = 1.4 \text{ m}^3 \text{ g}^{-1}$  for liquid water content. The first term on the right hand side of Equation 2.8 is called the dry refractivity term and is dominant below  $\sim 60$  km to 90 km. The second term is called the moist refractivity term and becomes important in humid lower tropospheric regions (especially in the tropics) since water vapor produces 15 to 20 times the refractivity per molecule as a dry air molecule. The first two terms were originally given by Smith and Weintraub (1953) (cf. Equation 4.2) and are accurate to within 0.02% for the dry term and  $< 2\%$  for retrieved humidity. The third term describes the ionospheric contribution mentioned above and becomes important above  $\sim 60$  km to 90 km. The last term is due to scattering of liquid water droplets or ice crystals but is very small in comparison with the other terms and is usually neglected.

After having corrected for the ionospheric dispersion, only the first two terms remain. In regions which are dry only the first term is relevant. These regions are located above an altitude at which the temperature amounts to less than 230 K. At this temperature the error introduced by the “dry temperature” estimation amounts to less than 0.1 K (Foelsche *et al.*, 2007a). In the atmosphere dry temperature profiles thus are virtually identical to physical temperature profiles down to an altitude of about 8 km in winter at polar latitudes and about 14 km in the tropics. The dry air retrieval as used in this study makes use of the ideal gas law to give dry density as a function of refractivity from

Equation 2.8:

$$\rho_{\text{dry}}(z) = \frac{N(z) \mu_{\text{d}}}{k_1 R^*} = \frac{p(z) \mu_{\text{d}}}{T(z) R^*}, \quad (2.9)$$

with  $z$  being altitude,  $R^* = 8.3145 \text{ J (mol K)}^{-1}$  the ideal gas constant (*Lide, 1993*), and  $\mu_{\text{d}} = 28.964 \text{ kg kmol}^{-1}$  is the molecular mass of dry air (*Lide, 1993*) which is known a constant in the homosphere (below  $\sim 100 \text{ km}$ ). Dry pressure is obtained from dry density by integrating the equation of the hydrostatic equilibrium

$$p_{\text{dry}}(z) = \frac{\mu_{\text{d}} g(\varphi)}{k_1 R^*} \int_z^\infty dz' N(z') \quad (2.10)$$

with  $g(\varphi)$  the gravitational acceleration at the surface dependent on latitude  $\varphi$ . Dry temperature profiles can then be retrieved with the dry refractivity term of [Equation 2.8](#).

The retrieval of water vapor is not directly possible with the above mentioned process since there are only three equations but four unknowns which can be summarized to

$$p_w = \frac{N T^2 - k_1 p T}{k_2}. \quad (2.11)$$

This is called the water vapor ambiguity and can only be solved with additional background information. In practice, temperature estimates are taken from weather analyses and  $N(z)$ ,  $p(z)$ , and  $p_w(z)$  are calculated iteratively for each altitude step from [Equation 2.9](#), through [Equation 2.11](#) to obtain a water vapor profile. Alternatively, and in fact preferably, in most areas, a one-dimensional variational (1D-VAR) approach can be applied, which enables to jointly retrieve temperature and water vapor in an optimal estimation sense (e.g., *Healy and Eyre, 2000*)

## 2.3 Climate Benchmark Requirements for RO Measurements

*Ohring et al. (2005)* have discussed accuracy and instrument stability needs for future satellite missions in general. The accuracy is determined by the systematic error of the data, the stability of a measurement instrument is considered as the repeatability and reproducibility of the measurement over a long time period such as a decade. The accuracy and stability requirements were thought of in the context of the current understanding of the climate system and expected climate change and trends in the future. Furthermore, it is vital to consider both requirements at the same time because one without the other will not suffice for creating a climate benchmark record. To detect climate change in the temperature signal within the free atmosphere, *Ohring et al. (2005)* set the limit of the accuracy in the troposphere and stratosphere to 0.5 K and for the stability to 0.04 K per decade and 0.08 K per decade, respectively.

*Leroy et al. (2007)* have undertaken a study on how long it will take in general to detect a climate trend signal from satellite measurements and came up with accuracy

requirements for satellite climate benchmark missions. They found that the signal detection times and requirements are dictated by natural variability of the climate signal to be detected and dependent on instrument lifetime. A climate model was used to investigate the signal detection time of the 500 hPa temperature with an assumed trend of 0.2 K per decade. If the measurement uncertainty was 0.02 K the detection time was found to be 33.6 years and 34.0 years with a satellite lifetime of 2 years and 6 years, respectively. The signal detection time increases as both the measurement uncertainty and the satellite lifetime increases. The reason for the latter connection is that the uncertainty of the satellites' measurements is uncorrelated to each other and thus average out with more satellites.

For GPS RO measurements one can come up with the same accuracy and stability requirements and signal detection times, however, since temperature is not the prime measurand it is more useful to give those numbers in refractivity. *Leroy et al.* (2006b) have performed a climate signal detection study with a climate model analyzing the sensitivity of refractivity derived from GPS occultation measurements by means of the Bayesian statistics. They found that refractivity is suited very well as an observable for climate monitoring. However, their results of climate models forced by a 1% per year increase of CO<sub>2</sub> showed a very small trend in the troposphere despite tropospheric warming. This is explained by the fact that not only temperature is increasing but also pressure as a function of geopotential height. Because refractivity is proportional to density, the overall effect following the ideal gas law is one of cancellation and a trend of less than 0.1% per decade is seen throughout much of the troposphere (*Leroy et al.*, 2006b).

*Leroy et al.* (2006b) have determined the accuracy which is needed for a refractivity measurement to emerge above the background noise of natural inter-annual variability to 0.2% in the stratosphere in order to detect changes in the Brewer-Dobson circulation and a mere 0.01% in the troposphere in order to detect changes in the hydrological cycle or the storm track. To achieve the latter requirements of course is very challenging.

### 2.3.1 S.I. Traceability

For a data set to be used as a climate benchmark record the highest requirements set out for observational data have to apply (see above). These requirements must be as strict and generic so that users in a few decades from now are still able to completely reproduce the data and understand all significant constraints to it. One key component of producing a benchmark data record is to assure "S.I. traceability" (e.g., *Ohring et al.*, 2005; *Mannucci et al.*, 2006), i.e., to ensure that the measurement is tied to the International System of Units (S.I.). This system provides the most accurate foundation possible for measurements including the six physical units of the second, meter, kilogram, ampere, kelvin, candela, and mole. For RO measurements, the unit to be traceable to is the second, since the prime measurement is the atmospheric Doppler shifted phase delay in unit time (cf. [Section 2.2](#)).

The method to apply for a correct phase delay measurement is the double differencing technique as explained in *Wickert et al.* (2001a); *Hajj et al.* (2002). In principle, the

ground station not only tracks the signal of the occulting GPS satellite but in addition that of a reference GPS satellite. With the clock of the ground station calibrated against an atomic clock, clock errors of the GPS satellites can be removed and the occultation measurement thus is S.I. traceable. With this method, mm accuracy of orbit and satellite velocity determination is possible. *Mannucci et al.* (2006) state that to achieve the above mentioned accuracy in temperature of 0.5 K the error in satellite velocities has to be less than 0.05 mm/sec. Drifts in orbit determination due to ground station and satellite clock drifts is minimized intrinsically because the measurement itself does not last longer than about 100 seconds.

A measurement which is S.I. traceable is consequently long term stable because the S.I. unit which it is traced to is long term stable. This feature by itself is of utmost importance for building climate records, however, neither the radiosonde measurements nor satellite based (A)MSU measurements fulfill this requirement (cf. [Section 1.1](#)). As of now, it was not yet possible to test long term stability of RO measurements because the RO data record only about reaches a sufficient length to perform trend studies (*Steiner et al.*, 2007). But it is expected that RO measurements exhibit a drift less than 0.1 K per decade in temperature. *Hajj et al.* (2004) has found that GPS soundings are effectively free of instrumental bias and drift.

But even after the phase delays have been determined with the double differencing method, some challenges still remain to assure the measurement be fully S.I. traceable. *Mannucci et al.* (2006) have performed a thorough error analysis to assess RO measurements as a climate benchmark observation. One big concern poses ionospheric activity which on the one hand can vary abruptly following a sudden solar burst and on the other hand varies very gradually within the solar cycle by a factor of five to ten. Furthermore, *Mannucci et al.* (2006) have investigated the effect of the loss of the L2 frequency at lower altitudes on temperature trends and point out of possibly introducing spurious trends greater than the desired stability requirement of 0.04 K per decade. Ideally, even though ionospheric corrections are being applied within the retrieval algorithm (cf. [Section 2.2](#)), information of ionospheric variability has to be obtained as well, at least to sufficiently compensate for noise and to know when not to use an occultation anymore (*Leroy et al.*, 2006b).

In order to create a benchmark measurement, not only the prime measurement but also any relating data have to be stored for a full reproduction later on. In case of RO measurements these include firstly the phase delay measurements, secondly positions and velocities of the LEO and GPS satellites, and thirdly information about the LEO and ground station receivers. All these information are already available and stored at processing centers as the GFZ (*Wickert et al.*, 2001a) or the COSMIC Data Analysis and Archive Center (CDAAC), Boulder, Colorado, USA. However, the state of the ionosphere, especially turbulent activity, is not collected and stored additionally which may turn out to be a major set back in the future for RO measurements to become a fully recognized climate benchmark record.



# 3 Climate Processing System and Set-Up

The RO retrieval system applied to CHAMP phase delay and orbital data is developed at WEGCENTER/UNI GRAZ (*Gobiet and Kirchengast, 2004; Steiner et al., 2004*) in close connection with developments of the End-to-end Generic Occultation Performance Simulator (EGOPS) (*Kirchengast et al., 2004*). After an initial separate development of the retrieval scheme outside of the EGOPS software system (*Gobiet and Kirchengast, 2004; Gobiet, 2005*), recent work has focused on merging the code optimized for the retrieval of CHAMP data back to the new EGOPS OPS (Occultation Performance System). Further work concerning GPS occultation retrieval within the EGOPS OPS includes the retrieval of satellites other than CHAMP, like GPS/MET, SAC-C, COSMIC, and the option for many more in the near future. However, the latter work was not the focus in the present thesis.

In *Borsche et al. (2006a), Borsche et al. (2006b), Foelsche et al. (2007a), and Gobiet et al. (2007)* a summary of the retrieval scheme used for this study is given. In the following sections the processing system will be introduced which handles the data stream and processing of the data at WEGCENTER/UNI GRAZ. In addition, new developments compared to *Gobiet and Kirchengast (2004)* and *Gobiet (2005)* will be outlined.

## 3.1 Status of the Pre-Operational Processing System

At WEGCENTER/UNI GRAZ a pre-operational processing system has been established, which includes data transfer from GFZ and ECMWF, retrieval of atmospheric parameters, quality control, creation of climatologies, and storage of the data. Data has been made available to the public via a web interface at the beginning of December 2007 and can be found at the homepage of WEGCENTER/UNI GRAZ (<http://www.wegcenter.at/>).

The retrieval chain starts with CHAMP data provision by GFZ Potsdam. After its start in June 2001 and an initial phase of a varying amount of RO measurements, the CHAMP satellite has been recording continuously around 230 RO profiles per day (*Wickert et al., 2001b; Wickert et al., 2004*) since March 2002. After the GFZ-internal calibration process (*Schmidt et al., 2005*) on the original data,  $\sim 180$  atmospheric excess phase profiles remain per day and are transferred to WEGCENTER/UNI GRAZ. Here at the WEGCENTER/UNI GRAZ the data are again checked and a rigorous quality control is performed throughout the retrieval system. At the end for all the CHAMP data on average 80% of the profiles are labeled with the best quality flag 0 when during the

retrieval process no or only minor discrepancies occur. For a detailed description of the quality flags used refer to *Gobiet (2005)*. In the study presented here, only profiles with quality flag 0 are used for creating seasonal climatologies which amount to about 140 daily temperature profiles.

At this stage, the processing system operates in an automated way up to the RO retrieval and quality control, whilst the automated creation of the climatologies will be integrated in the very near future. The aim is to establish a data stream from GFZ which downloads 7-day packages of data within a time delay of two days and to provide the final WEGCENTER/UNI GRAZ climatology products within a timeliness limit of 14 days.

Up to the present, CHAMP data provision by GFZ had not been as regular as would have been necessary for this automated operation to work reliably. Instead, all data available were transferred manually via a secure ftp connection from GFZ to WEGCENTER/UNI GRAZ. So far, the data transferred cover a time span from September 2001 to October 2007, which amounts to a total of 22 seasons or 66 months. The first six months of this data set span a period of sparse global sampling amounting to only about 50 to 150 events per day (cf. [Figure 3.1](#)). Nevertheless, sampling of this time period is sufficient for creating zonal mean seasonal climatologies and creating its corresponding error fields, however, when interpreting results of the first half year one has to act with caution (see [Section 4.2.1](#)). This study will use data from September 2001 to August 2006 which sums up to five years of continuously measured RO data.

As reference data, 6-hourly analysis fields of the European Centre for Medium-Range Weather Forecasts (ECMWF) are used. These analyses are produced by the Integrated Forecasting System (IFS) by combining a short-range forecast with observational data by means of four-dimensional variational assimilation (*ECMWF, 2004*). These forecasts consist of four time layers per day at 6 UTC, 12 UTC, 18 UTC, 24 UTC, which are downloaded directly from ECMWF. The operational analyses have undergone continuous enhancement with one major update in February 2006 in which the resolution of the analyses were increased by about 50%. Until February 2006, the analyses consist of 60 vertical model levels (reaching 0.1 hPa) and a spectral representation with triangular truncation at wave number 511 in the horizontal (T511L60). From then onwards, the vertical model levels were increased to 91 (reaching 0.01 hPa) with a truncation number to 799 (*ECMWF, 2005; Untch et al., 2006*) which significantly influenced the comparison results (cf. [Section 5.1](#)). For a more detailed description of the ECMWF analyses used refer to [Section 4.2](#).

ECMWF analysis fields are automatically downloaded directly from ECMWF comprising 6-hourly fields with four time layers including the parameters of orography, temperature, specific humidity, and logarithm of surface pressure. ECMWF data covering the same time span as the CHAMP data were transferred and stored locally at WEGCENTER/UNI GRAZ. The retrieval of the data is an ongoing process and is being performed continuously on newly received data.

The newest update of the ECMWF analyses so far concerning RO data, which has no impact on the results of the study presented here but has already become a main study focus at WEGCENTER/UNI GRAZ, concerns the assimilation process which cre-

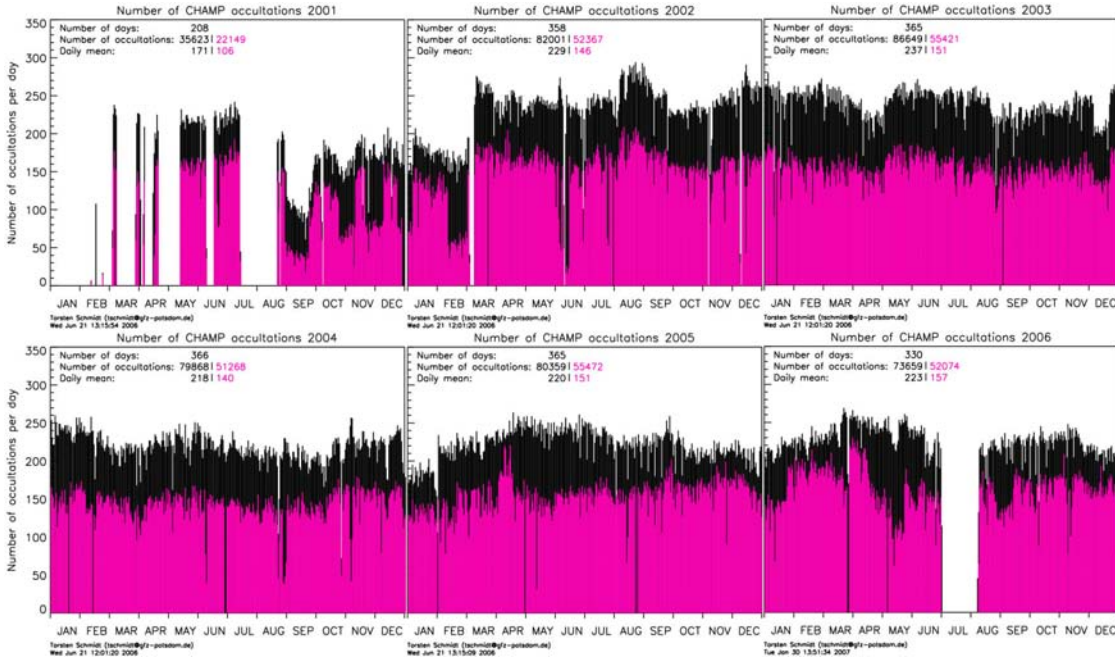


**Figure 3.1:** CHAMP RO daily statistics of measured profiles (black) and profiles which passed the GFZ internal quality control (magenta). Graphics are provided by GFZ and can be found under [http://www.gfz-potsdam.de/pb1/GASP/GASP2/CHAMP/STATISTICS/index\\_ro\\_statistics.html](http://www.gfz-potsdam.de/pb1/GASP/GASP2/CHAMP/STATISTICS/index_ro_statistics.html).

ates the analyses. Since the 12th of December 2006 RO data of the COSMIC satellites are assimilated operationally into the analyses whereas CHAMP and GRACE-A data have been assimilated operationally only for a short period of time until February 2007 (*ECMWF, 2006; Healy, 2007*). The impact of this improvement is that the analyses are no longer independent of the RO measurements and thus cannot be used as background data anymore. Instead it is planned on using 24 hrs and 30 hrs forecast files and combine them in such a way that they mimic the former operational analyses files. Due to the chosen length of the forecast, these files have, on the one hand, already become essentially independent of the analyses and therefore independent of the assimilated RO data, but on the other hand, the 24 hrs forecast files still represent an accurate state of the atmosphere. In that way they provide an excellent first guess of the state of the atmosphere.

### 3.1.1 Enhancement of the Profile Retrieval: Tropopause Parameters

Within the CHAMPCLIM project (*Foelsche et al., 2005, 2006*) the retrieval system was enhanced compared to the last version as described in *Gobiet et al. (2004)*. The enhanced CHAMPCLIM Retrieval version 2.3 (CCRv2.3) (*Borsche et al., 2006a; Go-*

*biet et al.*, 2007) has implemented mainly three new features. First, calculation of tropopause parameters such as lapse rate tropopause height and temperature and cold point tropopause height and temperature, secondly, the calculation of the geoid height of the profiles, and finally, surface parameters of the reference data as well as satellite specific parameters were written out. The tropopause parameters serve new studies (cf. [Section 5.1](#)) whereas the switch to reference the profiles to the geoid as opposed to the reference ellipsoid improves the results systematically (see below). The newly written output surface parameters comprise the surface orography altitude at the position of the event, the surface (2 m) temperature, the skin temperature, and the surface pressure and humidity. Satellite parameters include the azimuth as well as the inclination of the occultation plane. Both the surface and the satellite parameters will also be used in future studies.

The lapse rate tropopause temperature and altitude were calculated according to the definition of the World Meteorological Organization (*WMO*, 1957). The definition and examples of global lapse rate tropopause distribution based on CHAMP RO measurements can be found in [Section 1.3](#). A major study conducted using lapse rate tropopause parameters is described in [Section 5.1](#). It is a sensitivity study in which tropopause temperature and altitude of the CHAMP RO measurements in the tropics were compared to the ones determined from ECMWF reference fields. In addition, cold point tropopause parameters were determined which are defined as the coldest point of the profile in the upper troposphere and lower stratosphere region.

### 3.1.2 Enhancement of the Profile Retrieval: Geoid Altitudes

The second new feature implemented in CCRv2.3 concerns the georeferencing of the profiles. They had been referenced relative to the reference ellipsoid, whereas now they are referenced relative to the geoid (which is equivalent to the mean sea level (MSL)). The vertical grid of the profiles is therefore determined above the geoid which changes the height allocation. In this study, the height above the geoid is called altitude to distinguish between the two.

By introducing altitude to the retrieved profiles, an inconsistency with the reference data was eliminated since those profiles have always been referenced to the geoid. However, compared to the reference ellipsoid the geoid can differ up to about 85 m above (around the island of New Guinea) and up to about 105 m below (northern Indian Ocean) as can be seen in [Figure 3.2](#). The figure depicts the difference between the geoid compared to the reference ellipsoid in meter. As long as the CHAMP profiles were referenced to the reference ellipsoid a systematic bias was introduced. Because in the worst case the profiles could be shifted more than 100 m to each other the bias could in theory amount up to 0.65 K due to the vertical adiabatic temperature gradient in the troposphere of 0.65 K per 100 m (temperature gradients in the lower stratosphere are much smaller).

To demonstrate this theory in practice on one example, in [Figure 3.3](#) and [3.4](#) the differences in temperature between CHAMP profiles referenced to the geoid compared to profiles referenced to the reference ellipsoid are shown. [Figure 3.3](#) depicts the zonal mean of the season JJA 2003 in which the effects on temperature of elevated and depressed

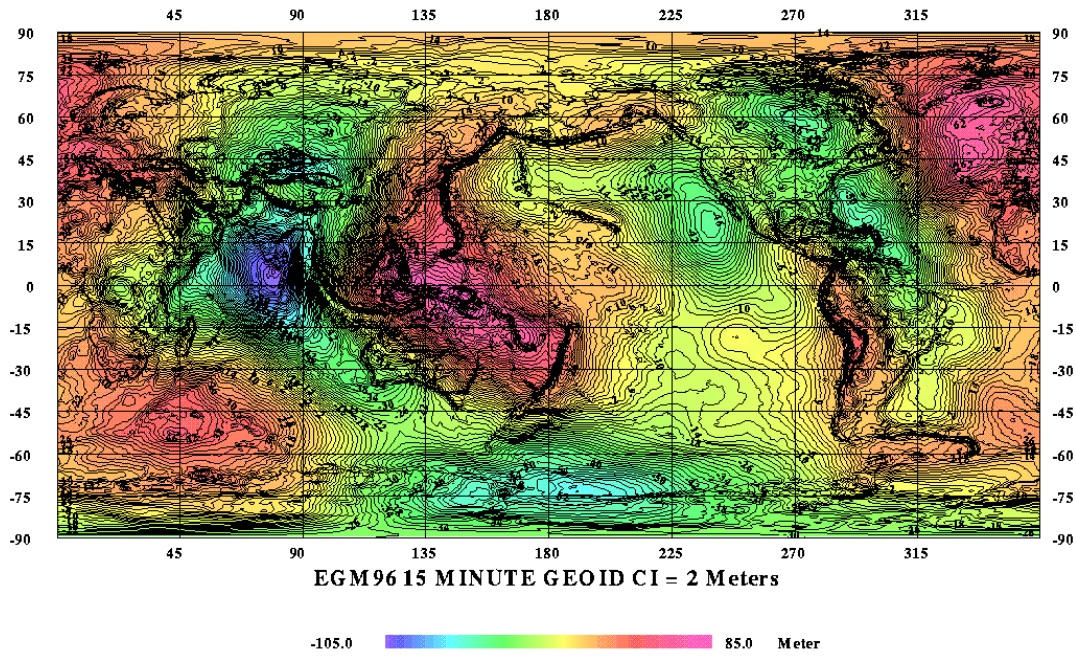


**Figure 3.2:** Latitude – Longitude map of the spherical harmonic Earth Gravitational potential Model (EGM96) by the U. S. National Space and Aeronautics Administration (NASA) and the National Imagery and Mapping Agency (NIMA) with a horizontal resolution of  $15 \times 15$  arc-Min. The geoid altitude is given in meters and ranges from  $\sim -105$  m to  $\sim +85$  m. The model is available at <http://earth-info.nga.mil/GandG/wgs84/gravitymod/index.html>

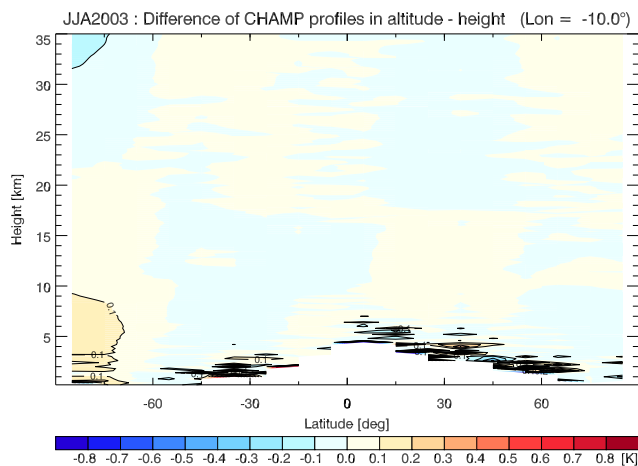


**Figure 3.3:** Zonal difference of CHAMP temperature profiles referenced to the geoid compared to temperature profiles referenced to the ellipsoid in the height range from the ground to 35 km. In the zonal mean there is virtually no difference to be observed except for the lower troposphere. The blank space in the low-latitude lower troposphere is due to the lack of CHAMP data in that region.

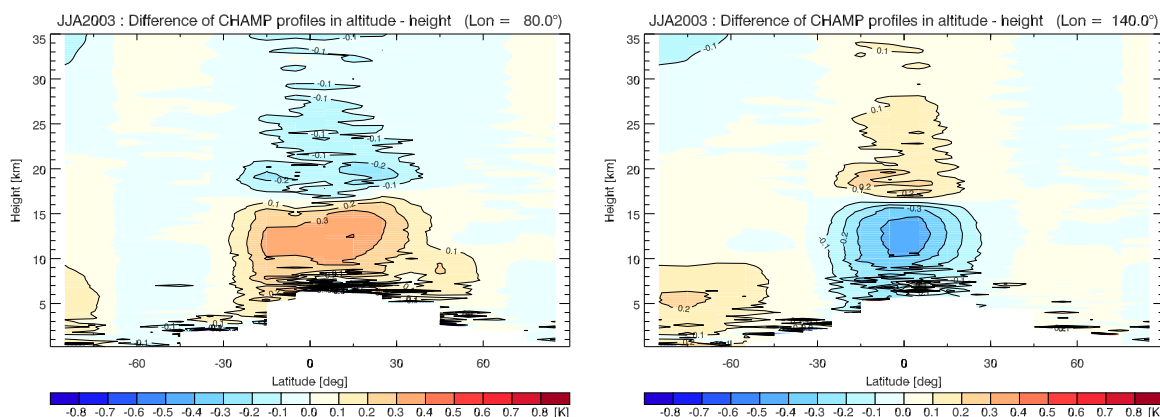


**Figure 3.4:** Difference of CHAMP temperature profiles referenced to the geoid compared to profiles referenced to the ellipsoid in the height range from the ground to 35 km for two latitude slices: On the left the latitude slice is centered around  $80^\circ$  E, on the right around  $140^\circ$  E, corresponding to the locations of the greatest depression and highest elevation of the geoid, respectively.

landmasses of the geoid cancel each other out. However, instead of using the zonal mean, profiles on a smaller scale using latitude slices of an extent of  $60^\circ$  latitude may be used. On the left of [Figure 3.4](#) a latitude slice centered around  $80^\circ$  E longitude is depicted (including the northern Indian Ocean with deepest depression of less than 100 m) and on the right a slice centered around  $140^\circ$  E longitude (including New Guinea with highest elevation of more than 80 m). In the first case (depression) the difference is positive in the troposphere because the profiles start lower, and vice versa in the second case (elevation). Obviously, the effect switches in the lower stratosphere because of the reversed temperature gradient in that altitude region. But as mentioned above the vertical temperature gradient is much weaker and therefore the difference is much smaller.

## 3.2 Set-Up of Climatologies

Within the CHAMPCLIM project, the implementation of the climatologies as final product was pursued in two different ways. On the one hand, a global 3D-Var analysis by assimilation of CHAMP data into ECMWF short-term forecast fields was developed, which is described by *Löscher and Kirchengast (2008)* and *Löscher et al. (2008)*. On the other hand, CHAMP profiles were sorted into defined geographic domains (“bins”) by means of a direct-binning grid strategy. This strategy was implemented in two modes leading to the final climatologies as well as their corresponding errors obtained via difference profiles (“binning and averaging”). How the climatologies are obtained from single profiles, collecting them into so-called bins, and then averaging them will be the focus of this section.

### 3.2.1 Vertical Resolution of the Climatologies

For the creation of gridded pure RO based climatologies several factors and requirements concerning the spatial and temporal resolution of the measured profiles have to be taken into account. The spatial and temporal resolution of a single measurement and the measurement density distribution are the limiting factors for the resolution of any gridded data set derived from measurements. For RO measurements, the vertical resolution amounts to around 1 km to 1.5 km (*Kursinski et al., 1997*) whereas the horizontal resolution in the direction of the ray amounts to about 250 km to 300 km. Since the CHAMP satellite over-samples (higher measurement density than physical resolution) in the order of a factor of ten because of its measurements frequency of 50 Hz, it is possible to provide gridded CHAMP data on a denser vertical grid than it would correspond to the measurement's physical resolution. However, in such a case it must be clearly stated that neighboring values of the grid are not independent of each other.

The physical resolution of the WEGCENTER/ECMWF retrieval scheme has been determined as an example on a test set of 12 CHAMP profiles, for each season one profile from high-, mid-, and low-latitudes, respectively. To determine the vertical resolution of the retrieval scheme the method of the perturbation theory was used. The perturbation theory states that an initial infinitesimal narrow ( $\delta$ ) perturbation of the input to a continuous system will result in a gaussian-like shaped response. The full width at half maximum of the gaussian distribution can then be considered as the inherent resolution of the system. In that manner, each profile was perturbed at phase delay level to determine the resolution of the WEGCENTER/ECMWF retrieval.

**Figure 3.5** depicts a preliminary result of such a perturbation of one CHAMP profile at different altitudes. This particular profile was recorded on March 1st, 2005 at 06:01 UTC and 30.1°S and 164.4°E. The perturbation of the profile was performed in an altitude of 20 km, 14 km, and 9 km. Shown are four plates for each perturbation displaying the initially disturbed phase delay (upper left), bending angle (upper right), refractivity (lower left) and temperature (lower right). The phase delay had to be disturbed at such a ray number which corresponds to the desired altitude of 20 km, 14 km, or 9 km in the retrieved parameter of refractivity and temperature, respectively. The phase delay profile was perturbed to amount to  $\sim 110\%$  of the input value (i. e., perturbation size of  $\sim 10\%$ ) which was found to resemble a reasonable amount because lower values tend to be consumed and smoothed by the retrieval process whereas higher values at worst just crash the retrieval process.

The perturbation propagates through the retrieval system and the response function changes according to the operator used: bending angle retrieval, refractivity retrieval, and finally the temperature retrieval. Because of the Doppler shift differentiation in the bending angle retrieval, the response to the initial perturbation is slant symmetrical – as opposed to a gaussian shaped response of linear operators. After the refractivity and temperature retrievals this shape has changed to an asymmetrical slant response of third order which is far from easy to interpret regarding the intrinsic retrieval resolution. Adding to the difficulty in interpretation are the vastly different outcomes at different altitudes which at least result in the same pattern of being slant asymmetrical of third order.

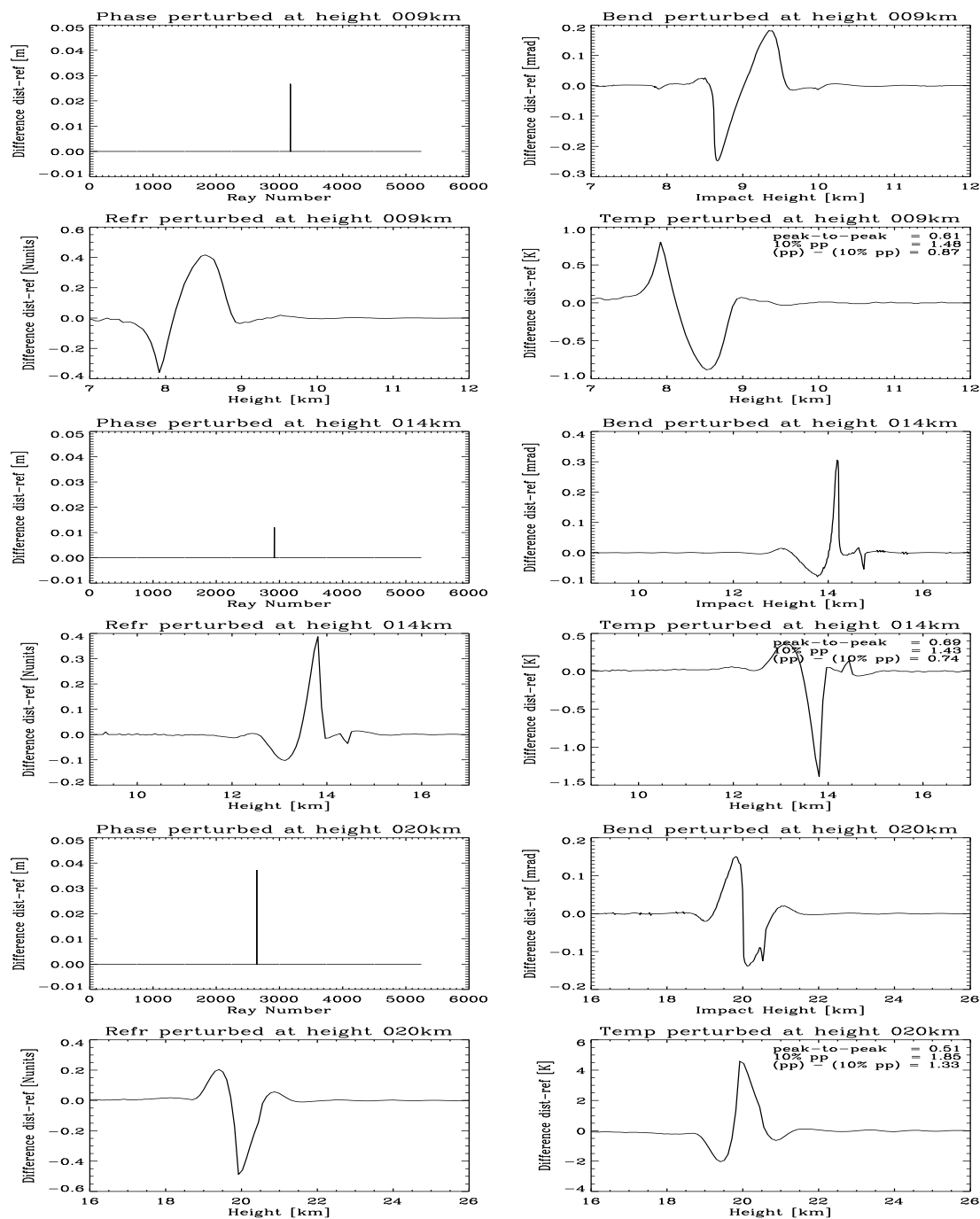


**Figure 3.5:** Perturbation of a CHAMP profile at 9 km, 14 km, and 20 km altitude from top to bottom, respectively, by means of a delta perturbation with an amplitude of  $\sim 10\%$ . After propagating through the retrieval algorithm, the resolution can be estimated by the response amplitude at 10% of peak-to-peak, at peak-to-peak, and as the difference of both. The latter is thought to resemble best the actual physical vertical resolution amounting to 0.9 km, 0.7 km, and 1.3 km, respectively.

With the given response geometry the inherent resolution of the system cannot be inferred from the full width at half maximum of the perturbation distribution function. But other means of interpretation have to be thought of as the peak-to-peak value, “10% peak-to-peak” value, and the difference of both of these. The first of these represents arguably the highest resolution, whereas the second value, which is met where the value of each peak has decreased again to 10% of its maximum, might already be underestimating the resolution. The difference of these values seems to be a feasible value resulting in 1.33 km, 0.74 km, and 0.87 km for that particular profiles at 20 km, 14 km, and 9 km altitude, respectively. All three values are listed in the fourth plate of each altitude panel in [Figure 3.5](#).

As the example above showed, it is rather difficult to determine the vertical resolution of a temperature profile retrieved from RO measurements. Applying the method introduced in this section, however, yields a very thorough approach to identify the inherent resolution of a complex retrieval algorithm. Here, the vertical resolution was determined for three altitudes demonstrating the fact that it is a function of altitude and increases with increasing altitude. A good value for the resolution is thus certainly about 1 km below an altitude of 20 km and  $\leq 1.5$  km from 20 km upwards into the lower stratosphere.

The CHAMP satellite samples with a constant rate of 50 Hz which results in a high oversampling near the ground with one measurement of roughly every 10 m to 20 m and still oversampling at an altitude of 40 km with one measurement roughly every 200 m. Having these two figures in mind, the physical and the sampling vertical resolution, the vertical grid of the climatologies as developed in this study was chosen to be fixed at 200 m. Of course, with these dense vertical grid points two adjacent data values are not independent from each other. For the user of the climatologies this is advantageous, however, because it avoids artificial smoothing by interpolation processes, as was already mentioned by *Gobiet (2005)*.

### 3.2.2 Binning Strategy for the Climatologies

The vertical resolution of a single profile was the first consideration to be taken into account when geographically gridding globally distributed measurements. The second consideration deals with the measurement density and distribution of the data when putting all measurements together. Each of the geographic domains (“bins”) has to contain a sufficient number of profiles to ensure the representativeness of the measurements for the mean location and time of the bin. In the horizontal, the spatial measurement density depends on the temporal averaging period and on geometrical properties of the measurement system. The CHAMP satellite yields some 150 globally distributed atmospheric profiles per day with higher density (referred to equal areas) at high-latitudes compared to lower latitudes.

Additionally, it is of interest to evenly sample the diurnal cycle. Because the CHAMP satellite drifts in local time the diurnal cycle is ideally scanned within  $\sim 130$  days which implies that even seasonal means (90 to 92 day period) do not completely sample it. However, error studies focusing on the diurnal effect show that seasonal and even monthly sampling periods are not very much degraded by this sampling error (*Pirscher et al., 2007a*).

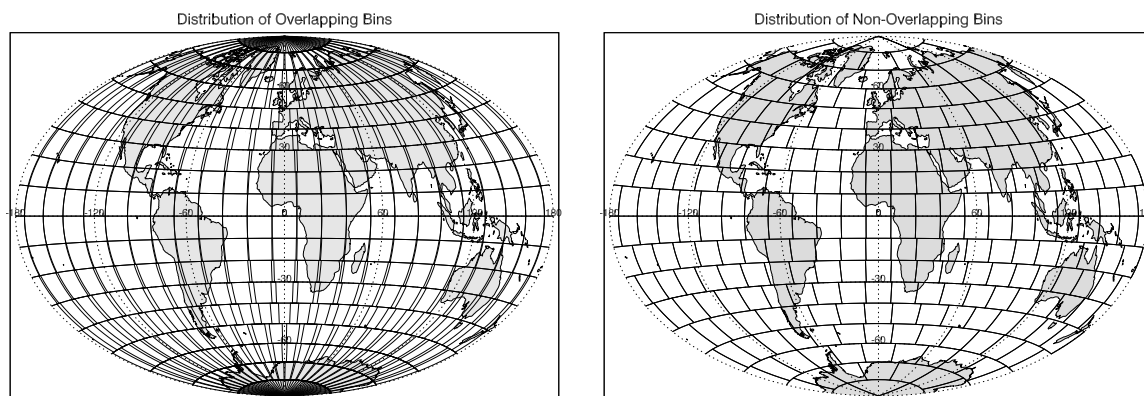


**Figure 3.6:** Two modes of binning. Overlapping equal-area bins at a regular  $18 \text{ lat} \times 24 \text{ lon}$  grid on the left, and non-overlapping almost equal-area bins at  $18 \text{ lat} \times \text{lat-dependent lon}$  grid on the right.

Concluding from the arguments above, a principle set-up in two modes seemed reasonable for binning the CHAMP profiles as shown in [Figure 3.6](#). The two modes of gridding the bins differ on how the equal area bins are arranged. Along latitude, both modes have the meridian divided into 18 bins of  $10^\circ$  width which allows for distinguishing the latitudinal temperature variations while considering the sparse CHAMP sampling. Along longitude, the first mode (left panel of [Figure 3.6](#)) uses 24 fixed bins (baseline) at all latitudes leading to bin overlapping. The latitude – longitude extent of the fixed bins thus results in  $10^\circ \times 15^\circ$ . The second mode (right panel) uses a latitude-dependent number of bins to obtain non-overlapping almost equal area bins (within  $\pm 0.5^\circ$  exact; except for polar latitudes where the latitude extension differs up to  $7.9^\circ$  per bin). In addition to using  $10^\circ \times 15^\circ$  gridding, the first mode of fixed bins was also divided into six and only one bin, which result in  $10^\circ \times 60^\circ$  and zonal gridding, respectively.

Each one of the different modes of gridding has its own advantages when applied to climatologies. Based on the regular grid (lat $\times$ lon), climatologies are most convenient for the user to handle, because regular grids are easy to handle in a common  $n \times m$  matrix when analyzing the data and in addition almost all products dealing with global climatologies and meteorological data sets are organized this way. On the other hand, comparison to the second mode allows study of the potential relevance of error correlations between overlapping bins, especially systematic and sampling errors (cf. [Section 4.2.1](#) and [Section 4.2.2](#)).

Due to the high inclination of the CHAMP satellite ( $87.3^\circ$ ) the global distribution of measured profiles varies from sparse sampling in the equatorial region to high sampling in polar regions. Therefore, the gridding scheme has to be chosen carefully in order for all bins to have a sufficient number of profiles. For bins which contain less than three profiles it is not feasible to perform statistical evaluation like determining a mean, standard deviation, etc. To assure a climatological meaningful representation of the value represented by such a bin, the minimum number of profiles to be contained in a

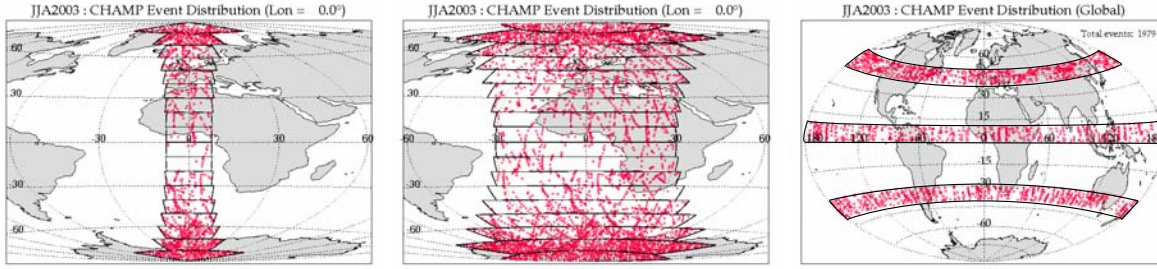


**Figure 3.7:** CHAMP profile distribution for the gridding schemes of  $10^\circ \times 15^\circ$ ,  $10^\circ \times 60^\circ$  and zonal ( $10^\circ \times 360^\circ$ ) taken as an example from season JJA 2003.  $10^\circ \times 15^\circ$  and  $10^\circ \times 60^\circ$  gridding are shown as latitude slices centered around the prime meridian. Discernible here is the distribution minimum around the equator while increasing towards the poles.

bin was chosen to be at least ten.

In [Figure 3.7](#) the overlapping binning mode is shown for all three gridding schemes mentioned above, exemplified for season JJA 2003. In the left panel the finest gridding of  $10^\circ \times 15^\circ$  is shown. The distribution of the profiles is uneven due to a decrease towards the equator. Furthermore, the few profiles that are located in the equatorial bins are in this particular case very much clustered as opposed to evenly distributed as in the polar bins. The calculation of a mean temperature in such an equatorial bin, though statistically robust, would result in a biased representation of the parameter under consideration, for instance temperature.

For season JJA 2003 in the equatorial bins, though unevenly distributed, there were a sufficient number of profiles for a statistical robust determination of a mean, standard deviation, etc. However, throughout the five years of CHAMP data, a few seasons exist without any measured profiles in the equatorial bins leading to climatologies with missing parts. Even though the concept of a  $10^\circ \times 15^\circ$  gridding is in principle correct, it should not be applied to a one-satellite mission retrieving only setting RO measurements like CHAMP in order to get the best possible and error-free climatologies. In a combination of satellites of, for instance, CHAMP and SAC-C, or for the multi-satellite mission FORMOSAT-3/COSMIC this concept might be flawlessly applicable.

When gridding seasonal RO measurements into  $10^\circ \times 60^\circ$  bins, as shown in the middle panel of [Figure 3.7](#), even for the CHAMP mission there always are enough profiles to ensure robust statistical calculation of climatologies. As will be explained in detail in [Section 4.2.2](#), however, even that gridding exhibits artifacts within climatologies which are not favorable and should therefore be avoided.

These findings lead to the conclusion that for a one-satellite mission as CHAMP (with only setting RO measurements available) the only climatological useful set-up (of the options presented) is a zonal gridding with a width of  $10^\circ$  latitude. In this mode, all profiles around the globe are collected into one bin as shown on the right side of [Figure 3.7](#). With this approach the longitudinal temperature differences within one specific  $10^\circ$  latitude band are lost because of the averaging. But considering the unique opportunity of continuous RO measurements over more than five years of one satellite

(CHAMP) for the first time, building zonally averaged high quality climatologies marks a great step forward in climatological studies.

# 4 Atmospheric Climatologies from CHAMP

RO profiles from the CHAMP satellite were analyzed in a climatological respect for the time period from September 2001 to November 2006 resulting in more than five years of continuous RO data. Of these 21 seasons, the first two were affected by a low and highly varying measurement density. Within the season before last (JJA 2006), from July 3th through August 8th a period of 37 days of CHAMP data are missing. Fortunately, that gap could be bridged by RO data from the Gravity Recovery And Climate Experiment (GRACE) satellite (*Wickert et al., 2005*).

The receiver of the GRACE satellite is an enhanced one of that one used for the CHAMP mission thus featuring similar characteristics. Recent studies (*Foelsche et al., 2007b; Luntama et al., 2007; Steiner et al., 2007*) have shown that real world measurements from different RO missions reveal excellent agreement when inter-comparing them as well as when comparing them to an independent source as the (A)MSU instruments on board the NOAA platforms. Because of the results presented in these studies, for the climatological study presented here it was thought adequate to fill the gap of missing CHAMP data with GRACE measurements and still treat the whole data set uniquely as if it consisted of CHAMP data only.

In this Chapter CHAMP climatologies from the CCRv2.3 precessing version are presented for the four atmospheric parameters dry temperature, refractivity, dry pressure, and dry geopotential height. The climatologies represent seasonal climatologies which are averaged mainly zonally shown as two dimensional latitude versus altitude figures. As explained in [Chapter 3](#), every RO profile of a season which passed the quality control only with the best quality flag, QF= 0, which in total sums up to about 80% of all profiles measured, is binned into zonal bins with a width of 10° latitude. For each of the resulting 18 zonally averaged bins, the mean profile of either one of the four atmospheric parameters under consideration is obtained, as exemplified for dry temperature, by

$$\overline{T_{\text{dry}}(z)} = \left( \sum_{i=1}^{N_{\text{prof}}(z)} \cos(\varphi_i) \right)^{-1} \cdot \sum_{i=1}^{N_{\text{prof}}(z)} \left( T_{\text{dry}_i}(z, \varphi_i) \cos(\varphi_i) \right), \quad (4.1)$$

where  $N_{\text{prof}}(z)$  determines the number of profiles in each bin dependent on altitude. The number of profiles decreases with decreasing height because the signal tracking of a setting occultation loses the signal for each profile at different altitudes depending mainly on atmospheric conditions. Additionally, the profiles of each bin are weighted by the cosine of the latitude,  $\varphi$ , to account for the area average within the 10° latitude bin. At this gridding resolution the cosine weighting becomes relevant only in polar regions,

but will be important throughout when averaging over larger latitude extent. The 18 mean profiles of each zonal latitude bin are resolved onto a 200 m vertical grid.

*Gobiet* (2005) has shown first results of climatologies with a horizontal resolution for zonal and  $10^\circ \times 15^\circ$  gridding. In this study, mainly the zonal approach has been pursued because of the sparsity of measurements even for climatological studies (as pictured in [Section 4.2.2](#)). However, when averaging over a larger latitudinal extent, for instance  $40^\circ$  around the Equator in  $15^\circ$  longitudinal steps, a further and very instructive insight into the CHAMP data set can be achieved. For that reason in addition to the latitude versus altitude plots, longitude versus altitude plots will be shown. These feature a  $40^\circ \times 15^\circ$  binning around the Equator ( $\pm 20^\circ$ ) picturing the longitudinal variation of the four atmospheric parameters under consideration.

In the following sections only selected seasons are shown (Northern Hemisphere (NH) summer of each year), in which many features observed in the complete time period occur. In the Appendix the temporal evolution of the entire CHAMP data set will be shown in form of seasonal climatologies of dry temperature and all of the corresponding error fields discussed below. The remaining atmospheric parameters have not yet been approved to be of such satisfying quality as to present them in form of a collection as in the Appendix. Ongoing research at WEGCENTER/UNI GRAZ is still needed to eliminate persistent inconsistencies in parameters other than dry temperature.

## 4.1 Multi-Year Climatologies

To begin with, in [Figure 4.1](#) the global distribution of CHAMP profiles which passed the quality control with  $QF=0$  are displayed. [Figure 4.1](#) shows from top to bottom the NH summer seasons JJA 2002 to JJA 2006 with the distribution of the profiles shown on a global map on the left and the number of profiles within  $10^\circ$  latitudinal steps of that distribution on the right. The total number of profiles of each season is listed in the upper right corner of the global map which states that there are considerably more than 12,000 profiles per summer season except for JJA 2004. The same can be seen in the panels on the right side which state the global average of profiles per bin amount to about 700, except for JJA 2004 with only around 600 profiles per bin.

Profiles are mainly uniformly distributed over the globe, but for some seasons there are patterns in which the profiles are clustered leading to non-uniform distribution with no coverage over some places. The strongest such clustering can be observed in JJA 2005 and weaker also in JJA 2002 and JJA 2004. These patterns in distribution result from special constellation geometry of the CHAMP and GPS satellites which drifts and changes with time. This clustering of profiles has an influence on the quality of the climatologies. It does not exhibit an intrinsic error source of the measurement method (as described in [Chapter 2](#)) but rather an external source determining the measurement. As a direct result the sampling error increases as shown in [Section 4.2.2](#) because the sampling situation worsens as a whole. The accumulated error field of the climatologies thus includes external factors, as in this case constellation geometry of the satellites.

The histograms on the right side of [Figure 4.1](#) describe the absolute abundance of

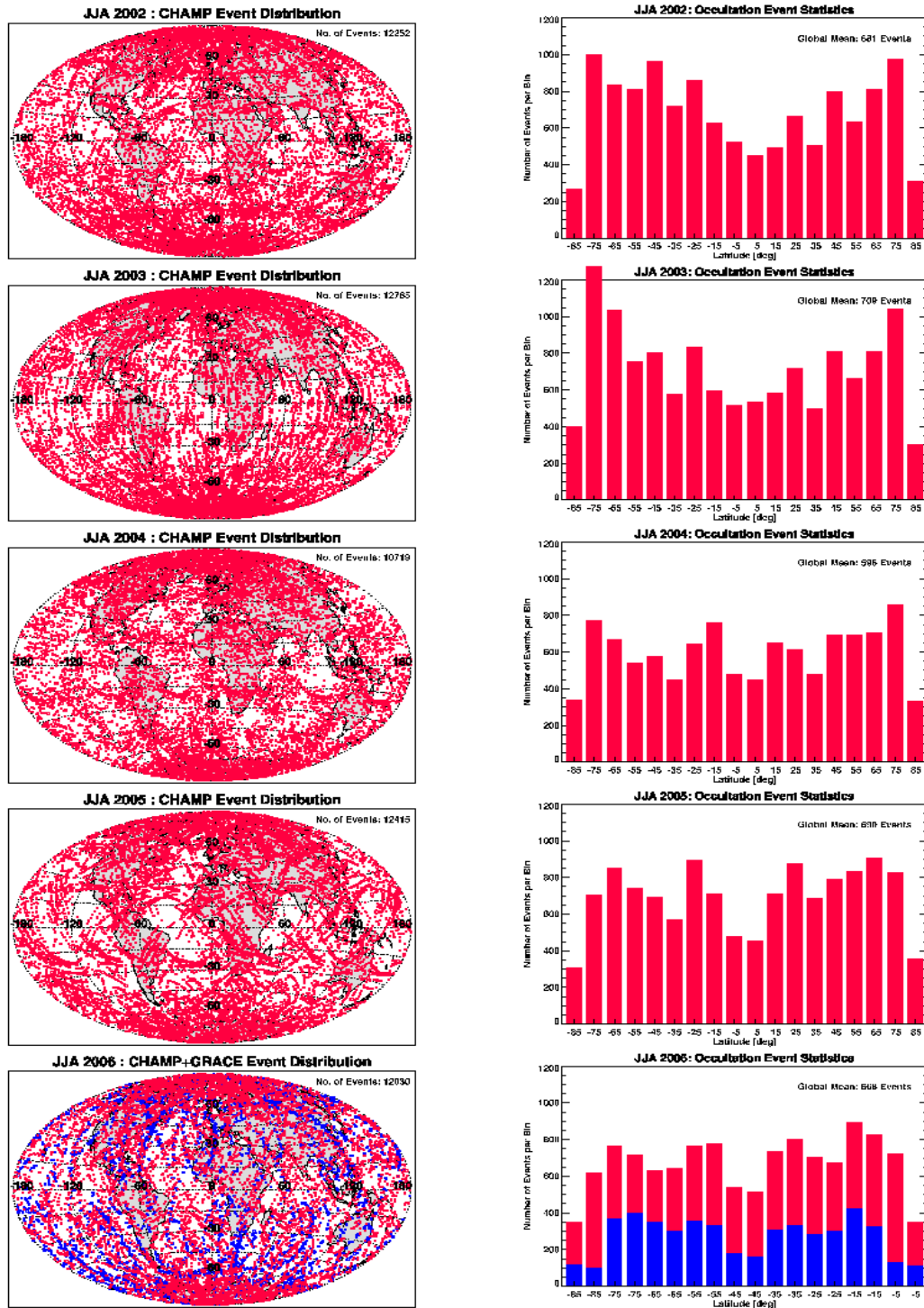


**Figure 4.1:** Global distribution of CHAMP profiles of NH summer seasons JJA 2002 to JJA 2006 over a global map on the left and, in absolute abundance, for each zonal bin on the right side. Season JJA 2006 consists of CHAMP and GRACE profiles due to a lack of 37 days in CHAMP measurements; for that season GRACE profiles are shown in blue.

profiles occurring in each of the 18 zonal bins. The x-axis labels determine the mean latitude of each bin. In every season there is a minimum abundance at the North and South Pole, respectively, which is due to the small absolute area of the polar regions compared to lower latitudes. The high inclination of the CHAMP satellite of  $87.2^\circ$  assures measurements in polar regions in the first place but is still not enough for a direct overflight. In almost all seasons, including most of the NH summer seasons, the maximum abundance of profiles occurs at high-latitudes directly adjacent to the polar bin (at  $70^\circ$  to  $80^\circ$ ) or one further towards the Equator (at  $60^\circ$  to  $70^\circ$ ). The minimum is reached at the Equator with only a half of the profiles measured at the maximum. This measurement distribution is due only to the orbital geometry of the CHAMP satellite which is characteristic of polar satellites in general. The residence time of polar orbiting satellites is shortest over low-latitudes (the Equator) and longest at high-latitudes. In this case the measurement distribution is proportional to the residence time at a given latitude since the occurrence of a RO event is independent of latitude due to the even distribution of the GPS satellites.

### 4.1.1 Climatology of Dry Temperature

Dry temperature can be calculated with the RO retrieval system with no additional a priori data (cf. [Chapter 2](#)). In this section, dry temperature climatologies are shown and discussed as an example for the NH summer seasons JJA 2002 to JJA 2006. Climatologies have been calculated using [Equation 4.1](#).

In [Figure 4.2](#) zonally averaged seasonal climatologies are shown for JJA 2002 on the top to JJA 2006 on the bottom with CHAMP RO measurements on the left and ECMWF operational analyses fields on the right. CHAMP climatologies were created as explained in [Chapter 3](#), whereas ECMWF climatologies consist of the complete analysis fields of all four time layers as introduced in [Section 3.1](#). In the following, which is especially important when considering error fields, the ECMWF analyses are considered the true state of the atmosphere against which the measured CHAMP profiles and CHAMP climatologies are compared to. ECMWF operational analyses provide a very high quality state of the atmosphere by assimilation of an enormous amount of operational measurements from ground, in-situ, and satellite platforms. Additionally, these were the only high resolution analyses available for this study. Thus, the assumption that the ECMWF operational analyses resemble the true state of the atmosphere is the best assumption which could be proposed within this study (for further details cf. [Section 4.2](#)).

The climatologies are displayed in a two dimensional contour plot in which the temperature is shown as a function of latitude and altitude. The latitude ranges from North to South Pole and altitude from 0 km to 35 km. The climatologies are cut off dependent on latitude between 4 km at the poles and 8 km around the Equator (see [Table 4.1](#)). This cut-off criterion results from a “dry sampling error” which is a special feature intrinsic to the RO method (for a detailed discussion see [Section 4.2.2](#)). The altitude range of around 5 km to 35 km marks that range in which the RO technique delivers the most accurate results (see [Chapter 2](#)) and in which the single retrieved profiles are very much independent of the background information (*Gobiet et al.*, 2007).

**Table 4.1:** Cut-off altitude of climatologies.

| Latitude range | Cut-off altitude |
|----------------|------------------|
| 90° to 60°N/S  | 4.0 km           |
| 60° to 50°N/S  | 5.0 km           |
| 50° to 40°N/S  | 6.0 km           |
| 40° to 30°N/S  | 7.5 km           |
| 30°N to 30°S   | 8.0 km           |

The temperature fields of the summer seasons as displayed in [Figure 4.2](#) reveal two prominent cold regions, which are located in the tropical tropopause and at southern high-latitudes of the polar vortex. The tropical tropopause cools down to less than 195K (around  $-80^{\circ}\text{C}$ ) as discussed in [Section 1.3](#). Very cold southern winter polar vortices can reach temperatures as low as 182K (less than  $-90^{\circ}\text{C}$ ) averaged over the complete summer season. On the other side of the globe, in the free atmosphere of the North Pole temperatures are much warmer amounting to about 230K (around  $-40^{\circ}\text{C}$ ) than anywhere in the tropical free atmosphere or in the southern hemisphere.

The main temperature features of the atmosphere remain constant throughout the years but inter-annual variation can still be observed and is confined to small scale features. For instance, temperature in the southern polar vortex seems to be subject to a two year mode of warmer and colder phases with the 185K isotherm emerging in JJA 2003, the coldest recorded year in the southern vortex within this data set, and in JJA 2005. In the boreal summers of JJA 2002, JJA 2004, and JJA 2006 the austral vortex was warmer. Another feature of variability can be seen when looking at the 230K isotherm in the Tropics. In JJA 2002 the 230K isotherm reaches an altitude of almost 35km over the Equator which it reaches again every two years. In the years in between, JJA 2003 and JJA 2005, it resides at a much lower altitude of around 30km. This temperature variation is linked to the Quasi Biennial Oscillation (QBO) (*Foelsche et al., 2007a*) which is characterized by a biennial oscillation in temperature in the tropical lower to mid stratosphere as well as by a downward propagation of easterly and westerly wind regimes (e.g. *Baldwin et al., 2001; Ramaswamy et al., 2001*).

On the right side of [Figure 4.2](#) the reference fields of the ECMWF operational analyses for the five summer seasons are displayed. Mainly the same features as for the CHAMP data can be seen and differences are marginal. However, some differences can already be spotted with the naked eye: at its edges, the southern polar vortex exhibits a wavy structure which can clearly be distinguished in all seasons except for JJA 2006 and which does not exist in the CHAMP data. Also, the minimum temperature of the polar vortex is lower in the analyses in which, for instance, the 180K isotherm emerges in JJA 2003. Additionally, the tropical tropopause seems a bit colder in the analyses as well, seen again clearly for example in season JJA 2003 where the 195K isotherm exists but not in the corresponding CHAMP data. Further systematic differences and a detailed discussion of them will be given in [Section 4.2.1](#) below.

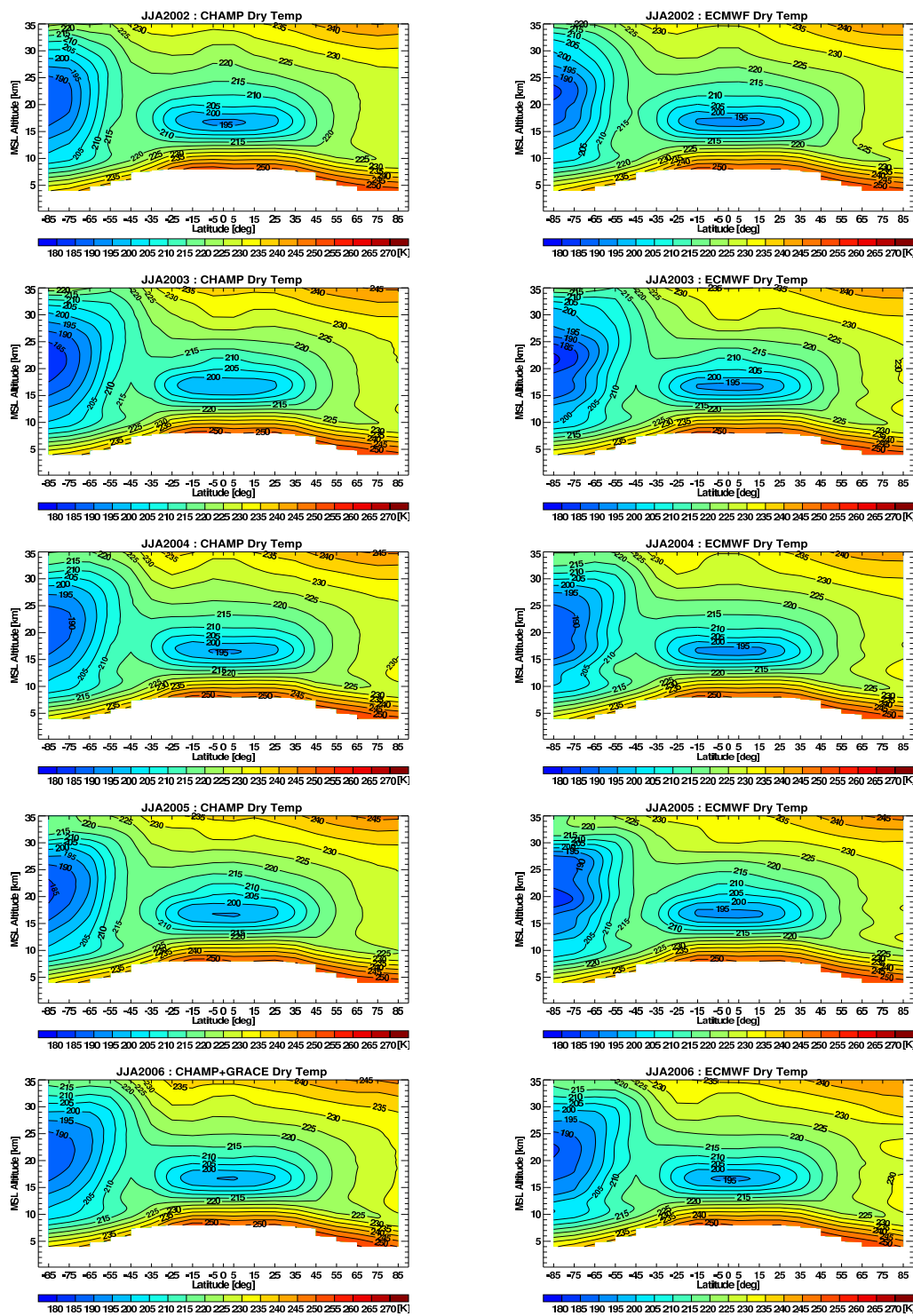


Figure 4.2: Dry temperature climatologies [K] of NH summer seasons JJA 2002 to JJA 2006 for CHAMP measurements on the left and ECMWF analyses on the right side. Climatologies are shown from Pole to Pole, and plotted from the cut-off altitude to 35 km.

In [Figure 4.3](#) dry temperature climatologies are shown in a longitudinal perspective. The four bins closest to the Equator,  $20^\circ$  to  $10^\circ$  and  $10^\circ$  to  $0^\circ$  North and South with an area of  $10^\circ \times 15^\circ$ , were arithmetically averaged resulting in a bin with a resolution of  $40^\circ \times 15^\circ$ . Since the resolution thus has become four times as large as with the original  $10^\circ \times 15^\circ$  bins also the amount of profiles has increased proportionally. The minimum amount of profiles within the five summer season in such an enlarged bin amounts to 150, the average of all bins to around 400 with the maximum as high as almost 700 profiles. Thus, with the enlargement of the bins it is possible to create climatologies in  $15^\circ$  longitudinal steps even around the sparsely sampled Equator. [Figure 4.3](#) shows such climatologies for the five NH summer seasons from  $180^\circ$  E to  $180^\circ$  W in  $15^\circ$  longitudinal steps  $\pm 20^\circ$  latitude around the Equator in a height range from 8 km (cut-off altitude at low-latitudes) to 35 km.

What can be seen in those climatologies at first sight is that the temperature does not change very much as a function of longitude in the equatorial region. The temperature characteristics are already known, including a strong decrease of temperature in the free atmosphere up to a very cold tropical tropopause and a weak increase of temperature in the lower and mid stratosphere up to 35 km. The coldest part of the tropical tropopause is located in the western hemisphere between  $100^\circ$  W and  $160^\circ$  W over an area generally referred to as the Pacific “Warm Pool Atmosphere” (e.g. *Tian et al.*, 2001), where throughout all summer seasons the averaged temperature reaches below 195 K. The warmest part seems to be opposite in the eastern hemisphere between around  $90^\circ$  E and the Prime Meridian, which in this case was easier to derive from the ECMWF analysis fields.

The most important result from the longitudinal illustration of the CHAMP temperature climatology is that hardly any climatological information gets lost when averaging CHAMP profiles in zonal bins. As was explained in [Section 3.2](#) will be illustrated in [Section 4.2](#), a  $10^\circ \times 15^\circ$  gridding, if at all possible, degrades the quality of the climatologies due to an insufficient number of measured CHAMP profiles. By enlarging the bins to  $40^\circ \times 15^\circ$  a fine longitudinal gridding is possible, however hardly revealed more information than a zonal mean in a climatological point of view by averaging over such a long period as a season.

### 4.1.2 Climatology of Refractivity

In the previous section, dry temperature climatologies were shown and discussed for the summer seasons JJA 2002 to JJA 2006. In the course of the study presented, climatologies of additional parameters as refractivity, dry pressure, and dry geopotential height were created, in each case applying [Equation 4.1](#) to obtain the corresponding climatologies. In this section climatologies of refractivity will be discussed.

Microwave refractivity is related proportionally to atmospheric pressure  $p$ , temperature  $T$ , and water vapor partial pressure  $e$ , via (*Smith and Weintraub*, 1953):

$$N \equiv 10^6(n - 1) = k_1 \frac{p}{T} + k_2 \frac{e}{T^2}, \quad (4.2)$$

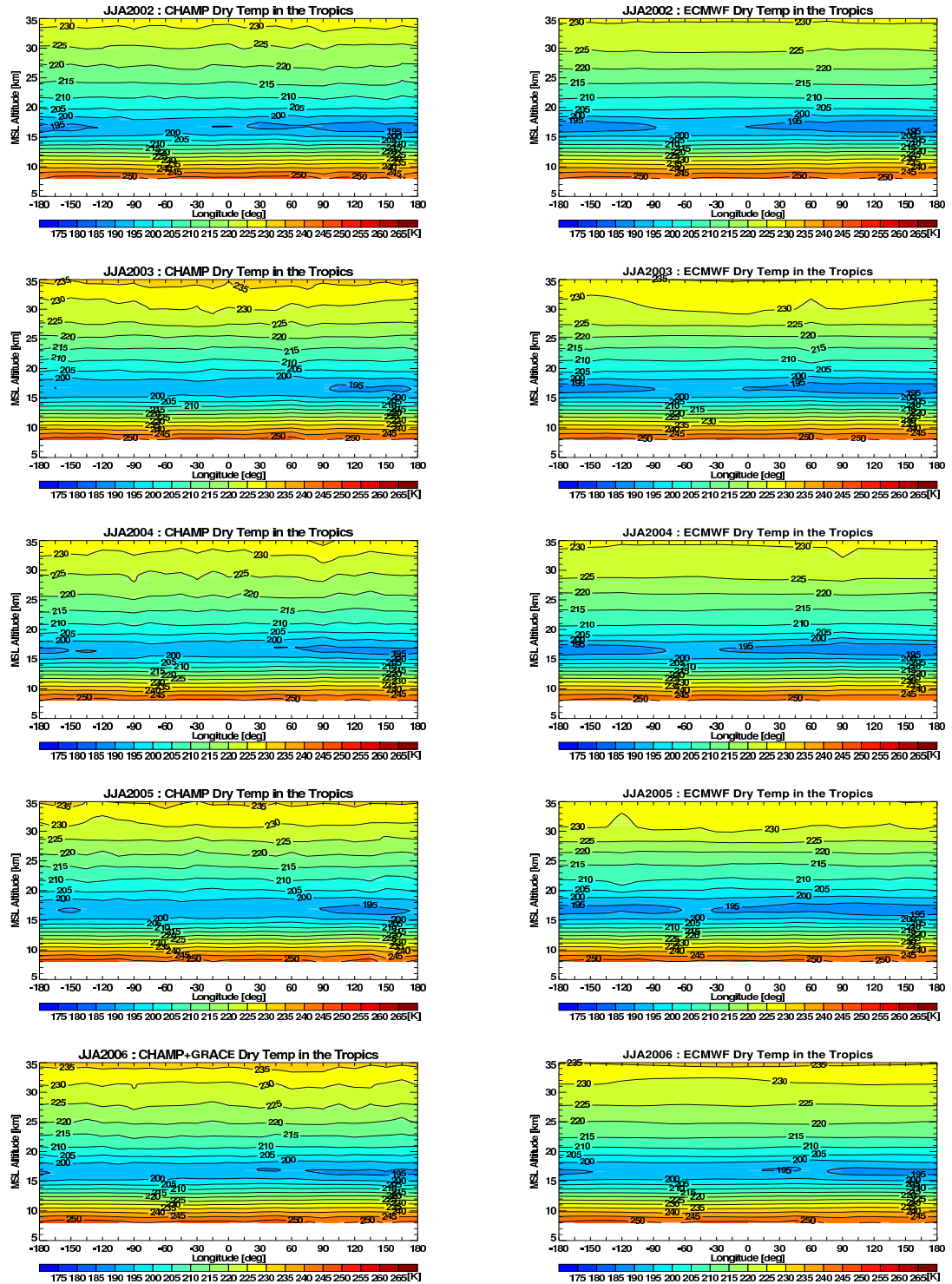


**Figure 4.3:** Longitudinal dry temperature climatologies [K] of NH summer seasons JJA 2002 to JJA 2006 with a gridding of  $40^{\circ} \times 15^{\circ}$  (lat $\times$ lon) centered around the Equator, for CHAMP RO data on the left and ECMWF analyses on the right side.

wherein  $n$  is the index of refraction,  $k_1 = 77.6 \text{ K hPa}^{-1}$  and  $k_2 = 3.73 \cdot 10^5 \text{ K}^2 \text{ hPa}^{-1}$  are empirically determined constants. The first term on the right side of Equation 2.8 describes refractivity in atmospheric conditions without water vapor, i.e. in dry conditions, whereas the second term includes contributions of water vapor (also cf. Section 2.2). If these contributions are neglected and the refractivity field is governed only by dry conditions, refractivity is directly proportional to air density via the ideal gas law. In the free atmosphere dry air conditions are present anywhere above 8 km to 14 km altitude, as introduced for dry temperature above. In the lower troposphere, where moisture is not negligible anymore, refractivity depends further on water vapor partial pressure (second term on the right side of Equation 2.8).

The refractivity field is not a common meteorological parameter but is mainly used in the radio occultation community. However, it has turned out that refractivity provides a valuable complement to other and already established data sets because it reacts differently to climate change than does for instance temperature. Furthermore, it has been identified to be a good climate change indicator (*Vedel and Stendel, 2003; Leroy et al., 2006b*) as well as a means to test the prediction confidence of climate models (*Leroy et al., 2006a*).

Figure 4.4 shows the climatologies for the NH summer seasons JJA 2002 to JJA 2006, for the CHAMP RO measurements on the left side and the reference data of ECMWF operational analyses on the right. Since refractivity, being a measure of the refractive index of the atmosphere, is directly proportional to air density through the ideal gas law, refractivity climatologies reflect the decrease of density with altitude.

As could be seen in the dry temperature climatologies, see Figure 4.2, the atmosphere throughout the whole column is coldest around the South Pole in the boreal summer seasons. Therefore, in that region density/refractivity, at a given altitude, is lower than elsewhere around the globe: The zonal seasonal mean shows a very constant refractivity field for all latitudes except for the southern high-latitudes, which can be seen quite clearly when looking at the 2.0 N-unit isoline. Only at southern high-latitudes it reaches as low as about 31 km while staying constantly higher at about 35 km at all other latitudes. If looked at very closely, the cold tropical tropopause can be spotted. This can be done best with the 30.0 N-unit and 50.0 N-unit isolines which increase in altitude at around 35° North and South corresponding well with the climatological extent of the tropical tropopause (see Figure 4.2).

Figure 4.5 shows the longitudinal climatologies for the summer seasons. As for dry temperature in Figure 4.3, the longitudinal variability of refractivity was investigated in 40°×15° gridding ensuring enough profiles for each bin for a robust climatological representation. What can be seen, however, is a completely flat longitudinal distribution of refractivity which results from the above discussed flat distribution of dry temperature.

### 4.1.3 Climatology of Dry Pressure

In this section, climatologies of dry pressure in five NH summer seasons will be shown and discussed. Dry pressure can be computed by integrating refractivity to get the pressure at altitude  $h$  as was explained in Section 2.2 (cf. Equation 2.10).

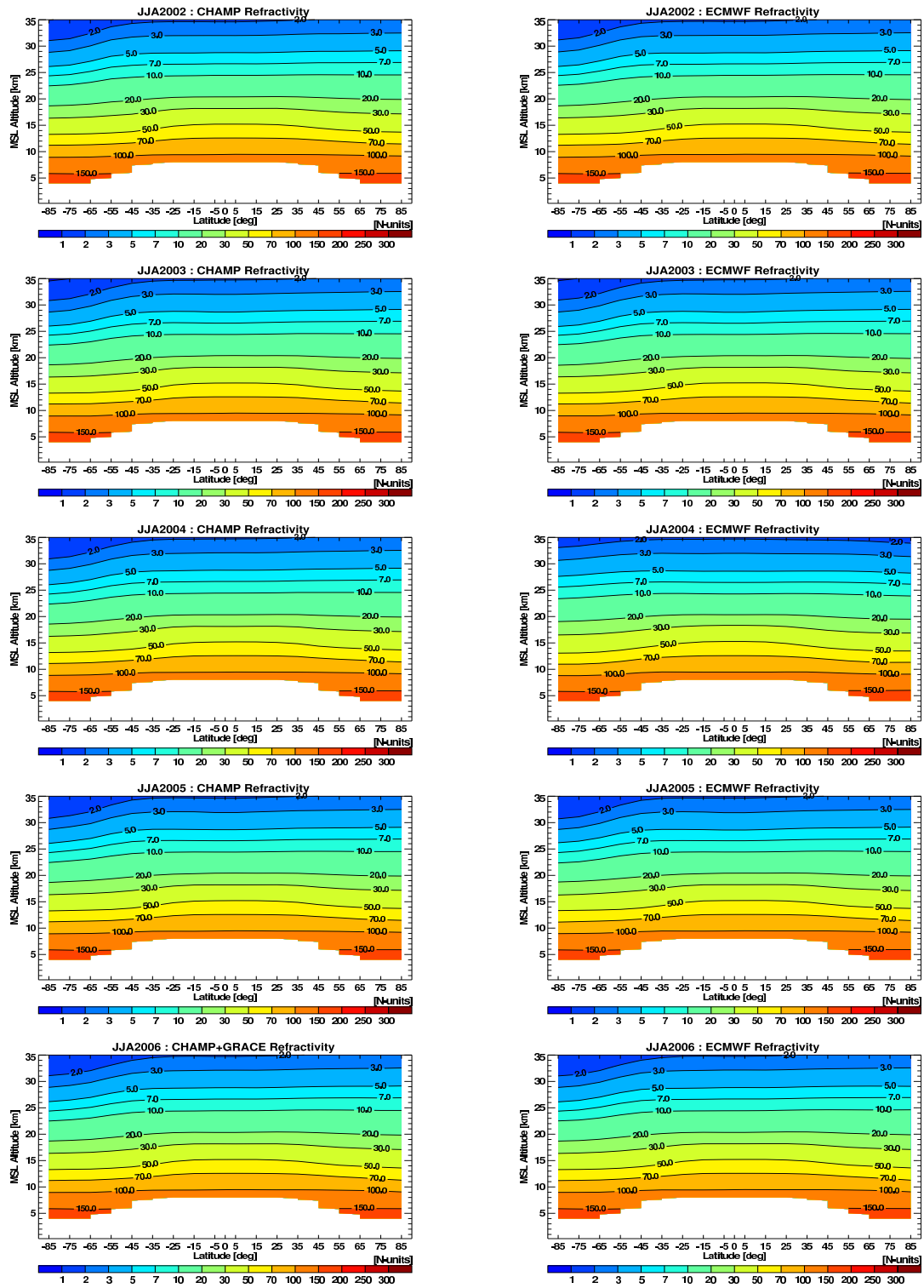


Figure 4.4: Refractivity climatologies [N units] of NH summer seasons JJA 2002 to JJA 2006; same layout as Figure 4.2.

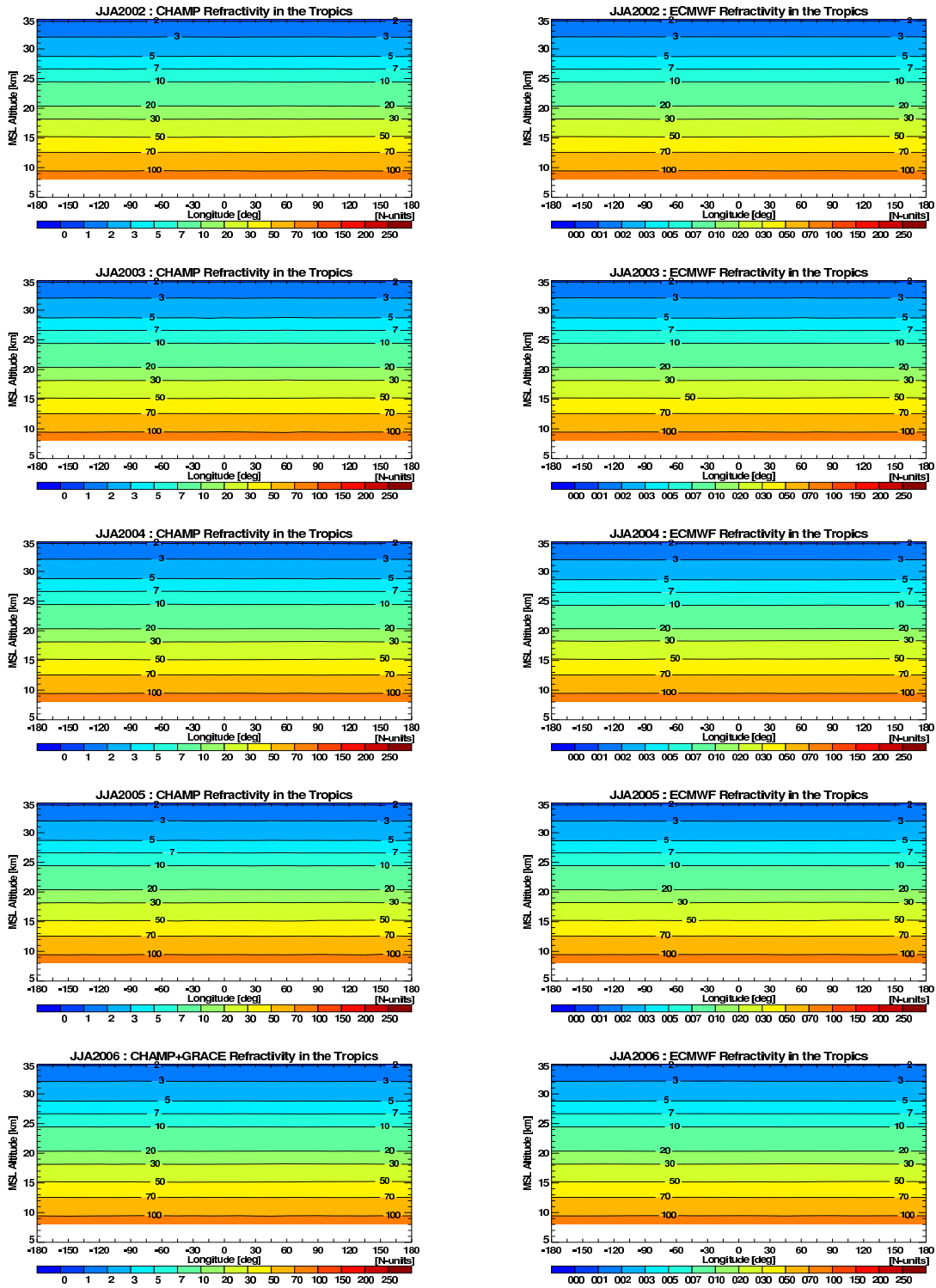


Figure 4.5: Longitudinal refractivity climatologies [N units] of the summer seasons JJA 2002 to JJA 2006; same layout as Figure 4.3.

Since pressure is directly related to refractivity above the mid-troposphere in dry conditions, pressure becomes equally important in climate trend detections as refractivity (Leroy, 1997). When examining pressure in dry conditions, i. e., above the cut-off altitude, here pressure is referred to as dry pressure (which is not to be confused with the partial pressure of dry air at the surface). Since pressure follows directly from refractivity by Equation 2.10, the seasonal summer means of refractivity and dry pressure equal each other very much.

Figure 4.6 depicts the 10° zonal means of the NH summer seasons 2002 to 2006 for the CHAMP data on the left and the reference ECMWF analyses on the right. Labels in this and the next Figure are chosen to coincide with the mandatory pressure levels introduced in Section 1.1 up to 10 hPa. Pressure decreases exponentially as altitude increases and reaches 7 hPa above the North Pole and mere 3 hPa above the South Pole at an altitude of 35 km. The isobars almost remain at a fixed altitude throughout the whole latitude range with minor variations around the cold tropical tropopause and with a major decrease in pressure at a given altitude in the southern polar vortex.

Figure 4.7 shows the longitudinal perspective of the pressure climatologies. However, there is no variation to be seen neither throughout the longitude nor within the temporal evolution of the five years. For instance, the 30 hPa isobar for all years resides at more or less exactly 24 km altitude.

#### 4.1.4 Climatology of Dry Geopotential Height

Finally in this section climatologies of dry geopotential height will be discussed. Geopotential height,  $Z$ , is related to geometrical height by the ratio of the gravitational acceleration at a given height  $g(z)$ , obtained from a model of gravity, and the WMO standard gravitational acceleration at the surface  $g_0 = 9.80665 \text{ m/s}^2$  via

$$dZ = \frac{g(z)}{g_0} dz . \quad (4.3)$$

In the troposphere this ratio is practically equal to 1 which results in a very close match of geopotential height and altitude. In meteorology and climatology, geopotential height is usually used to depict the height of a pressure level. Geopotential height of constant pressure levels can be directly measured when applying the RO method by using the absolute information of the GPS system and the hydrostatic equation (Kursinski *et al.*, 1997; Leroy, 1997). Geopotential height acts as a climate indicator for example by registering when the troposphere warms on a global scale and expands as a result of that warming (e. g., Leroy *et al.*, 2006a).

The dry geopotential height climatologies as displayed in Figure 4.8 and Figure 4.9 are shown as a function of “pressure altitude”  $z_p$  in units of “pressure km” [pkm]:

$$z_p = H \cdot \ln \left( \frac{p}{p_0} \right) , \quad (4.4)$$

where  $H = RTg_0^{-1}$  is the atmospheric scale height set to a constant value of  $H = 7 \text{ km}$ ,

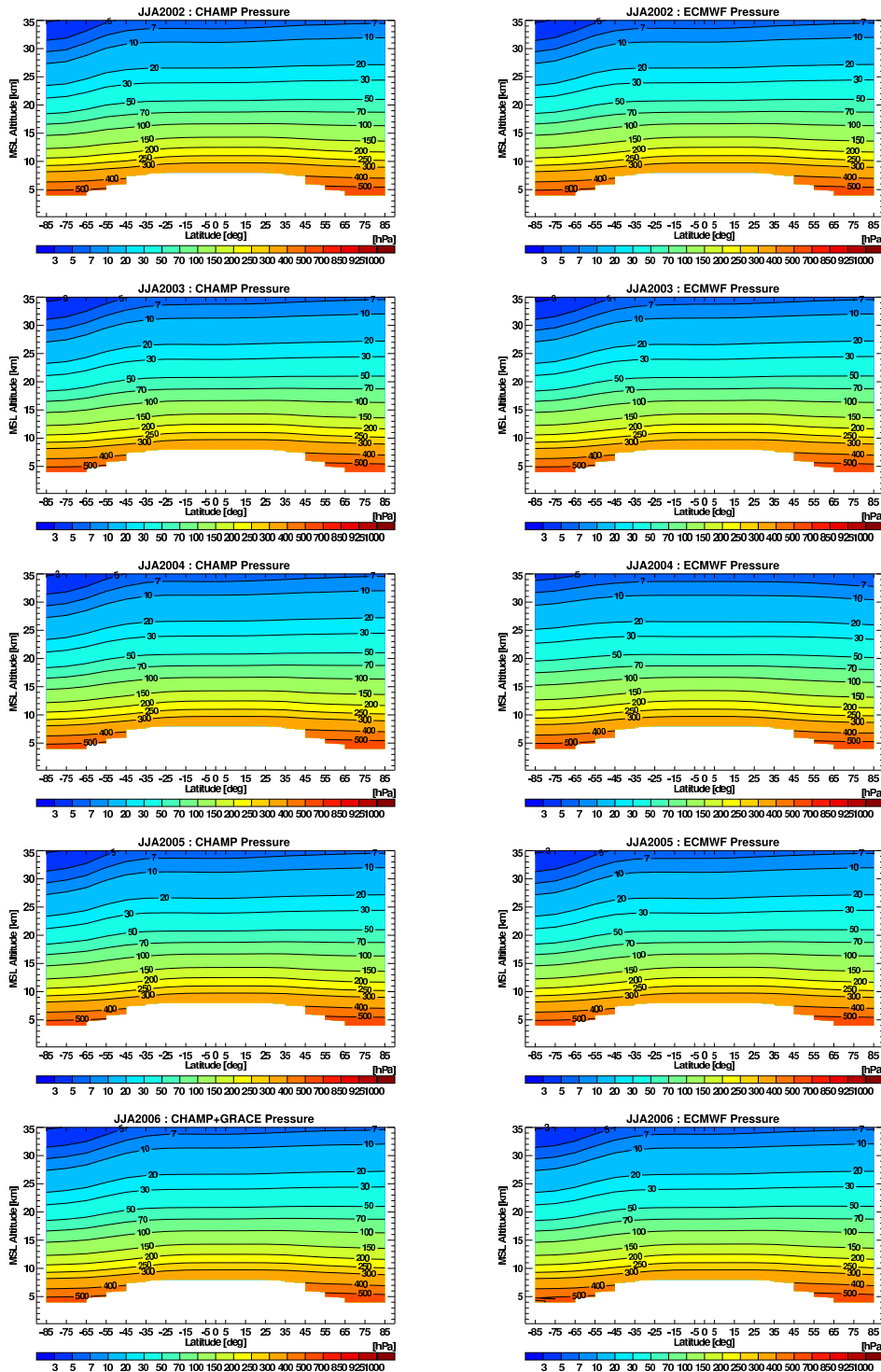
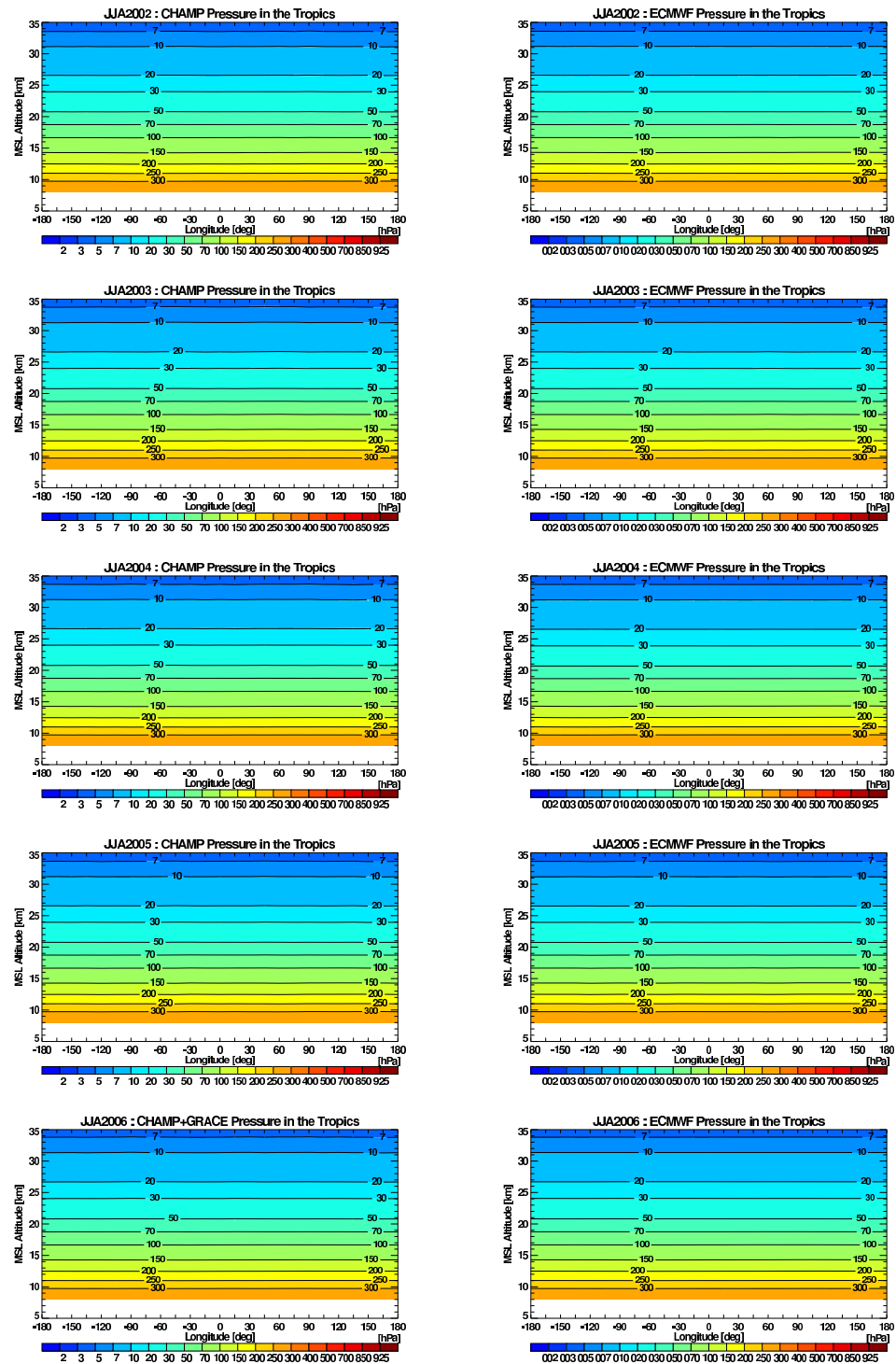


Figure 4.6: Dry pressure climatologies [hPa] of NH summer seasons JJA 2002 to JJA 2006 with pressure labels coinciding with mandatory pressure levels; same layout as Figure 4.2.



**Figure 4.7:** Longitudinal dry pressure climatologies [hPa] of NH summer seasons JJA 2002 to JJA 2006 with pressure labels coinciding with mandatory pressure levels; same layout as Figure 4.2.

$R$  the specific gas constant of air, and  $p_0 = 1013.25$  hPa is standard ground pressure to which  $p$ , a constant pressure level in hPa, is normalized to.

Dry geopotential height climatologies of the CHAMP RO measurements are shown for the same summer seasons as the other atmospheric parameters discussed above. The seasonal  $10^\circ$  zonal mean for all summer seasons show very similar structures for the measurement data as shown in [Figure 4.8](#). Geopotential height increases linearly with increasing altitude as expected, except for the southern polar regions. Here, the same dry geopotential height resides at a higher pressure altitude. This is directly related to the fact that in southern polar boreal summer regions lower pressure prevails (cf. [Figure 4.6](#)) which in turn is related to the cold air mass. As was true for refractivity only minor deviations from the linear increase with increasing pressure altitude can be found for dry geopotential height in the cold tropical tropopause region.

[Figure 4.9](#) pictures the longitudinal variation of dry geopotential height for the five NH summer seasons. Hardly any variations in longitude can be spotted. The variation of dry geopotential height compared to pressure altitude, however, can be clearly distinguished for the tropical region. For instance, the dry geopotential height of 18 km is equal to a pressure altitude of 18 km. Below that pressure altitude, dry geopotential height is nominally less than pressure altitude, and larger above. Trends in these relative distances, especially in the Tropics because of its well defined temperature profiles but also in any other region, are an excellent indicator of climate change as discussed in [Leroy et al. \(2006a\)](#).

## 4.2 Error Analysis of Climatologies

After having solved all the challenges of creating climatologies from RO data, the scientifically most interesting aspect remains, and that is of the absolute quality of the climatologies. For that to judge, a reference which can thoroughly be trusted has to be chosen. As already mentioned before, in this study ECMWF operational analyses were chosen for this purpose with a temporal resolution of 4 timer layers each day separated by six hours starting at 00 UTC. The horizontal resolution was chosen to roughly match the one of the RO data of about 250 km to 300 km and was fixed to “T42”. The ECMWF model is a spectral model and horizontal resolution is denoted by the highest wave number represented in the model. The notation “T42” means that the highest wave number represented is 42 which corresponds to a wavelength of about 300 km. “T” in that notation stands for “triangular spectral truncation” (e.g., [Untch et al., 2006](#)).

The operational analyses are created by a 4-D Var assimilation of all available ground based, in-situ, and satellite measurements. The assimilation window of the operational configuration is twelve hours long running from 03 UTC to 15 UTC for the 12 UTC assimilation product and from 15 UTC to 03 UTC the next day for the 00 UTC assimilation product. The 06 UTC and 18 UTC products are created in a separated quick assimilation step ([ECMWF, 2004, Part II](#)).

These analyses were taken as the true state of the atmosphere against which the RO climatologies were compared to. The main assumption with this approach is that the

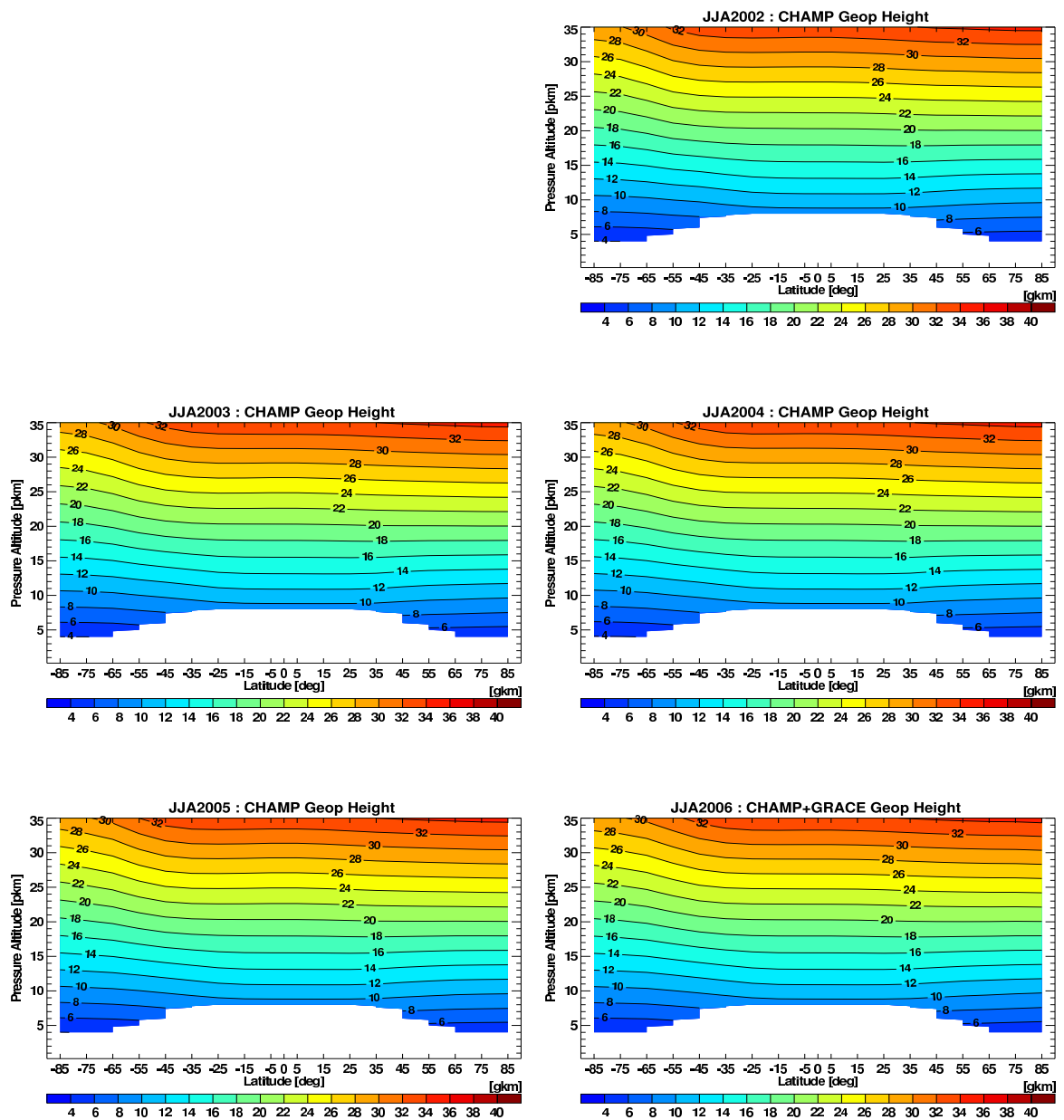


**Figure 4.8:** Dry geopotential height climatologies of NH summer seasons JJA 2002 to JJA 2006 for CHAMP measurements. Dry geopotential height is given in geopotential kilometers [gkm] from pole to pole and in pressure altitude from the cut-off altitude to 35 km.

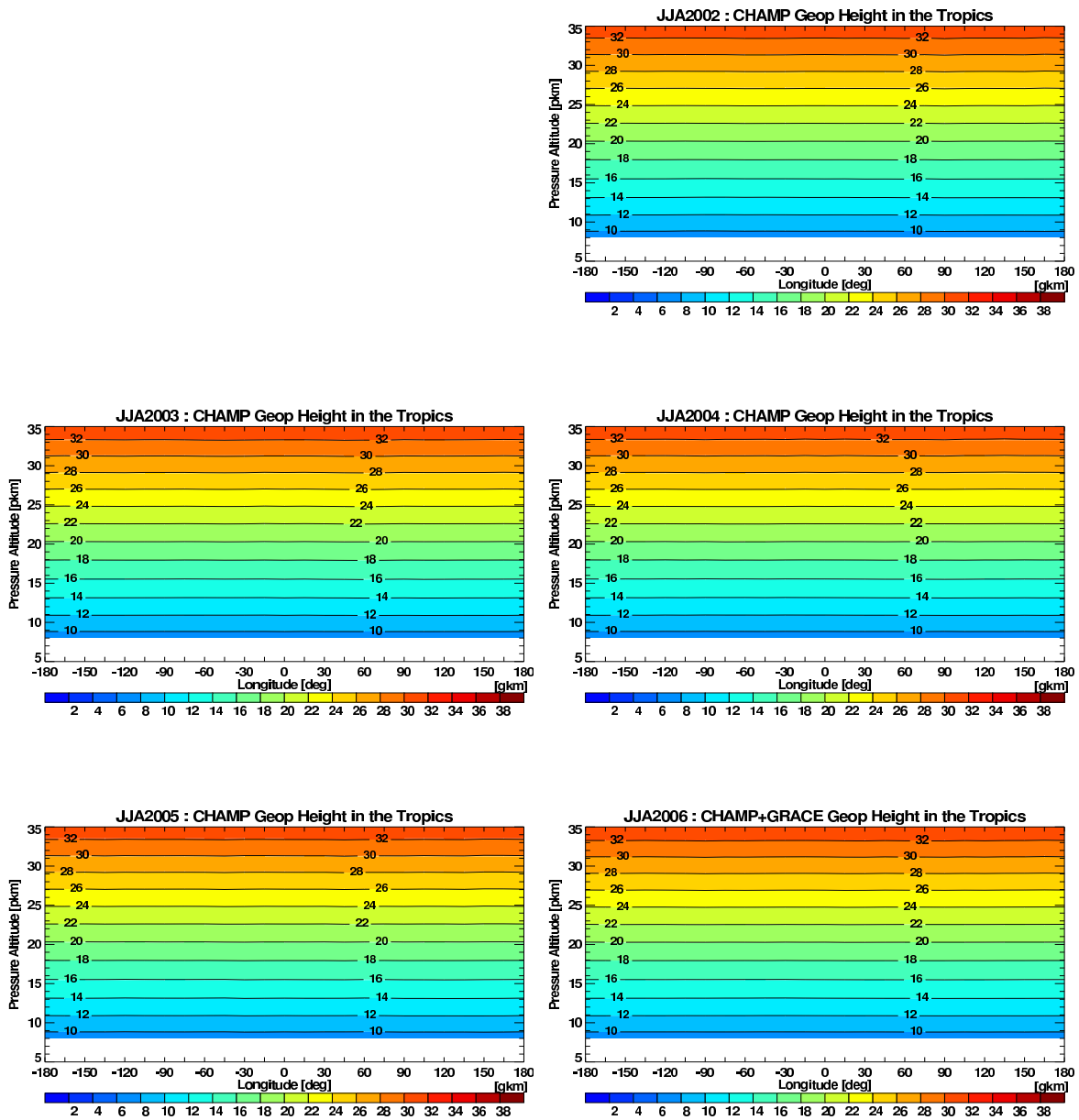


**Figure 4.9:** Longitudinal dry geopotential height climatologies of NH summer seasons JJA 2002 to JJA 2006 for CHAMP measurements; further details similar to [Figure 4.8](#).

analyses were the true state of the atmosphere which of course they are not. The spatio-temporal variability of the atmosphere cannot be completely resembled with only four time layers and the chosen horizontal resolution. Furthermore, the analyses themselves may be erroneous which may lead to ambiguous results in the error analysis.

Results presented in the following two sections have already been published in numerous papers. A short and concise summary can be found in *Luntama et al. (2007)*, whereas in *Foelsche et al. (2007a)* a detailed description of RO climatologies and their error fields are given. In the first following section the systematic error fields of all four parameters will be discussed in detail. In the last section of this chapter the sampling error is introduced and discussed on the basis of all four retrieved parameters.

### 4.2.1 Systematic Difference

The systematic difference denotes the difference of the CHAMP RO climatology to the corresponding co-located ECMWF climatology. Differences of climatologies are calculated simply by means of difference error statistics. Herein, a mean profile of each bin of, for instance, a season is computed for both climatologies and then subtracted from each other. In the case of the systematic difference only the co-located part of the ECMWF analyses are considered in the difference error statistics. If the complete reference field was taken the error statistics would reveal the total error between both climatologies. The total error, which will not be shown here, is denoted as the sum of the systematic and the sampling error. It was considered adequate to only discuss both summands separately.

Co-located ECMWF profiles are obtained by an interpolation in space to a CHAMP profile and by an allocation to an ECMWF time layer. An ECMWF profile is considered co-located in time to a CHAMP profile when the latter occurs within three hours before or after the beginning of one of the four time layers. The spatial co-location of the non-vertical CHAMP profile to a ECMWF profile is obtained by defining the mean location of the CHAMP profile as the latitude and longitude of the point, where the straight-line connection between transmitting and receiving satellite during the occultation event touches the Earth's ellipsoidal surface (corresponding to the tangent point location of real RO profiles at about 12km to 15km altitude) (*Foelsche et al., 2007a*). When performing the difference error statistics, only mean profiles are considered which result from at least ten single profiles to assure robust statistical calculations.

*Gobiet et al. (2005)*, *Borsche et al. (2007)*, *Gobiet et al. (2007)*, and others, have shown that there are indeed quite some absolute errors inherent within the ECMWF operational analyses. From a climatological point of view, these errors are not present within the CHAMP data and the difference otherwise between the analyses and CHAMP climatologies is fairly small, as will be shown below. Because of these new findings, not the ECMWF analyses were considered as reference data anymore but the CHAMP climatologies themselves. The implication of this is that the difference of co-located ECMWF relative to CHAMP climatologies will be examined, which hereafter is referred to as the systematic difference between these two atmospheric fields.

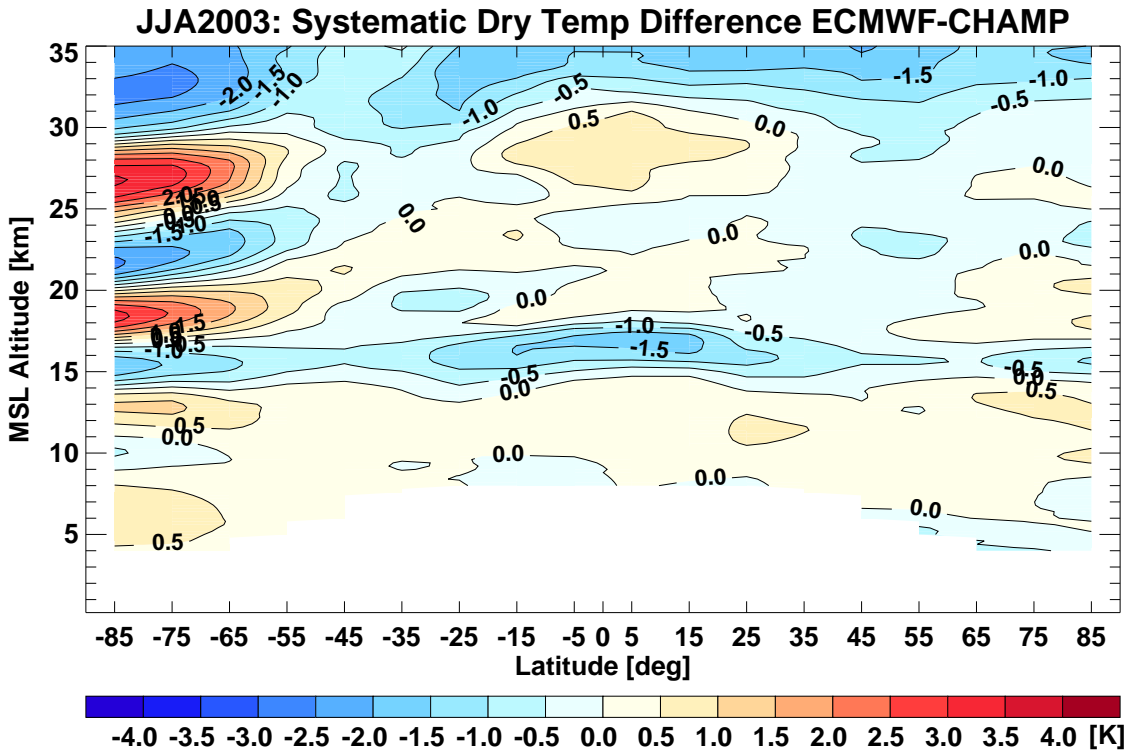


**Figure 4.10:** ECMWF – CHAMP systematic dry temperature difference of season JJA 2003 in an altitude range from the applied cut-off altitude to 35 km and from pole to pole. In most areas the difference ranges around 0 K, except for the tropical tropopause region, above 30 km over all latitudes, and at high southern latitudes in the low and mid stratosphere.

### Systematic Dry Temperature Difference

Figure 4.10 depicts the temperature systematic difference of the season JJA 2003. The differences are given in steps of 0.5 K and the plot region equals that of the climatologies as discussed earlier ranging from North Pole to South Pole in latitude extent and from ground to 35 km applying the cut-off altitude at the bottom. Overall, the agreement between the CHAMP RO climatologies and the ECMWF operational analyses are obviously in good agreement of better than 0.5 K in most regions. However, there are three major regions in which the systematic difference exceeds 1 K and at times even 3 K. These regions are confined to the boreal summer southern high-latitudes, the altitude range above 30 km, and the tropical tropopause.

Deviations reach highest within the cold southern polar winter vortex, with differences of more than  $\pm 3$  K resulting in a wave-like structure of alternating positive and negative systematic differences. The tropical tropopause region exhibits a pronounced cold deviation which amounts to about  $-1.5$  K. And finally, the region higher than 30 km which at all latitudes is again colder in the analyses of around 1.0 K to 2.0 K.

The causes behind these major systematic differences are manifold and have all been

addressed in different publications. The southern polar vortex difference was actually one of the first major findings of an earlier study conducted by *Gobiet (2005)* and published in *Gobiet et al. (2005)*. The exciting part of these studies were that for the first time it was possible to validate the operational ECMWF analyses with RO data on a climatological basis. It turned out that the systematic difference indeed originates essentially from the analyses and that the RO measurements provided a more accurate view of the atmospheric state in that region.

The reason for the analyses to perform that poorly in the southern polar regions results from the fact that especially in austral wintertime there are hardly any ground based measurements, and in general only relatively few satellite measurements reach the highest latitudes. The main observation source from satellites within high-latitudes which are assimilated into the analyses are obtained by the AMSU-A instrument and since October 2003 from the Advanced Infrared Sounder (AIRS) instrument (*ECMWF, 2003*). These two measurements are characterized by vertically broad weighting functions which peak at that altitude in which the maximum of the observed systematic differences occurs (*Foelsche et al., 2007a*). The outcome of the assimilation process when trying to minimize the cost function within the assimilation using radiance information with such broad weighting functions resulted in a temperature profile which deviates with the observed wave-like pattern against RO measurements.

The systematic difference above 30 km which occurs more or less uniformly from pole to pole has been investigated in *Gobiet et al. (2007)*. In that study five different analyses, two independent instruments from the ENVISAT satellite, and two retrieval chains were compared to each other. One result of *Gobiet et al. (2007)* was that the ECMWF operational analyses are colder than all other investigated analyses, the CCRv2.3 retrieval chain, and both of the satellite measurements. Only the retrieval chain of the GFZ yields temperatures about as cold or even colder than the ECMWF analyses at altitudes higher than 30 km because in that retrieval the initialization altitude of the hydrostatic integral reaches as low as 43 km. With that low initialization altitude the retrieved CHAMP profiles will still have much information content of the background used at altitudes higher than 30 km.

The last of the three mentioned areas of large systematic difference is the tropical tropopause region. It was first mentioned in *Gobiet et al. (2005)* and discussed in detail in *Borsche et al. (2007)*. Also in [Section 5.1](#) a detailed discussion of that difference can be found. To quickly summarize, this difference too can be attributed to a limited representation of the atmospheric state in the operational analyses. It was strongly indicated that this difference was due to a under representation of atmospheric wave activity in the lower stratosphere and upper troposphere region as well as to an insufficient vertical resolution to capture atmospheric variability in an adequate manner. Since a comprehensive update of the ECMWF analyses in horizontal and vertical resolution but also in improving the physical representation of atmospheric variability (*Untch et al., 2006*), the differences compared to RO measurements decreased considerably with season MAM2006.

In [Figure 4.11](#) the temporal evolution of the systematic dry temperature difference between ECMWF analyses and CHAMP RO climatologies is shown. The temporal

evolution is discussed for the whole time period even though the abundance of CHAMP profiles within the first two seasons is only half of that of the remaining seasons (see [Figure A.1](#)). In addition, the number of measurements had not been as continuous for the first half year as they were in the time following but varied quite dramatically (cf. [Section 3.1](#) and [Figure 3.1](#)). On the basis of seasons it is still feasible to investigate that period, however, when interpreting results caution has to be exercised especially with the first two seasons of CHAMP data.

In order to visualize the temporal evolution over the complete time period of available CHAMP data and over the whole globe, the CHAMP climatologies were subdivided into six latitude ranges. These represent northern and southern high-, mid-, and low-latitudes ranging from  $90^\circ$  to  $60^\circ$ ,  $60^\circ$  to  $30^\circ$ , and  $30^\circ$  to  $0^\circ$  North and South, respectively. For each of these latitude range three of the corresponding original  $10^\circ$  latitude bands were averaged. With this method, the systematic difference could be visualized for the complete period of five years, for all latitudes, and for altitude ranges between 4 km and 35 km at high-, 6 km and 35 km at mid-, and between 8 km and 35 km at low-latitudes in accordance to the cut-off criterion. Note, however, that data was averaged into  $30^\circ$  latitude ranges which can reduce latitudinal variability as seen in the climatologies discussed above with a latitude extend of  $10^\circ$  for each bin.

At all latitude ranges the above described difference structures can be detected. The deviation above 30 km exists throughout the whole time period and at a similar amount at all latitude ranges. At high-latitudes the continuous negative deviation is intermitted at times by warm deviations which, however, result from the discussed polar vortex assimilation problem in the analyses. The negative deviation in the tropical tropopause can distinctly be seen in both low-latitudes bands even though they form an average over  $30^\circ$  latitude. This difference starts from the very beginning of the time period, varies a bit in amount but always stays colder than 1.0 K compared to the CHAMP RO measurements, and finally decreases considerably beginning with season MAM 2006 (cf. [Figure 5.1](#) and [Section 5.1](#)).

The temporal evolution of the high-latitude systematic difference is most interesting. The differences which occurred in austral winter of 2003 as seen in [Figure 4.10](#) were much stronger than in JJA 2002 and JJA 2004. Additionally, in JJA 2004 the phase of the oscillating difference seems to have inverted: where there were negative deviations in JJA 2003 there are now positive deviations and vice versa but much weaker than in JJA 2003. In October 2003 AIRS radiances were assimilated operationally (*ECMWF*, 2003) and it was hoped that the systematic differences at southern high-latitudes would diminish or at least decrease which was true for JJA 2004. However, in JJA 2005 the differences increased again and were even stronger than in JJA 2003 with an introduction of a further phase of the oscillation: in this season there are now four phases of positive deviation and three phases of negative deviation within the same altitude interval of around 10 km to 35 km as before. The signs of the highest three phases are completely flipped compared to JJA 2003. In JJA 2006 it seems as though the differences have finally diminished and the oscillating character of the difference has collapsed in the southern hemisphere (SH). However, for the first time within the considered time period of available CHAMP data, in JJA 2006 the oscillating systematic difference pattern

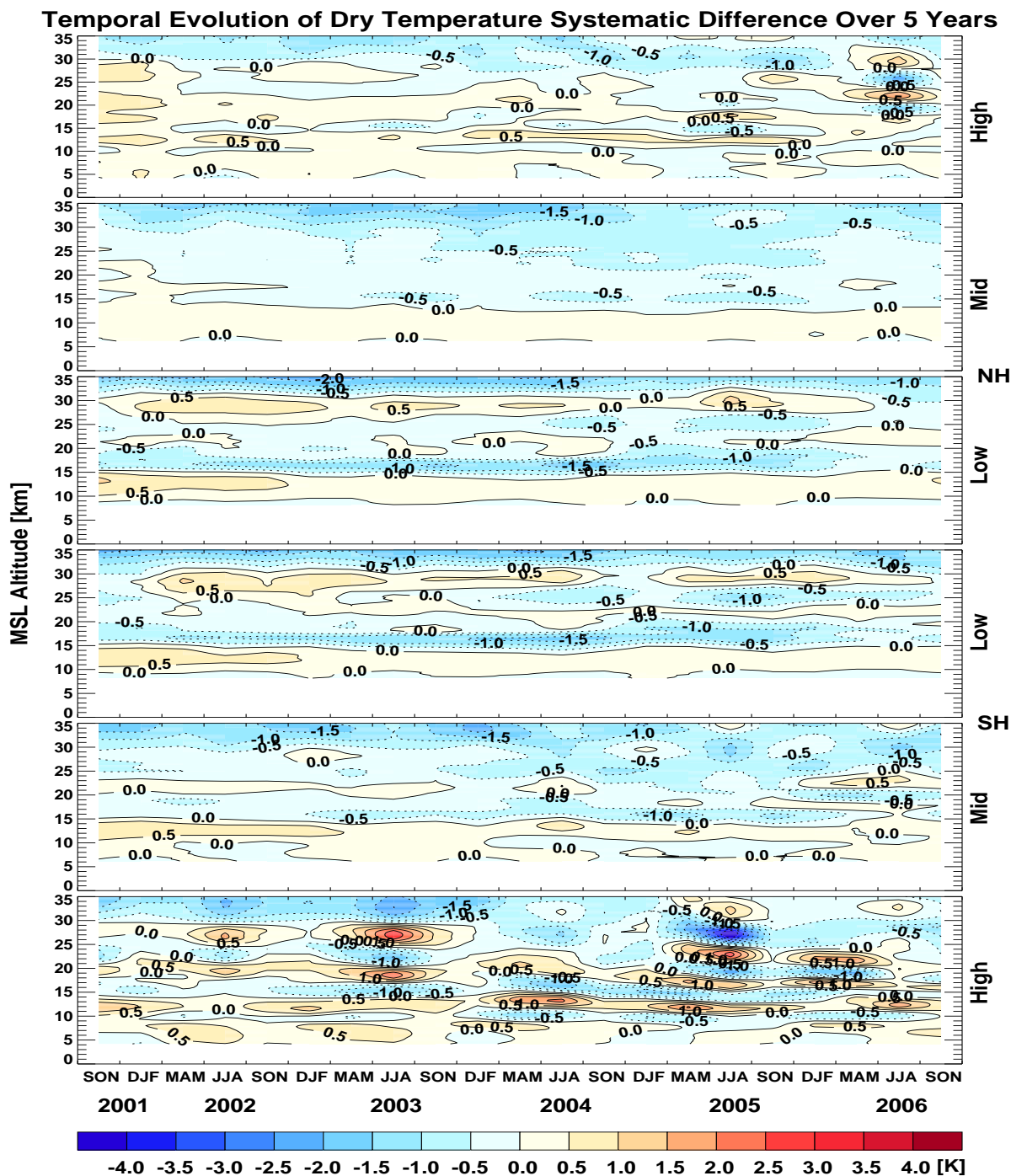


**Figure 4.11:** Temporal evolution of systematic dry temperature difference in six latitude ranges for northern high-, mid-, and low- and for southern low-, mid-, and high-latitudes (from top to bottom), shown for altitudes ranging from 5 km, 6 km, and 8 km for high-, mid-, and low-latitudes, respectively, to 35 km for the complete time period of available CHAMP data of more than five years.

occurs in the northern polar regions, although not as pronounced in amount and time extent. In addition, this structure now occurs in the summertime at northern high-latitudes as opposed to having occurred in the wintertime at southern high latitudes.

In the discussion above, the focus concerning the time of occurrence of the structure was laid on the boreal summer season. But as can be seen easily in [Figure 4.11](#), the structure persists throughout the seasons however extenuated in some seasons and almost diminished in others. The boreal wintertime seems to be a season in which it is developed the least, strengthening in boreal springtime and decreasing in boreal fall.

At mid-latitudes the systematic difference is smallest throughout the time period under consideration and no systematic structures can be spotted. At low-latitudes and altitudes of 25 km to 30 km a further systematic positive deviation between the ECMWF analyses and CHAMP climatologies can be detected. Almost continuously throughout the seasons the deviation amounts to +0.5 K.

### Systematic Refractivity Difference

As was shown in the previous section, refractivity decreases exponentially with increasing altitude. For that reason the systematic differences of refractivity RO climatologies compared to ECMWF operational analyses are presented in [%], because the spread of the absolute differences for the shown altitude range is hard to visualize otherwise. Because refractivity is inversely proportional to temperature in dry air conditions (cf. [Equation 2.8](#)), the systematic differences are inverse of those shown before for dry temperature.

[Figure 4.12](#) depicts the systematic refractivity difference for the season JJA 2003 corresponding to [Figure 4.10](#) for dry temperature. Here, the structures as discussed before remain the same with larger differences in the tropical tropopause and the southern polar vortex region. The deviation at altitudes above 30 km are not as pronounced in refractivity as in temperature. For refractivity the systematic differences are positive in the tropical tropopause and opposite in southern high-latitudes due to the inverse relationship of each other. The differences amount to about 0.8% in the tropical tropopause and between less than -1.0% and more than +2.0% for the oscillating deviation at southern high-latitudes.

The temporal evolution of refractivity throughout the complete time period of available CHAMP data, as shown in [Figure 4.13](#), resembles that of dry temperature (cf. [Figure 4.11](#)) and structures over all remain the same. At low-latitudes the tropical tropopause is distinctly visible from the beginning up to MAM 2006 by a narrow band of deviations amounting 0.8% between 16 km and 18 km. In the second half of the time period negative systematic refractivity differences are visible between 25 km and 30 km. These differences amount to between 0.25% and 0.5%. Interestingly, in dry temperature these differences have occurred throughout the complete time period. Except for the two regions mentioned, deviations at low-latitudes only range between  $\pm 0.25\%$ .

At mid-latitudes the differences are in general positive with the highest values around the tropopause at about 15 km. Other than that no structure can be spotted and differences occur rather randomly distributed. At southern high latitudes the oscillating

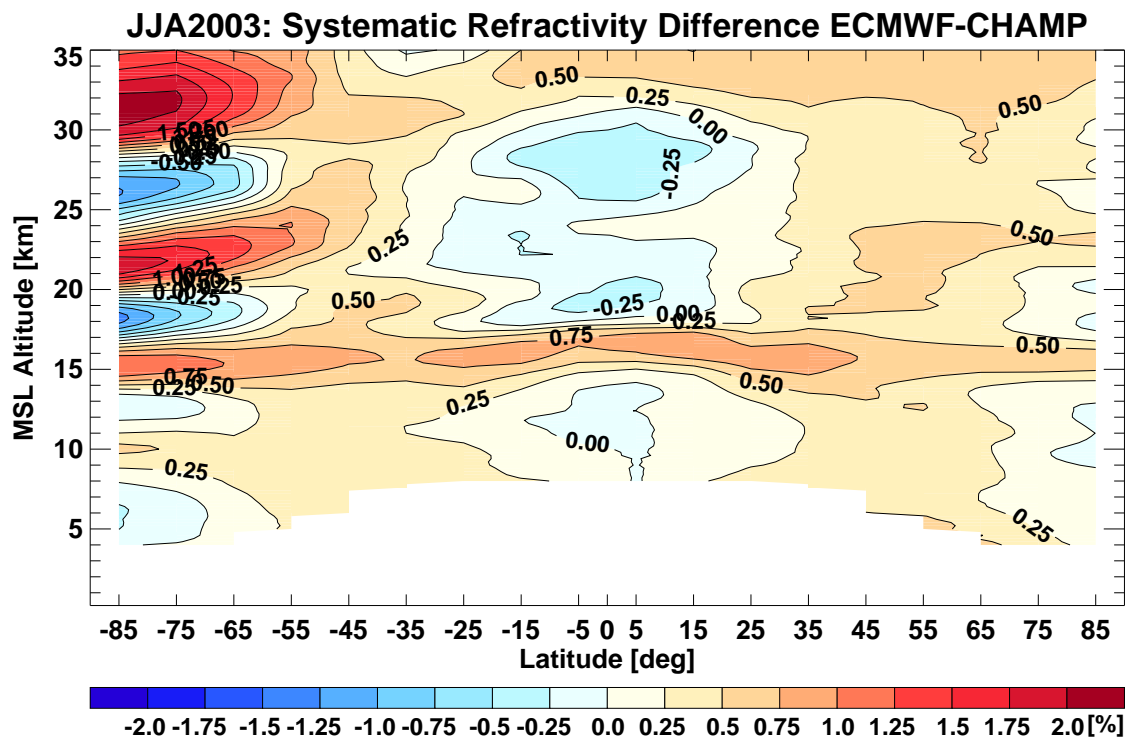


**Figure 4.12:** ECMWF – CHAMP systematic refractivity difference of season JJA 2003 in an altitude range from the cut-off criterion to 35 km and from pole to pole. Differences are given in [%] due to the exponential decrease of refractivity with altitude.

difference, which has been discussed in detail for dry temperature, exists for refractivity as well. For the years 2002, 2003, and 2004 these differences are mostly confined to the boreal summer seasons and occur within a latitude range of 10 km to 35 km. For the second half of the time period and the lower altitude part the differences are drawn over the complete years up to season MAM 2006. In analogy to dry temperature, the oscillating pattern can be found for season JJA 2006 in the NH. Beside that, the northern hemispheric high-latitude deviations are in general positive and randomly distributed amounting between 0.0% and 0.5% without any significant pattern readily visible.

### Systematic Dry Pressure Difference

The systematic dry pressure difference will be discussed in this section. In the RO method pressure is a direct product of refractivity (cf. Equation 2.10). The systematic dry pressure difference is shown in [%] because of the same exponential decrease with increasing altitude as for refractivity. In Figure 4.14 the systematic dry pressure difference is shown for season JJA 2003. The overall pattern visible here was termed “butterfly” (or “tripole” feature by Foelsche *et al.* (2007a)) because of the almost symmetrical pattern at northern and southern mid and high-latitudes throughout almost the whole altitude

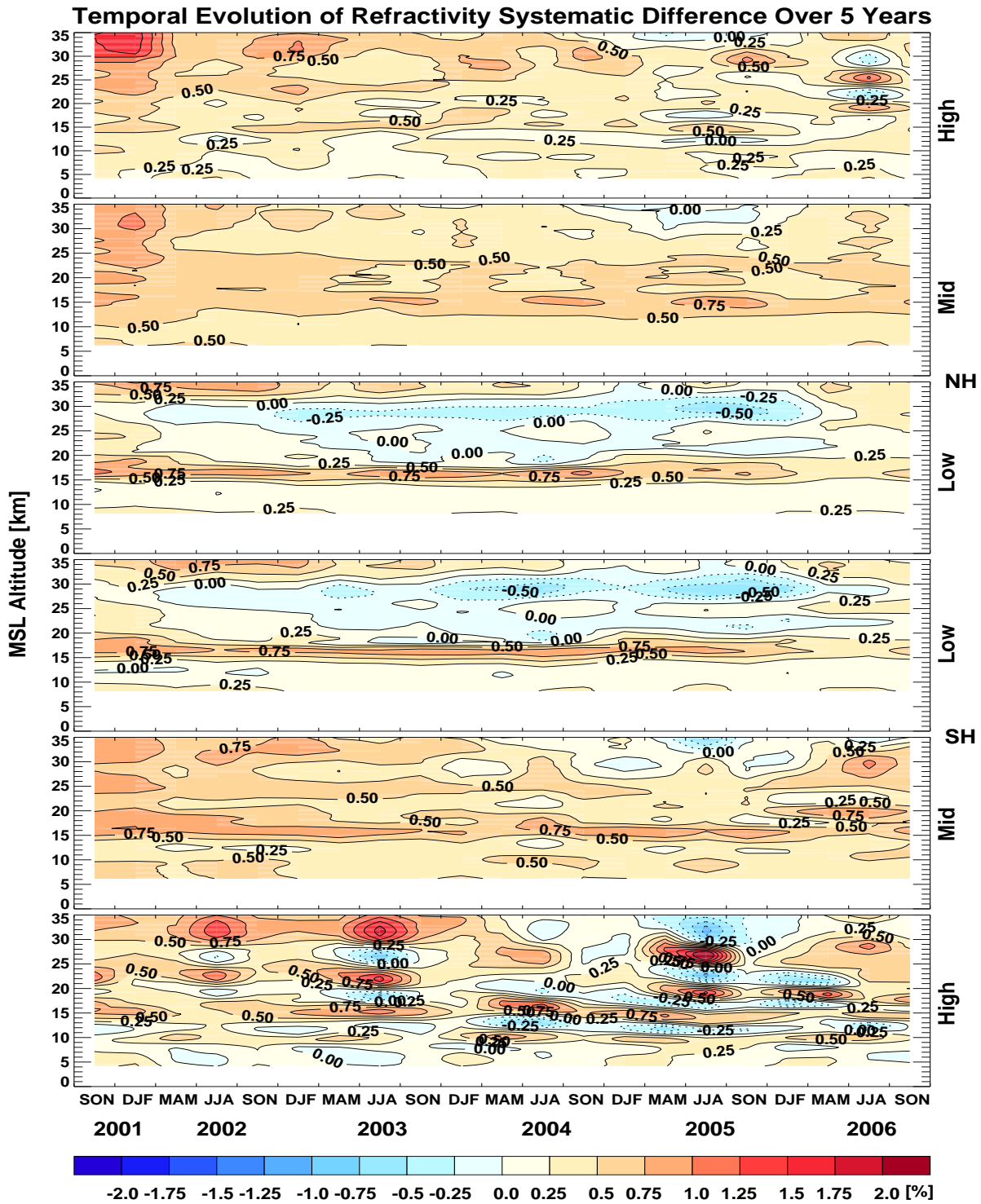


**Figure 4.13:** Temporal evolution of systematic refractivity difference for more than five years of available CHAMP data; differences are given in [%] due to the exponential decrease of refractivity with altitude. Further details similar to [Figure 4.11](#).

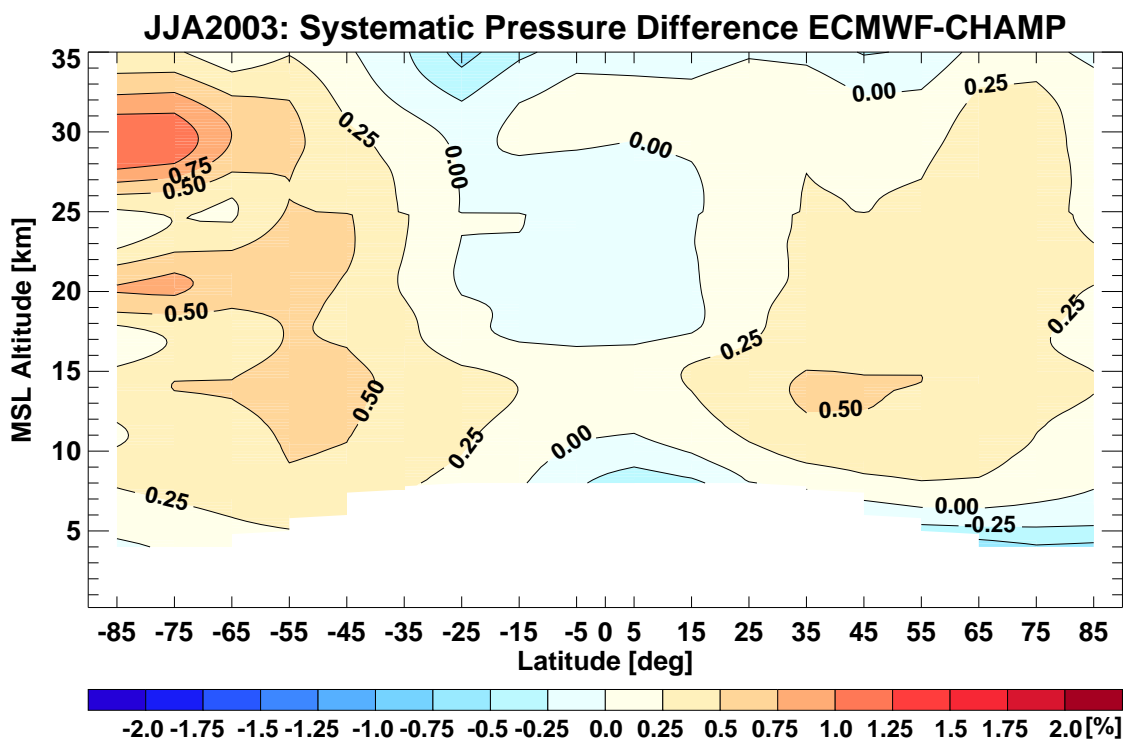


**Figure 4.14:** ECMWF – CHAMP systematic dry pressure difference of season JJA 2003 in an altitude range from the cut-off criterion to 35 km and from pole to pole. Differences are given in [%] due to the exponential decrease of pressure with altitude. The positive deviations at mid to high northern and southern latitudes are partly due to an approximate (1<sup>st</sup> order ellipsoid) height allocation within the CCRv2.3 processing system and amount up to 0.5%.

range. The differences within that pattern amount to about 0.5% in the northern and southern hemispheres.

The strong deviations between ECMWF analyses and CHAMP RO climatologies in the southern polar vortex region, as were visible for temperature and refractivity, do not result in a as strongly pronounced oscillating structure for dry pressure. They are still present and in this season amount to more than 0.8% at around 30 km. At low-latitudes the systematic difference remains very small throughout all altitudes and amounts to  $0.0 \pm 0.2\%$ . The “butterfly effect” results from an only approximate (1<sup>st</sup> order) representation of the Earth’s ellipsoid within the CCRv2.3 retrieval system and will be mitigated in future processing versions by using accurate Earth figure modeling.

Unfortunately, the “butterfly effect” is not real but results from an inconsistency within the retrieval system. Very recently, one error was found in calculating the radius of the Earth at a given location by correcting with the reference ellipsoid. The results of these corrections are not yet shown in the presentation of this study, but are promising by reducing the effect by about a half.

The temporal evolution of dry pressure, as shown in [Figure 4.15](#), reflects what is

already known from season JJA 2003. At low-latitudes the systematic difference is very low with the exception of the tropical tropopause region where it amounts to more than 0.25%, however, not as continuous in time as it was the case for dry temperature and refractivity. The mid-latitudes are characterized by high deviations due to the error in the retrieval process. It seems to be confined to lower altitudes leveling off at altitudes of 30 km and above. Furthermore, this artifact seems to be decreasing in amount and in altitude extent over time. For high-latitudes the same is true. Only in season JJA 2003 and JJA 2005 the oscillating difference pattern in the SH can be seen, however much weaker than for dry temperature and refractivity. In JJA 2006 this pattern is seen neither at southern nor at northern high-latitudes.

### Systematic Dry Geopotential Height Difference

Due to the fact that dry geopotential height is very closely related to dry pressure, as discussed in [Section 4.1.3](#), the absolute systematic difference of CHAMP dry geopotential height climatologies compared to ECMWF analyses is very similar in structure to the relative pressure difference shown above. In [Figure 4.16](#) systematic dry geopotential difference is shown as a function of latitude and pressure altitude, which was introduced in [Equation 4.4](#). The known positive deviations at mid to high northern and southern latitudes are again visible in season JJA 2003 where deviations amount up to  $\sim 30$  geopotential meters (gm). At southern polar regions the oscillating structure in systematic difference can also be anticipated in dry geopotential height, which in this case is overlaid by the deviations resulting from an approximate (1<sup>st</sup> order ellipsoid) height allocation within the CCRv2.3 processing system.

[Figure 4.17](#) shows the temporal evolution of dry geopotential height for the five years of CHAMP data. Deviations are very closely mirrored of those from dry pressure (cf. [Figure 4.15](#)) and amount to values of around 20 gm, tentatively slightly decreasing with time. At low-latitudes deviations are much lower and negative at higher altitudes amounting to less than  $-20$  gm. Again in season JJA 2005 the oscillating structure at southern high-latitudes is formed most distinctly and at northern high-latitudes in JJA 2006 this structure is not visible.

In DJF 0506 at almost all latitudes and higher altitudes a negative deviation of around 40 gm to 60 gm occurs which is due to an inconsistency in the retrieval system of the version discussed here (CCRv2.3) which is relevant only for dry geopotential height in January 2006. In this version, this inconsistency was not yet corrected. However, in newer versions of the retrieval system, with which the complete data set was reprocessed, this and other minor inconsistencies do not exist anymore including a series of other improvements performed. First results with this newly processed data were published in *Foelsche et al. (2007a,b)* as well as in *Steiner et al. (2007)*.

#### 4.2.2 Sampling Error

In this section the sampling error will be introduced and discussed firstly for the example season JJA 2003 and then for the temporal evolution of the complete time period of

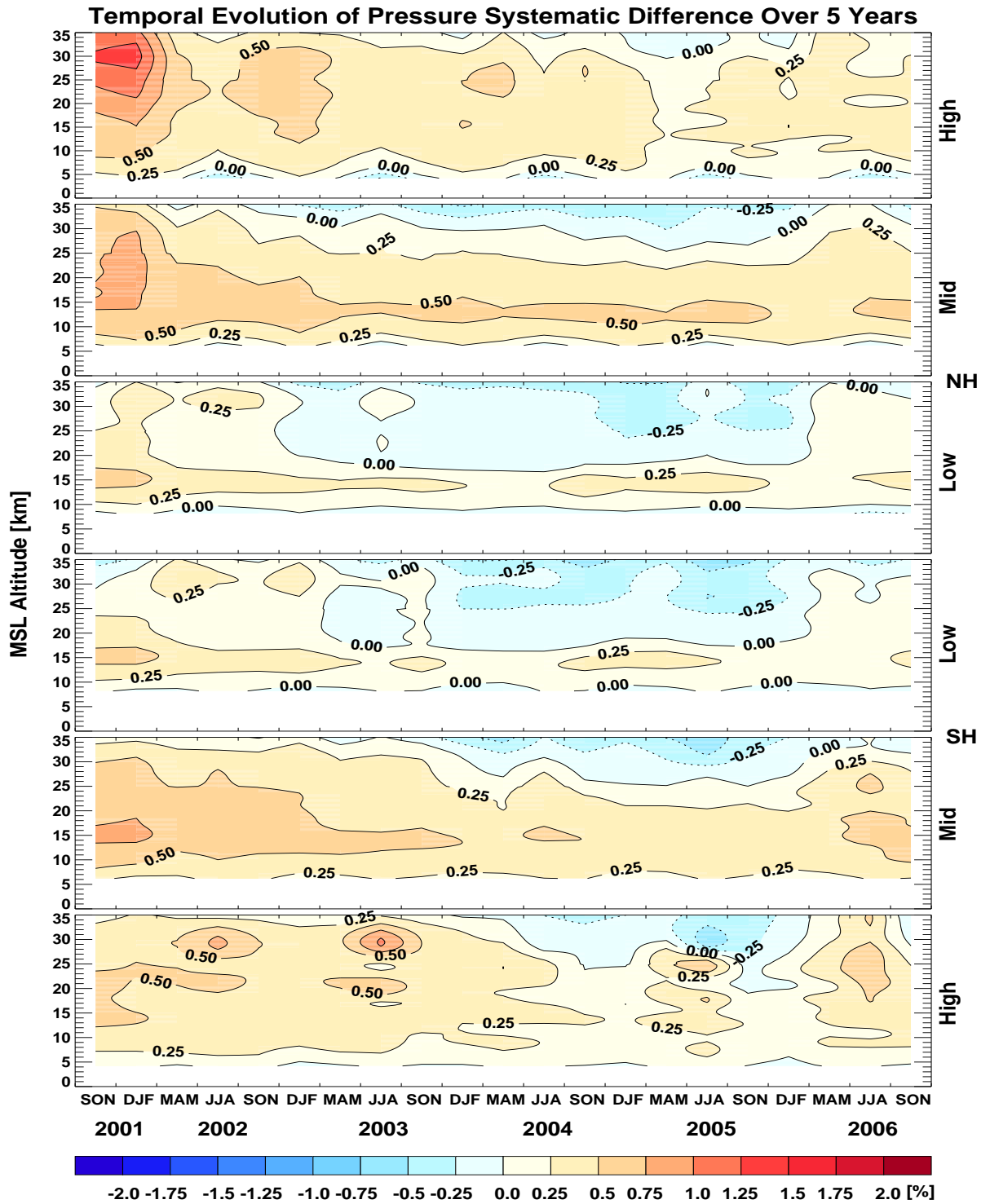


**Figure 4.15:** Temporal evolution of systematic dry pressure difference for more than five years of available CHAMP data; differences are given in [%] due to the exponential decrease of pressure with altitude. Further details similar to [Figure 4.11](#).

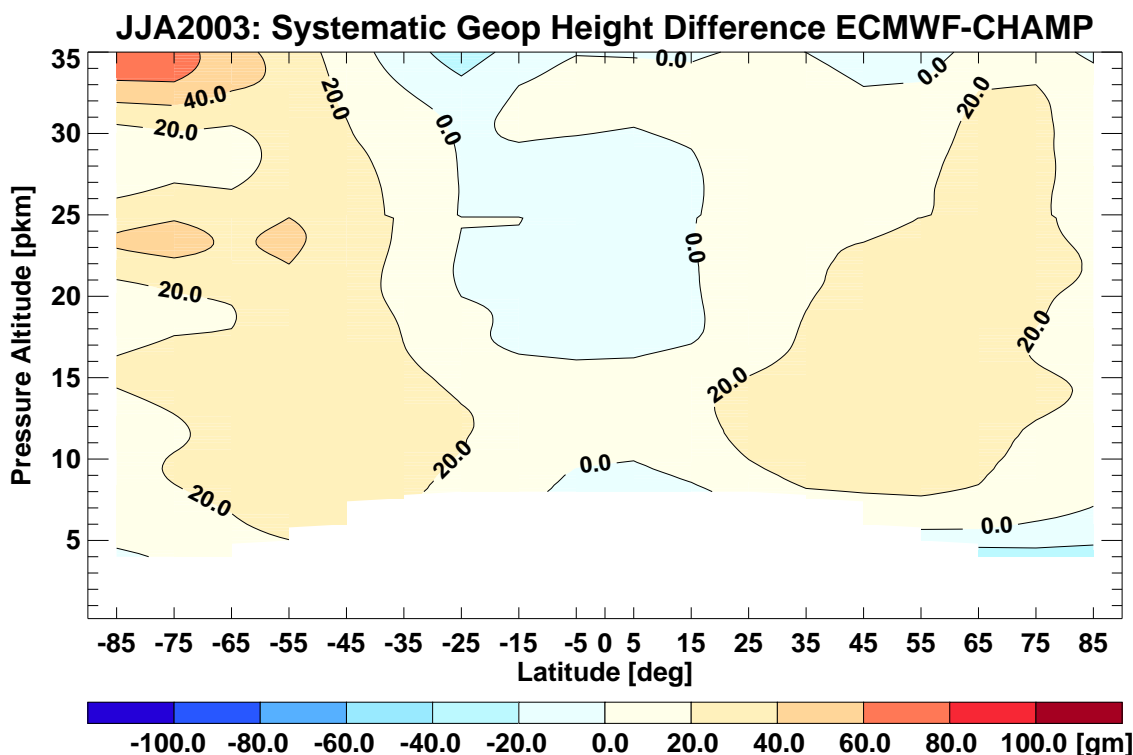


**Figure 4.16:** ECMWF – CHAMP systematic geopotential height differences given in geopotential meters for season JJA 2003 in an altitude range from the cut-off criterion to 35 km and from pole to pole. Positive deviations at mid to high northern and southern latitudes are partly due to an approximate (1<sup>st</sup> order ellipsoid) allocations within the CCRv2.3 processing system and amount up to  $\sim 30$  gm.

available CHAMP data. When creating climatologies with measurements, the sampling error plays an important role and needs to be carefully investigated.

In the previous section it has turned out that the CHAMP profiles contain a higher degree of information content than the profiles of the ECMWF analyses, even though there are much less CHAMP profiles per unit time. Therefore, the CHAMP profiles were declared reference and the systematic differences were calculated as the difference between the ECMWF and CHAMP profiles.

For the sampling error, in order to calculate it reasonably, the ECMWF analyses are considered reference; the CHAMP profiles go into the calculations only indirectly via co-located ECMWF profiles. The analyses, as introduced before, represent a discrete state of the atmosphere with four time layers divided into steps of six hours equally over the day. The spatial resolution was chosen to amount  $2.5^\circ \times 2.5^\circ$ , which roughly equals that of RO measurements. To obtain that resolution, the operational analyses were sampled by means of a discrete grid with  $144 \times 72 = 10,368$  grid points. These resemble profiles up to an altitude of 0.1 hPa (0.01 hPa from February 2006 onwards) with 60 (91) vertical model levels. Including all four time layers, the analyses provide 41,472 profiles

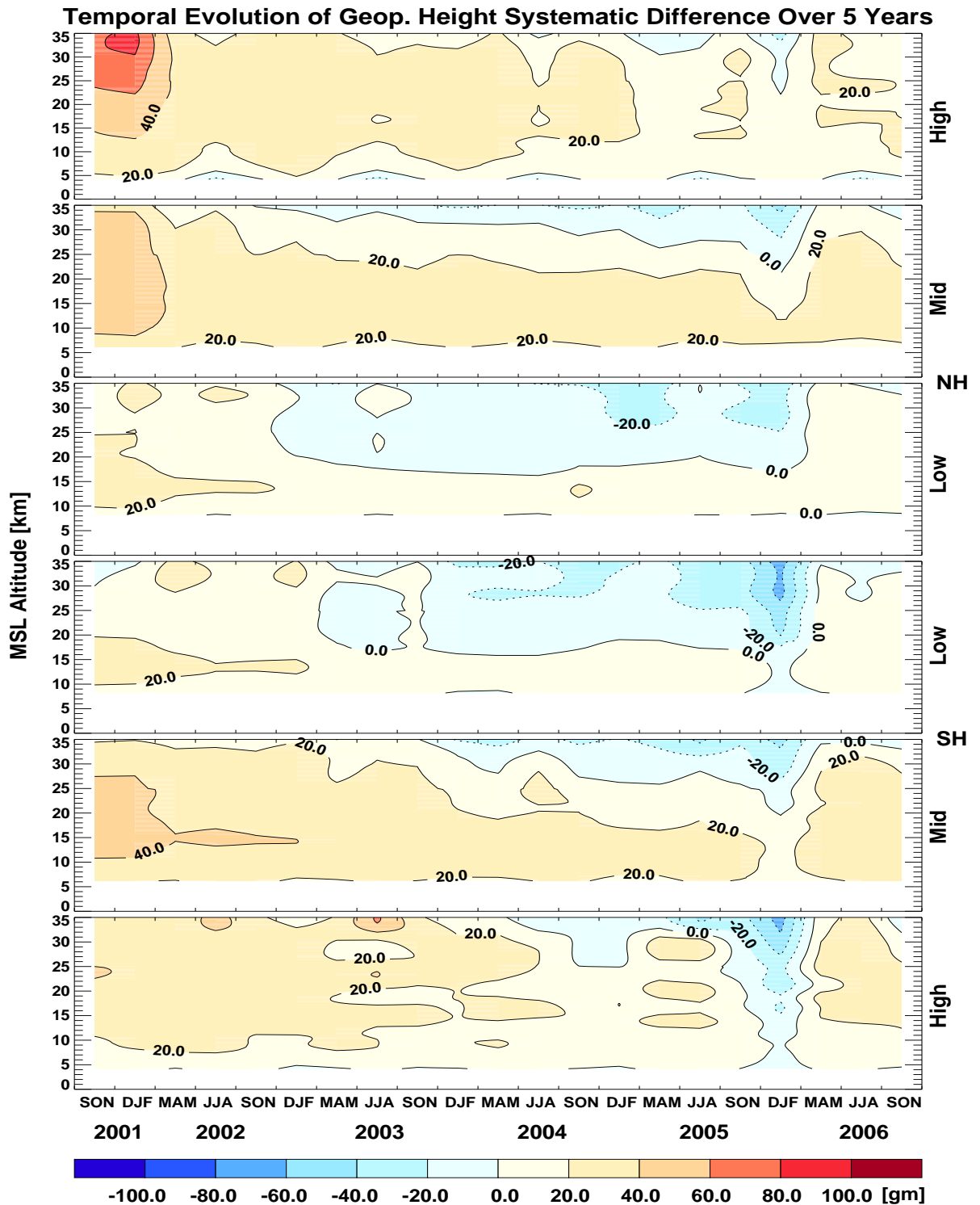


Figure 4.17: Temporal evolution of systematic dry geopotential height difference for more than five years of available CHAMP data; further details similar to Figure 4.11.

to describe the state of the atmosphere throughout one day. In comparison, the CHAMP satellite performs about 250 soundings within the same time period of which on average only 150 profiles can be retrieved into temperature profiles.

With the above numbers in mind it is comprehensible that the CHAMP measurements – or any other measurement as a matter of fact – even if they were perfect measurements, i. e., without any observational error, could never reproduce the ECMWF analyses exactly. This is due to the fact that the sampling of the measurements is unequal compared to (in this case always less than) that of the analyses. The error which is thus introduced is called the sampling error.

The sampling error is calculated by subtracting the co-located ECMWF field from the complete ECMWF field. The co-located ECMWF field describes a subset of the complete ECMWF field and is comprised of profiles co-located to every CHAMP measurement in space (on the latitude, longitude grid) and time (one of the four time layers). Thus, the sampling error is determined only from spatial and temporal information of the measurement; the information content of the profiles results completely from the analyses. The sampling error is very small and for monthly zonal mean climatologies amounts to about 0.3 K (*Pirscher et al., 2007a*). One limitation of the process of calculating the sampling error is that the temporal resolution of the CHAMP measurements is degraded to the four time layers of the analyses.

The sampling error is heavily influenced by the geographical distribution of the CHAMP profiles, as is also nicely shown in *Foelsche et al. (2007a)*. **Figure 4.18** displays April 2003 on the left side and June 2003 on the right side to demonstrate this influence. Even though monthly climatologies are not the focus of this study, these two months are shown here because the influence of geographical distribution of CHAMP measurements can be nicely illustrated on these two months for the complete set of CHAMP data. In April 2003 the measured CHAMP profiles are geographically clustered as opposed to two months later in June 2003 where profiles are quite uniformly distributed providing a better sampling of the atmosphere. Even though there are roughly the same number of profiles within both months, the information content which is gathered of the atmosphere is quite different and less for April 2003.

Consequently, the dry temperature sampling error, which is shown at the bottom part of **Figure 4.18**, overall is higher for April 2003 (left) than for June 2003 (right). For June the sampling error ranges around zero for most parts of the whole latitude and altitude range. Only at two spots at low level mid-latitude, the sampling error reaches and exceeds 0.5 K. For April 2003 the distribution and amount of the sampling error amounts to much larger deviations of more than 1 K and a much bigger extent.

In principle, the same accounts for seasons, however not as pronounced as for months. As could be seen in **Figure 4.18** the distribution geometry of the measured profiles can change rapidly within three months from clustered to quasi uniformly distributed. Still, the distribution geometry of profiles recorded in MAM 2003, displayed in **Figure 4.19** (upper left), on average looks quite clustered compared to the next season JJA 2003 (upper right), where profiles are quite uniformly distributed. Because of the averaging over one season, the sampling error is smoothed even for season MAM 2003 but marked deviations can still be spotted. These are located at high latitudes throughout the

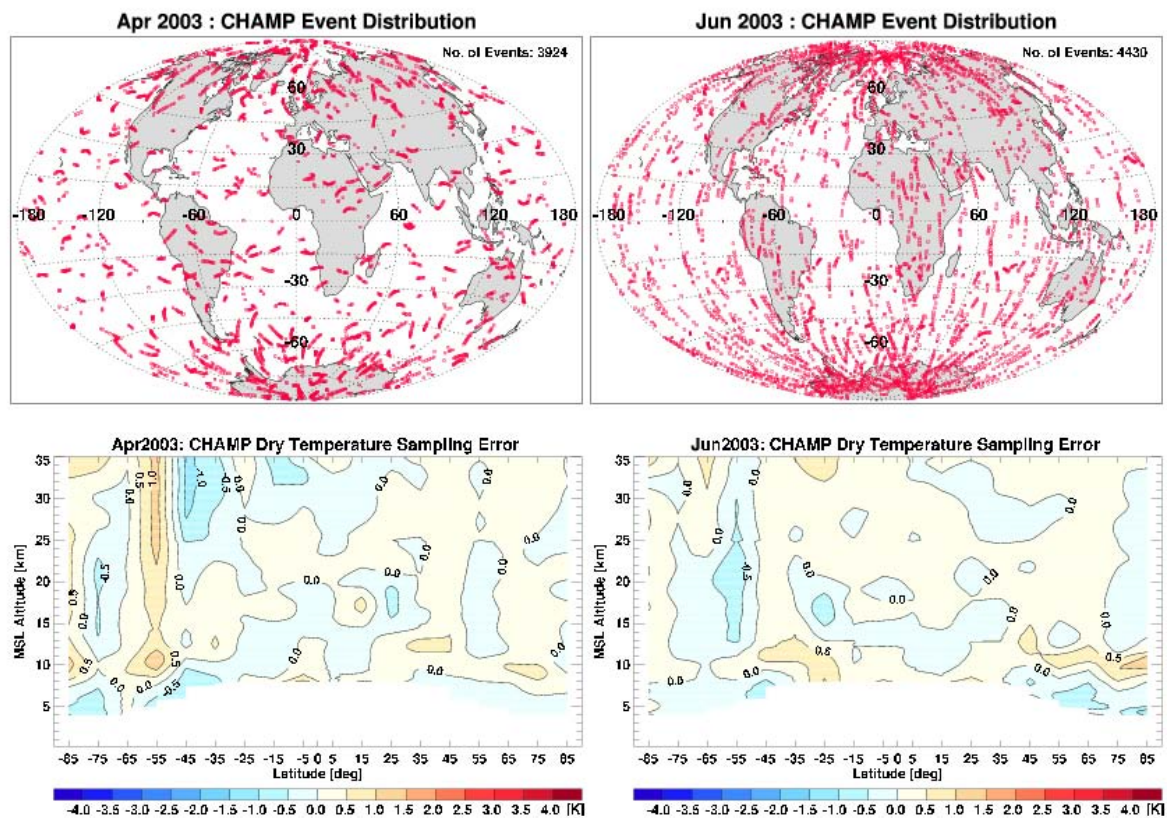


**Figure 4.18:** Global distribution of CHAMP profiles in the two months April 2003 and June 2003 (upper two panels) and corresponding dry temperature sampling errors, respectively (lower two panels). For a clustered distribution of CHAMP profiles as in April 2003 the sampling error is larger than for a more uniform distribution of profiles as in June 2003.

complete altitude range from 4 km up to 35 km amounting to less than  $-1.5\text{K}$  in the SH and around  $0.5\text{K}$  at the northern part. The sampling error for season JJA 2003 is even smaller than for June 2003 with less pronounced structures and fewer locations at which it reaches above or below  $0.5\text{K}$ .

An additional reason for the large sampling error at high-latitudes in MAM 2003 might be the climatological atmospheric situation. In boreal spring at both hemisphere's high-latitudes rapid temperature changes occur. Whereas the less confined northern polar vortex breaks and warms the much more confined southern polar vortex forms and cools. Within a season these rapid temperature changes might call for a particular high and uniform sampling in order to capture those changes correctly. As can be seen in [Figure A.6](#) of [A](#) large sampling errors usually occur in either boreal spring or autumn seasons at around or more polewards of  $70^\circ$  North or South, which about marks the border of the polar vortex temperature gradient.

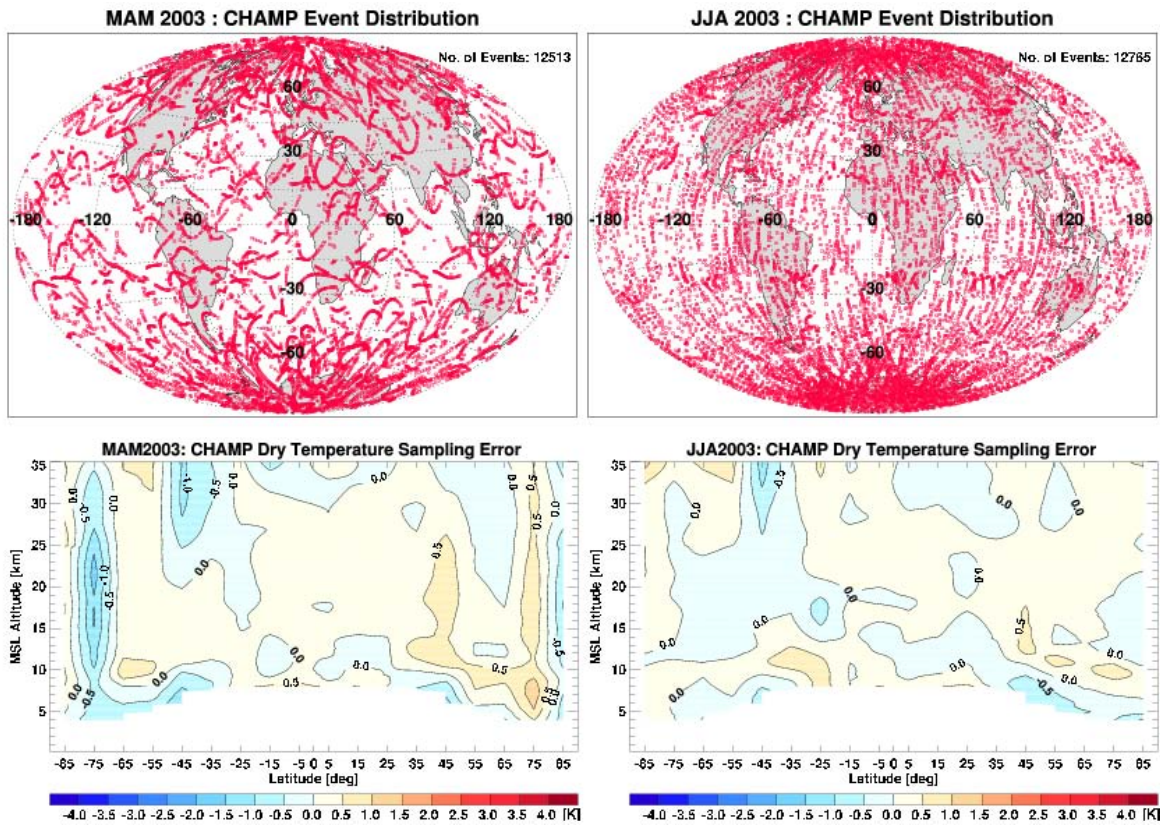


**Figure 4.19:** Global distribution of CHAMP profiles in the two seasons MAM2003 and JJA 2003 (upper two panels) and corresponding dry temperature sampling errors, respectively (lower two panels). In the case of seasons the sampling error is smoothed somewhat more but in principle the same applies as for months (cf. Figure 4.18).

### Temporal Evolution of the Sampling Error

The temporal evolution of the sampling error for the parameters dry temperature, refractivity, and dry pressure are displayed in Figure 4.20, Figure 4.21, and Figure 4.22, respectively. For dry temperature, the sampling error at mid and low-latitudes only ranges around 0.0 K with no structure in distribution and amount. Even at high-latitudes the sampling error only occasionally reaches over 0.5 K which takes place in SON 2002 at southern high-latitudes and in MAM 2006 at northern high-latitudes. This relatively small sampling error, however, is partly due to the averaging over  $30^\circ$  latitude in this Figure.

The sampling error for refractivity, Figure 4.21, and dry pressure, Figure 4.22, is given in [%] as was done so and reasoned in Section 4.2.1. Refractivity and dry pressure sampling error will be discussed together because the two errors quantitatively amount to similar values and distribution characteristics due to the inherent connection between these two parameters (cf. Equation 2.10).

At low-latitudes the sampling error ranges around 0.0% increasing to about  $\pm 0.25\%$

at mid-latitudes. In both latitude ranges no structure in amount and distribution could be determined. Only in MAM 2006 the large sampling error from high-latitudes has diffused into mid-latitudes resulting in a positive error at northern and a negative error at southern latitudes.

At high-latitudes the sampling error remains quite small between 4 km and about 20 km throughout the complete time period. At higher altitudes between about 20 km and 35 km it can reach as high as  $\pm 1.5\%$ . Negative and positive errors repeatedly occur in boreal spring and autumn in these latitude and altitude ranges. For instance, the largest sampling error occurs in both hemispheres in SON 2002 and JJA 2006 with errors reaching more than  $+1.25\%$  at southern and less than  $-1.25\%$  at northern high-latitudes in 2002 and more than  $+0.75\%$  at northern and less than  $-0.75\%$  at southern high-latitudes in 2006. At these latitude ranges, the sampling error temporal extent seems to be broader for dry pressure as well as the penetration depth into lower altitudes (15 km to 20 km for dry pressure as compared to 20 km to 25 km for refractivity) deeper than for refractivity.

### Dry Sampling Error

A further aspect of the sampling error by utilizing the RO technique is the dry sampling error which is most prominent in the tropical troposphere. This special kind of sampling error was already mentioned by *Foelsche et al.* (2006) and discussed in *Foelsche et al.* (2007a) and will only be discussed very briefly here.

The microwave GPS signals penetrate deeply into the atmosphere resulting in data even for cloudy parts, which marks one of the many advantages of the RO sounding method. However, if the atmosphere gets too humid signals are lost by the satellite receiver and profiles for these wet conditions stop at high altitudes whereas for drier parts of the atmosphere signals are lost much later, i. e., at lower altitudes. Not only does the receiver lose track of the signal in exceptionally wet atmospheric conditions but the geometric optics retrieval system stops processing these profiles earlier.

This intrinsic feature of the RO method leads to a “dry sampling” at lower altitudes. Dry sampling is realized by the fact that the dry sampled refractivity is smaller than the “real world” humid refractivity would be. Eventually, when converting the dry sampled refractivity into dry temperature it ends up to be much higher compared to correctly sampled dry temperature. This effect is most pronounced at low-latitudes because of the extreme humid conditions as well as the exceptionally low sampling in this region.

Dry sampling is an intrinsic limitation of the measurement method but might be mitigated by better receivers as has been done for the COSMIC (*Rocken et al.*, 2000) and the MetOp (*Loiselet et al.*, 2000) missions. Additionally, with much larger data sets, for instance by the COSMIC mission, than that obtained by the CHAMP satellite, dry sampling will be reduced by orders of magnitude. In addition, retrieval algorithms have been developed which especially focus on retrieving the humid part of profile like the wave optics (*Gorbunov*, 2002) approach.

The sampling error is displayed in [Figure 4.23](#) as an example for season JJA 2003 by omitting the cut-off criterion. The dry sampling error in the tropical troposphere

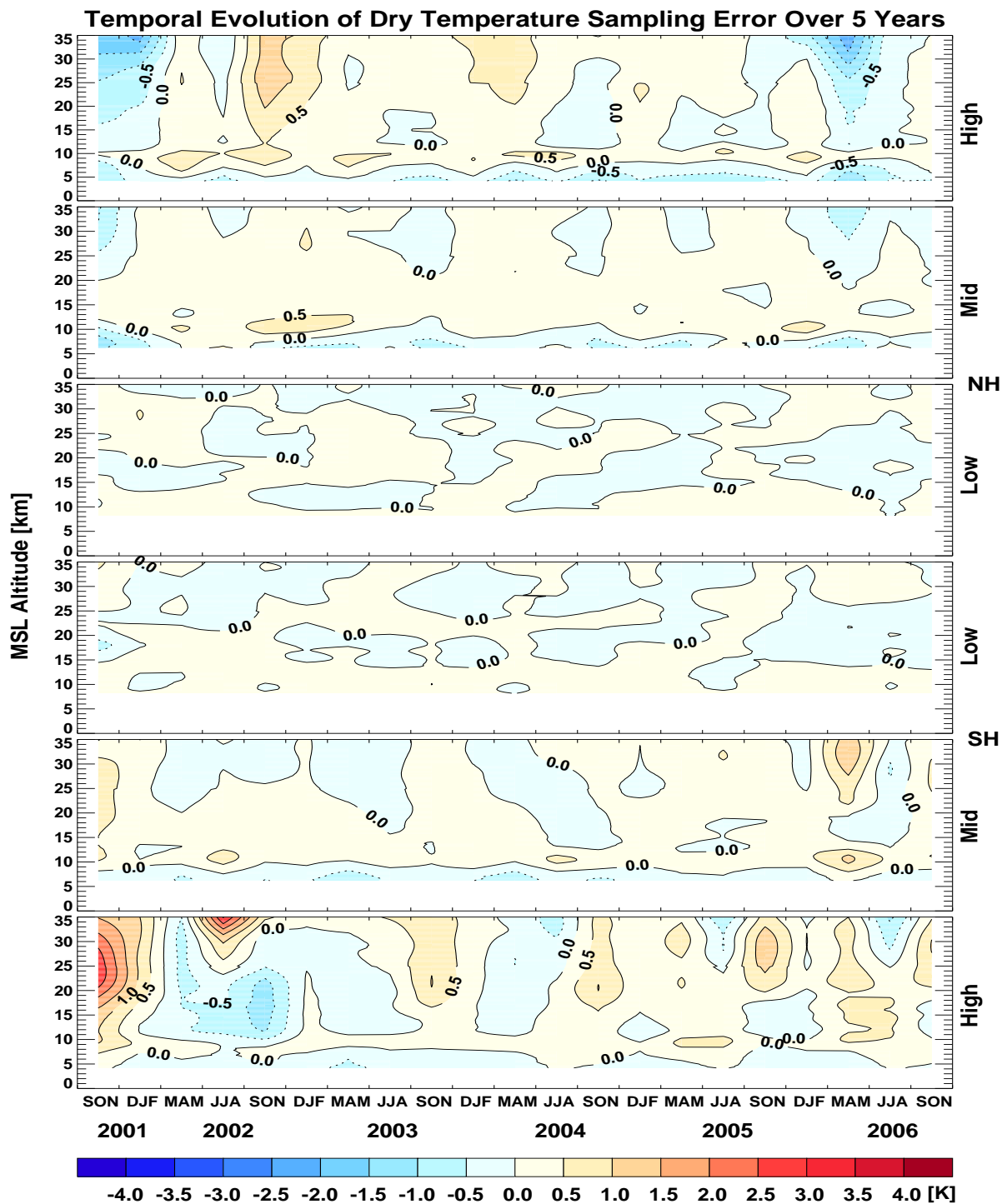


**Figure 4.20:** Temporal evolution of dry temperature sampling error [K] for the five years of available CHAMP data in six latitude ranges of northern high-, mid-, low- to southern low-, mid-, and high-latitudes from top to bottom. The altitude ranges from 0 km to 35 km and is cut off at 4 km, 6 km, and 8 km at high-, mid-, and low-latitudes, respectively.

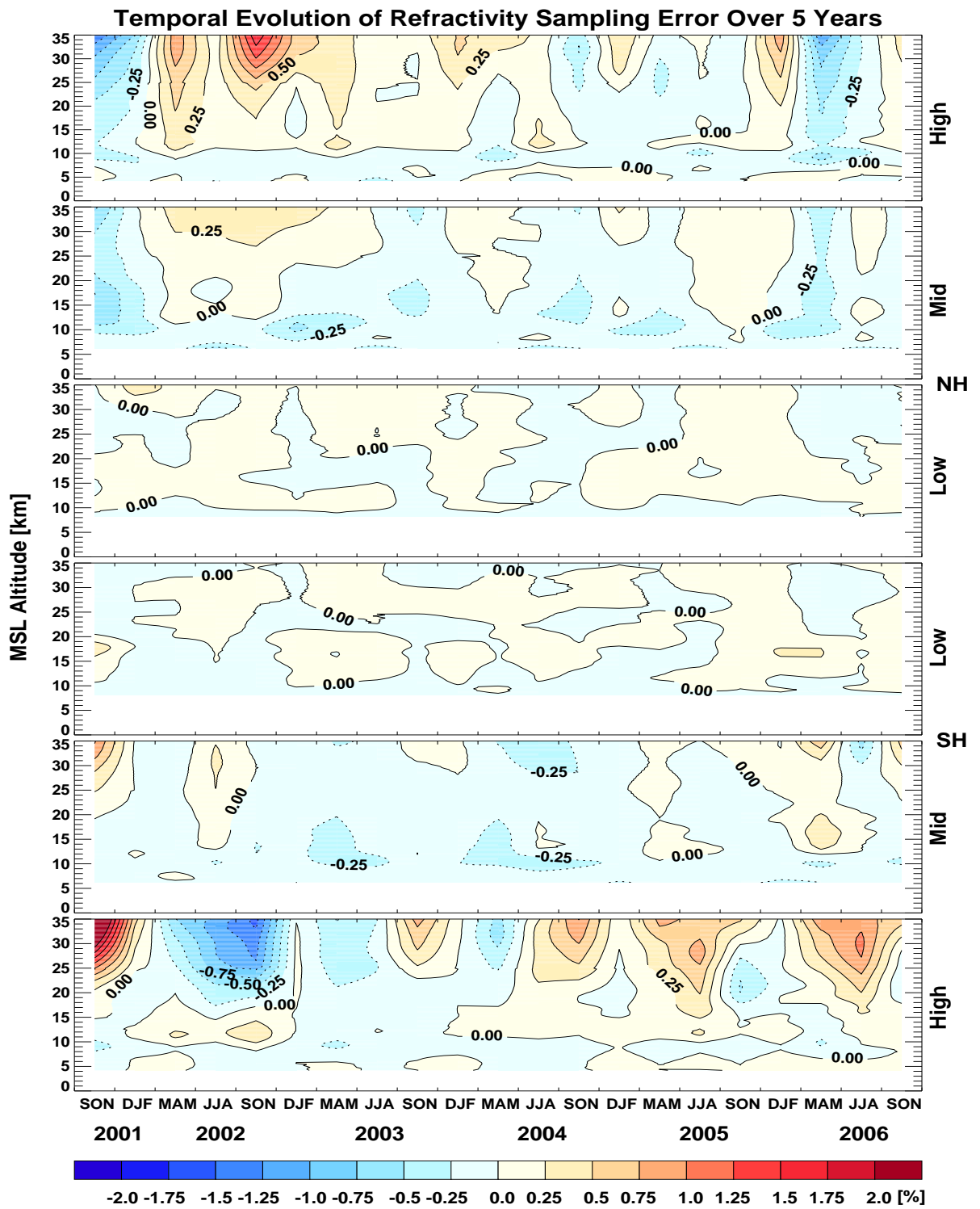


Figure 4.21: Temporal evolution of refractivity sampling error [%]; same layout as Figure 4.20.

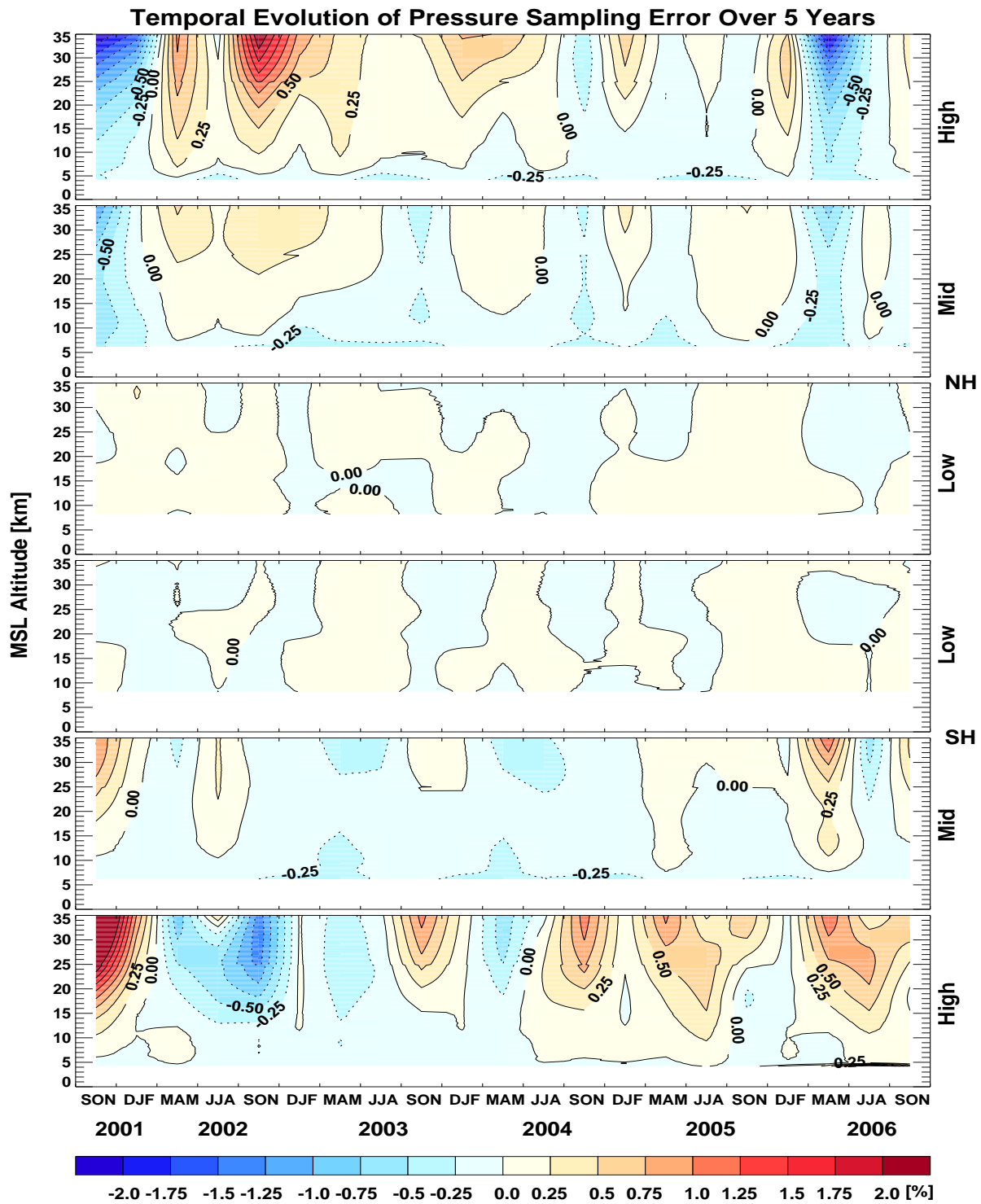
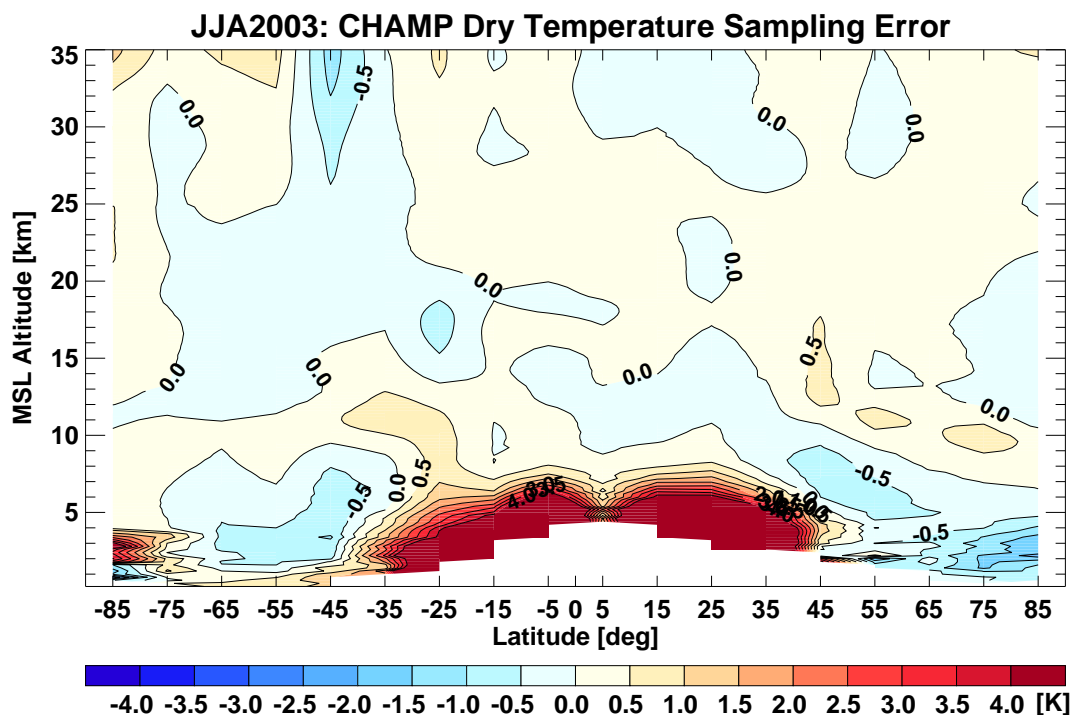


Figure 4.22: Temporal evolution of dry pressure sampling error [%]; same layout as Figure 4.20.



**Figure 4.23:** Dry temperature sampling error shown for season JJA 2003 for the complete altitude range from 0.0 km to 35 km and for all latitudes. At low tropical altitudes no CHAMP profiles penetrate down to the ground (white spaces). Huge sampling errors of more than 15 K occur in the free tropical troposphere due to a dry air biased sampling.

can clearly be distinguished which ranges even up to about  $40^\circ$  North and South. The structure of that error reflects about the mean distribution of high humidity in the free atmosphere with the horizontal resolution of RO profiles. The negative and positive sampling error at southern high latitudes results from an artifact due to the elevation of the antarctic continent. The white spaces at very low tropical altitudes reflect regions in which less than ten RO profiles per bin were recorded.

Because of the given distribution of the sampling error the cut-off criterion was introduced to blend out regions which cannot be climatologically investigated due to on the one hand the CHAMP satellite and its receiver and on the other hand the utilization of a dry air geometric optics retrieval.

# 5 Use of Climatologies in Climate Studies

In this chapter, two case studies are presented which make use of the above presented RO data and carefully developed temperature climatologies derived from the CHAMP satellite. The first study, presented in [Section 5.1](#), is aimed at a climatological investigation of the tropical tropopause region (*Borsche et al., 2007*). The variation and evolution of the lapse rate and cold point tropopause height and temperature are studied and compared to ECMWF operational analyses. By the change in both horizontal and vertical resolution of the analyses in February 2006 (*Untch et al., 2006*), the excellent quality of the RO data is impressively demonstrated.

The second case study comprises the development of an additional feature of the empirical observational model developed by *Steiner and Kirchengast (2005)* in form of an empirical temperature sampling error model which will be discussed in [Section 5.2](#). The development of a sampling error model, is important, because firstly the sampling error as such is an important quantity especially in a single-satellite mission as CHAMP, and secondly a model for using the sampling error will simplify the usage of the data set already comprising five years of data. At the WEGCENTER/UNI GRAZ, the retrieved CHAMP data is available at their web page (since Dec 2007), thus this model will complement the data set and simplify the handling of the data for less experienced users. Additionally, instead of having to download twice the amount of data (the sampling error in addition to, i. e., dry temperature), the amount of data to handle reduces significantly.

## 5.1 Tropical Tropopause Study

In this study CHAMP RO phase delay profiles were used and processed to dry temperature profiles using the CHAMPCLIM Retrieval version 2.3 (CCrv2.3) (*Borsche et al., 2006b*), as described in [Section 3.1](#). The data set comprises five years of CHAMP data from December 2001 to November 2006 divided into 20 seasons. In season JJA 2006, due to satellite problems, a lack of 37 days of CHAMP measurements from July 3rd to August 8th had occurred. This gap was filled up by data from the GRACE satellite (*Wickert et al., 2005*). The data set is comprised of 239,974 RO profiles in total including 4,881 GRACE profiles, all of which passed the quality control. Out of these, 32,736 profiles, including 692 GRACE profiles, are located within the tropical ( $15^{\circ}\text{N}$  to  $15^{\circ}\text{S}$ ) region being the geographical scope of this study.

As explained in [Section 2.2](#), the so-called dry temperature was calculated, which is directly derived from RO refractivity without need for a priori data (e. g., *Kursinski*

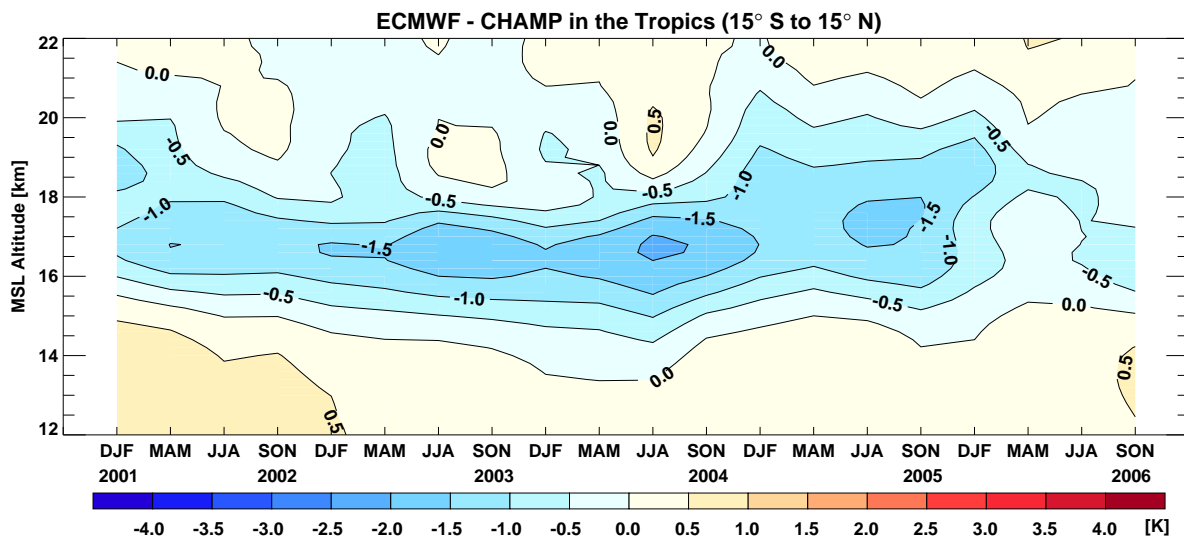


**Figure 5.1:** Temporal evolution of seasonal temperature differences between ECMWF analyses and CHAMP RO data in the tropical region DJF 010 to SON 2006.

*et al.*, 1997). In the tropics, the difference between dry and physical temperature is negligible above 14 km ( $< 0.1$  K) and can reach up to  $\sim 5$  K at 8 km height (Foelsche *et al.*, 2007a). Tropopause temperature and altitude were calculated using the WMO definition of the lapse rate tropopause (LRT) (WMO, 1957) as defined in Section 1.3.1. The LRT and CPT temperature and altitude were calculated for each CHAMP and co-located ECMWF analysis profile (see below). The altitudes of all profiles is calculated to be above mean sea level (MSL), i. e., referenced to the geoid.

As comparison data ECMWF operational analyses were used which are generated four times daily by the Integrated Forecasting System (IFS) assimilating millions of satellite, radiosonde, and ground based observational data (Untch *et al.*, 2006). Until February 2006, the IFS used 60 vertical levels and spectral representation with triangular truncation at wave number 511 (T511). Starting February 2006, the vertical resolution increased to 91 levels, effectively doubling the number of vertical levels in the region of the tropical tropopause, and the horizontal resolution increased to T799 (Untch *et al.*, 2006). By increasing the vertical and horizontal resolution it is expected that especially in the tropopause region the representation of atmospheric wave activity would be represented more accurately than before.

The calculation of the systematic ECMWF – CHAMP differences, as shown in Figure 5.1, is based on difference error statistics; in this case for the tropical region between  $15^{\circ}$ S and  $15^{\circ}$ N. For each CHAMP RO profile, a co-located ECMWF profile is used, which is computed by spatially interpolating to the CHAMP profile location using the nearest time layer of the six-hourly analyses. The sampling error (shown for context), is defined as the difference of the mean of co-located ECMWF profiles to the mean of the complete ECMWF field (Foelsche *et al.*, 2007a). In addition to ECMWF data, LRT temperature data were available for comparison from NCEP reanalyses; no full profiles

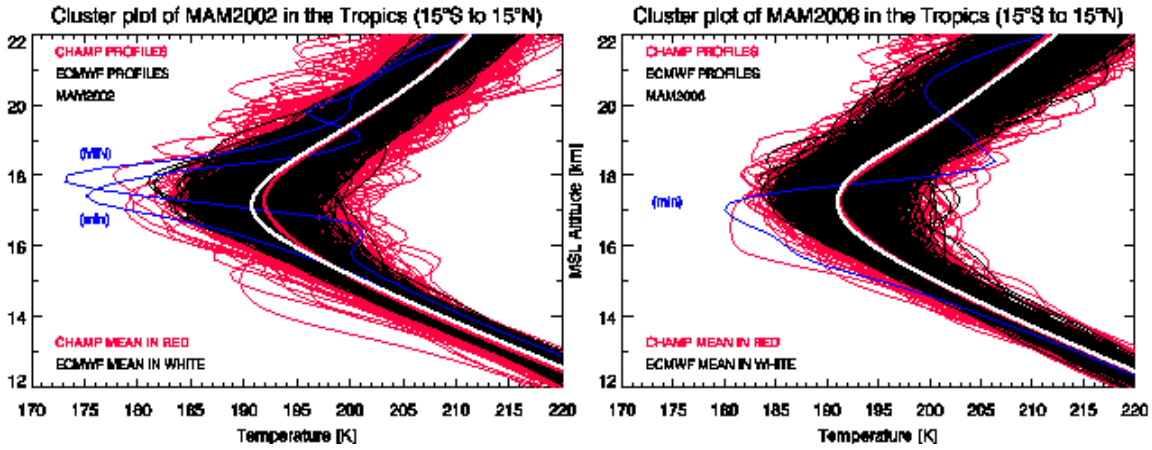


**Figure 5.2:** Cluster plot of individual CHAMP and ECMWF profiles for MAM 2002 (left) and MAM 2006 (right). Mean profiles for CHAMP and ECMWF are shown in red and white, respectively. Profiles denoted (min) represent the coldest CHAMP profiles of the season, the profile denoted (MIN) represents the coldest profile of the whole five years.

were used from NCEP as the vertical resolution in the tropopause region is too low for a scientific sound comparison.

The temporal evolution of systematic temperature differences in the tropical tropopause region between ECMWF and CHAMP seasonal mean profiles is shown from DJF 0102 to SON 2006 (winter: December, January, February to autumn: September, October, November) in [Figure 5.1](#). The differences are largest around the tropopause at about 16 km to 18 km amounting  $-1$  K to  $-2$  K throughout the whole time period except from MAM 2006 (spring: March, April, May) onwards. The varying features such as the increase of temperature difference towards JJA 2004 (summer: June, July, August) and the increased height of maximum difference in DJF 0506 point to changes in ECMWF tropical tropopause representation over the years. To closer understand the lower difference of the seasons starting MAM 2006, which were computed with the new higher-resolution ECMWF analysis data (*Untch et al., 2006*), season MAM 2002 was arbitrarily chose, which is representative of any other season previous to spring 2006, for comparison with MAM 2006.

The change in ECMWF – CHAMP temperature difference between seasons MAM 2002 and MAM 2006 is best visible looking at the single profiles of both CHAMP and ECMWF data clustered as in [Figure 5.2](#). At first, MAM 2002 is explained (left panel). Above about 14 km, individual CHAMP profiles start to increasingly deviate from the mean, representing atmospheric variability and wave activity. At the mean tropopause, the min-max deviation of individual profiles about the mean profile amounts to more than 25 K, in the stratosphere above to about 20 K. Furthermore, the CPT altitudes of individual CHAMP profiles vary considerably as a consequence of atmospheric variability. This leads to the seasonal mean CHAMP tropopause profile being somewhat smoothed around the seasonal mean CPT altitude, i. e., the profile peak is dragged towards warmer

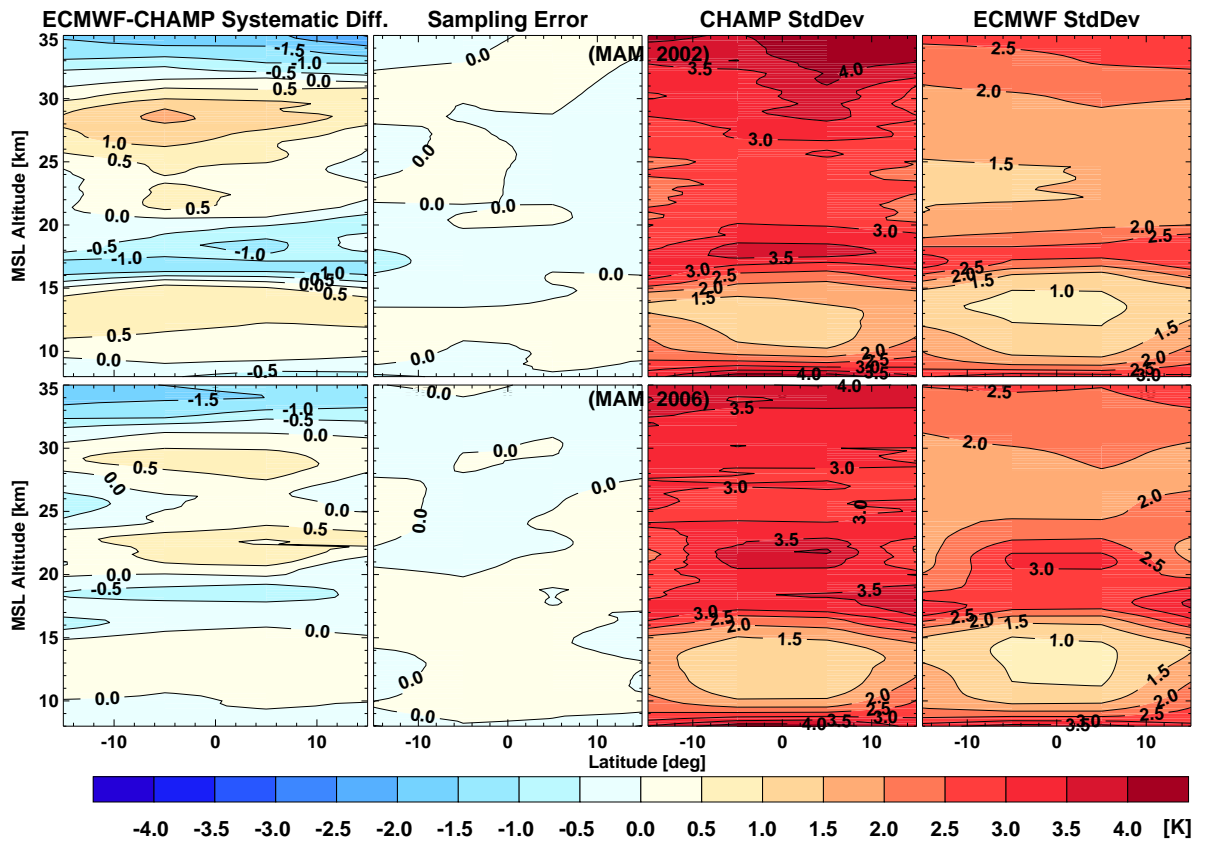


**Figure 5.3:** (left to right) Systematic difference between ECMWF analyses and CHAMP data, sampling error of CHAMP data compared to ECMWF model fields, standard deviation of CHAMP profiles, and standard deviation of ECMWF profiles. (top) MAM 2002, (bottom) MAM 2006.

temperatures. Individual ECMWF profiles, on the other hand, show rather small deviations from the mean, around 10 K or less, and also rather less variation in CPT altitude. That is why the seasonal mean ECMWF tropopause profile is in effect sharper and the seasonal mean tropopause temperature colder than for CHAMP.

Additionally, two profiles with extremely cold tropopause temperatures are shown in this panel, the coldest of the season (min) recorded April 12, 2002, reaching 175 K, and the coldest of the whole data set (MIN), respectively, recorded February 10, 2003, reaching 173 K ( $-100^{\circ}\text{C}$ ).

For MAM 2006, shown in the right panel of [Figure 5.2](#), the mean profiles of both data sets deviate significantly less than at any other season before. This is evidently achieved by allowing for enhanced variability in the ECMWF analyses due to increased vertical and horizontal resolution. As a result, atmospheric variability is much more realistically resembled in ECMWF since February 2006, reducing the difference to CHAMP measurements. Thus, the previous inability of the analyses to adequately reproduce the atmospheric variability, together with the fact that a mean of highly deviating profiles

is calculated, explains the difference between the mean CHAMP and ECMWF profiles. An important fact to be aware of is that the cold point of the mean profile is always systematically warmer than the mean of the cold point tropopause temperatures of the individual profiles, since the latter provide a genuine average of all “cold points” while the former emerges from fixed-height averages. The coldest profile of season MAM 2006 (min) reaches 180 K. Given the initial evidence that extremely cold tropical tropopauses reach at least 180 K typically in every season, and that one even reached  $-100^{\circ}\text{C}$ , a future study will more closely explore the meteorological conditions for tropopause temperatures  $< 180$  K.

Further backing the above explanations, [Figure 5.3](#) shows the systematic difference, sampling error, and CHAMP and ECMWF standard deviations (from left to right) for MAM 2002 (top) and MAM 2006 (bottom). Here, for each panel, four seasonal mean profiles were calculated in  $10^{\circ}$  latitude bins showing the latitudinal variation. The systematic difference panel confirms the strong reduction of deviations of ECMWF from CHAMP in MAM 2006. The very small sampling error for both seasons (middle left panel) reinforces that insufficient sampling by the CHAMP satellite does not play a significant role in climatological ECMWF – CHAMP differences discussed here. The depiction of standard deviations of both data sets (middle right and right panels) highlights the ECMWF quality enhancement since MAM 2006. The structure of standard deviation and the absolute amount of variability about the mean are reproduced much more accurately in MAM 2006 than in MAM 2002.

In [Figure 5.4](#) the temporal evolution of the seasonal mean LRT temperature and altitude (first two panels) of all profiles is shown over the five years of CHAMP data. Depicted are the mean values and their standard deviations (“error bars”) within each season for both the CHAMP (red) and ECMWF (blue) data set. In addition the LRT temperature of NCEP reanalyses (green) are included as publicly provided by NCEP. These latter LRT temperatures exhibit a salient offset compared to CHAMP LRT temperatures of about 4 K until end of 2004, which is consistent with the one found by [Randel et al. \(2000\)](#) when comparing to radiosonde data. The offset decreased to about 2 K from 2005 onwards.

The seasonal evolution of the CHAMP LRT data reveals known patterns (e. g., [Randel et al., 2000](#); [Seidel et al., 2001](#)). In winter, the tropical LRT temperature is lowest, reaching 189.0 K in DJF 0304 and highest in summer, reaching 194.8 K in JJA 2003. The average value of the seasonal tropical LRT temperature throughout the whole time period amounts to 191.7 K.

The second panel depicts the LRT altitude for ECMWF and CHAMP data (not publicly available for NCEP). The seasonal evolution of the LRT altitude proceeds opposite to the one of LRT temperature reaching highest in winter with 17.0 km (DJF 0304) and lowest in summer with 16.1 km (JJA 2003). The average of the seasonal LRT altitude amounts to 16.6 km. On average, the standard deviation of CHAMP LRT altitude ( $\sim 0.35$  km) is considerably higher than that of ECMWF ( $\sim 0.2$  km).

Also shown in this figure are the CPT temperature and altitude (second two panels) for both CHAMP and ECMWF data, whereas NCEP data were not publicly available. Patterns are mainly the same both for temperature and altitude compared to LRT pa-

rameters and exhibit almost the same annual variation. Lowest CPT temperatures and greatest CPT altitudes are reached in winter with the extreme values of the measured data reached in DJF 0304 amounting to 188.5 K temperature and to 17.7 km altitude. The opposite extremes of CPT parameters are reached in summer where in this case the maximum temperature is encountered in JJA 2003 with 194.2 K and the minimum altitude in JJA 2004 with 16.7 km. Thus, the extreme annual variation in LRT temperature amounts to 5.8 K compared to 5.7 K for CPT temperature, and that for LRT altitude amounts to 0.9 km compared to 1.0 km for CPT altitude. For commenting on potential tropopause parameter trends, the time record of five years is considered still to short.

The bottom two panels of [Figure 5.4](#) display the differences of the tropopause temperature and altitude in the second bottom and bottom panels, respectively. Shown are the differences of CHAMP – ECMWF LRT and CPT parameters as well as the difference of CHAMP LRT – CPT parameters.

The difference of CHAMP – ECMWF LRT and CPT temperature emphasize that ECMWF data are constantly colder than CHAMP by 0.9 K and 0.6 K on average, respectively. Maximum differences per season reach as high as 1.7 K and 1.3 K, respectively. LRT temperature differences are systematically larger than CPT temperature differences by around 1.3 K. In MAM 2006 and JJA 2006, the differences decrease and almost diminish as a result of the above described enhancement of the ECMWF data. On average, in the tropics the LRT temperature was measured by the CHAMP satellite to be 0.7 K warmer than the CPT temperature with a standard variation of a mere 0.05 K.

The differences in LRT and CPT altitude, as displayed in the bottom panel, do not exhibit such a clear picture. The difference in LRT altitude of CHAMP and ECMWF ranges around 0 km with the average being slightly negative which means that the CHAMP LRT altitude is almost that of ECMWF. This is remarkable because in their paper *Borsche et al. (2007)* stated that the CHAMP LRT altitude was systematically lower. That discrepancy is due to the fact that in this study here an enhanced version of the retrieved CHAMP data was used in which the retrieved profiles were filtered from small-scale residual noise prior to the determination of the tropopause parameters. Thus, the determination of tropopause parameters became more robust and yielded physically more consistent results.

RO measurements taken from the CHAMP satellite are currently the only ones available on a multi-year basis. Continuous measurements from the GRACE satellite mission should be available in the near future (*Wickert et al., 2005*). Two new and promising missions, the European (Meteorological Operational) MetOp satellite (*Loiselet et al., 2000*) (launched in October 2006) and the Taiwan/U.S. FORMOSAT-3/COSMIC (F-3C) constellation (*Anthes et al., 2000; Rocken et al., 2000*) (launched in April 2006), are expected to provide together several thousand RO measurements per day on an operational basis; the F-3C constellation already provides almost 2,000 profiles per day. Unfortunately, the MetOp satellite has experienced some operational ground segment problems (*von Engel et al., 2007*) which delayed RO measurements up to the present. The F-3/C mission, on the other hand, has turned out to be very successful (*Schreiner et al., 2007*), and within the first year of the mission RO measurements are obtained at almost maximum abundance.

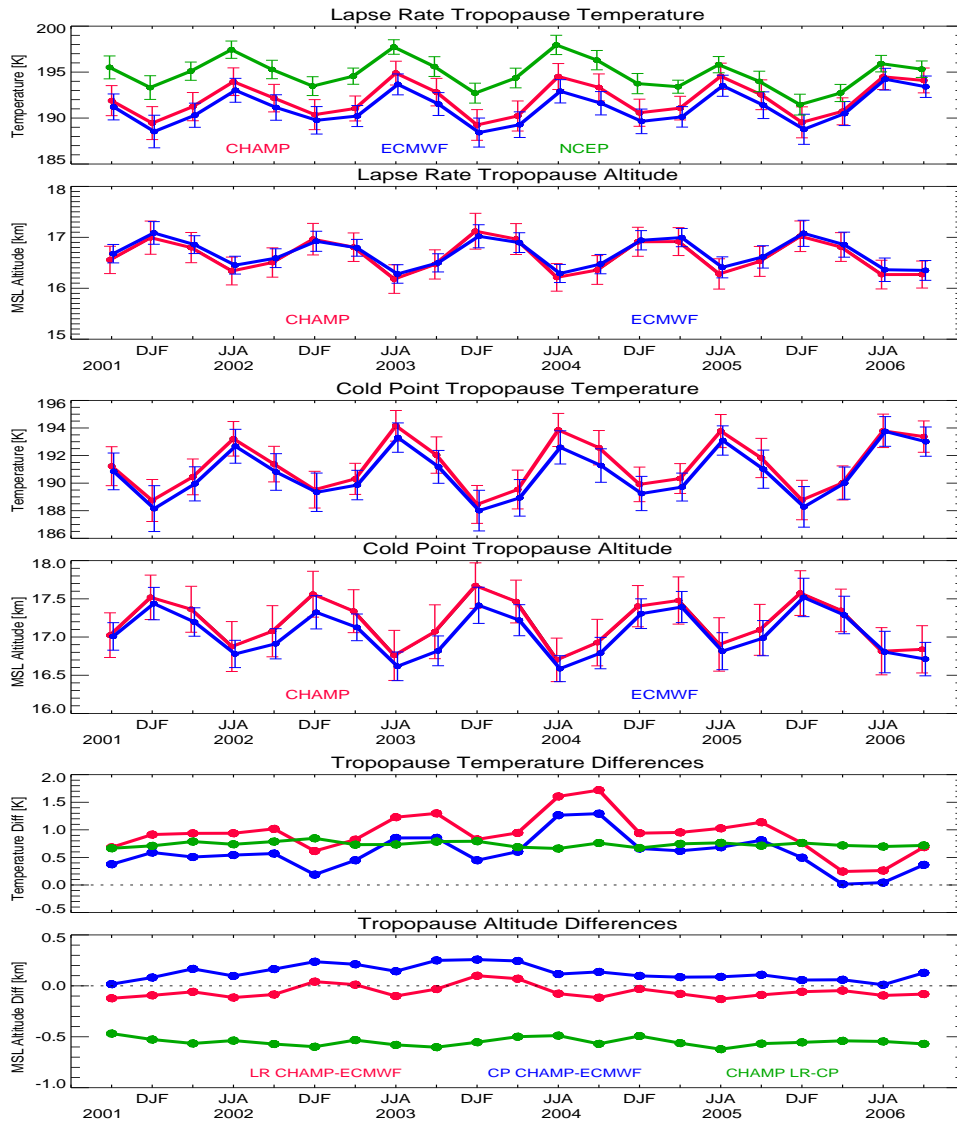


**Figure 5.4:** Upper two panels: temporal evolution of LRT temperature and altitude for CHAMP in red, ECMWF in blue, and NCEP in green (only temperature) data; middle two panels: CPT temperature and altitude for CHAMP and ECMWF data; lower two panels: differences of tropopause temperature and altitude for LR CHAMP – ECMWF in red, CP CHAMP – ECMWF in blue and CHAMP LR – CP in green.

A recent study by *Foelsche et al.* (2007b) has continued the study introduced above. In particular, the temporal evolution of tropical tropopause parameters calculated from CHAMP RO profiles has been supported by adding tropopause parameters determined from other RO mission like SAC-C, GRACE, and COSMIC. The values of all RO missions other than CHAMP are distributed temporally among the CHAMP data set with the SAC-C data within the first half, the GRACE data in July 2006 and the COSMIC

data up to the present. These additional values serve as “anchor points” with which the long term and inter-satellite stability of the RO technique can be tested. With those first results, from a climatological point of view the agreement of the different RO missions with each other turned out to be astonishingly good. Therefore, these different satellite missions will further strongly enhance the utility of RO data as accurate climate reference data sets as used in this study, and for improved operational monitoring of climate variability and change in the future.

## 5.2 Sampling Error Model for Climatologies

*Steiner and Kirchengast* (2005) have performed an error analysis for RO data based on end-to-end forward-inverse modeling using the End-to-end GNSS Occultation Performance Simulator version 4 (EGOPS) (*Kirchengast et al.*, 2002). Utilizing occultation profiles from September 15th, 1999, the Global navigation satellite system Receiver for Atmospheric Sounding (GRAS) receiver of the planned European MetOp satellite was simulated. Using an ensemble of 300 profiles, the retrieved profiles were compared to co-located “true” analysis fields of ECMWF. For all retrieved parameters including bending angle, refractivity, pressure, geopotential height, temperature, and specific humidity an empirical estimate of bias profiles as well as covariance matrices (standard deviation and covariance functions) was obtained resulting in a simple error model. The high flexibility and wide range of use of the model was shown when scaling parameters to fit CHAMP RO data were introduced, as presented in *Steiner et al.* (2006).

In this spirit, also an empirical sampling error model of dry temperature was developed and will be presented here. The sampling error was introduced in [Section 4.2.2](#) and its climatological relevance discussed. All available CHAMP data were used for this study on the basis of seasons, encompassing DJF 0102 to SON 2006. Because of too sparse data availability and uneven distribution of profiles leading to non-representatively high sampling errors, season SON 2001 was not included.

[Figure 5.5](#) displays the temporal evolution of the sampling error at all latitude ranges covering the globe (cf. [Figure 4.20](#)). The first latitude range shows northern high-latitudes (60° N to 90° N) followed by northern mid (30° N to 60° N) and low (0° N to 30° N) latitudes. The other three panels commence in opposite order starting at southern low to mid and high-latitudes. Each panel ranges in altitude from 0 km to 40 km as opposed to [Figure 4.20](#) because to fully describe the altitude range up to 35 km the sampling error model reaches up to 40 km. Furthermore, a closer look at the sampling error and its variation will be given here so the legend was changed to a finer stepping. According to the cut-off criterion introduced in [Section 4.1](#), data is shown only above the altitude of the dry sampling error (for a detailed discussion of the dry sampling error see [Section 4.2.2](#)): between 8 km to 40 km, 6 km to 40 km, and 4 km to 40 km at low-, mid-, and high-latitudes, respectively.

The temporal evolution of dry temperature sampling error does not exhibit any pattern, as does for example the dry temperature systematic difference (cf. [Section 4.2.2](#)). The temporal evolution changes quite randomly and varies around  $\pm 0.2\text{K}$  at low-latitudes. At mid-latitudes the variation is greater and does not exceed  $\pm 0.6\text{K}$  most

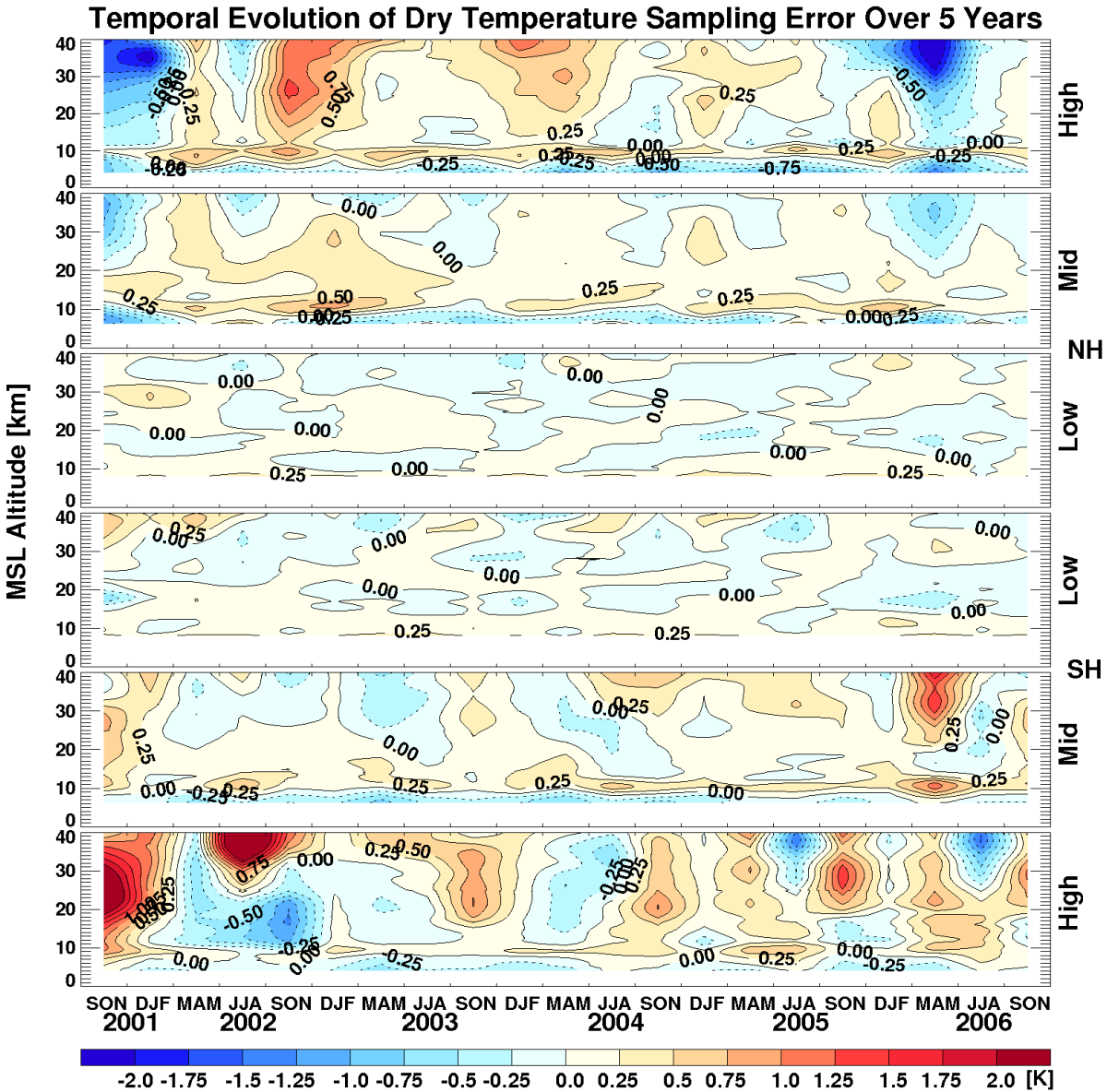


**Figure 5.5:** Temporal evolution of the sampling error starting in fall season 2001 up to fall season 2006 in six latitude ranges (refined view compared to [Figure 4.20](#)).

of the time. However, in MAM 2006 the sampling error passes this value and reaches as high as +1.5 K at southern mid-latitudes and lower than  $-0.75$  K at northern mid-latitudes. At high-latitudes the variations are much greater surpassing the limits of the color bar. To name only the two most outstanding occasions, in JJA 2002 between 30 km to 40 km the sampling error reaches in the most southern bin 6.4 K which results in an average for the southern high-latitudes of 4.0 K at that particular altitude level; and in MAM 2006 also between 30 km to 40 km at northern high-latitudes the sampling error reaches on average  $-2.8$  K.

Because of these irregular variations and missing patterns in the evolution of the sampling error it turned out to be challenging to condense the characteristics of the sampling error into a simplified model. At first, to look at the same evolution with different eyes, [Figure 5.6](#) illustrates what are herein called the systematic and statistical errors at different latitude ranges. From top to bottom, the sampling error is shown for the whole globe, the low-, mid-, and high-latitudes, respectively. From left to right, the ranges are divided into global, the NH and SH, respectively.

The systematic error profile as shown here is defined as the mean of all sampling error profiles (sampling error as a function of altitude) belonging to a given latitude bin or range. For example, the panel denoted “Global” is made up of 20 (number of seasons) times 18 (number of  $10^\circ$  latitude bins) equals 360 profiles. Consequently, the systematic error profile gives information about whether there are any “systematic” deviations of the sampling error throughout the whole period. Prominent such features can be found at mid-latitudes at the altitude of the tropopause between 10 km and 12 km where the sampling error amounts to around 0.3 K at both the NH and SH.

The statistical error profile is defined here as the standard deviation of all profiles contributing to a specific systematic error. For the “Global” panel, for example, the statistical error profile increases continuously with altitude to up to 0.9 K above 35 km while the systematic error profile stays constantly near zero at all altitudes above 12 km. That indicates high variability of the sampling error throughout the seasons which in turn renders the average of zero insignificant.

Not shown here are the results of the sampling error statistics in which each season was examined separately because no season is distinctly different from the other. That allowed for the above shown averaging over the whole time period. However, the average of three latitude bins ( $10^\circ$ ) to a latitude range ( $30^\circ$ ) might be too broad which suppresses latitudinal variation. In [Figure 5.7](#) sampling error statistics are shown for low- and mid-latitudes in  $10^\circ$  latitude steps but averaged over both hemispheres. Each panel thus includes 20 profiles which is a sufficient amount for statistically significant conclusions. High-latitudes were left out of the analysis because of the very high and random inter-seasonal variability occurring there, preventing construction of a simplified model at high-latitudes.

By splitting the statistics up into hemispherically averaged  $10^\circ$  latitude bins, they provide a different picture than before when averaged over a latitude range of  $30^\circ$ . Instead of the systematic error profile constantly increasing from a low value at around the equator to a high value at higher latitudes, as implied by the broader averaged statistics ([Figure 5.6](#)), the systematic error profile now exhibits even more distinct features. For example, the positive systematic sampling error at the altitude range of the tropopause increases at an almost constant rate throughout all panels except for the third one ( $20^\circ$  to  $30^\circ$ , subtropics), where it has an opposite sign, is centered at a higher altitude, and is broadened compared to the other latitude bins. Furthermore, at  $30^\circ$  to  $40^\circ$  the systematic sampling error profile starts to increase in the upper troposphere and lower stratosphere (UTLS) region and reaches about 0.3 K between 15 km and 20 km at  $40^\circ$  to  $50^\circ$ . However, even that feature changes again in the last latitude bin of  $50^\circ$  to  $60^\circ$  where the systematic sampling error profile amounts to zero above the tropopause and then increases constantly with altitude.

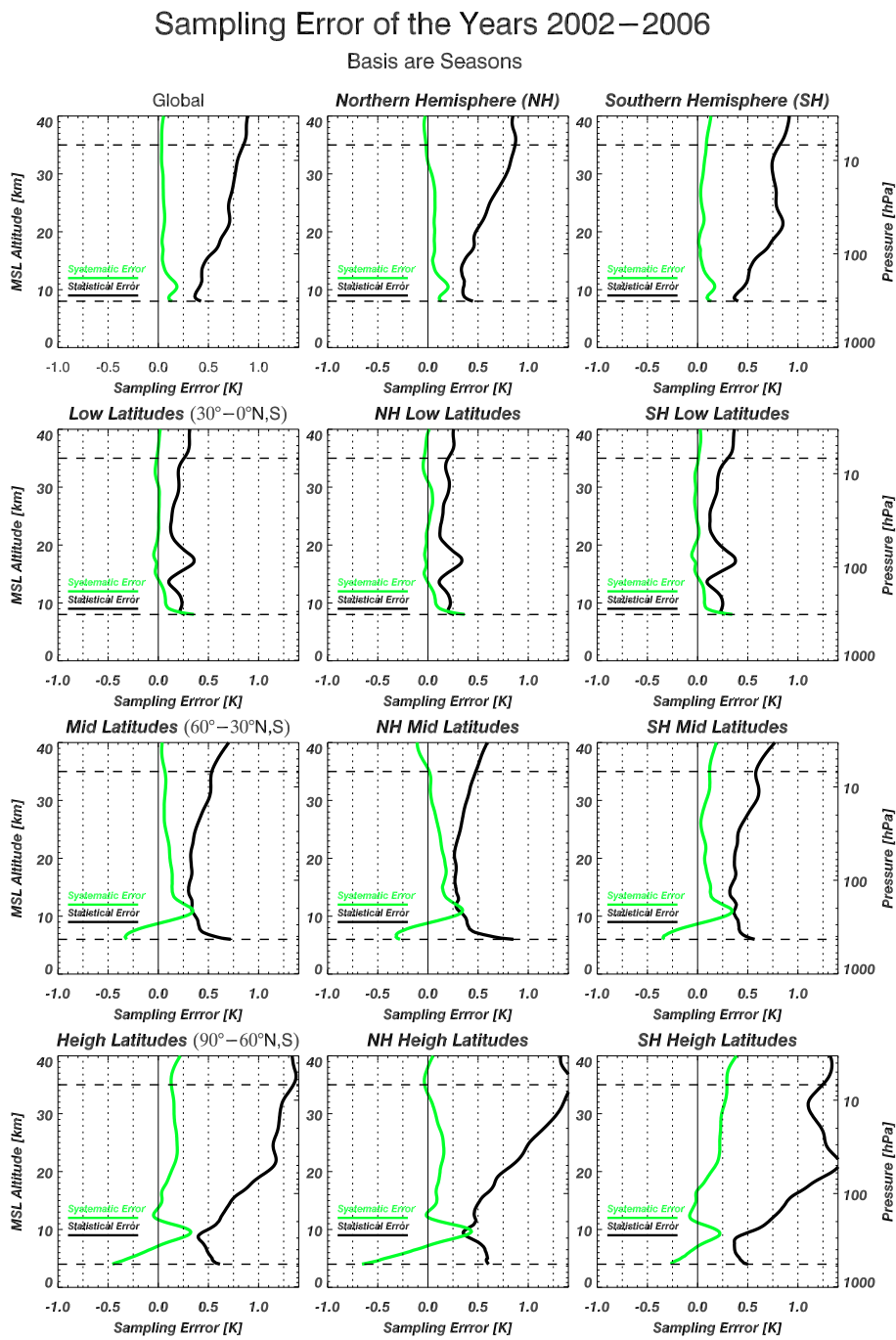


**Figure 5.6:** Sampling error statistics at global, low-, mid-, and high-latitudes displaying the systematic (green) and statistical (black) sampling error for the complete time period of 20 seasons from DJF 0102 to SON6.

## Sampling Error of the Years 2002–2006

Basis are Seasons

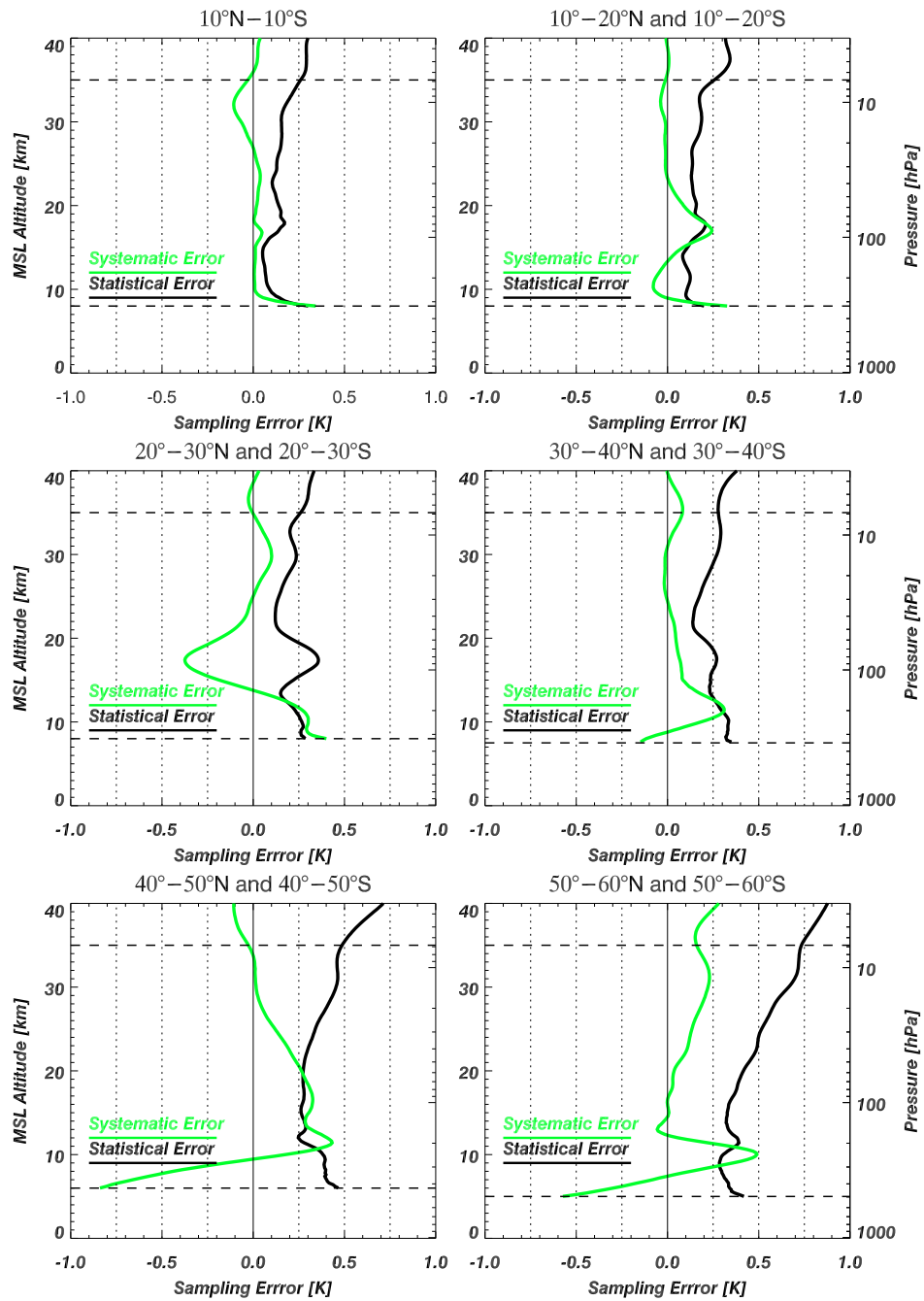


**Figure 5.7:** Sampling error statistics in  $10^\circ$  latitudes ranges at low- and mid-latitudes for the systematic and statistical sampling error.

The statistical error profile does not exhibit features as random as the systematic error profile and thus can be modeled much easier. The approach used here for modeling the statistical error profile was very much adopted from the work of *Steiner and Kirchengast (2005)*. The main aim for the development for the sampling error model was simplicity, even though the sampling error profiles turned out to behave quite randomly. Because of that, a least squares fit approach did not seem suitable. Splitting the profiles into three altitude ranges with every part obeying a different function (as pursued by *Steiner et al. (2006)*) was found a feasible option to well shadow the altitude-dependent behavior of the statistical error profiles. The function used for each of the three altitude ranges are very simple constant functions to model the course of both the systematic and statistical error profiles, as shown in [Figure 5.8](#).

The three altitude ranges of the modeled statistical error profiles range from the bottom to 10 km for the lower part, from 10 km to 20 km for the middle part, and from 20 km to 40 km for the upper part. The middle part was found to be best described by a constant value of 0.1 K in the equatorial bin (10° N to 10° S) which increases in 0.05 K steps to 0.35 K in the last latitude bin between 50° to 60°. In the bottom part below 10 km, the modeled profile follows a straight line between a mean lowermost level value and the constant value at 10 km to 20 km. In the third and upper altitude range between 20 km and 40 km, another straight line describes the modeled profile from 20 km to the uppermost level value.

In [Figure 5.8](#), the specified modeled statistical error profiles are shown as the broad red line which is depicted as an envelope around the systematic error profile. The thin green lines describe the statistical and systematic climatological error profiles for comparison to the modeled ones. The yellow lines represent the  $2\text{-}\sigma$  confidence range of the systematic sampling error, i. e., the uncertainty of the mean, and mark the envelope which separates statistically significant from insignificant systematic values.

As can be seen from [Figure 5.8](#), the systematic error profile becomes only statistically significant in the UTLS region; above its value diminishes to statistical insignificance by high variation of the single sampling error profiles. For that reason, the systematic error profile is modeled at only those altitudes in which it becomes statistically significant, otherwise it is set to zero. Except for the fifth panel in the latitude bin of 40° to 50°, the variations exhibit no fine features (which result as an artifact from averaging and do not represent the physical resolution). Therefore, for the 40° to 50° bin a 21 point (4 km) moving average was used to smooth the profile. All profiles, when crossing the barrier of the  $2\text{-}\sigma$  significance level, were linearly interpolated towards zero above this crossing height. Note, that in the last panel, between 50° and 60°, because the systematic sampling error becomes only almost as large as the  $2\text{-}\sigma$  significance level for all altitudes above 20 km and reaches this level just at around 30 km, the modeled systematic sampling error was chosen to equal zero. In [Figure 5.8](#) it is represented by the heavy blue line.

As a concluding illustration, [Figure 5.9](#) shows the modeled systematic sampling error with its corresponding  $2 - \sigma$  confidence envelope with the hemispherically averaged climatological sampling error profiles (20) of all seasons. As can be seen, this figure illustrates the presence of systematic sampling error. The most salient features identify

## Sampling Error Model for the Years 2002–2006

Basis are Seasons

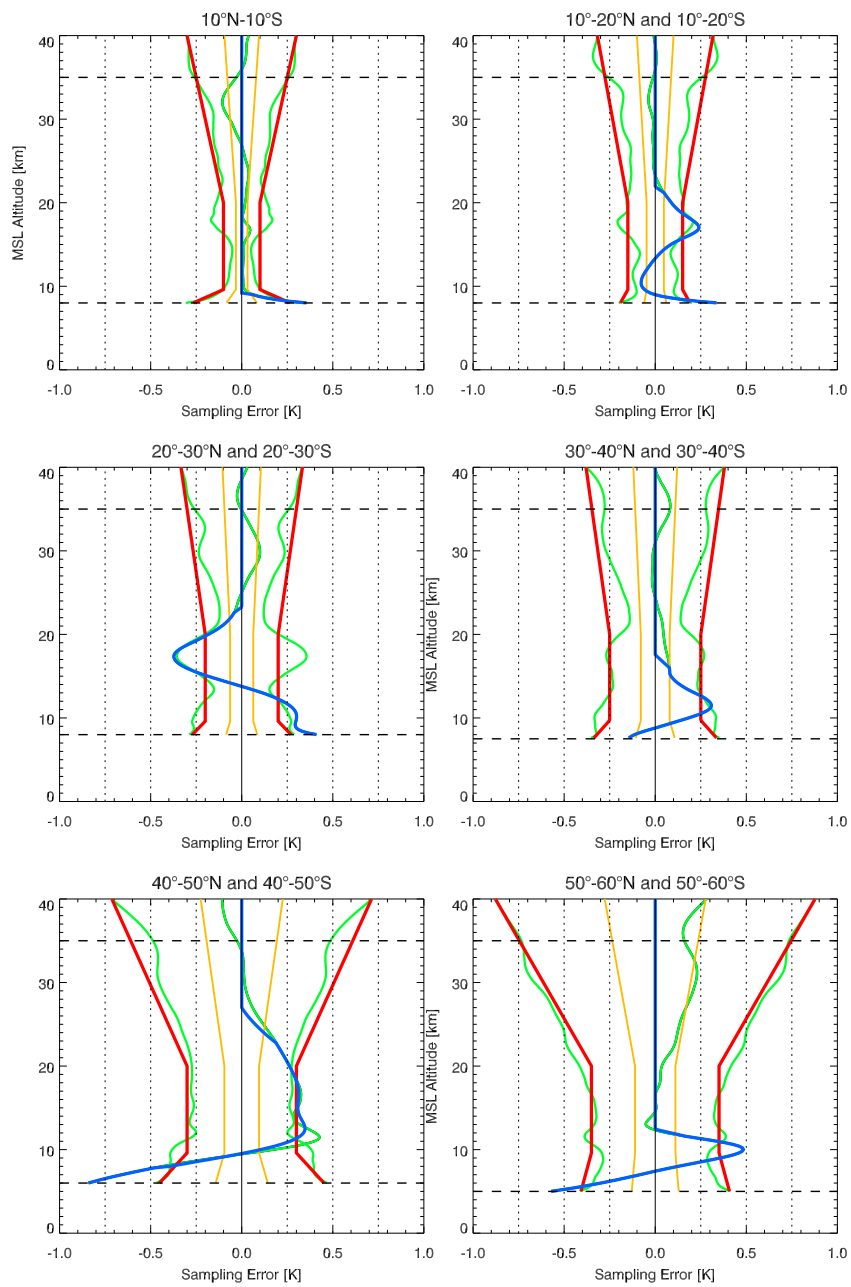


**Figure 5.8:** Sampling error model in  $10^\circ$  latitudes bins: modeled statistical error profiles (red),  $2\text{-}\sigma$  confidence envelope of the systematic error (yellow), modeled systematic error profiles (blue), and the corresponding measured systematic/statistical sampling error (green).

positive sampling errors at the altitude of the tropopause, which amount from 0.2 K to 0.5 K, except for the equatorial latitude bin where there is no deviation at any altitude above about 9 km, and except for the 20° to 30° latitude bin in which the systematic sampling error exhibits an opposite sign. At 40° to 50° a relatively large sampling error of around 0.3 K extends over a broader altitude range between 12 km and 20 km.

As noted above, the sampling error modeling at high-latitudes was excluded because of its very strong and random variations. But also at mid-latitudes the sampling error exhibits random variation which cannot easily be condensed into a model. Therefore, a matrix of six profiles was used to describe the systematic sampling error at low- and mid-latitudes, as illustrated in [Figure 5.8](#). The statistical sampling error could be described in a much simpler way. However, the top and bottom values of the profiles depend on latitude which leads to provide also the statistical error profile specification values within a separate small matrix.

In summary, Following the arguments above, the modeled systematic sampling error reproduces the measured and over 20 seasons averaged sampling error in a statistical meaningful sense and takes into account physical resolution constraints. The statistical sampling error was shown to represent a conservative estimate of the anticipated standard deviation. To conclude, for a satisfying first guess for a study within the low and mid-latitudes the user will be on the save side using the developed sampling error model of dry temperature profiles provided in the form of two matrices as systematic and statistical error profiles.

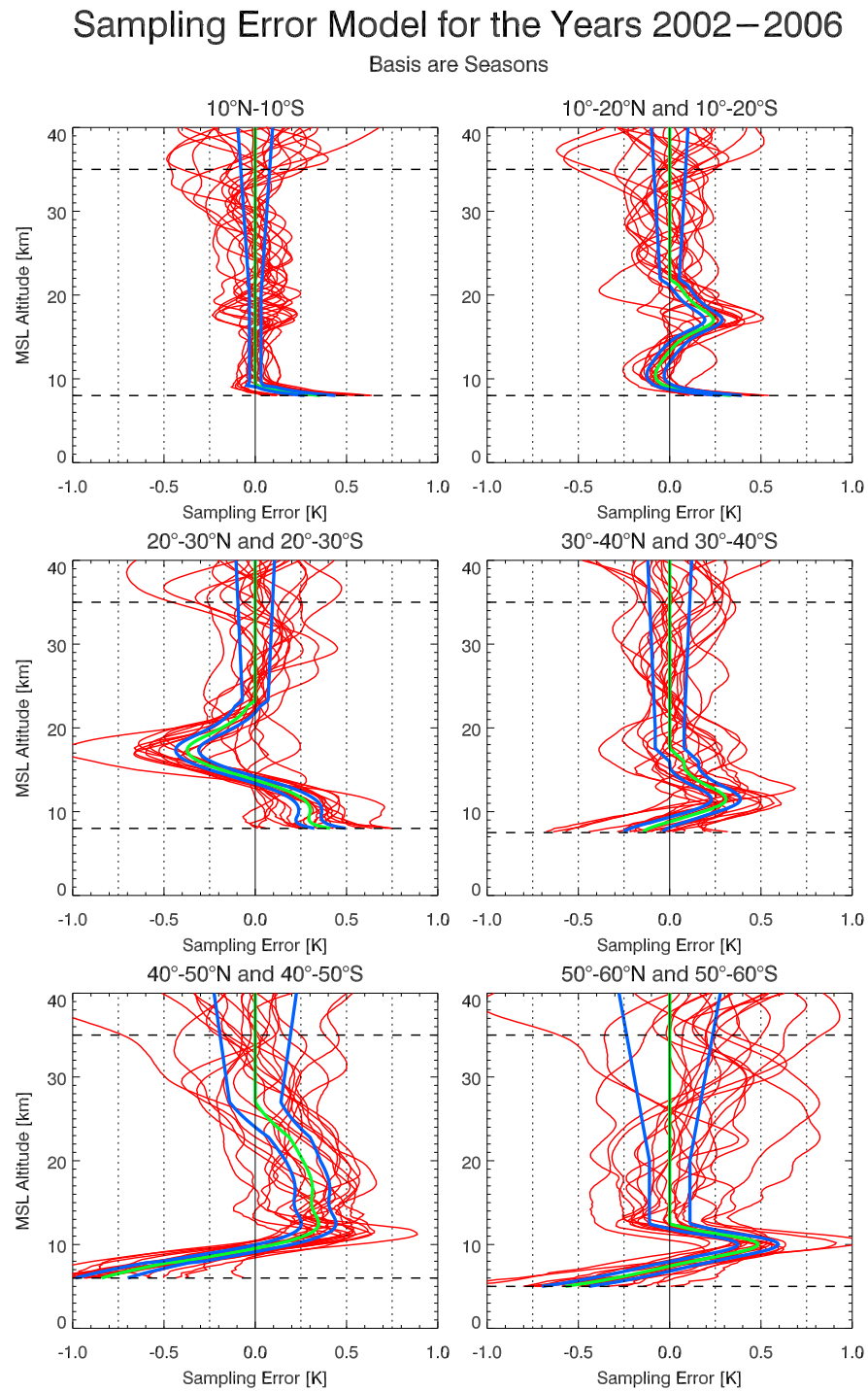


**Figure 5.9:** Sampling error model (green systematic error and blue  $2\text{-}\sigma$  confidence envelope of the it) illustrated on all hemispherically averaged climatology profiles of 20 seasons (red).

# Summary and Outlook

Radio occultation (RO) data obtained from the CHALLENGING Minisatellite Payload (CHAMP) satellite were retrieved with a dry air profiles retrieval system developed at the WEGCENTER/UNI GRAZ. The main objective of this thesis was to create global climatologies from CHAMP RO measurements. More than five years of data were analyzed covering the time span from September 2001 to November 2006. The CHAMP satellite thus provides the first opportunity to create multi-year RO based climatologies. During a period of missing CHAMP data from July 3rd, 2006 to August 8th, 2006 RO data of the Gravity Recovery And Climate Experiment (GRACE) satellite was used instead.

Much effort has been directed to creating seasonal mean climatologies for the atmospheric parameters of dry temperature, refractivity, dry pressure, and geopotential height. The climatologies are zonally averaged and divided into  $10^\circ$  latitude bands. At the bottom they are cut-off varying from 4 km at polar latitudes to 8 km in the tropics due to a dry sampling error inherent to the RO method at very low altitudes. The upper boundary of the climatologies resides at 35 km.

When comparing the obtained dry temperature climatologies against operational analyses of the European Centre for Medium-Range Weather Forecasts (ECMWF), systematic differences in most parts of the altitude and latitude range as well as throughout the seasons amount to less than 0.5 K. However, there are confined regions in which systematic differences are significantly larger. In the tropical tropopause region, the ECMWF analyses have turned out to be colder than CHAMP RO measurements by 1.0 K to 2.5 K for all seasons up to the northern hemisphere winter season (DJF) 2005/2006. Following that season the systematic difference diminished to less than 1.0 K due to a comprehensive update of the ECMWF analysis system indicating strongly this systematic difference originated mainly from the analyses.

In addition to the tropical tropopause region, two other regions within the RO climatologies were found to substantially differ in temperature compared to the ECMWF analyses. At southern high-latitudes during northern hemisphere summertime (JJA,) deviations up to JJA 2006 frequently exceed  $\pm 3$  K exhibiting an alternating structure between 10 km and 30 km (for example in JJA 2003). The climatologies show that this particular deviation varies with time and is not as pronounced in the years 2002 and 2004. In JJA 2005 the deviations are comparable to JJA 2003 again, however, the mode of the alternating structure has reversed. And in JJA 2006 the same structure of deviation emerges at high northern latitudes amounting to about  $\pm 1.5$  K whereas at southern latitudes it has essentially vanished. Finally, between 30 km and 35 km altitude the difference between the ECMWF analyses and CHAMP RO climatologies is negative for low and mid-latitudes exceeding  $-1$  K continuously throughout the five years analyzed.

Also these two structural deviations were found to mainly be inherent to the analyses.

Due to the exponential decrease with altitude, refractivity and dry pressure systematic differences were given in percent. Refractivity is inversely proportional to temperature, reflected in the fact that both dry temperature systematic differences and refractivity systematic differences amount to between  $-0.5\%$  and  $+0.75\%$ . Dry pressure systematic differences were found to be smaller amounting to between  $-0.25\%$  and  $+0.5\%$  throughout the time period and altitude range. These results confirm the general finding of this thesis that the RO based climatologies are of high accuracy and can even be used to point out discontinuities within the high-quality analyses of ECMWF.

The sampling error of the CHAMP climatologies was estimated by comparing against the ECMWF analyses. Due to the discrete and sparse CHAMP profile distribution, the measurements cannot capture the complete spatio-temporal variability of the atmosphere, even if each single profile was observed perfectly. Within this study a sampling error model was developed which estimates the climatological sampling error of the CHAMP RO measurements. Because of the large variability of the sampling error at high-latitudes the model can only be used at mid- and low-latitudes for which best-estimate sampling error profiles were derived in  $10^\circ$  latitude steps. The estimated climatological sampling error is a function of altitude and latitude with values reaching as high (and low) as  $+0.5\text{K}$  at  $50^\circ$  to  $60^\circ$  North and South (and  $-0.4\text{K}$  at  $20^\circ$  to  $30^\circ$  North and South) at tropopause altitudes.

As of today, RO data recorded by the Constellation Observing System for Meteorology, Ionosphere & Climate (COSMIC) are operationally assimilated into the ECMWF numeric weather prediction models, rendering any RO measurement not independent of the ECMWF analyses anymore. For that reason ECMWF forecast files have to be used as background data for the high-altitude initialization of the retrieved profiles instead. In order to assure more diverse comparison and evaluation in the future, reference data is aimed to be chosen additionally from the National Centers for Environmental Prediction (NCEP), who assimilate RO refractivity profiles of the COSMIC satellites operationally since May 1st, 2007.

Furthermore, the WEGCENTER/UNI GRAZ climate processing system is increasingly capable of retrieving atmospheric profiles from many other RO data like those obtained by the GPS/MET, SAC-C, COSMIC, and MetOp satellites. With all these data available, climate monitoring studies based on RO measurements allow for more detailed research, such as for inter-comparison between different satellites, for checking whether RO measurements truly are as long-term stable as expected, or for performing trend analyses. In addition, future RO based climate studies are less restricted to seasonal means but instead monthly means will become readily feasible due to much higher numbers of RO events per day which will allow for the detection of higher resolved climatic variability.

# Bibliography

- AMS (2000), AMS Glossary of Meteorology, available at: <http://amsglossary.allenpress.com/glossary> (December 2007). 1.1.2
- Anthes, R. A., C. Rocken, and Y. H. Kuo (2000), Applications of COSMIC to meteorology and climate, *Terr. Atmos. Oceanic Sci.*, 11(1), 115–156. 2.1, 2.1.2, 5.1
- Appenzeller, C., J. R. Holton, and K. H. Rosenlof (1996), Seasonal variation of mass transport across the tropopause, *J. Geophys. Res.*, 101, 15,071–15,078. 1.3.4, 1.3.4
- Baldwin, M. P., L. J. Gray, T. J. Dunkerton, K. Hamilton, P. H. Haynes, W. J. Randel, J. R. Holton, M. J. Alexander, I. Hirota, T. Horinouchi, D. B. A. Jones, J. S. Kinnersley, C. Marquardt, K. Sato, and M. Takahashi (2001), The Quasi-Biennial Oscillation, *Rev. Geophys.*, 39(2), 179–229. 4.1.1
- Bischoff, A., P. O. Canziani, and E. Yuchechechen (2007), The tropopause at southern extratropical latitudes: Argentine operational rawinsonde climatology, *Int. J. Climatol.*, 27(2), 189–209, doi: 10.1002/joc.1385. 1.3.2, 1.3.4
- Bjerknes, J., and E. Palmén (1937), Investigation of selected European cyclones by means of serial ascents, *Geophys. Publ.*, 12, 1–62. 1.3.2
- Borsche, M., U. Foelsche, A. K. Steiner, A. Gobiet, B. C. Lackner, B. Pirscher, and G. Kirchengast (2006a), Processing System for Provision of CHAMP Radio Occultation Based Climatologies, *Tech. Rep. for FFG-ALR No 1/2006*, Wegener Center for Climate and Global Change (WegCenter), University of Graz, Graz, Austria. 3, 3.1.1
- Borsche, M., A. Gobiet, A. K. Steiner, U. Foelsche, G. Kirchengast, T. Schmidt, and J. Wickert (2006b), Pre-operational retrieval of radio occultation based climatologies, in *Atmosphere and Climate: Studies by Occultation Methods*, edited by U. Foelsche, G. Kirchengast, and A. Steiner, pp. 315–323, Springer Verlag, Berlin, Heidelberg, doi: 10.1007/3-540-34121-8\_26. 3, 5.1
- Borsche, M., G. Kirchengast, and U. Foelsche (2007), Tropical tropopause climatology as observed with radio occultation measurements from CHAMP compared to ECMWF and NCEP analyses, *Geophys. Res. Lett.*, 34, L03,702, doi: 10.1029/GL027918. 1.3.3, 4.2.1, 4.2.1, 5, 5.1
- Brewer, A. M. (1949), Evidence for a world circulation provided by the measurements of helium and water vapor distribution in the stratosphere, *Quart. J. Roy. Meteorol. Soc.*, 175, 351–363. 1.3.4

- Chanin, M. L., and A. Hauchcorne (1981), Lidar observation of gravity and tidal waves in the stratosphere and mesosphere, *Geophys. Res. Lett.*, *86*, 9715–9721. [1.1.3](#)
- Chen, P. (1995), Isentropic cross-tropopause mass exchange in the extratropics, *J. Geophys. Res.*, *100*, 16,661–16,673. [1.3.4](#)
- Cho, S., and J.-K. Chung (2007), GPS Radio Occultation Mission in Korea Multi-Purpose Satellite KOMPSAT-5 [abstract], in *Occultations for Probing Atmosphere and Climate (OPAC-3 workshop)*, *17.09. – 21.09.2007*, University of Graz, Graz, Austria, available at: <http://www.uni-graz.at/opac3/>. [2.1.3](#)
- Christy, J. R., R. W. Spencer, and W. D. Braswell (2000), MSU Tropospheric Temperatures: Dataset Construction and Radiosonde Comparisons, *J. Atmos. Ocean. Technol.*, *17*(9), 1153–1170, doi: 10.1175/1520-0426(2000)017<1153:MTTDCA>. [1.1.1](#)
- Christy, J. R., R. W. Spencer, W. B. Norris, W. D. Braswell, and D. E. Parker (2003), Error estimates of Version 5.0 of MSU/AMSU bulk atmospheric temperatures, *J. Atmos. Ocean. Technol.*, *20*(5), 613–629, 10.1175/1520-0426(2003)20<613:EEOVOM>. [1.1.1](#)
- Christy, J. R., D. J. Seidel, and S. C. Sherwood (2006), What kinds of atmospheric temperature variations can the current observing systems detect and what are their strengths and limitations, both spatially and temporally?, in *Temperature Trends in the Lower Atmosphere: Steps for Understanding and Reconciling Differences.*, edited by T. R. Karl, S. J. Hassol, C. D. Miller, and W. L. Murray, A Report by the Climate Change Science Program and the Subcommittee on Global Research, Washington, DC, USA. [1.1](#), [1.1.1](#), [1.1.2](#)
- CIRA (2007), CIRA’s AMSU website, available at: <http://amsu.cira.colostate.edu/> (November 2007). [1.1.1](#)
- Defant, F., and H. Taba (1957), The three fold structure of the atmosphere and the characteristics of the tropopause, *Tellus*, *9*, 259–274. [1.3.2](#)
- Defant, F., and H. Taba (1958), The breakdown of the zonal circulation during the period January 8 to 13, 1956, the characteristics of temperature field and tropopause and its relation to the atmospheric field of motion, *Tellus*, *10*, 430–450. [1.3.2](#)
- Deser, C., A. S. Phillips, and J. W. Hurrell (2004), Pacific interdecadal climate variability: Linkages between the tropics and the north Pacific during boreal winter since 1900, *J. Climate*, *17*(16), 3109–3124, doi: 10.1175/1520-0442(2004)017<3109:PICVLB>. [1.2.1](#)
- Dunkerton, T. J., D. P. Delsi, and M. P. Baldwin (1998), Middle atmosphere cooling trend in historical rocketsonde data, *Geophys. Res. Lett.*, *25*(17), 3371–3374, doi: 10.1029/98GL02385. [1.1.3](#), [1.2.2](#)

- Durre, I., R. S. Vose, and D. B. Wuertz (2006), Overview of the integrated global radiosonde archive, *J. Climate*, *19*(1), 53–68, doi: 10.1175/JCLI3594.1. [1.1.2](#)
- ECMWF (2003), ECMWF Newsletter – No. 99, *Tech. rep.*, ECMWF, Reading, UK, available at: [http://www.ecmwf.int/publications/newsletters/chronological\\_list.html](http://www.ecmwf.int/publications/newsletters/chronological_list.html) (August 2007). [4.2.1](#), [4.2.1](#)
- ECMWF (2004), IFS Documentation CY28r1, *Tech. rep.*, ECMWF, Reading, UK, available at: <http://www.ecmwf.int/research/ifsdocs/CY28r1/index.html> (August 2007). [3.1](#), [4.2](#)
- ECMWF (2005), ECMWF Newsletter – No. 106, *Tech. rep.*, ECMWF, Reading, UK, available at: [http://www.ecmwf.int/publications/newsletters/chronological\\_list.html](http://www.ecmwf.int/publications/newsletters/chronological_list.html) (August 2007). [3.1](#)
- ECMWF (2006), ECMWF Newsletter – No. 110, *Tech. rep.*, ECMWF, Reading, UK, available at: [http://www.ecmwf.int/publications/newsletters/chronological\\_list.html](http://www.ecmwf.int/publications/newsletters/chronological_list.html) (August 2007). [3.1](#)
- Ertel, H. (1942), Ein neuer hydrodynamischer Wirbelsatz, *Meteorol. Zeitschr.*, *59*, 277–281. [1.3.1](#)
- Fischer, H., F. G. Wienhold, P. Hoor, O. Bujok, C. Schiller, M. Siegmund, M. Ambaum, H. A. Scheeren, and J. Lelieveld (2000), Tracer correlations in the northern high latitude lowermost stratosphere: Influence of cross-troposphere mass exchange, *Geophys. Res. Lett.*, *27*, 97–100. [1.3.1](#)
- Fjeldbo, G., and R. Von Eshleman (1968), The atmosphere of mars analyzed by integral inversion of the Mariner IV occultation data, *Planet. Space Sci.*, *16*(8), 1035–1055, doi: 10.1016/0032-0633(68)90020-2. [2](#)
- Fjeldbo, G., R. Von Eshleman, and A. J. Kliore (1971), The neutral atmosphere of Venus as studied with the Mariner V radio occultation experiments, *Astron. J.*, *76*, 123–140. [2.2](#)
- Foelsche, U., A. Gobiet, A. Loescher, G. Kirchengast, A. Steiner, J. Wickert, and T. Schmidt (2005), The CHAMPCLIM project: An overview, in *Earth Observation with CHAMP: Results from Three Years in Orbit*, edited by C. Reigber, H. Luehr, P. Schwintzer, and J. Wickert, pp. 615–619, Springer Verlag, Berlin. [3.1.1](#)
- Foelsche, U., A. Gobiet, A. Steiner, G. Kirchengast, M. Borsche, T. Schmidt, and J. Wickert (2006), Global climatologies based on radio occultation data: The CHAMPCLIM project, in *Atmosphere and Climate: Studies by Occultation Methods*, edited by U. Foelsche, G. Kirchengast, and A. Steiner, pp. 303–314, Springer Verlag, Heidelberg, Berlin, doi:10.1007/3-540-34121-8\_25. [3.1.1](#), [4.2.2](#)

- Foelsche, U., M. Borsche, A. K. Steiner, G. Gobiet, B. Pirscher, G. Kirchengast, J. Wickert, and T. Schmidt (2007a), Observing upper troposphere-lower stratosphere climate with radio occultation data from the CHAMP satellite, *Climate Dyn.*, doi: 10.1007/s00382-007-0337-7. [2.2](#), [3](#), [4.1.1](#), [4.2](#), [4.2.1](#), [4.2.1](#), [4.2.1](#), [4.2.1](#), [4.2.2](#), [4.2.2](#), [5.1](#), [5.1](#)
- Foelsche, U., B. Pirscher, M. Borsche, G. Kirchengast, and J. Wickert (2007b), Climate Monitoring with Radio Occultation Data: From CHAMP to FORMOSAT-3/COSMIC, *Terr. Atmos. Oceanic Sci.*, in press 2008. [4](#), [4.2.1](#), [5.1](#)
- Free, M., and D. J. Seidel (2005), Causes of differing temperature trends in radiosonde upper-air datasets, *J. Geophys. Res.*, *110*, D07,101, doi: 10.1029/2004JD005481. [1.2.1](#)
- Free, M., D. J. Seidel, J. K. Angell, J. R. Lanzante, I. Durre, and T. C. Peterson (2005), Radiosonde Atmospheric Temperature Products for Assessing Climate (RATPAC): a new data set of large-area anomaly time series, *J. Geophys. Res.*, *110*, D22,101, doi: 10.1029/2005JD006169. [1.1.2](#)
- Fu, Q., C. M. Johanson, S. Warren, and D. Seidel (2004), Contribution of stratospheric cooling to satellite-inferred tropospheric temperature trends, *Nature*, *429*, 55–58, doi: 10.1038/nature02524. [1.2.1](#)
- Gaffen, D. J., B. D. Santer, J. S. Boyle, J. R. Christy, N. E. Graham, and R. J. Ross (2000a), Multi-decadal changes in the vertical temperature structure of the tropical tropopause, *Science*, *287*, 1239–1241, doi: 10.1126/science.287.5456.1239. [1.3.5](#)
- Gaffen, D. J., M. A. Sargent, R. E. Habermann, and J. R. Lanzante (2000b), Sensitivity of tropospheric and stratospheric temperature trends to radiosonde data quality, *J. Geophys. Res.*, *13*, 1776–1796. [1.3.5](#)
- Gibson, J., A. Hernandez, P. Kallberg, E. Nomura, E. Serrano, and S. Uppala (1997), ERA Description, *ECMWF Re-Analysis Project Report Series 1*, ECMWF, Reading, U.K. [1.3.4](#)
- Gobiet, A. (2005), Radio occultation data analysis for climate change monitoring and first climatologies from CHAMP, Ph.D. thesis, Wegener Center for Climate and Global Change and Inst. for Geophysics, Astrophysics and Meteorology (IGAM)/Institute for Physics, University of Graz, Graz, Austria. [2.2](#), [2.2](#), [3](#), [3.1](#), [3.2.1](#), [4](#), [4.2.1](#)
- Gobiet, A., and G. Kirchengast (2004), Advancements of GNSS radio occultation retrieval in the upper stratosphere for optimal climate monitoring utility, *J. Geophys. Res.*, *109*, D24,110, doi: 10.1029/2004JD005117. [2.2](#), [3](#)
- Gobiet, A., A. K. Steiner, C. Retscher, U. Foelsche, and G. Kirchengast (2004), Radio Occultation Data and Algorithms Validation Based on CHAMP/GPS Data, *Tech. Rep. for ASA No. 1/2004*, Institute of Geophysics, Astrophysics and Meteorology, University of Graz, Graz, Austria. [3.1.1](#)

- Gobiet, A., U. Foelsche, A. Steiner, M. Borsche, G. Kirchengast, and J. Wickert (2005), Climatological validation of stratospheric temperatures in ECMWF operational analyses with CHAMP radio occultation data, *Geophys. Res. Lett.*, *32*, L12,806, doi: 10.1029/2005GL022617. [4.2.1](#), [4.2.1](#)
- Gobiet, A., G. Kirchengast, L. Manney, M. Borsche, C. Retscher, and G. Stiller (2007), Retrieval of temperature profiles from CHAMP for climate monitoring: intercomparison with Envisat MIPAS and GOMOS and different atmospheric analyses, *Atmos. Chem. Phys.*, *7*(13), 3519–3536. [3](#), [3.1.1](#), [4.1.1](#), [4.2.1](#), [4.2.1](#)
- Goodrum, G., K. B. Kidwell, and W. Winston (2000), NOAA KLM User's Guide: Advance Microwave Sounding Unit-A, Available at: <http://www2.ncdc.noaa.gov/docs/klm/html/c3/sec3-3.htm> (November 2007), by National Oceanic and Atmospheric Administration (NOAA). [1.1.1](#)
- Gorbunov, M. E. (2002), Canonical transform method for processing radio occultation data in the lower troposphere, *Radio Sciences*, *37*(2), 1076, doi: 10.1029/2000RS002592. [4.2.2](#)
- Grody, N. C., K. Y. Vinnikov, M. D. Golberg, J. T. Sullivan, and J. D. Tarpley (2004), Calibration of multi-satellite observations for climatic studies: Microwave Sounding Unit (MSU), *J. Geophys. Res.*, *109*, D24,104, doi: 10.1029/2004JD005079. [1.1.1](#)
- Hajj, G., E. Kursinski, L. Romans, W. Bertinger, and S. Leroy (2002), A technical description of atmospheric sounding by GPS occultation, *J. Atmos. Solar-Terr. Phys.*, *64*, 451–469. [2.2](#), [2.1](#), [2.3.1](#)
- Hajj, G. A., C. O. Ao, B. A. Iijima, and D. Kuang (2004), CHAMP and SAC-C atmospheric occultation results and intercomparisons, *J. Geophys. Res.*, *109*, D06,109, doi: 10.1029/2003JD003909. [2.1.2](#), [2.3.1](#)
- Hauchcorne, A., M. L. Chanin, and P. Keckhut (1991), Climatology and trends of the middle atmospheric temperature (33–87 km) as seen by Rayleigh Lidar over the south of France, *J. Geophys. Res.*, *96*(D8), 15,297–15,309. [1.1.3](#), [1.2.2](#)
- Healy, S. (2007), Operational assimilation of GPS radio occultation measurements at ECMWF, *Newsletter*, *111*, 6–10. [2.1.2](#), [3.1](#)
- Healy, S. B., and J. R. Eyre (2000), Retrieving temperature, water vapour and surface pressure information from refractive index profiles derived by radio occultation: A simulation study, *Quart. J. Roy. Meteorol. Soc.*, *126*, 1661–1683. [2.2](#)
- Highwood, E. J., and B. J. Hoskins (1998), The tropical tropopause, *Quart. J. Roy. Meteorol. Soc.*, *124*, 1579–1604. [1.3.1](#)
- Hoerling, M. P., T. K. Schaak, and A. J. Lenzen (1991), Global objective tropopause analysis, *Mon. Weather Rev.*, *119*, 1816–1831. [1.3.3](#)

- Hoinka, K. P. (1997), The tropopause: Discovery, definition and demarcation, *Meteorol. Z., N.F.*, *6*, 281–303. [1.3.1](#)
- Hoinka, K. P. (1998), Statistics of the global tropopause pressure, *Mon. Weather Rev.*, *126*, 3303–3325. [1.3.1](#), [1.3.1](#), [1.3.3](#), [1.3.5](#)
- Hoinka, K. P. (1999), Temperature, humidity, and wind at the global tropopause, *Mon. Weather Rev.*, *127*, 2248–2265. [1.3.3](#), [1.3.5](#)
- Holton, J. R., M. E. Haynes, A. R. McIntyre, R. B. Douglass, B. Rood, R., and L. Phister (1995), Stratosphere-troposphere exchange, *Rev. Geophys.*, *43*, 27–35. [1.3.1](#), [1.3.4](#), [1.10](#), [1.11](#), [1.3.4](#)
- Hoor, P., H. Fischer, L. Lange, J. Lelieveld, and D. Brunner (2002), Seasonal variations of a mixing layer in the lowermost stratosphere as identified by the CO–O<sub>3</sub> correlation from in situ measurements, *J. Geophys. Res.*, *107*, 4044–4055, doi: 10.1029/2000JD000289. [1.3.1](#)
- Hoskins, B. J. (1991), Towards a PV-theta view of the general circulation, *Tellus*, *43*, 27–35. [1.3.1](#), [1.3.4](#)
- James, P., A. Stohl, C. Forster, S. Eckhardt, P. Seibert, and A. Frank (2003a), A 15-year climatology of stratosphere-troposphere exchange with a Lagrangian particle dispersion model: 1. Methodology and validation, *J. Geophys. Res.*, *108*, 8519, doi: 10.1029/2002JD002637. [1.3.4](#)
- James, P., A. Stohl, C. Forster, S. Eckhardt, P. Seibert, and A. Frank (2003b), A 15-year climatology of stratosphere-troposphere exchange with a Lagrangian particle dispersion model: 2. Mean climate and seasonal variability, *J. Geophys. Res.*, *108*, 8522, doi: 10.1029/2002JD002639. [1.3.4](#)
- Joeckel, P., C. A. M. Brenninkmeijer, M. G. Lawrence, A. B. M. Jeurken, and P. F. J. v. Velthoven (2002), Evaluation of stratosphere-troposphere exchange and the hydroxyl radical distribution in three-dimensional global atmospheric models using observations of cosmogenic <sup>14</sup>CO, *J. Geophys. Res.*, *107*, 4446–4467, doi: 10.1029/2001JD001324. [1.3.1](#)
- Johanson, C. M., and Q. Fu (2006), Robustness of Tropospheric Temperature Trends from MSU Channels 2 and 4, *J. Climate*, *19*(17), 4234–4242, doi: 10.1175/JCLI3866.1. [1.2.1](#)
- Kalney, M., and et al. (1996), The NCEP/NCAR 40-year reanalysis project, *Bull. Amer. Meteorol. Soc.*, *77*(3), 437–471, doi: 10.1175/1520-0477(1996)077<0437:TNYRP>. [1.3.5](#)

- Karl, T. R., S. H. Hassol, C. D. Miller, and W. L. Murray (Eds.) (2006), *Temperature Trends in the Lower Atmosphere: Steps for Understanding and Reconciling Differences*, A Report by the Climate Change Science Program and the Subcommittee on Global Change Research, Washington, DC. **1, 1.1, 1.1.1, 1.1, 1.2.1, 1.2.1, 1.3.5**
- Keckhut, P., A. Hauchcorne, and M. L. Chanin (1993), A Critical Review of the Database Acquired for the Long-Term Surveillance of the Middle Atmosphere by the French Rayleigh Lidars, *J. Atmos. Ocean. Technol.*, *10*(6), 850—867, doi: 10.1175/1520-0426(1993)010<0850:ACROTD>2.0.CO;2. **1.1.3**
- Keckhut, P., A. Hauchcorne, and M. L. Chanin (1995), Midlatitude long-term variability of the middle atmosphere: Trends and cyclic and episodic changes, *J. Geophys. Res.*, *100*(D9), 18,887–18,897, doi: 10.1029/95JD01387. **1.1.3, 1.2.2, 1.4**
- Keckhut, P., F. J. Schmidlin, A. Hauchecorne, and M. L. Chanin (1999), Stratospheric and mesospheric cooling trend estimates from U.S. rocketsondes at low latitudes (8°S–34°N), taking into account instrumental changes and natural variability, *J. Atmos. Solar-Terr. Phys.*, *61*(6), 447–459, doi: 10.1016/S1364-6826(98)00139-4. **1.1.3, 1.2.2, 1.5**
- Kirchengast, G., and S. Schweitzer (2007), ACCURATE LEO-LEO infrared laser occultation initial assessment: Requirements, payload characteristics, scientific performance analysis, and breadboarding specifications, *Tech. Rep. for FFG-ALR No. 3/2007*, Wegener Center for Climate and Global Change (WegCenter), University of Graz, Graz, Austria. **2.1.3**
- Kirchengast, G., J. Fritzer, and J. Ramsauer (2002), End-to-end GNSS Occultation Performance Simulator Version 4 (EGOPS4) Software User Manual (Overview and Reference Manual), *Tech. Rep. for ESA/ESTEC 2/2002*, Institute of Geophysics, Astrophysics, and Meteorology, University of Graz, Graz, Austria. **5.2**
- Kirchengast, G., S. Schweitzer, J. Ramsauer, and J. Fritzer (2004), End-to-end Generic Occultation Performance Simulator Version 5 (EGOPS5) Software User Manual (Overview-, Reference-, and File Format Manual), *Tech. Rep. for ESA/ESTEC No. 6/2004*, Institute for Geophysics, Astrophysics and Meteorology, University of Graz, Graz, Austria. **3**
- Kirchengast, G., S. Schweitzer, and F. Ladstädter (2007), ACCURATE – Observing Greenhouse Gases, Isotopes, Wind, and Thermodynamic Variables by Combined MW Radio and IR Laser Occultation [abstract], in *Occultations for Probing Atmosphere and Climate (OPAC-3 workshop)*, 17.09. – 21.09.2007, University of Graz, Graz, Austria, available at: <http://www.uni-graz.at/opac3/>. **2.1.3**
- Kubicki, A., P. Keckhut, M.-L. Chanin, A. Hauchecorne, E. Lysenko, and G. S. Golitsyn (2006), Temperature trends in the middle atmosphere as seen by historical Russian rocket launchers: Part I, Volgograd (48.68°N, 44.35°E), *J. Atmos. Solar-Terr. Phys.*, *68*(10), 1075–1086, doi: 10.1016/j.jastp.2006.02.001. **1.1.3, 1.5, 1.2.2**

- Kursinski, E. R., G. A. Hajj, J. T. Schofield, R. P. Linfield, and K. R. Hardy (1997), Observing Earth's atmosphere with radio occultation measurements using the Global Positioning System, *J. Geophys. Res.*, *102*, 23,429–23,465. [2.2](#), [2.2](#), [3.2.1](#), [4.1.4](#), [5.1](#)
- Kursinski, E. R., G. A. Hajj, S. S. Leroy, and B. herman (2000), The GPS Radio Occultation Technique, *Terr. Atmos. Oceanic Sci.*, *11*(1), 53–114. [2.2](#)
- Kursinski, E. R., D. Feng, D. Flitter, G. Hajj, B. Herman, F. Romberg, S. Sydergaard, D. Ward, and T. Yunck (2004), An Active Microwave Limb Sounder for Profiling Water Vapor, Ozone, Temperature, Geopotential, Clouds, Isotopes and Stratospheric Winds, in *Occultations for Probing Atmosphere and Climate*, edited by G. Kirchengast, U. Foelsche, and A. Steiner, pp. 173–187, Springer Verlag, Berlin–Heidelberg–New York. [2.1.3](#)
- Kursinski, E. R., D. Ward, A. Otarola, B. Herman, C. Groppi, C. Walker, and M. Schein (2007), CM and MM Wavelength LEO-LEO Occultations for Climate – The ATOMMS Project [abstract], in *Occultations for Probing Atmosphere and Climate (OPAC-3 workshop)*, 17.09. – 21.09.2007, University of Graz, Graz, Austria, available at: <http://www.uni-graz.at/opac3/>. [2.1.3](#)
- Lanzante, J. R., S. A. Klein, and D. J. Seidel (2003a), Temporal homogenization of monthly radiosonde temperature data. Part I: Methodology, *J. Climate*, *16*(2), 224–240, doi: 10.1175/1520-0442(2003)016<0224:THOMRT>. [1.1.2](#)
- Lanzante, J. R., S. A. Klein, and D. J. Seidel (2003b), Temporal homogenization of monthly radiosonde temperature data. Part II: Trends, sensitivities, and MSU comparison, *J. Climate*, *16*(2), 241–262, doi: 10.1175/1520-0442(2003)016<0241:THOMRT>. [1.1.2](#)
- Lanzante, J. R., T. C. Peterson, F. J. Wentz, and K. Y. Vinnikov (2006), What do observations indicate about the change of temperatures in the atmosphere and at the surface since the advent of measuring temperatures vertically?, in *Temperature Trends in the Lower Atmosphere: Steps for Understanding and Reconciling Differences.*, edited by T. R. Karl, S. J. Hassol, C. D. Miller, and W. L. Murray, A Report by the Climate Change Science Program and the Subcommittee on Global Research, Washington, DC, USA. [1.2.1](#), [1.2.1](#)
- Larsen, G. B., S. Syndergaard, and P. Høeg (2005), Single frequency processing of Ørsted GPS radio occultation measurements, *GPS Solutions*, *9*, 144–155, doi: 10.1007/s10291-005-0142-x. [2.1.1](#)
- Leroy, S. S. (1997), Measurement of geopotential heights by GPS radio occultation, *J. Geophys. Res.*, *102*(D6), 6971–6986. [4.1.3](#), [4.1.4](#)
- Leroy, S. S., J. G. Anderson, and J. A. Dykema (2006a), Testing climate models using GPS radio occultation: A sensitivity analysis, *J. Geophys. Res.*, *111*, D17,105, doi: 10.1029/2005JD006145. [1.3.5](#), [4.1.2](#), [4.1.4](#), [4.1.4](#)

- Leroy, S. S., J. A. Dykema, and J. G. Anderson (2006b), Climate Benchmark Using GNSS Occultation, in *Atmosphere and Climate: Studies by Occultation Methods*, edited by U. Foelsche, G. Kirchengast, and A. Steiner, pp. 287–301, Springer Verlag, Heidelberg, Berlin. [2.3](#), [2.3.1](#), [4.1.2](#)
- Leroy, S. S., J. G. Anderson, and G. Ohring (2007), Climate Signal Detection Times and Constraints on Climate Benchmark Accuracy Requirements, *J. Climate*, *6*, accepted manuscript. [2.3](#)
- Lide, D. R. (Ed.) (1993), *Handbook of Chemistry and Physics*, 74<sup>th</sup> ed., CRC Press, Boca Radon, Florida, USA. [2.2](#)
- Loiselet, M., N. Stricker, Y. Menard, and J. P. Luntama (2000), GRAS – Metop’s GPS-based atmospheric sounder, *ESA Bulletin 102*, European Space Agency. [4.2.2](#), [5.1](#)
- Luntama, J. P., G. Kirchengast, M. Borsche, U. Foelsche, A. K. Steiner, S. Healy, A. v. Engeln, and C. Marquardt (2007), Prospects of the EPS GRAS Mission for Operational Atmospheric Applications, *Bull. Amer. Meteorol. Soc.*, revised manuscript 2007. [4](#), [4.2](#)
- Löscher, A., and G. Kirchengast (2008), Variational data assimilation for deriving global climate analyses from GNSS radio occultation data, *GPS Solut.*, in press. [3.2](#)
- Löscher, A., C. Retscher, L. Fusco, P. Goncalves, F. Brito, and G. Kirchengast (2008), Variational optimization for global climate analysis on ESA’s high performance computing grid, *Remote Sens. Environ.*, in press. [3.2](#)
- Mannucci, A. J., C. O. Ao, T. P. Yunck, L. E. Young, G. A. Hajj, B. A. Iijima, D. Kuang, T. K. Meehan, and S. S. Leroy (2006), Generating climate benchmark atmospheric soundings using GPS occultation data, in *Atmospheric and Environmental Remote Sensing Data Processing and Utilization II: Perspective on Calibration/Validation Initiatives and Strategies; Proceedings of the SPIE*, vol. 6301, edited by A. H. L. Huang and H. J. Bloom, p. 630108, doi: 10.1117/12.683973. [2.2](#), [2.3.1](#)
- Mears, C. A., and F. W. Wentz (2005), The effect of diurnal correction on satellite lower tropospheric temperature, *Science*, *309*, 1548–1551, doi: 10.1126/science.1114772. [1.1.1](#)
- Mears, C. A., M. C. Schabel, and F. W. Wentz (2003), A reanalysis of the MSU channel 2 tropospheric temperature record, *J. Climate*, *16*(22), 3650–3664, doi: 10.1175/1520-0442(2003)016<3650:AROTMC>. [1.1.1](#)
- Mears, C. A., C. E. Forest, R. W. Spencer, R. S. Vose, and R. W. Reynolds (2006), What is our understanding of the contribution made by observational or methodological uncertainties to the previously reported vertical differences in temperature trends?, in *Temperature Trends in the Lower Atmosphere: Steps for Understanding and Reconciling Differences.*, edited by T. R. Karl, S. J. Hassol, C. D. Miller, and W. L. Murray,

- A Report by the Climate Change Science Program and the Subcommittee on Global Research, Washington, DC, USA. [1.1.2](#)
- NASA (2007), Aqua home page, Available at: <http://aqua.nasa.gov/index.php> (November 2007). [1.1.1](#)
- Ohring, G., B. Wielicki, R. Spencer, B. Emery, and R. Datla (2005), Satellite Instrument Calibration for Measuring Global Climate Change, *Bull. Amer. Meteorol. Soc.*, *86*(9), 1303–1313, doi: 10.1175/BAMS-86-9-1303. [2.3](#), [2.3.1](#)
- Pan, L. L., W. J. Randel, B. L. Gary, M. J. Mahoney, and E. J. Hintsala (2004), Definitions and sharpness of the extratropical tropopause: A trace gas perspective, *J. Geophys. Res.*, *109*, D23,103, doi: 10.1029/2004JD004982. [1.6](#), [1.3.1](#), [1.3.2](#), [1.7](#), [1.3.2](#), [1.3.4](#)
- Parker, D. E., and D. I. Cox (1995), Towards a consistent global climatological rawinsonde data base, *Int. J. Climatol.*, *15*(5), 473–496, doi: 10.1002/joc.3370150502. [1.1.2](#)
- Perona, G., A. Sutera, M. Petitta, A. Speranza, N. Tartaglione, M. Materassi, R. Nartarpietro, S. Casotto, and F. Vespe (2007), ROSA – The Italian Radio Occultation Mission On-board the Indian OCEANSAT-2 Satellite [abstract], in *Occultations for Probing Atmosphere and Climate (OPAC-3 workshop)*, 17.09. – 21.09.2007, University of Graz, Graz, Austria, available at: <http://www.uni-graz.at/opac3/>. [2.1.3](#)
- Pirscher, B., U. Foelsche, B. C. Lackner, and G. Kirchengast (2007a), Local time influence in single-satellite radio occultation climatologies from Sun-synchronous and non-Sun-synchronous satellites, *J. Geophys. Res.*, *112*, D11,119, doi:10.1029/2006JD007934. [3.2.2](#), [4.2.2](#)
- Pirscher, B., B. C. Lackner, I. Thaler, M. Pock, U. Foelsche, A. K. Steiner, and G. Kirchengast (2007b), Initial Validation of GRAS Occultation Data from MetOp and Setup of Regional Climate Monitoring including the IPCC Land and Ocean Regions, *Tech. Rep. for FFG-ALR No. 5/2007*, Wegener Center for Climate and Global Change (WegCenter), University of Graz, Graz, Austria. [2.1.2](#)
- Plumb, R. A. (1996), A "tropical pipe" model of the stratospheric transport, *J. Geophys. Res.*, *101*, 3957–3972. [1.3.4](#)
- Prabhakara, C., J. R. Iacovacci, J.-M. Yoo, and G. Dalu (2000), Global warming: Evidence from satellite observations, *Geophys. Res. Lett.*, *27*(21), 3517–3520. [1.1.1](#)
- Ramaswamy, V., M.-L. Chanin, J. Angell, J. Barnett, D. Gaffen, M. Gelman, P. Keckhut, Y. Koshelkov, K. Labitzke, J.-J. R. Lin, A. O'Neill, J. Nash, W. Randel, R. Rood, K. S. M. Shiotani, and R. Swinbank (2001), Stratospheric Temperature Trends: Observations and Model Simulations, *Rev. Geophys.*, *39*(1), 71–122. [1.5](#), [4.1.1](#)

- Randel, W., and F. Wu (2006), Biases in Stratospheric and Tropospheric Temperature Trends Derived from Historical Radiosonde Data, *J. Climate*, *19*(10), 2094–2104, doi: 10.1175/JCLI3717.1. [1.1.2](#)
- Randel, W. J., F. Wu, and D. J. Gaffen (2000), Interannual variability of the tropical tropopause derived from radiosonde data and NCEP reanalyses, *J. Geophys. Res.*, *105*, 15,509–15,023. [1.3.3](#), [1.3.5](#), [5.1](#)
- Reed, R. J. (1955), A study of a characteristic type of upper level frontogenesis, *Quart. J. Roy. Meteorol. Soc.*, *12*, 226–237. [1.3.1](#)
- Rocken, C., R. Anthes, M. Exner, D. Hunt, S. Sokolovskiy, R. Ware, M. Gorbunov, W. S. Schreiner, D. Feng, Herman, Y.-H. Kuo, and X. Zou (1997), Verification of GPS/Met Data in the Neutral Atmosphere, *J. Geophys. Res.*, *102*(D25), 29,849–29,866. [2.1.1](#)
- Rocken, C., Y. H. Kuo, W. S. Schreiner, D. Hunt, S. Sokolovskiy, and C. McCormick (2000), COSMIC system description, *Terr. Atmos. Oceanic Sci.*, *11*(1), 21–52. [2.1.2](#), [4.2.2](#), [5.1](#)
- Santer, B. D., R. Sausen, T. M. L. Wigley, J. S. Boyle, K. AchutaRao, C. Doutriaux, J. E. Hansen, G. A. Meehl, E. Roeckner, R. Ruedy, G. Schmidt, and K. E. Taylor (2003), Behavior of tropopause height and atmospheric temperature models, reanalyses, and observations: Decadal changes, *J. Geophys. Res.*, *108*, 4002, doi: 10.1029/2002JD002258. [1.3.5](#)
- Santer, B. D., et al. (2004), Identification of anthropogenic climate change using a second-generation reanalysis, *J. Geophys. Res.*, *109*, D21,104, doi: 10.1029/2004JD005075. [1.3.3](#), [1.3.5](#)
- Scherhag, R. (1948), *Neue Methoden der Wetteranalyse und Wetterprognose*, Springer Verlag, 300 pp. [1.3.1](#)
- Schmidlin, F. J. (1981), Repeatability and measurement uncertainty of the United States meteorological rocketsonde, *J. Geophys. Res.*, *86*, 9599–9603. [1.1.3](#)
- Schmidt, T., J. Wickert, G. Beyerle, and C. Reigber (2004), Tropical tropopause parameters derived from GPS radio occultation measurements with CHAMP, *J. Geophys. Res.*, *109*, D13,105, doi: 10.1029/2004JD004566. [1.3.1](#), [1.3.3](#)
- Schmidt, T., S. Heise, J. Wickert, G. Beyerle, and C. Reigber (2005), GPS radio occultation with CHAMP and SAC-C: global monitoring of the thermal tropopause parameters, *Atmos. Chem. Phys.*, *5*(6), 1473–1488. [2.1.2](#)
- Schmidt, T., J. Wickert, G. Beyerle, R. Koenig, R. Galas, and C. Reigber (2005), The CHAMP Atmospheric Processing System for Radio Occultation Measurements, in *Earth Observation with CHAMP: Results from Three Years in Orbit*, edited by C. Reigber, H. Luehr, P. Schwintzer, and J. Wickert, pp. 597–602, Springer Verlag, Berlin. [3.1](#)

- Schmidt, T., G. Beyerle, S. Heise, J. Wickert, and M. Rothacher (2006), A climatology of multiple tropopauses derived from GPS radio occultations with CHAMP and SAC-C, *Geophys. Res. Lett.*, *33*, L04,808, doi: 10.1029/2005GL024600. [1.3.2](#), [1.3.3](#)
- Schreiner, W., C. Rocken, S. Sokolovskiy, S. Syndergaard, and D. Hunt (2007), Estimates of the precision of GPS radio occultations from the COSMIC/FORMOSAT-3 mission, *Geophys. Res. Lett.*, *34*, L04,808, doi: 10.1029/2006GL027557. [5.1](#)
- Seidel, D. J., and J. R. Lanzante (2004), An assessment of three alternatives to linear trends for characterizing global atmospheric temperature changes, *J. Geophys. Res.*, *109*, D14,108, doi: 10.1029/2003JD004414. [1.2.1](#), [1.2.1](#)
- Seidel, D. J., and W. J. Randel (2006), Variability and trends in the global tropopause estimated from radiosonde data, *J. Geophys. Res.*, *111*, D21,101, doi: 10.1029/2006JGD007363. [1.3.3](#), [1.3.5](#)
- Seidel, D. J., R. J. Ross, J. A. Angell, and G. C. Reid (2001), Climatological characteristics of the tropical tropopause as revealed by radiosondes, *J. Geophys. Res.*, *106*(D8), 7857–7878. [1.3.1](#), [1.3.3](#), [1.3.5](#), [5.1](#)
- Seidel, D. J., J. Angell, J. K. Christy, M. Free, J. R. Klein, S. A. Lanzante, C. Mears, D. Parker, M. Schabel, R. Spencer, A. Sterin, P. Thorne, and F. Wentz (2004), Uncertainty in Signals of Large-Scale Climate Variations in Radiosonde and Satellite Upper-Air Temperature Datasets, *J. Climate*, *17*(11), 2225–2240, doi: 10.1175/1520-0442(2004)017<2225:UISOLC>. [1.2.1](#)
- Sherwood, S. C., J. R. Lanzante, and C. L. Meyer (2005), Radiosonde Daytime Biases and Late-20th Century Warming, *Science*, *309*, 1556–1559, doi: DOI: 10.1126/science.1115640. [1.1.2](#)
- Simmons, A. J., and J. Gibson (2000), The ERA-40 Project Plan, *ERA-40 Project Report Series No.1*, ECMWF, Reading, U.K. [1.3.5](#)
- Smith, E. K., and S. Weintraub (1953), The constants in the equation for atmospheric refractive index at radio frequencies, *Proceedings of the Institute of Radio Engineers*, *41*(8), 1035–1037. [2.2](#), [4.1.2](#)
- Soloman, S., D. Qin, M. Manning, Z. Chen, M. Marquis, K. B. Averyt, M. Tignor, and H. L. Miller (Eds.) (2007), *Climate Change 2007: The Physical Science Basis. Contribution of Working Group I to the Fourth Assessment Report of the Intergovernmental Panel on Climate Change*, p. 996, Cambridge University Press, Cambridge, United Kingdom and New York, NY, USA. ([document](#)), [1](#)
- Spencer, R. W., and J. R. Christy (1992), Precision and radiosonde validation of satellite gridpoint temperature anomalies, part II: a tropospheric retrieval and trends during 1979–90, *J. Climate*, *5*(8), 858–866, doi: 10.1175/1520-0442(1992)005<0858:PARVOS>. [1.2.1](#)

- Spencer, R. W., J. R. Christy, and N. C. Grody (1990), Global Atmospheric Temperature Monitoring with Satellite Microwave Measurements: Method and Results 1979–1984, *J. Climate*, *3*, 1111–1128. [1.1.1](#), [1.1.1](#)
- Spencer, R. W., J. R. Christy, W. D. Braswell, and W. B. Norris (2006), Estimation of Tropospheric Temperature Trends from MSU Channels 2 and 4, *J. Atmos. Ocean. Technol.*, *23*(3), 417–423, 10.1175/JTECH1840.1. [1.1.1](#)
- Sprenger, M., and H. Wernli (2003), A northern hemispheric climatology of cross-tropopause exchange for the ERA15 time period (1979–1993), *J. Geophys. Res.*, *108*, 8521, doi:10.1029/2002JD002636. [1.3.2](#)
- Sprenger, M., M. C. Maspoli, and H. Wernli (2003), Tropopause folds and cross-tropopause exchange: A global investigation based upon ECMWF analyses for the time period March 2000 to February 2001, *J. Geophys. Res.*, *108*, 8518, doi:10.1029/2002JD002587. [1.3.4](#)
- STACCATO Team (2002), Influence of stratosphere-troposphere exchange in a changing climate on atmospheric transport and oxidation capacity, *Tech. Rep. final report, contract EVK2-CT-1999-00050*, Lehrstuhl fuer Bioklim. und Immissionsforsch., Tech. Univ. Muenchen, Munich, Germany. [1.3.4](#), [1.3.4](#)
- Steiner, A., A. Gobiet, U. Foelsche, and G. Kirchengast (2004), CHAMPCLIM-Radio occultation data analysis advancement and climate change monitoring based on the CHAMP/GPS experiment, *Tech. Rep. for ASA No. 3/2004*, Institute of Geophysics, Astrophysics and Meteorology, University of Graz, Graz, Austria. [3](#)
- Steiner, A. K., and G. Kirchengast (2005), Error analysis for GNSS radio occultation data based on ensembles of profiles from end-to-end simulations, *J. Geophys. Res.*, *110*, D15,307, doi: 10.1029/2004JD005251. [2.2](#), [5](#), [5.2](#), [5.2](#)
- Steiner, A. K., A. Loescher, and G. Kirchengast (2006), Error Characteristics of Refractivity Profiles Retrieved from CHAMP Radio Occultation Data, in *Atmosphere and Climate: Studies by Occultation Methods*, edited by U. Foelsche, G. Kirchengast, and A. Steiner, pp. 27–36, Springer Verlag, Heidelberg, Berlin, doi: 10.1007/3-540-34121-8\_3. [5.2](#), [5.2](#)
- Steiner, A. K., G. Kirchengast, M. Borsche, U. Foelsche, and T. Schoengassner (2007), A multi-year comparison of lower stratospheric temperatures from CHAMP radio occultation data with MSU/AMSU records, *J. Geophys. Res.*, *112*, D22,110, doi: 10.1029/2006JD008283. [1.2.1](#), [2.3.1](#), [4](#), [4.2.1](#)
- Stohl, A. (2001), A 1-year Lagrangian "climatology" of airstreams in the Northern Hemisphere troposphere and lowermost stratosphere, *J. Geophys. Res.*, *106*, 7263–7279. [1.3.4](#), [1.3.4](#)

- Stohl, A., et al. (2003), Stratosphere-troposphere exchange: A review, and what we have learned from STACCATO, *J. Geophys. Res.*, *108*(D12), 8516–8531, doi: 10.1029/2002JD002490. [1.3.1](#), [1.3.4](#), [1.3.4](#), [1.3.4](#), [1.12](#), [1.3.4](#)
- Swinbank, R., and A. O’Neill (1994), A stratosphere-troposphere data assimilation system, *Mon. Weather Rev.*, *122*, 686–702. [1.3.2](#), [1.3.4](#)
- Syndergaard, S. (1998), Modeling the impact of the Earth’s oblateness on the retrieval of temperature and pressure profiles from limb sounding, *J. Atmos. Solar-Terr. Phys.*, *60*(2), 171–180. [2.2](#)
- Syndergaard, S. (1999), Retrieval Analysis and Methodologies in Atmospheric Limb Sounding Using the GNSS Radio Occultation Technique, Ph.D. thesis, Danish Meteorological Institute, Copenhagen, Denmark. [2.2](#)
- Taubenheim, J., G. Entzian, and K. Berendorf (1997), Long term decrease of mesospheric temperature, 1963 – 1995, inferred from radiowave reflection heights, *Adv. Space Res.*, *20*(11), 2059–2063. [1.1.3](#), [1.2.2](#), [1.3](#)
- Thorne, P. W., D. E. Parker, J. R. Christy, and C. A. Mears (2005a), Uncertainties in Climate Trends, *Bull. Amer. Meteorol. Soc.*, *86*(10), 1437–1442, doi: 10.1175/BAMS-86-10-1437. [1](#), [1.1](#), [1.2.1](#)
- Thorne, P. W., D. E. Parker, S. F. B. Tett, P. D. Jones, M. McCarthy, H. Coleman, and P. Brohan (2005b), Revisiting radiosonde upper air temperature from 1958 to 2002, *J. Geophys. Res.*, *110*, D18,105, doi: 10.1029/2004JD005733. [1.1.2](#), [1.2.1](#)
- Tian, B., G. J. Zhang, and V. Ramanathan (2001), Heat Balance in the Pacific Warm Pool Atmosphere during TOGA COARE and CEPEX, *J. Climate*, *14*(8), 1881–1893, doi: 10.1175/1520-0442(2001)014<1881:HBTPW>. [4.1.1](#)
- Trenberth, K. E. (1990), Recent observed interdecadal climate changes in the Northern Hemisphere, *Bull. Amer. Meteorol. Soc.*, *71*, 988–993. [1.2.1](#)
- Trenberth, K. E., and J. W. Hurrell (1994), Decadal atmosphere-ocean variations in the Pacific, *Climate Dyn.*, *9*, 303–319. [1.2.1](#)
- Trenberth, K. E., P. D. Jones, P. Ambenje, R. Bojariu, D. Easterling, A. Klein Tank, D. Parker, F. Rahimzadeh, J. A. Renwick, M. Rusticucci, B. Soden, and P. Zhai (2007), Observations: Surface and atmospheric climate change, in *Climate Change 2007: The Physical Science Basis. Contribution of Working Group I to the Fourth Assessment Report of the Intergovernmental Panel on Climate Change*, edited by S. Solomon, D. Qin, M. Manning, Z. Chen, M. Marquis, K. B. Averyt, M. Tignor, and H. L. Miller, Cambridge University Press, Cambridge, United Kingdom and New York, NY, USA. [1](#), [1.1.2](#), [1.2.1](#), [1.2](#)

- Untch, A., M. Miller, M. Hortal, R. Buizza, and P. Janssen (2006), Towards a global meso-scale model: The high-resolution system T799L91 and T399L62 EPS, *Newsletter*, 108. 3.1, 4.2, 4.2.1, 5, 5.1
- Vedel, H., and M. Stendel (2003), On the direct use of GNSS refractivity measurements for climate monitoring, in *Proc 4th Oersted Science Team Conf (OIST-4)*, edited by P. Stauning et al., pp. 275–278, Danish Meteorological Institute, Copenhagen. 4.1.2
- Vinnikov, K. Y., N. C. Grody, A. Robock, R. J. Stouffer, P. D. Jones, and M. D. Goldberg (2006), Temperature trends at the surface and in the troposphere, *J. Geophys. Res.*, 111, D03,106, doi: 10.1029/2005JD006392. 1.1.1
- von Engel, A., C. Marquardt, E. O. Clerigh, Y. Andres, J.-P. Luntama, and K. B. Lauritsen (2007), GRAS on MetOp: The First Operational Radio Occultation Instrument [abstract], in *Occultations for Probing Atmosphere and Climate (OPAC-3 workshop)*, 17.09. – 21.09.2007, University of Graz, Graz, Austria, available at: <http://www.uni-graz.at/opac3/>. 2.1.2, 5.1
- Vorob'ev, V. V., and T. G. Krasil'nikova (1994), Estimation of the accuracy of the atmospheric refractive index recovery from Doppler shift measurements at frequencies used in the NAVSTAR system, *Phys. Atmos. Ocean*, 29, 602–609. 2.2
- Ware, R., C. Rocken, F. Solheim, M. Exner, W. Schreiner, R. R. Anthes, D. Feng, B. Herman, M. Gorbunov, S. Sokolovski, K. Hardy, Y.-H. Kuo, X. Zou, K. Trenberth, T. Meehan, W. Melbourne, and S. Businger (1996), GPS Sounding of the Atmosphere from Low Earth Orbit: Preliminary Results, *Bull. Amer. Meteorol. Soc.*, 77(1), 19–40, doi: 10.1175/1520-0477(1996)077<0019:GSOTAF>2.0.CO;2. 2.1.1
- Waugh, D. W. (1996), Seasonal variation of isentropic transport out of the tropical stratosphere, *J. Geophys. Res.*, 101, 4007–4023. 1.3.4
- Wei, M.-Y. (1987), A new formulation of the exchange of mass and trace constituents between the stratosphere and troposphere, *J. Atmos. Sci.*, 44, 3079–3086. 1.3.4
- Wernli, H. (1997), A Lagrangian-based analysis of extratropical cyclones, II, A detailed case study, *Quart. J. Roy. Meteorol. Soc.*, 123, 1677–1706. 1.3.4
- Wernli, H., and M. Bourqui (2002), A "1-year climatology" of (deep) cross-tropopause exchange in the extratropical Northern Hemisphere, *J. Geophys. Res.*, 107, 4021, doi: 10.1029/2001JD000812. 1.3.4, 1.3.4
- Wernli, H., and H. Davis (1997), A Lagrangian-based analysis of extratropical cyclones, *Quart. J. Roy. Meteorol. Soc.*, 123, 467–489. 1.3.4
- Wickert, J., R. Galas, G. Beyerle, R. König, and C. Reigber (2001a), GPS ground Station data for CHAMP radio occultation measurements, *Phys. Chem. Earth*, 26(6-8), 503–511. 2.2, 2.3.1

- Wickert, J., C. Reigber, G. Beyerle, R. König, T. Marquardt, C. Schmidt, L. Grunwaldt, R. Galas, T. K. Meehan, W. G. Melbourne, and K. Hocke (2001b), Atmosphere sounding by GPS radio occultation: First results from CHAMP, *Geophys. Res. Lett.*, *28*, 3263–3266. [2.1.2](#), [3.1](#)
- Wickert, J., T. Schmidt, G. Beyerle, R. König, C. Reigber, and N. Jakowski (2004), The radio occultation experiment aboard CHAMP: Operational data analysis and validation of vertical atmospheric profiles, *J. Meteorol. Soc. Jpn.*, *82*(1B), 381–395, doi: 10.2151/jmsj.2004.381. [2.1.2](#), [2.2](#), [3.1](#)
- Wickert, J., G. Beyerle, R. König, S. Heise, L. Grunwaldt, G. Michalak, C. Reigber, and T. Schmidt (2005), GPS radio occultation with CHAMP and GRACE: A first look at a new and promising satellite configuration for global atmospheric sounding, *Ann. Geophysicae*, *23*, 653–658. [2.1.2](#), [4](#), [5.1](#), [5.1](#)
- Wickert, J., G. Beyerle, S. Heise, N. Jakowski, R. König, C. Mayer, G. Michalak, M. Rothacher, T. Schmidt, and C. Viehweg (2007a), GPS radio occultation with CHAMP, GRACE, FORMOSAT-3/COSMIC and TerraSAR-X: Recent results from GFZ [abstract], in *Second FORMOSAT-3/COSMIC Data Users Workshop, 22.10. – 24.10.2007*, Boulder, Colorado U.S.A., available at: <http://www.cosmic.ucar.edu/oct2007workshop/program.html>. [2.1.2](#)
- Wickert, J., G. Michalak, T. Schmidt, G. Beyerle, C. Falck, R. Galas, S. Heise, S. Healy, C. Viehweg, F. Flechtner, L. Grunwaldt, W. Köhler, R. König, F. H. Massmann, D. Offiler, A. Rhodin, C. Reigber, M. Rothacher, and B. Tapley (2007b), GPS radio occultation: Operational sounding of the atmosphere with GRACE [abstract], in *European Geosciences Union 2007, 15.04. – 20.04.2007*, vol. 9 (08524), Vienna, Austria, sRef-ID: 1607-7962/gra/EGU2007-A-08524. [2.1.2](#)
- WMO (1957), Meteorology – A three dimensional science, *Tech. rep.*, World Meteorological Organization (WMO), Geneva, WMO Bull. 6. [1.3.1](#), [1.3.2](#), [1.3.2](#), [1.3.3](#), [3.1.1](#), [5.1](#)
- WMO (1986), Atmospheric ozone 1985, *WMO Global Ozone Res. and Monit. Proj. Rep.*, World Meteorological Organization (WMO), Geneva. [1.3.1](#), [1.3.1](#)
- WMO (1992), International Meteorological Vocabulary – WMO/OMM/BMO, *Tech. Rep. 182 (Second Edition)*, Secretariat of the World Meteorological Organization, Geneva. [1.3.1](#), [1.3.2](#)
- Yunck, T. P., C.-H. Liu, and R. Ware (2000), A History of GPS Sounding, *Terr. Atmos. Oceanic Sci.*, *11*(1), 1–20. [2](#), [2.1](#), [2.1.3](#)
- Yunck, T. P., C. C. McCormick, and C. Lenz (2007), The CICERO Project [abstract], in *Second FORMOSAT-3/COSMIC Data Users Workshop, 22.10. – 24.10.2007*, Boulder, Colorado U.S.A., available at: <http://www.cosmic.ucar.edu/oct2007workshop/program.html>. [2.1.3](#)

Zhou, C.-Z., M. D. Goldberg, Z. Cheng, N. C. Grody, J. T. Sullivan, C. Cao, and D. Tarpley (2006), Recalibration of microwave sounding unit for climate studies using simultaneous nadir overpasses, *J. Geophys. Res.*, *111*, D19,114, doi: 10.1029/2005JD006798. [1.1.1](#)

Zhou, X. L., M. A. Geller, and M. Zhang (2001), Tropical cold point tropopause characteristics derived from ECMWF reanalyses and soundings, *J. Climate*, *14* (8), 1823–1838, doi: 10.1175/1520-0442(2001)014<1823:TCPTCD>. [1.3.3](#), [1.3.5](#)



# List of Abbreviations

|           |   |
|-----------|---|
| AIRS      | Advanced Infrared Sounder   |
| AMSU      | Advanced Microwave Sounding Unit  |
| AR4       | Fourth Assessment Report (of the IPCC)  |
| CDAAC     | COSMIC Data Analysis and Archive Center   |
| CHAMP     | CHallenging Minisatellite Payload   |
| CHAMPCLIM | Radio Occultation Data Analysis Advancement and Climate Change Monitoring based on the CHAMP/GPS Experiment – research project in the Austrian Space Appl. Programme (ASAP) carried out by WEGCENTER/UNI GRAZ |
| CICERO    | Community Initiative for Continuing Earth Radio Occultation   |
| COSMIC    | Constellation Observing System for Meteorology, Ionosphere & Climate  |
| CNSES     | Compass Navigation Satellite Experimental System  |
| CNSS      | Compass Navigation Satellite System   |
| CPT       | Cold Point Tropopause   |
| DJF       | Winter season December, January, February   |
| ECMWF     | European Centre for Medium-Range Weather Forecasts  |
| EGOPS     | End-to-end GNSS Occultation Performance Simulator   |
| ENSO      | El Niño/Southern Oscillation  |
| ERA       | ECMWF Reanalyses (15 and 40 year time span)   |
| EUMETSAT  | European Organisation for the Exploitation of Meteorological Satellites   |
| GCM       | General Circulation Model   |
| GLONASS   | GLOBAL Navigation Satellite System  |
| GNSS      | Global Navigation Satellite System  |
| GFZ       | GeoForschungsZentrum Potsdam  |
| gm        | geopotential meters   |
| GRACE     | Gravity Recovery And Climate Experiment   |

---

|           |  |
|-----------|--|
| GRAS      | Global navigation satellite system Receiver for Atmospheric Sounding |
| GPS       | Global Positioning System (US)                                       |
| GPS/MET   | GPS/Meteorology  |
| HadAT2    | Hadley Centre Atmospheric Temperature Data Set Version 2             |
| HALOE     | Halogen Occultation Experiment                                       |
| IPCC      | Intergovernmental Panel on Climate Change                            |
| JJA       | Summer season June, July, August                                     |
| KOMPSAT-5 | KOrea Multi-Purpose SATellite 5                                      |
| LRT       | Lapse Rate Tropopause  |
| MAM       | Spring season March, April, May                                      |
| MetOp     | Meteorological Operational satellite                                 |
| MLS       | Microwave Limb Sounder   |
| MSL       | Mean Sea Level   |
| MSU       | Microwave Sounding Unit  |
| NAO       | North Atlantic Oscillation   |
| NASA      | National Aeronautics and Space Administration                        |
| NCAR      | National Center for Atmospheric Research                             |
| NCEP      | National Centers for Environmental Prediction                        |
| NH        | Northern Hemisphere  |
| NOAA      | National Oceanic and Atmospheric Administration                      |
| NWP       | Numerical Weather Prediction   |
| OPS       | Occultation Performance System                                       |
| QBO       | Quasi-Biennial Oscillation   |
| RATPAC    | Radiosonde Atmospheric Temperature Products for Assessing Climate    |
| RO        | Radio Occultation  |
| RSS       | Remote Sensing Systems   |
| SAC-C     | Satellite de Aplicaciones Científicas-C                              |
| S.I.      | Système International d'Unités                                       |
| SH        | Southern Hemisphere  |
| SON       | Winter season September, October, November                           |
| STE       | Stratosphere-Troposphere Exchange                                    |

|         |   |
|---------|---|
| STT     | Stratosphere-Troposphere Transport        |
| UAH     | University of Alabama Huntsville          |
| UMd     | University of Maryland                    |
| TIROS-N | Television Infrared Observation Satellite |
| TOVS    | TIROS Operational Vertical Sounder        |
| TST     | Troposphere-Stratosphere Transport        |
| TTL     | Tropical Tropopause Layer                 |
| UKMO    | United Kingdom Meteorological Office      |
| WMO     | World Meteorological Organization         |



# List of Figures

|      |  |    |
|------|--|----|
| 1.1  | Weighting functions of the MSU and mimiced by radiosondes . . . . .          | 5  |
| 1.2  | Long term temperature anomalies from MSU and radiosonde measurements         | 14 |
| 1.3  | Column-mean Temperature from radio wave reflection heights . . . . .         | 16 |
| 1.4  | Temperature trend profile from Rayleigh lidar . . . . .                      | 17 |
| 1.5  | Temperature trend profile from a Russian rocketsonde sounding . . . . .      | 18 |
| 1.6  | Tropospheric-stratospheric trace gas schematic . . . . .                     | 20 |
| 1.7  | Double tropopause measured from aircraft . . . . .                           | 22 |
| 1.8  | CHAMP dry temperature profiles illustrating the tropopause . . . . .         | 24 |
| 1.9  | Seasonal global tropopause distribution as obtained from CHAMP . . . . .     | 25 |
| 1.10 | Global potential temperature and temperature distribution in the UTLS        | 27 |
| 1.11 | Dynamical aspects of STE of 1995 . . . . .                                   | 28 |
| 1.12 | Dynamical aspects of STE of 2003 . . . . .                                   | 30 |
| 2.1  | Radio occultation geometry . . . . .   | 41 |
| 3.1  | CHMAMP RO statistics from 2001 to 2006 . . . . .                             | 51 |
| 3.2  | The EGM 96 Geoid . . . . .   | 53 |
| 3.3  | Difference of reference ellipsoid to geoid: 10° zonal mean . . . . .         | 53 |
| 3.4  | Difference of reference ellipsoid to Geoid: 80° and 140° longitude slices .  | 54 |
| 3.5  | Determination of vertical resolution at different heights . . . . .          | 56 |
| 3.6  | Overlapping and non-overlapping gridding . . . . .                           | 58 |
| 3.7  | CHAMP profile distribution: 10°×15°, 10°×60°, and 10° zonal band . . . .     | 59 |
| 4.1  | Global distribution of CHAMP profiles of NH summer seasons . . . . .         | 63 |
| 4.2  | Dry temperature climatologies of NH summer seasons . . . . .                 | 66 |
| 4.3  | Longitudinal dry temperature climatologies within the equator region . .     | 68 |
| 4.4  | Refractivity climatologies of NH summer seasons . . . . .                    | 70 |
| 4.5  | Longitudinal refractivity climatologies within the equator region . . . . .  | 71 |
| 4.6  | Dry pressure climatologies of NH summer seasons . . . . .                    | 73 |
| 4.7  | Longitudinal dry pressure climatologies within the equator region . . . . .  | 74 |
| 4.8  | Dry geopotential height climatologies of NH summer seasons . . . . .         | 76 |
| 4.9  | Longitudinal dry geopotential height climatologies within the equator region | 77 |
| 4.10 | Systematic dry temperature difference of JJA 2003 . . . . .                  | 79 |
| 4.11 | Temporal evolution of systematic dry temperature difference . . . . .        | 82 |
| 4.12 | Systematic refractivity difference of JJA 2003 . . . . .                     | 84 |
| 4.13 | Temporal evolution of systematic refractivity difference . . . . .           | 85 |
| 4.14 | Systematic dry pressure difference of JJA 2003 . . . . .                     | 86 |

---

|      |   |     |
|------|---|-----|
| 4.15 | Temporal evolution of systematic dry pressure difference . . . . .        | 88  |
| 4.16 | Systematic dry geopotential height difference of JJA 2003 . . . . .       | 89  |
| 4.17 | Temporal evolution of systematic dry geopotential height difference . . . | 90  |
| 4.18 | Profile distribution and dry temp sampling error of April and June 2003 . | 92  |
| 4.19 | Profile distribution and dry temp sampling error of MAM and JJA 2003 .    | 93  |
| 4.20 | Temporal evolution of dry temperature sampling error . . . . .            | 95  |
| 4.21 | Temporal evolution of refractivity sampling error . . . . .               | 96  |
| 4.22 | Temporal evolution of dry pressure sampling error . . . . .               | 97  |
| 4.23 | Dry temperature sampling error in JJA 2003 . . . . .                      | 98  |
|      |   |     |
| 5.1  | Tropical UTLS temporal evolution of systematic dry temp difference . . .  | 100 |
| 5.2  | Cluster plot of MAM 2002 and MAM 2006 CHAMP profiles . . . . .            | 101 |
| 5.3  | MAM 2002 and MAM 2006 dry temp error fields . . . . .                     | 102 |
| 5.4  | Temporal evolution of LRT and CPT temperature and altitude . . . . .      | 105 |
| 5.5  | CHAMP sampling error evolution from 2001 to 2006 . . . . .                | 107 |
| 5.6  | Complete CHAMP sampling error statistics . . . . .                        | 109 |
| 5.7  | Final CHAMP sampling error statistics . . . . .                           | 110 |
| 5.8  | Sampling error model . . . . .  | 112 |
| 5.9  | Sampling error model illustrated on measured data . . . . .               | 114 |
|      |   |     |
| A.1  | Global distribution of CHAMP profiles for seasons SON 2001 to SON 2006    | 142 |
| A.2  | Global distribution statistics for seasons SON 2001 to SON 2006 . . . . . | 143 |
| A.3  | CHAMP dry temperature climatologies . . . . .                             | 144 |
| A.4  | ECMWF dry temperature climatologies . . . . .                             | 145 |
| A.5  | ECMWF – CHAMP systematic dry temperature difference . . . . .             | 146 |
| A.6  | CHAMP dry temperature sampling error . . . . .                            | 147 |
| A.7  | CHAMP dry temperature standard deviation . . . . .                        | 148 |

# A Appendix

In this Appendix, all available CHAMP CCRv2.3 seasonal mean climatologies of dry temperature and their corresponding error fields for SON 2001 to SON 2006, amounting to 21 seasons, are presented. Climatologies are calculated as zonal means in  $10^\circ$  latitude bands in an altitude range from the ground to 35 km. The lowest part, the humid troposphere, is cut off at altitudes ranging from 4 km in polar regions to 8 km at tropical latitudes (see [Chapter 4](#), [Table 4.1](#)). The other parameters have not yet been fully approved and will be shown and discussed in later studies.

[Figure A.1](#) shows the global distribution of CHAMP profiles for each season displayed over a world map to give an idea how the atmosphere was sampled. [Figure A.2](#) gives an insight into how the CHAMP profiles were distributed for each of the 18 zonal latitude bins within each season. The actual dry temperature climatologies are shown in [Figure A.3](#) for CHAMP measurements and in [Figure A.4](#) for the complete field of ECMWF operational analyses.

The following figures display error fields which have been created throughout the presented study and comprise the systematic difference of ECMWF – CHAMP climatologies, [Figure A.5](#), taking the CHAMP climatologies as reference because they have proven to be of very high quality. In [Figure A.6](#) the sampling error is displayed which serves as a measure of the error introduced by the sampling of the CHAMP satellite compared to the full-field-average ECMWF analyses. The last figure, [Figure A.7](#), shows the standard deviation of the ECMWF – CHAMP difference dry temperature climatologies. In general, the standard deviation increases with increasing altitude, which means that at higher altitudes the deviation between the CHAMP profiles and the co-located ECMWF profiles becomes greater.

In summary, this collection of seasonal CHAMP climatologies serves as a small atlas to give a closer and comprehensive overview of the CCRv2.3 dry temperature data analyzed. In this way, the temporal evolution of dry temperature is pictured to a rather full extend. With the error fields shown in addition, the wealth of retrieved data may be easily but informatively browsed through.

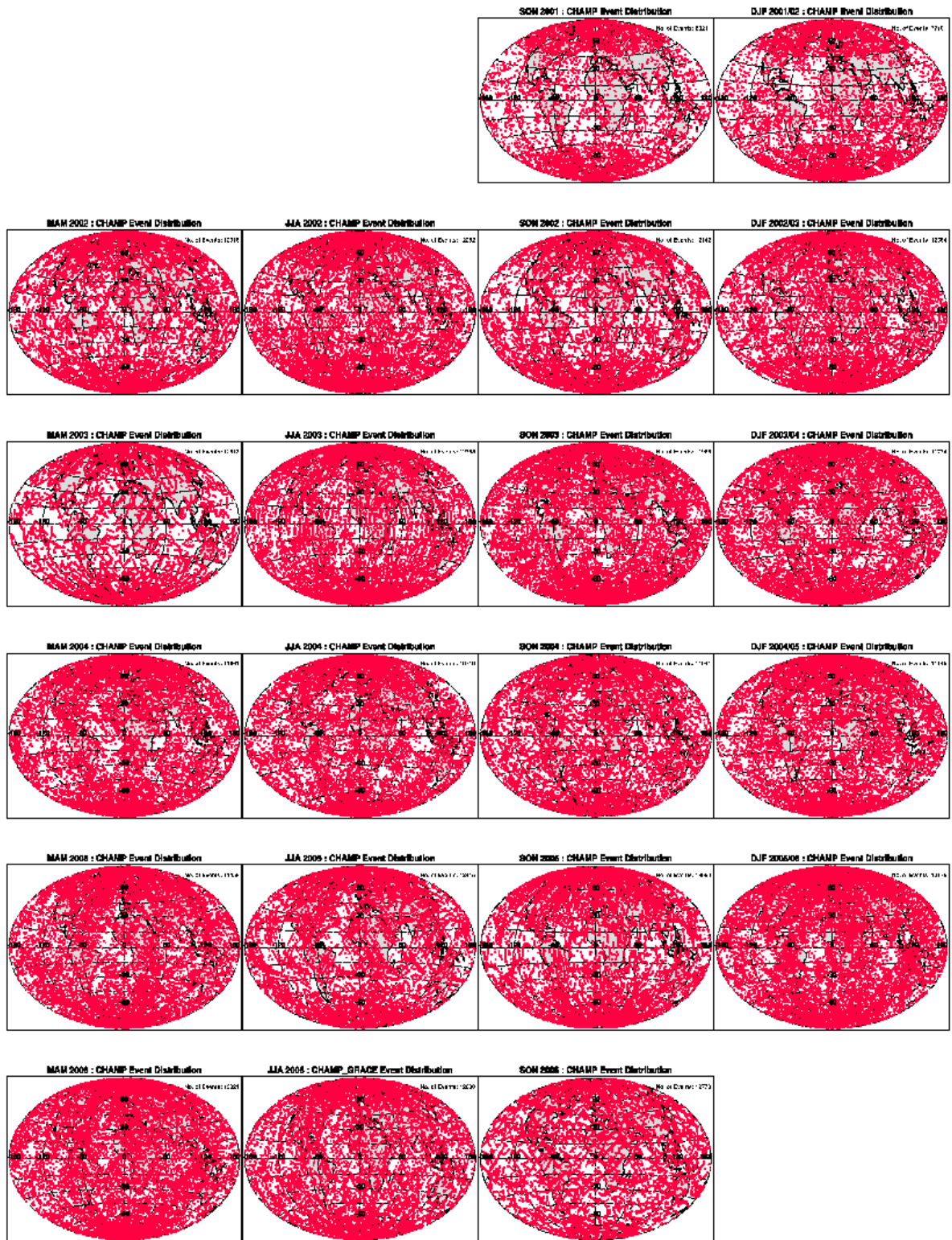


Figure A.1: CHAMP profiles distribution on a global map for seasons SON 2001 to SON 2006.

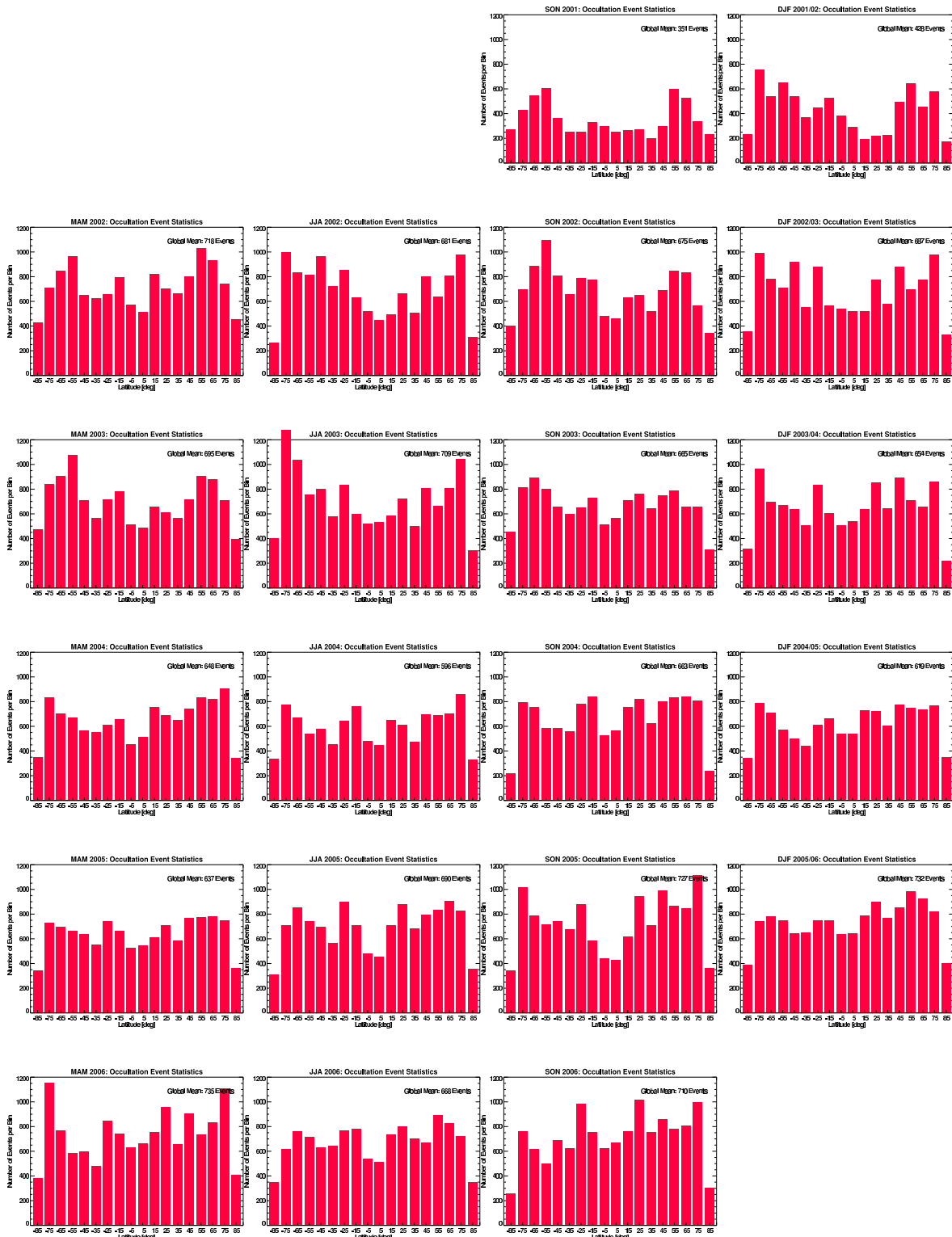


Figure A.2: Global distribution statistics for each zonal bin of seasons SON 2001 to SON 2006.

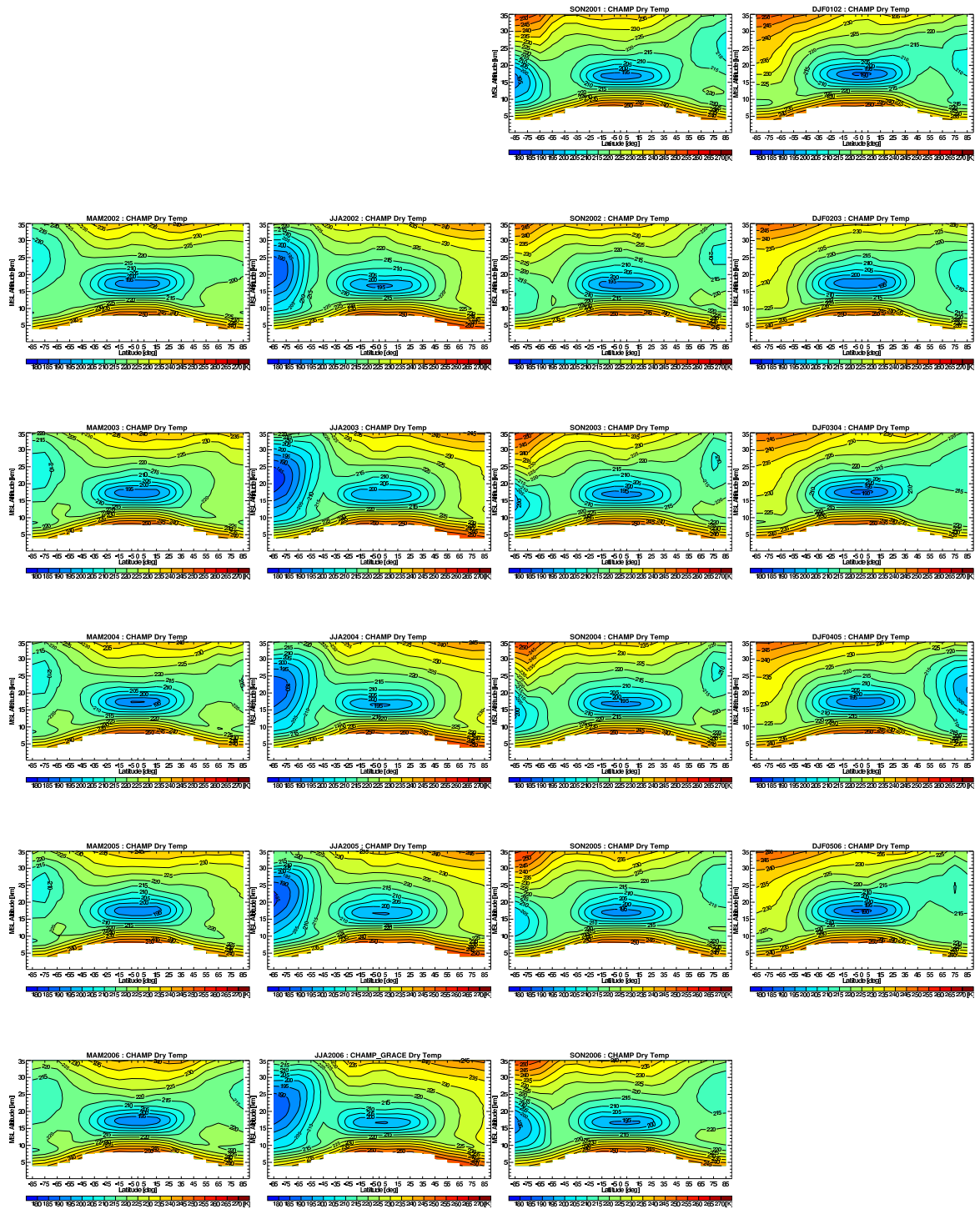


Figure A.3: CHAMP dry temperature climatologies for seasons SON2001 to SON2006.

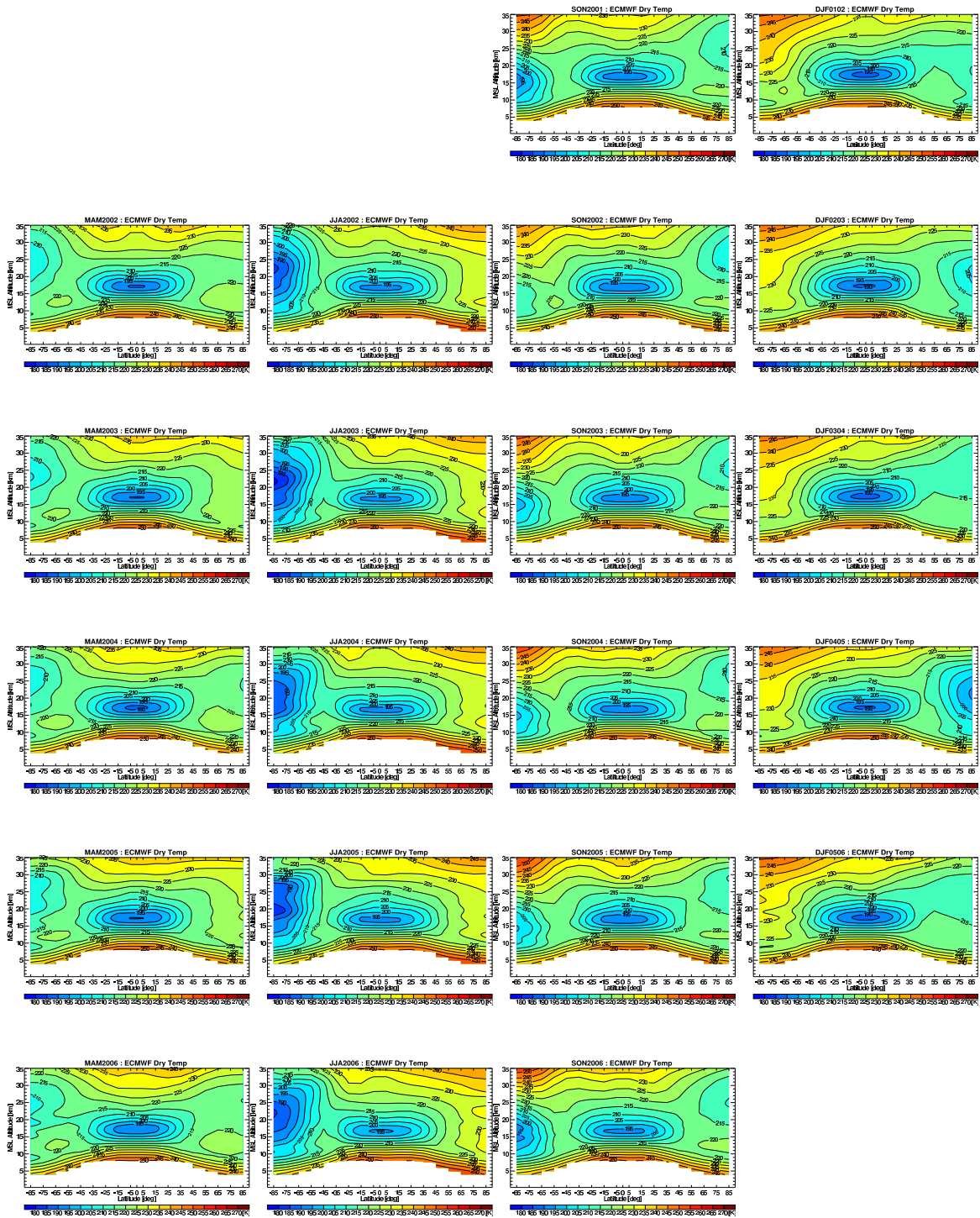


Figure A.4: ECMWF dry temperature climatologies for seasons SON 2001 to SON 2006.

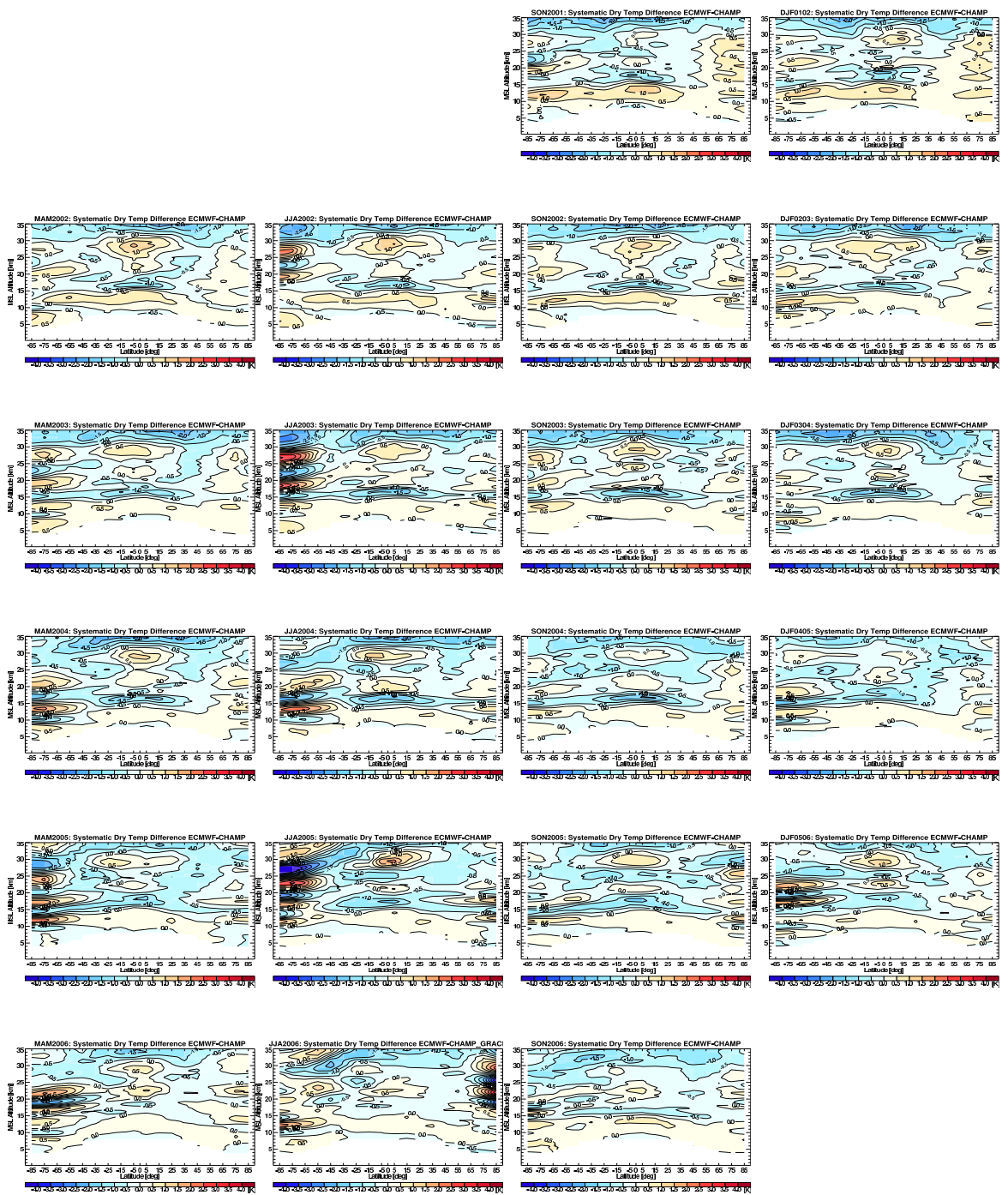


Figure A.5: ECMWF – CHAMP systematic dry temperature difference for seasons SON 2001 to SON 2006.

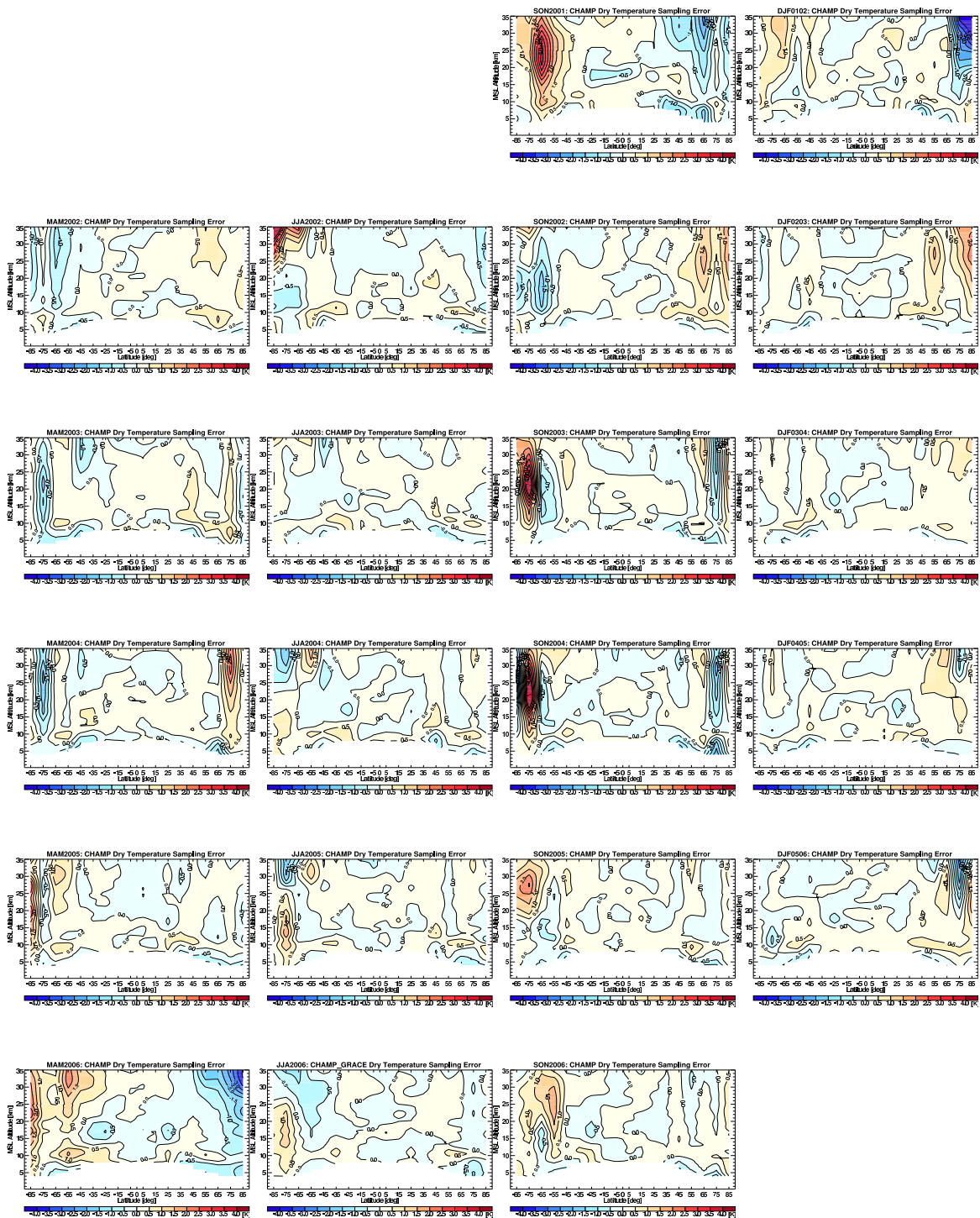


Figure A.6: CHAMP dry temperature sampling error for seasons SON 2001 to SON 2006.

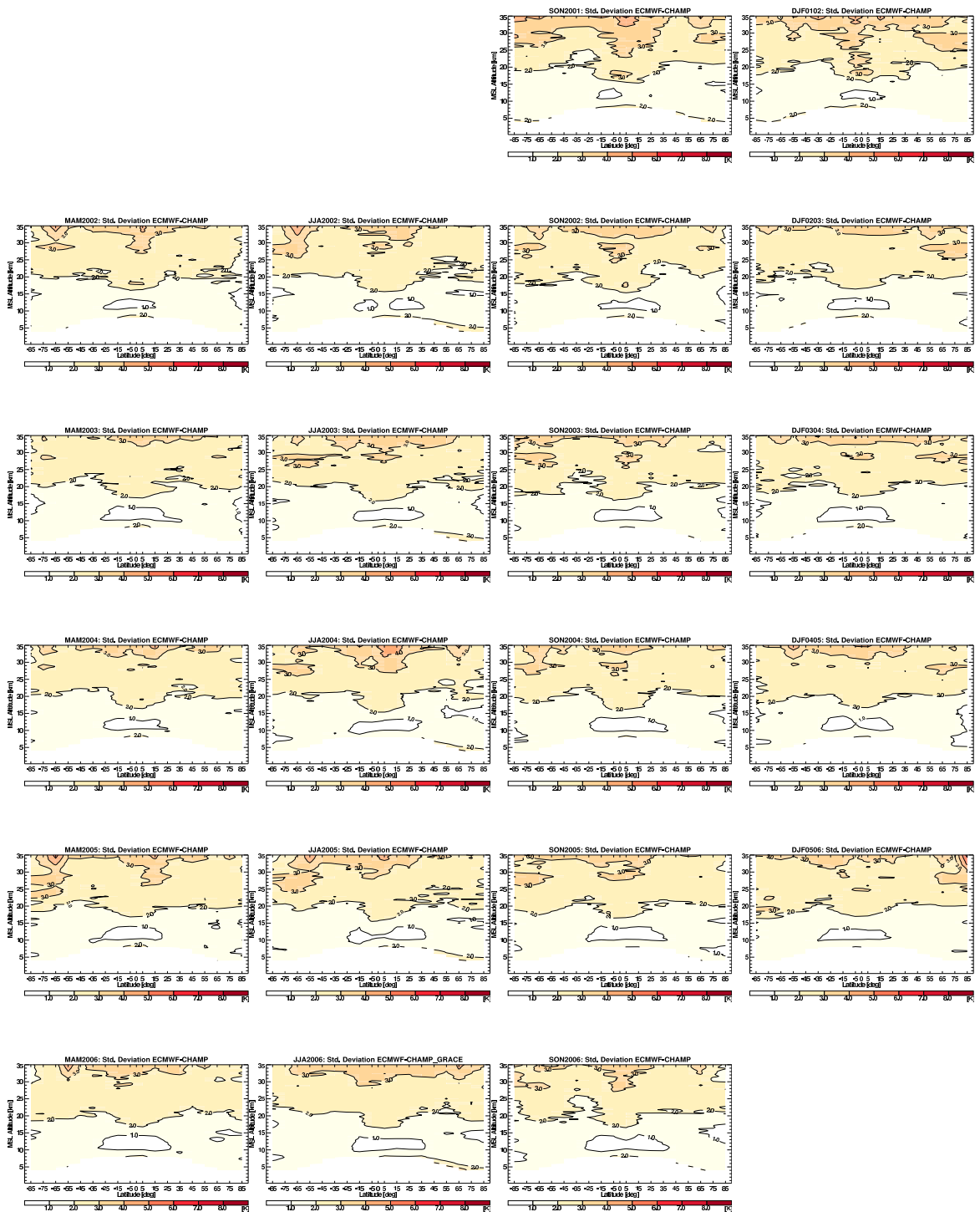


Figure A.7: CHAMP dry temperature standard deviation for seasons SON 2001 to SON 2006.



*Abstract:*

Radio occultation data obtained from the CHALLENGING Minisatellite Payload (CHAMP) satellite were processed with a dry air retrieval algorithm developed at the WegCenter. The main objective of this work was to create zonally averaged seasonal mean climatologies for the atmospheric parameters refractivity, dry temperature, dry pressure, and dry geopotential height. More than five years of data were analyzed covering the time span from September 2001 to November 2006. Climatologies of all parameters and seasons were compared to operational analyses of the European Centre for Medium-Range Weather Forecasts (ECMWF) and systematic differences were investigated. In general, good agreement was found, with systematic temperature differences below 0.5 K, but three regions exhibit larger deviations: altitudes above 30 km, where CHAMP climatologies are about 1 K warmer than ECMWF analyses; the austral winter polar vortex where deviations of up to about  $\pm 3.5$  K exist; and the tropical tropopause region which is up to 2 K colder in the ECMWF analyses. The deviations were found to mainly point to improvement options of the ECMWF analyses. Furthermore, the sampling error of the CHAMP climatologies was studied with the aid of the ECMWF analysis fields. A sampling error model was developed, estimating this error as a function of altitude and latitude (up to 60°N/S), generally obtaining values within  $\pm 0.5$  K.

*Zusammenfassung:*

Radiookkultationsmessungen des CHALLENGING Minisatellite Payload (CHAMP) Satelliten wurden mit einem am WegCenter entwickelten Prozessierungssystem analysiert. Das Hauptziel der vorliegenden Arbeit war es, zonal gemittelte saisonale Klimatologien der atmosphärischen Parameter Refraktivität, Temperatur, Druck und Geopotenzielle Höhe zu erstellen (letztere drei unter Annahme trockener Luft). Die Daten decken mehr als fünf Jahre von September 2001 bis November 2006 ab. Klimatologien aller Parameter und Saisonen wurden mit den operationellen Analysen des Europäischen Zentrums für Mittelfristwettervorhersage (EZMW) verglichen und systematische Differenzen untersucht. Generell liegen die systematischen Temperaturdifferenzen unter 0.5 K aber es gibt drei Regionen, in denen größere Abweichungen auftreten: in Höhen über 30 km sind die CHAMP Klimatologien ca. 1 K wärmer als die EZMW Analysen, im polaren Vortex im südhemisphärischen Winter treten Abweichungen bis zu ca.  $\pm 3.5$  K auf, und die tropische Tropopause ist in den EZMW Analysen um ca. 2 K kühler. Es zeigte sich, dass diese Abweichungen hauptsächlich auf Verbesserungspotenzial der EZMW Analysen hinweisen. Weiters wurde der Sampling-Fehler der CHAMP Klimatologien mit Hilfe der EZMW Analysen abgeschätzt. Ein Sampling-Fehler-Modell wurde erstellt, welches diesen Fehler als Funktion der Höhe und geographischen Breite (bis 60°N/S) abschätzt; die Werte liegen generell innerhalb  $\pm 0.5$  K.